TECHNISCHE UNIVERSITÄT MÜNCHEN

Munich School of Engineering

Research group “Control of Renewable Energy Systems”

Dissertation

Modelling and control of large-scale direct-drive wind turbine systems under open-switch faults in the machine-side converter

Korbinian Schechner, M.Sc.

TECHNISCHE UNIVERSITÄT MÜNCHEN

Munich School of Engineering

Research group "Control of Renewable Energy Systems"

Modelling and control of large-scale direct-drive wind turbine systems under open-switch faults in the machine-side converter

Korbinian Schechner, M.Sc.

Vollständiger Abdruck der von der Munich School of Engineering der Technischen Universität München zur Erlangung des akademischen Grades eines

Doktor–Ingenieurs

genehmigten Dissertation.

Vorsitzender:		Prof. Dr. Rolf Witzmann
Prüfer der Dissertation:	1.	Prof. Dr. Christoph M. Hackl
	2.	Prof. Dr. Thomas Hamacher
	3.	Assoc. Prof. Dr. Marko Hinkkanen

Die Dissertation wurde am 10.04.2019 bei der Technischen Universität München eingereicht und durch die Munich School of Engineering am 27.05.2020 angenommen.

Ich erkläre an Eides statt, dass ich die bei der promotionsführenden Einrichtung

Munich School of Engineering

der TUM zur Promotionsprüfung vorgelegte Arbeit mit dem Titel:

Modelling and control of large-scale direct-drive wind turbine systems under open-switch faults in the machine-side converter

in der Forschergruppe "Regelung von regenerativen Energiesystemen" unter der Anleitung und Betreuung durch:

Prof. Dr.-Ing. Christoph M. Hackl

ohne sonstige Hilfe erstellt und bei der Abfassung nur die gemäß § 6 Abs. 6 und 7 Satz 2 angegebenen Hilfsmittel benutzt habe.

[x] Ich habe keine Organisation eingeschaltet, die gegen Entgelt Betreuerinnen und Betreuer für die Anfertigung von Dissertationen sucht, oder die mir obliegenden Pflichten hinsichtlich der Prüfungsleistungen für mich ganz oder teilweise erledigt.

[x] Ich habe die Dissertation in dieser oder ähnlicher Form in keinem anderen Prüfungsverfahren als Prüfungsleistung vorgelegt.

[ ] Die vollständige Dissertation wurde in ___ veröffentlicht. Die promotionsführende Einrichtung Munich School of Engineering hat der Vorveröffentlichung zugestimmt.

[x] Ich habe den angestrebten Doktorgrad noch nicht erworben und bin nicht in einem früheren Promotionsverfahren für den angestrebten Doktorgrad endgültig gescheitert.

[ ] Ich habe bereits am ___ bei der Fakultät für ___ der Hochschule ___ unter Vorlage einer Dissertation mit dem Thema ___ die Zulassung zur Promotion beantragt mit dem Ergebnis: ___

Die öffentlich zugängliche Promotionsordnung der TUM ist mir bekannt, insbesondere habe ich die Bedeutung von § 28 (Nichtigkeit der Promotion) und § 29 (Entzug des Doktorgrades) zur Kenntnis genommen. Ich bin mir der Konsequenzen einer falschen Eidesstattlichen Erklärung bewusst. Mit der Aufnahme meiner personenbezogenen Daten in die Alumni-Datei bei der TUM bin ich

[x] einverstanden,
[ ] nicht einverstanden.

Steinhöring, 28.03.2019 Korbinian Schaeche

Ort, Datum Unterschrift

This document is typeset with LaTeX/TeX.

Danksagung

Mein erster Dank gilt Prof. Dr.-Ing. Christoph M. Hackl, für die Möglichkeit diese Dissertation zu verfassen. Seine hervorragende Betreuung, sein Drängen, Sachverhalte immer genau zu verstehen und seine Bereitschaft jederzeit für Fragen und Diskussionen zur Verfügung zu stehen, waren von unschätzbarem Wert für mich. Genauso wichtig war, dass er mir stets die Freiheit eingeräumt hat, selbständig zu arbeiten und eigene Wege zu gehen.

Ein weiterer Dank gilt Prof. Dr. Thomas Hamacher für die Übernahme des Zweitgutachtens und seine große Unterstützung als Direktor der MSE. Prof. Dr. Marko Hinkkanen gilt mein Dank für die Übernahme des Drittgutachtens. Außerdem möchte ich Prof. Dr.-Ing. Rolf Witzmann für die Übernahme des Prüfungsvorsitzes danken. Ein besonderer Dank gilt meinem Mentor Dr. Sc. Vlaho Petrović für seine Unterstützung und seine Ratschläge.

Ein sehr großes Danke geht an Christian Dirscherl. Durch die intensive gemeinsame Arbeit, die unzähligen Diskussionen und die Möglichkeit, jederzeit Ideen gemeinsam zu überprüfen, wurde es erst möglich, das für diese Arbeit notwendige tiefe Verständnis zu erlangen. Dazu haben auch meine Kollegen Hisham Eldeeb, Julian Kullick und Markus Landerer beigetragen. Bei ihnen und den weiteren Mitgliedern unserer Forschergruppe, Mohamed Abdelrahem, Katharina Bär, Athina Birda, Simon Krüner, Cristian Ladisla und Zhenbin (James) Zhang möchte ich mich zusätzlich für die schöne gemeinsame Zeit außerhalb der gemeinsamen Arbeit bedanken. Dafür und für den guten Zusammenhalt danke ich auch den weiteren MSE-Doktoranden, Mihael Čorić, Oliver Filonik, Akhila Jambagi, Michael Kramer, Jenny Lebert, Thomas Lickleder und Stephan Pröller.

Ein weiterer großer Dank gilt meinen Studenten, Andjelka Bujandric, Marion Eigner, Fahad Hassan, Jonas Hauser, Benjamin Kalmbach, Mariem Khemir, Max Lindner, Salma Mansi, Richard Moderegger, Niklas Monzen, Laura Mora, Urs Pecha, Jiufang Peng, Ingrid Sánchez, Philipp Schmitz, Chun Wei Tan, Eva Wittgen und Minghao Xu für ihre Unterstützung und die gute Zusammenarbeit. Besonders hervorheben möchte ich Max Lindner, der als Wissenschaftliche Hilfskraft tätig war. Seine Aufbauten waren unerlässlich für meine Messungen.

Für die Unterstützung im Labor und bei allen praktischen Fragen möchte ich mich bei den Kollegen vom Lehrstuhl für elektrische Antriebssysteme und Leistungselektronik bedanken, Prof. Dr.-Ing. Dr. h.c. Ralph Kennel, Florian Bauer, Hannes Börngen, Julien Cordier, Wolfgang Ebert, Ali El-Hafni, Alexander Florian, Heidi Jonas, Stefan Klaß, Sascha Kühl, Peter Landsmann, Eyke Liegmann, Darshan Manoharan, Julia Menz, Dirk Paulus und Dietmar Schuster.

Ein weiterer Dank gebührt den Kollegen vom Lehrstuhl für Windenergie, Prof. Dr. Carlo L. Bottasso, Marta Bertelè, Pietro Bortolotti, Stefano Cacciola, Filippo Campagnolo, Mark Capellaro, Elli Matzner, Johannes Schreiber, Jesse Wang und Robin Weber, die mich und unsere Gruppe nicht nur fachlich unterstützt haben, sondern uns auch über zwei Jahre ein Zuhause gegeben haben. Für die schöne Gemeinschaft in unserem neuen Zuhause möchte ich allen "ZEI-Mitbewohnern" danken.

Bedanken möchte ich mich auch bei der MSE-Verwaltung für deren Unterstützung bei jeglichen Belangen, besonders bei Angela Brunnbauer, Christiane Hamacher, Sabine Kutscherauer und Monika Knürr.

Für das Korrekturlesen dieser Arbeit bin ich Tanja und Sebastian Bartsch, Christian Dirscherl, Hisham Eldeeb, Julian Kullick, Thomas Küntzler und Markus Landerer sehr dankbar.

Mein Dank gilt auch dem Bayerischen Staatsministerium für Bildung und Kultus, Wissenschaft und Kunst, welches die Forschergruppe “Regelung von regenerativen Energiesystemen” finanzierte. Die lange Projekt- und Vertragslaufzeit waren eine Voraussetzung für die langfristig angelegte und gründliche Forschungsarbeit.

Zum Abschluss gilt ein sehr großer Dank meinen Eltern und meiner Familie, ohne ihre umfassende Unterstützung wäre weder mein Studium noch meine Promotion in dieser Weise durchführbar gewesen.

Steinhöring, August 2020 Korbinian Schechner

Contents

Nomenclature

Mathematical symbols and functions with description:

$\mathbb{N}, \mathbb{R}, \mathbb{C}$	natural, real and complex numbers.
$\boldsymbol{x} := (x_1, \ldots, x_n)^\top \in \mathbb{R}^n$	column vector, $n \in \mathbb{N}$ where "$^\top$" and ":=" mean "transposed" (interchanging rows and columns of matrix or vector) and "is defined as", respectively.
$\mathbf{0}_n := (0, \ldots, 0)^\top \in \mathbb{R}^n$	zero vector.
$\mathbf{0}_{n\times m} \in \mathbb{R}^{n\times m}$	zero matrix.
$\mathbf{1}_n := (1, \ldots, 1)^\top \in \mathbb{R}^n$	unity vector.
$\boldsymbol{a}^\top \boldsymbol{b} := a_1 b_1 + \cdots + a_n b_n$	scalar product of the vectors $\boldsymbol{a} := (a_1, \ldots, a_n)^\top$ and $\boldsymbol{b} := (b_1, \ldots, b_n)^\top$.
$\|\boldsymbol{x}\| := \sqrt{\boldsymbol{x}^\top \boldsymbol{x}} = \sqrt{x_1^2 + \cdots + x_n^2}$	Euclidean norm of $\boldsymbol{x}$.
$\boldsymbol{A} \in \mathbb{R}^{n\times n}$	(square) matrix with n rows and n columns.
$\boldsymbol{A}^{-1}$	inverse of $\boldsymbol{A}$ (if exists).
$\det(\boldsymbol{A})$	determinant of $\boldsymbol{A}$.
$\mathrm{round}(a)$	nearest natural number (in $\mathbb{N}$) to $a \in \mathbb{R}$ (for .5 the larger value is chosen).
$\mathrm{diag}(a_1, \ldots, a_n) \in \mathbb{R}^{n\times n}$	diagonal matrix with entries $a_1, \ldots, a_n \in \mathbb{R}$, $n \in \mathbb{N}$.
$\boldsymbol{I}_n := \mathrm{diag}(1, \ldots, 1) \in \mathbb{R}^{n\times n}$	identity matrix.
$\alpha \overset{(\#1)}{\underset{(\#2)}{=}} \beta$	equivalence of α and β follows directly by invoking Eq. (#1) and Eq. (#2) (same notation is also used for relations, e.g. $<$, $\leq$, $\geq$ and $>$).
$\boldsymbol{x}$ (in X)^n	physical quantities $\boldsymbol{x} \in \mathbb{R}^n$, each of the n elements has SI-unit X.
$\boldsymbol{\xi}^{abc} := \left(\xi^a, \quad \xi^b, \quad \xi^c\right)^\top \in \mathbb{R}^3$	quantities $\boldsymbol{\xi}^{abc}$ (may represent currents, voltages and flux linkages, i.e. $\boldsymbol{\xi} \in \{\boldsymbol{i}, \boldsymbol{u}, \boldsymbol{\psi}\}$) in the three-phase *abc*-reference frame.
$\boldsymbol{\xi}^{a\text{-}b\text{-}c} := \left(\xi^{a\text{-}b}, \quad \xi^{b\text{-}c}, \quad \xi^{c\text{-}a}\right)^\top \in \mathbb{R}^3$	line-to-line quantities $\boldsymbol{\xi}^{a\text{-}b\text{-}c}$.

$\boldsymbol{\xi}^{\alpha\beta} := \left(\xi^{\alpha},\ \ \xi^{\beta}\right)^{\top} \in \mathbb{R}^2$	quantities $\boldsymbol{\xi}^{\alpha\beta}$ in the stator-fixed $\alpha\beta$-reference frame.
$\boldsymbol{\xi}^{dq} = \left(\xi^{d},\ \ \xi^{q}\right)^{\top} \in \mathbb{R}^2$	quantities $\boldsymbol{\xi}^{dq}$ in the arbitrarily rotating dq-reference frame.
$f_{\hat{a}}(x) := \begin{cases} 0 & , x > \hat{a} \\ 1 & , x \leq \hat{a} \end{cases}$	Step function $f_{\hat{a}} \colon \mathbb{R} \to [0,\, 1]$ at $\hat{a} \in \mathbb{R}$.
$f_{u_{\min},u_{\max}}(x,e) := \begin{cases} 0 & , \begin{smallmatrix}(x>u_{\max} \text{ and } e>0)\\ \text{or}\\ (x<u_{\min} \text{ and } e<0)\end{smallmatrix} \\ 1 & , \text{otherwise} \end{cases}$	Transition function $f_{u_{\min},u_{\max}} \colon \mathbb{R}^2 \to [0,\, 1]$ for $u_{\min},\, u_{\max},\, e \in \mathbb{R}$.
$\operatorname{sat}_a^b(x) := \begin{cases} b & , x \geq b \\ x & , a < x < b \\ a & , x \leq a. \end{cases}$	Scalar saturation function $\operatorname{sat}_a^b \colon \mathbb{R} \to [a,\, b]$ with $b > a$.
$\mathbf{sat}_{\widehat{u}}(\boldsymbol{x}) := \begin{cases} \widehat{u}\frac{\boldsymbol{x}}{\|\boldsymbol{x}\|} & , \|\boldsymbol{x}\| \geq \widehat{u} \\ \boldsymbol{x} & , \|\boldsymbol{x}\| < \widehat{u}. \end{cases}$	Vector-valued saturation function $\mathbf{sat}_{\widehat{u}} \colon \mathbb{R}^n \to \{\boldsymbol{x} \in \mathbb{R}^n \mid \|\boldsymbol{x}\| \leq \widehat{u}\}$ for $\widehat{u} > 0$.

In order to preserve clarity, the units and dependencies of values could be left out in formulas.

Abstract

This thesis discusses the modelling and control of large-scale direct-drive wind turbine systems (WTSs) under open-switch faults in the machine-side converter. The two machine types used in direct-drive WTSs are the permanent magnet synchronous machine (PMSM) and the electrically excited synchronous machine (EESM). For the EESM, a nonlinear dynamic model including damper windings is derived. A method is developed to measure the nonlinear flux linkage maps of the EESM. Current and torque controllers are designed based on the nonlinear flux linkage maps. For linear PMSMs and nonlinear EESMs, post-fault control strategies are developed. Such strategies cover an improved anti-windup strategy, a modified space-vector modulation, and an optimal d-axis current injection for PMSMs and a fault-optimal current reference generation for EESMs. The impacts of the post-fault control strategies on WTSs are investigated in the laboratory. For that, the dynamics of large-scale wind turbine systems are down-scaled for real-time emulation to small-scale laboratory setups based on the ratios of physical SI-units. The measurement results show that it is possible for both machines to produce almost the same amount of energy as in the fault-free case, when the proposed post-fault strategies are applied to WTSs with open-switch converter faults.

Kurzzusammenfassung

Diese Arbeit befasst sich mit der Modellierung und Regelung von Windkraftanlagen (WKAn) mit Schalterfehlern im maschinenseitigen Umrichter. Die in diesen WKAn eingesetzten elektrischen Maschinen sind die Permanentmagnet-Synchronmaschine (PMSM) und die elektrisch erregte Synchronmaschine (EESM). Für die EESM wird ein nichtlineares dynamisches Modell hergeleitet welches auch die Dämpferwicklungen berücksichtigt. Für diese Modellierung der EESM werden Flusskarten benötigt. Hierfür wird eine Methode zur Messung der Flusskarten von EESMn entwickelt. Mittels dieser Flusskarten werden die Stromregler ausgelegt und eine Momentensteuerung entworfen. Sowohl für lineare PMSMn als auch für nichtlineare EESMn werden Regelstrategien für den Fehlerfall entwickelt. Diese beinhalten ein angepasstes "Anti-windup" in der Stromregelung, eine modifizierte Raumzeigermodulation und für PMSMn eine fehleroptimale d-Stromeinprägung, bzw. für EESMn eine fehleroptimale Stromreferenzgenerierung. Die Auswirkungen der Regelstrategien für den Fehlerfall auf WKAn werden im Labor untersucht. Dafür wird die Dynamik von WKAn großer Leistung auf Laborprüfstände kleiner Leistung skaliert. Diese Skalierung basiert auf den Verhältnissen physikalischer SI-Einheiten. Die Messergebnisse zeigen, dass es, unter Verwendung der für diesen Fall angepassten Regelstrategien, für beide Maschinentypen möglich ist, auch im Fehlerfall annähernd die gleiche Energiemenge wie im fehlerfreien Fall zu erzeugen.

List of Publications

During my employment at the Technische Universität München (TUM), as member of the research group *"Control of renewable energy systems"* (CRES) of the Munich School of Engineering (MSE) several publications were written. The research group was part of the project Energy Valley Bavaria (EVB) and was funded by the Bavarian State Ministry of Education, Science and Arts.

Publications related to the dissertation

Parts of this thesis are based on the following publications which have already been published:

- K. Schechner, C. M. Hackl, "Scaling of the drive train dynamics of large-scale wind turbine systems for real-time emulation in small-scale laboratory setups", *IEEE Transactions on Industrial Electronics*, vol. 66, pp. 6779-6788, Sep. 2019, [1].

- C. M. Hackl, U. Pecha, K. Schechner, "Modeling and Control of Permanent-Magnet Synchronous Generators Under Open-Switch Converter Faults", *IEEE Transactions on Power Electronics*, vol. 34, pp. 2966-2979, March 2019, [2].

- C. M. Hackl, P. Jané-Soneira, M. Pfeifer, K. Schechner, S. Hohmann, "Full- and Reduced-Order State-Space Modeling of Wind Turbine Systems with Permanent Magnet Synchronous Generator", *Energies*, vol. 11 no. 7, 2018, [3].

- C. Dirscherl, C. M. Hackl, K. Schechner, "Modellierung und Regelung von modernen Windkraftanlagen: Eine Einführung", pp. 1540-1614 in D. Schröder *"Elektrische Antriebe – Regelung von Antriebssystemen"* (4. edition), Springer-Verlag, 2015, [4].

Further publications

- K. Schechner, F. Bauer, C. M. Hackl, "Nonlinear DC-link PI Control for Airborne Wind Energy Systems During Pumping Mode", pp. 241-276 in R. Schmehl *"Airborne Wind Energy: Advances in Technology Development and Research"*, Springer-Verlag, 2018, [5].

- K. Schechner, C. M. Hackl, "Detection of rotational periodic torque deviations in variable-speed wind turbine systems using disturbance observer and phase-locked loop", *Journal of Physics: Conference Series (JPCS)*, vol. 1037, no. 3, 2018, [6].

- C. M. Hackl, K. Schechner, "Non-ideal feedforward torque control of wind turbines: Impacts on annual energy production and gross earnings", *Journal of Physics: Conference Series (JPCS)*, vol. 753, no. 11, 2016, [7].

- C. Dirscherl, C. M. Hackl, and K. Schechner, "Pole-placement based nonlinear state-feedback control of the DC-link voltage in grid-connected voltage source power converters: A preliminary study", *Proceedings of the 2015 IEEE Conference on Control Applications (CCA)*, pp. 207-214, (Sydney, Australia), 2015, [8].
- C. Dirscherl, C. M. Hackl, K. Schechner, "Explicit model predictive control with disturbance observer for grid-connected voltage source power converters", *Proceedings of the 2015 IEEE International Conference on Industrial Technology (ICIT)*, pp. 999-1006, (Seville, Spain), 2015, [9].

Chapter 1

Introduction

Wind turbine systems (WTSs) generate renewable electric energy at competitive costs. According to [10], onshore WTSs are already today one of the most cost-efficient renewable energy sources to produce electric energy in Germany. Also, the costs are expected to decrease further [10]. In Germany in 2017, a total capacity of 56 356 MW of wind power was installed [11] (worldwide: 513 547 MW [12]). The WTSs in Germany produced 107.5 TW h of electric energy, which corresponds to 16.4 % of the total energy generation or 49.7 % of the renewable energy generation in 2017 [11]. Therefore, wind energy already today plays a crucial role in the electric power system [13]. As it is planed to further increase the total capacity of wind power [11], the importance of wind power for the overall power system will increase in the future. Hence, the reliability of WTSs would directly influence the reliability of the overall power system.
This chapter is divided as follows: Section 1.1 illustrates the motivation for this work. In Sect. 1.2 the state-of-the-art is depicted and Sect. 1.3 highlights the contributions of this thesis. The following sections are partially based on [1, 2] in which parts have already been published.

1.1 Motivation

Direct-drive WTSs using a permanent magnet synchronous machine (PMSM) or an electrically excited synchronous machine (EESM) as generator account for about 40 % of the totally installed onshore WTSs in Germany [10]. Figure 1.1 shows an overview of the components of a direct-drive WTS. In the direct-drive configuration, the gear box is waived between turbine and the generator (PMSM/EESM). The stator of both machines is connected to a back-to-back

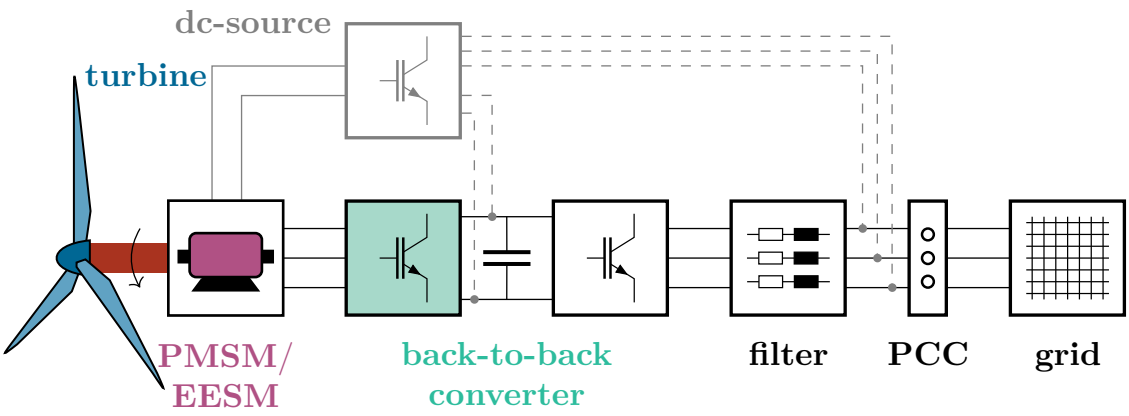

Figure 1.1: *Overview of the components of a direct-drive wind turbine system with PMSM or EESM.*

converter. Additionally, for the EESM, the exciter is connected to a dc-source for powering the electromagnets. The back-to-back converter feeds the power via a filter at the point of common coupling (PCC) into the grid.

As these direct-drive systems do *not* have a gear box between turbine and generator (see Fig. 1.1), a subsystem that causes long downtimes and high maintenance costs is already absent in this type of WTSs [14–16]. According to [14], the electric subsystems of WTSs cause 25 % of the total failures and 14 % of the total down time of WTSs. For power converters—the heart of the electric subsystem—the power semiconductors are within the top three reasons for failures. In the survey [17], the power semiconductors were named as the most fragile components. Capacitors and gate drivers followed on rank two and three, respectively.

A typical fault of a power semiconductor is the open-switch fault. Open-switch faults in converters for electric drives have gained increasing attention in the last years. An open-switch fault can be caused by thermic cycling, driver failures, or by a rupture of the insulated-gate bipolar transistor (IGBT) that is induced by a short-circuit fault [18–20]. Unlike short-circuit faults, open-switch faults do usually *not* trigger a system shutdown, but degrades the system performance and can cause—without proper countermeasures—secondary faults in other components (see [21, 22]). Without adequate fault-tolerant modifications, the faulty converter will cause increased losses and large torque ripples/oscillations which will harm the mechanical components and the generator of the wind turbine [23]. Open-switch faults are therefore a crucial type of faults in converters and should be considered in the design of a robust and fault-tolerant (hence more reliable) electric drive system.

This far, especially the detection of faults in the converter and the identification of the faulty switch have been the focus of research. Various detection methods have already been reported [18, 21–35]. Therefore, fault detection will *not* be discussed in this thesis.

After the detection of an open-switch fault, the WTS is usually shut down—to avoid secondary faults—until maintenance is carried-out. Especially for offshore WTSs, the maintenance is challenging. Depending on the weather conditions and reachability such fault might cause long downtimes of the WTS. Hence, a huge portion of energy production is lost and the revenue is significantly decreased due to an open-switch fault [36]. Developing a post-fault control strategy *without* the need of additional hardware equips the WTS operator with a simple option to reliably produce electric energy and gain earnings even in the faulty case. It is shown at the end of this thesis that it is possible to produce (almost) the same amount of energy as in the fault-free case when the proposed post-fault control strategies are used. Hence, with simple control strategy manipulations (no changes in the hardware necessary), the WTS is still able to produce energy instead of being shut down.

1.2 State-of-the-art

In this section, a brief overview on the state-of-the-art of this thesis's topics are provided and the corresponding contributions of this work are highlighted. First, a literature review on the post-fault control of electric machines for open-switch converter faults is given[1]. Afterwards, the state-of-the-art for modelling and control of electrically excited synchronous machines is discussed. Finally, the scaling approaches of wind turbine systems for laboratory setups found in literature are reviewed[2]. The following sections describe the strengths and weaknesses of the existing approaches.

[1] This review (for PMSMs) was already published in [2] and was extended for this thesis.

[2] This review was already published in [1] and was extended for this thesis.

1.2.1 Post-fault control of electric machines for open-switch converter faults

To ensure a safe and uninterrupted operation of electric drives for open-switch converter faults, a fault-tolerant control strategy has to be implemented. In [37–40], a modified space-vector modulation (SVM) is proposed for two-level converters. These publications adapt the switching patterns and replace those space-vectors which cannot be applied due to the open-switch fault. However, these papers neither consider optimal phase shift angles between applied voltage and current vector nor adapt their current controllers to the post-fault operation, although—as will be shown later—these measures additionally and significantly improve the overall post-fault control performance.

For three-level converters using neutral-point clamped (NPC) or T-type configurations, the redundancy in the switching states can be used to compensate for the infeasible switching states and to generate the desired voltage output, see [24,26,41,42]. In addition, [42] proposes to inject an additional d-axis current to shift the phase angle between reference voltage and current to 0° if an open-switch fault occurs in one of the outer switches. This helps to avoid infeasible switching states, and therefore reduces the current distortion in the faulty phase of the generator. However, the use of redundant switching vectors can not be used for two-level converters, since there is no sufficient redundancy within the available switching states. The impact of an open-switch fault reduces the feasible voltage area in the voltage hexagon of a two-level converter significantly. Moreover, in [24,26,41,42], the current control system and its impact on the control performance during faults are not discussed in detail.

In [43], it is proposed to consider converters with open-switch faults as *three-switch three-phase rectifiers* (all upper or lower switches are assumed to be simply diodes). This publication investigates the possible avoidance of infeasible zero switching vectors in space-vector modulation. To achieve a minimal current distortion, a phase shift of 180° between current and voltage vector is proposed. This phase shift is achieved by injecting an appropriate d-current. Further investigations in this thesis will show that, for the considered permanent magnet synchronous machine, 180° is not the *optimal* phase shift angle to guarantee a minimal current distortion. Moreover, in [43], the impact of the open-switch fault on the control performance of the current controller (such as windup effects) is neither addressed nor tackled, and a generic converter model covering open-switch faults e.g. for simulation purposes is not provided.

Another possibility to ensure a continued operation of the generator is the use of fault-tolerant converter configurations. Different topologies and methods to control faulty converters are described in [43–48]. For example, in case of open-switch faults, a fourth converter leg can be used, or the neutral point of the machine can be connected to the midpoint of the dc-bus. Both solutions can compensate for the loss of the phase with the faulty switch. However, additional and costly hardware components or reconfigurations are required in contrast to standard converter configurations.

As shown above, there exist publications on the post-fault control of PMSMs. In [49], the post-fault control of an induction machine is discussed. But to the best knowledge of the author, there are no publications tackling the issue of post-fault control of EESMs for open-switch converter faults.

Investigations in [50] show that the machine-side converter of WTSs fails more often than the grid-side converter. Hence, this thesis will focus on post-fault control of the machine-side converter of a WTS under an open-switch fault.

1.2.2 Modelling and control of electrically excited synchronous machines

While the dynamic modelling and control of a PMSM including saturation effects and magnetic cross-couplings can be found in literature (see [51, Sect. 14.3.2], [52]), obtaining such a model

for EESMs is more complex. The modelling approaches for EESMs found in textbooks usually assume linear magnetization, neglecting iron-core saturation and cross-coupling (mutual) inductances [53, Chap. 6], [54, Chap. 6], [55, Chap. 2,5], [56, Chap. 16], [57, Chap. 6,7]. The modelling is performed in field orientation. It is a well known fact that, especially for high torques, EESMs are affected by magnetic saturation [58]. Hence, some books do consider saturation effects but only for steady state operation, or for direct connection to the power grid, or only in *d*-direction of the stator [59], [60, Chap. 5], [61, Chap. 4], [62, Chap. 5].

Papers focusing on the dynamics of the EESM usually do not model damper windings [63–74]. Also in these papers, the modelling in most cases assumes linear magnetization (no saturation) and neglects cross-coupling inductances. But some approaches in literature try to include saturation effects in the modelling. The authors in [67] consider the impact of saturation on the machine torque by measuring the torque for different stator and rotor currents and storing this information in a torque lookup table. In [58], finite element analysis (FEA) data of the nonlinear flux linkage maps is approximated by polynomials and used for online computation of a maximum torque per current (MTPC) trajectory. FEA flux linkage maps are used in [68] for the online computation of the MTPC trajectory and to switch the control strategy when reaching the voltage limit. In [72], also FEA flux linkage maps are used for the computation of the MTPC trajectory and additionally the cross-coupling (mutual) inductances are considered for the stator. But the excitation current, its dynamics, the (coupling) inductances and its flux linkage is not taken into account. The authors in [73] derive a dynamic model of an EESM allowing for saturation. Therefore, current dependent secant/absolute and differential inductances (including cross-coupling) are used for the model. A model for the damper windings is missing and no information on obtaining these inductances is given. In most cases, the excitation resistance is assumed to be constant or only depending on temperature. A model considering the dependency of this resistance on the excitation current was not found. To the best knowledge of the author, a nonlinear dynamic model of the EESM with damper windings, excitation current dependent excitation resistance, measured flux linkage maps and current dependent differential inductances including cross-coupling (mutual) inductances does not exist in literature.

For the current controller, usually field-oriented control using PI-controllers (see [53, Chap. 6], [54, Chap. 6], [55, Chap. 2,5], [68], [71]), sliding mode controllers (see [64, 66]), passivity based controllers (see [63]) or state-feedback controllers (see [65]) are used. However these controllers do not consider the cross-coupling inductances and the stator-exciter coupling inductances.

As described above, nonlinear machine modelling is usually only used to compute better current references for feedforward torque control. This is done offline and numerically. Using a linear model for the magnetization of the machine, analytical solutions for the MTPC trajectory and field weakening (FW) can be calculated (see [68, 69, 71]). As these models do not consider saturation effects, the resulting torque might differ from the demanded torque for large regions of operation.

Some publications use FEA data of EESMs to consider saturation in machines as described above (see [68, 69, 72, 75]). Unfortunately, in many cases it is not clear for how many operation points these flux linkage maps are available and whether they cover the whole operation range for the stator currents and the excitation current [74, 76]. Obtaining FEA data is only possible with precise knowledge of the machine geometry, material properties, winding diagram, etc. This information is usually *not* available. Hence, measuring flux linkage maps is a more convenient approach. To the best knowledge of the author, the measurement of EESM flux linkage maps covering both stator flux linkages and the excitation flux linkage has not been reported in literature.

1.2.3 Scaling of wind turbine systems for laboratory setups

To be able to quantify the effects of a post-fault control strategy on the overall WTS, measurements are necessary. Measurements at a large-scale WTS or at a full-size wind turbine test-bench [77] were not possible. Hence, the dynamics of the large-scale WTS have to be scaled to a small-scale laboratory test-bench with reduced power rating. The test-bench comprises one electric machine, which emulates the wind turbine coupled to a second machine emulating the generator (see Fig. 1.2).

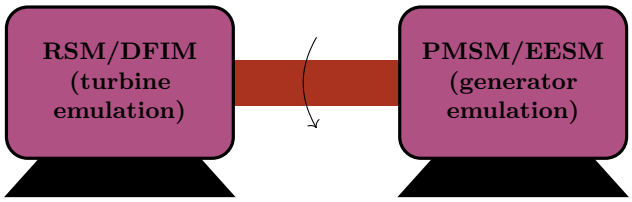

Figure 1.2: *Laboratory test-bench for emulation of the WTS by using a scaled WTS model.*

Using the model of a small-scale WTS is not suitable for modelling the behaviour of a large-scale WTS. The relations governing the interaction between the wind speed, torque and rotational speed of WTSs for small power ratings are different to the relations of multi-mega-watt turbines. Hence, a realistic emulation of large-scale WTS by a well-founded and structured down-scaling method is crucial. A few guidelines for a proper scaling of the WTS dynamics exist in literature to achieve a realistic behaviour emulated by the small-scale test-bench. While the scaling of the turbine aerodynamics (e.g. for wind tunnel tests) is well known and proven guidelines do exist [78–83], the scaling of the turbine power and its drive train for drive train emulation with small-scale electric drive test-benches is not that mature. Most papers which conduct small-scale laboratory experiments (i) do not explain on what basis the scaling has been performed, e.g. [84, 85]. Others (ii) scale only the turbine output torque by a scaling factor [86], (iii) scale the active and reactive power output [87] (for setups without electric machines), (iv) achieve scaling based on the transfer function of the flexible shaft [88, 89], or (v) simply use data from small-scale WTSs [90].
Some of the proposed models used for small-scale WTS emulation in the laboratory take into account (a) friction of the test-bench, [88, 89], (b) inertia emulation [86, 90] and (c) a flexible shaft [88,89]. But the respective models do *not* consider (α) the scaling of the wind turbine [88], (β) inertia emulation [88,89], or (γ) friction [86, 90], or simply do *not* scale (δ) the overall wind turbine drive-train system based on the ratios of physical SI-units [86, 88–90]. Summarizing, all available models this far do either neglect some crucial physical aspects or use simplified scaling methods.

1.3 Contributions

After reviewing the state-of-the-art, the contributions of this thesis can be stated as follows:

(i) Dynamic modelling of an EESM with damper windings including magnetic saturation by using nonlinear flux linkage maps, differential inductances (including cross-coupling (mutual) inductances) and excitation current dependent excitation resistance (see Sect. 2.3.3);

(ii) Development of a method for measuring EESM flux linkage maps for stator and exciter and providing step-by-step instructions (due to readability reasons, this is placed in Appendix B of this thesis);

(iii) EESM controller design including saturation effects, by using the obtained flux linkage maps for current control and torque control (see Sect. 3.2.3);

(iv) Derivation of a mathematical model for a converter with open-switch fault (see Sect. 2.4.3);

(v) Development of a post-fault control strategy for open-switch converter faults in WTSs with PMSM (see Sect. 3.3.1);

(vi) Development of a post-fault control strategy for open-switch converter faults in WTSs with EESM (see Sect. 3.3.2);

(vii) Deriving a scaling method of the drive train dynamics of large-scale WTS for real-time emulation by small-scale laboratory setups based on the ratios of physical SI-units (see Sect. 4.2);

(viii) Experimental investigation of the impact of the post-fault control strategy on the overall performance of WTSs with PMSM (see Sect. 4.3.1); and

(ix) Experimental investigation of the impact of the post-fault control strategy on the overall performance of WTSs with EESM (see Sect. 4.3.2).

The focus of this thesis is on a fault-tolerant modification of the WTS control system such that, even in presence of an open-switch fault in the machine-side converter, a continuous operation of the turbine is feasible. This is of particular interest for offshore wind turbine systems, where maintenance is expensive and depends on the weather conditions (e.g. whether ships can access the turbine or not). It will be shown that with the proposed fault-tolerant control system, the wind turbine can still be used until regular maintenance is planned and weather conditions are suitable. Consequently, instead of shutting down the WTS, continuous operation and energy production are ensured, limiting the corresponding financial losses.
This thesis is structured as follows. Chapter 2 introduces the mathematical models for all relevant components of the WTS. For the considered two-level converters, also the model for open-switch faults is presented. Chapter 3 explains the controller design for the turbine and the drive. Modifications of the control system for the post-fault control are derived for PMSM and EESM. In Chapter 4, the impact of the post-fault control strategy on WTS will be investigated. The scaling of a large-scale WTS to the laboratory setup is derived and the experimental results are discussed. Chapter 5 concludes this thesis by summarizing the results and providing an outlook.

Chapter 2

Modelling of large-scale direct-drive wind turbine systems

Modelling of the wind turbine system—including the mechanics—is necessary to fully understand the impacts of open-switch faults. For the investigation (in Chap. 4) of the usability of the post-fault control strategy—that will be proposed in Sect. 3.3—for wind turbine systems, a WTS model including the fundamental mechanical components is indispensable. This chapter is partially based on [2–4] were parts have already been published. The fundamental components of a wind turbine system, as depicted in Fig. 2.1, are

- turbine (see Sect. 2.1),
- drive train (see Sect. 2.2),
- electric machine/generator (see Sect. 2.3),
- power converter (see Sect. 2.4.2 without open-switch fault and Sect. 2.4.3 with open-switch fault),
- filter (for further information see e.g. [3, 4, 8, 91]),
- grid (for further information see e.g. [3, 4, 92]).

In the following, only the modelling of *turbine*, *drive train*, *electric machine* and *power converter* will be explained in detail. For all other components details can be found in the references above.

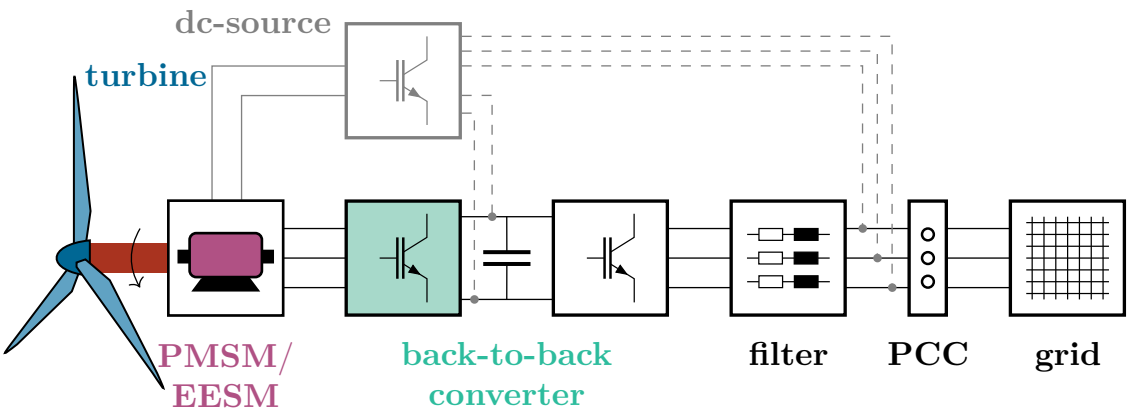

Figure 2.1: *Overview of the components of a direct-drive wind turbine system with PMSM or EESM.*

2.1 Turbine

The modelling of the fault-free components of a WTS starts with the turbine/rotor itself. There are different ways of modelling a turbine (see [93–96]). As the focus of this thesis is on the electric components of a WTS, the approach using a power coefficient is used. Hence, the turbine torque can be calculated based on the wind power. The wind turbine extracts from the wind power

$$p_W(v_W) = \tfrac{1}{2}\rho\pi r_T^2 v_W^3 \quad \text{(in W)}, \tag{2.1}$$

the turbine power

$$p_T(v_W, \omega_T, \beta) = c_P(v_W, \omega_T, \beta) p_W(v_W) \quad \text{(in W)}, \tag{2.2}$$

related by the power coefficient

$$\begin{aligned} c_P(\lambda, \beta) := 0.73 \Bigg[151 \left(\frac{1}{\lambda - 0.02\beta} - \frac{0.003}{\beta^3 + 1} \right) - 0.58\beta - 0.002\beta^{2.14} \\ - 13.2 \Bigg] \cdot \exp\left(-18.4 \left(\frac{1}{\lambda - 0.02\beta} - \frac{0.003}{\beta^3 + 1} \right) \right). \end{aligned} \tag{2.3}$$

The wind power depends on air density ρ (in $\frac{\text{kg}}{\text{m}^3}$), turbine radius r_T (in m) and (time-varying) wind speed v_W (in $\frac{\text{m}}{\text{s}}$). The power coefficient $c_P(\lambda, \beta) = c_P(v_W, \omega_T, \beta)$ is a function of the tip speed ratio $\lambda := \frac{r_T \omega_T}{v_W}$ (depending on turbine radius r_T, turbine rotational speed ω_T (in $\frac{\text{rad}}{\text{s}}$) and wind speed v_W) and the pitch angle β (in °). It is a mathematical approximation of the aerodynamical behaviour of the wind turbine. For more details and limitations of this way of modelling of the turbine (aerodynamics), see [3, 4, 94, 96–99]. For this thesis, the model is sufficient.

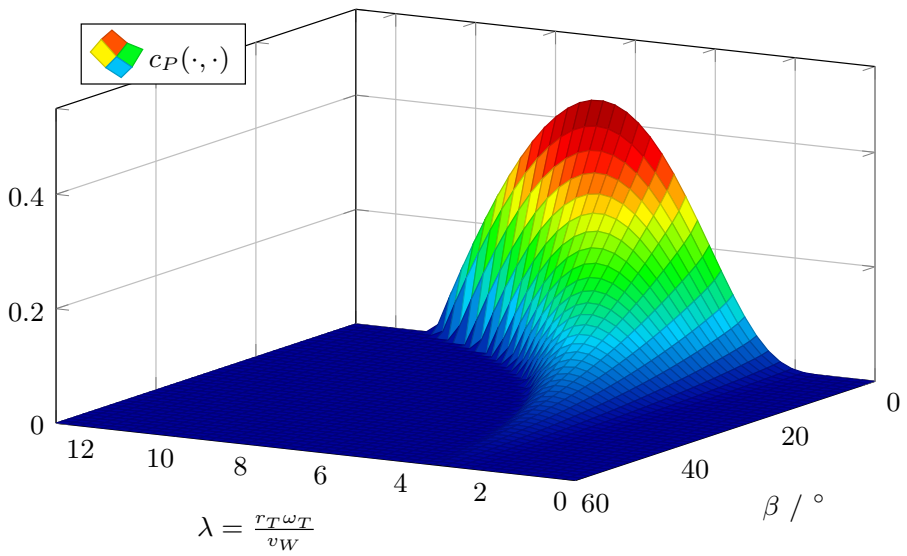

Figure 2.2: *Graph of the power coefficient for a* 2 MW *wind turbine.*

The graph of a power coefficient[3] $c_P(\lambda, \beta)$, as in (2.3), for a 2 MW turbine [4] is shown in Fig. 2.2. The curve has its maximum value $c_{P,\text{opt}}$ at λ_{opt} and β_{opt}. c_P decreases for increasing pitch angle

[3] For $\beta_{\text{opt}} = 0°$, $c_P(\cdot, \beta_{\text{opt}})$ has its maximum at $\lambda_{\text{opt}} := \left(\frac{\frac{151}{18.4} + 13.2}{151} + 0.003 \right)^{-1} \approx 6.91$ with $c_{P,\text{opt}} := c_P(\lambda_{\text{opt}}, \beta_{\text{opt}}) = 0.441$.

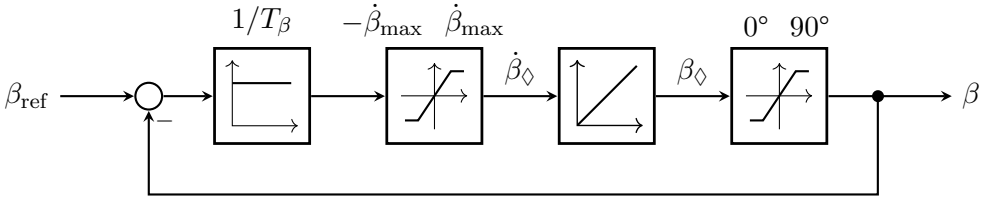

Figure 2.3: *Approximation of pitch system.*

β and tip speed ratios λ veering away from λ_{opt} in positive and negative λ-direction. In view of (2.1) and (2.2), the turbine torque τ_T (in N m) can be expressed as

$$p_T = \tau_T \omega_T \quad \Rightarrow \quad \tau_T(v_W, \omega_T, \beta) = \frac{p_T(v_W, \omega_T, \beta)}{\omega_T} \underset{(2.2)}{\overset{(2.1)}{=}} \tfrac{1}{2}\rho\pi r_T^2 v_W^3 \frac{c_P(v_W, \omega_T, \beta)}{\omega_T}. \tag{2.4}$$

The pitch system allows to control the pitch angle β to its reference value β_{ref} (in °). The nonlinear dynamics of the pitch control system are approximated by [3][4]

$$\left.\begin{aligned} \tfrac{\mathrm{d}}{\mathrm{d}t}\beta_\Diamond &= \operatorname{sat}_{-\dot{\beta}_{\max}}^{\dot{\beta}_{\max}}\Big(\tfrac{1}{T_\beta}\big(-\beta + \beta_{\text{ref}}\big)\Big), \\ \beta &= \operatorname{sat}_{0°}^{90°}\big(\beta_\Diamond\big), \end{aligned}\right\} \tag{2.5}$$

with unsaturated pitch angle $\beta_\Diamond$ (in °) and initial value $\beta_\Diamond(0) = \beta_{\Diamond,0} \geq 0$ (in °), where $\dot{\beta}_{\max} > 0$ (in $\frac{^\circ}{\text{s}}$) and T_β (in s) are the maximally feasible change rate of the pitch angle and the (approximated) pitch control system time constant, respectively. Figure 2.3 shows the block diagram of approximation (2.5) of the pitch system. The underlying current, speed and position control dynamics are neglected (for details see e.g. [51, Sec. 11.2]). The overall approximated dynamics show the dynamic behaviour of a first-order lag system where output and change rate are saturated.

2.2 Drive train

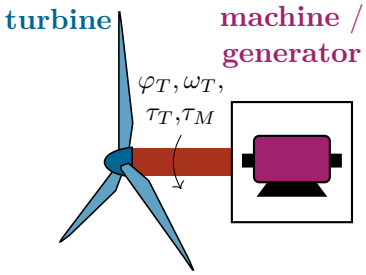

Figure 2.4: *Drive train of a direct-drive wind turbine system.*

The shaft of a direct-drive wind turbine system connects the turbine to the generator *without* gear box (see Fig. 2.4). As the focus of this thesis is on the electric components of the wind turbine system, the following assumption is imposed:

Assumption (AS.1) *The shaft of the wind turbine system is assumed to be rigid. Hence, turbine speed ω_T and machine speed ω_M are equal, i.e. $\omega_T = \omega_M$ (both in $\frac{\text{rad}}{\text{s}}$). The same holds for turbine angle φ_T and machine angle φ_M, i.e. $\varphi_T = \varphi_M$ (both in* rad*).*

[4] A simplification of the pitch system dynamics given in [94, Sect. 2.3, 5.5].

Then, the drive train dynamics are given by

$$\left.\begin{array}{l} \frac{\mathrm{d}}{\mathrm{d}t}\omega_T = \frac{1}{\Theta_T+\Theta_M}\left(\tau_T + \tau_M - \nu_T\omega_T - f_T(\omega_T)\right) \\ \frac{\mathrm{d}}{\mathrm{d}t}\varphi_T = \omega_T \end{array}\right\} \tag{2.6}$$

depending on turbine torque τ_T, machine torque τ_M (both in $\mathrm{N\,m}$), turbine inertia Θ_T, machine inertia[5] Θ_M (both in $\mathrm{kg\,m^2}$), linear friction coefficient ν_T (in $\frac{\mathrm{N\,m\,s}}{\mathrm{rad}}$) and nonlinear friction torque[6] f_T (in $\mathrm{N\,m}$). $\omega_T(0) = \omega_{T,0}$ and $\varphi_T(0) = \varphi_{T,0}$ are the initial values of the turbine speed and turbine angle, respectively.

Remark 2.2.1. *To obtain a more precise approximation of the drive train dynamics, many publications recommend to model the drive train of a wind turbine system at least as two-mass-system[7] (TMS) (see [100]). As the drive train dynamics are not the focus of this work, modelling with rigid shafts is sufficient. For details on the modelling of a wind turbine system with TMS, see [1].*

2.3 Electric machines

After modelling turbine and shaft, the two relevant types of electric machines for direct-drive wind turbine systems—PMSM and EESM—are modelled. The models are chosen to be simple, but to still cover all the relevant physical effects. Using these models, the physics can be emulated in simulations and the mathematical models are used for the controller design. Hence, precise modelling is indispensable for a good overall result.

2.3.1 General assumptions for machine modelling

For the analytical modelling of the overall electric machine (instead of modelling the electromagnetic processes in each finite element of the machine) some assumptions are necessary. These assumptions are reasonable for the investigated electric machines (this can be seen by the matching of simulation results and experimental results, e.g. see Sect. 3.2.3.3 or Appendix B.3). Hence, following assumptions are imposed:

Assumption (AS.2) *The machine is designed symmetrically. The windings of three-phase winding systems are sinusoidally distributed over the surface with a electric shift of* 120° *and the number of windings for each phase is equal. Harmonics are not considered.*

Assumption (AS.3) *The three-phase windings are star-connected. Hence, the sum of the phase currents is zero.*

Assumption (AS.4) *Stator and rotor of the machine are laminated. Hence, eddy currents are negligible.*

Assumption (AS.5) *Hysteresis effects are not considered.*

Assumption (AS.6) *Changes of the electric machine parameters with temperature, like resistances and inductances are not considered*[8]*.*

[5] Machine and turbine inertia may also comprise the respective inertias of shaft, etc.

[6] Not only the turbine, but also the electric machine and all elements of the drive train are affected by friction. Here, all friction effects are summarized in ν_T and f_T. For details on modelling friction see [51, Chap. 11].

[7] For the modelling of a TMS see e.g. [51, Chap. 12].

[8] This assumption is reasonable, as WTS usually work for a longer period of time and are usually equipped with a cooling system to regulate the temperature.

2.3.2 Permanent magnet synchronous machine (PMSM)

In this section two analytical models of a PMSM will be derived. The nonlinear model is valid for all types of PMSMs. The linear model is only valid for PMSMs especially designed to behave linear[9]. The modelling of the PMSM is based on the ideas given in [51, Sect. 14.3.2]. For further modelling approaches see e.g. [56, 101, 102].

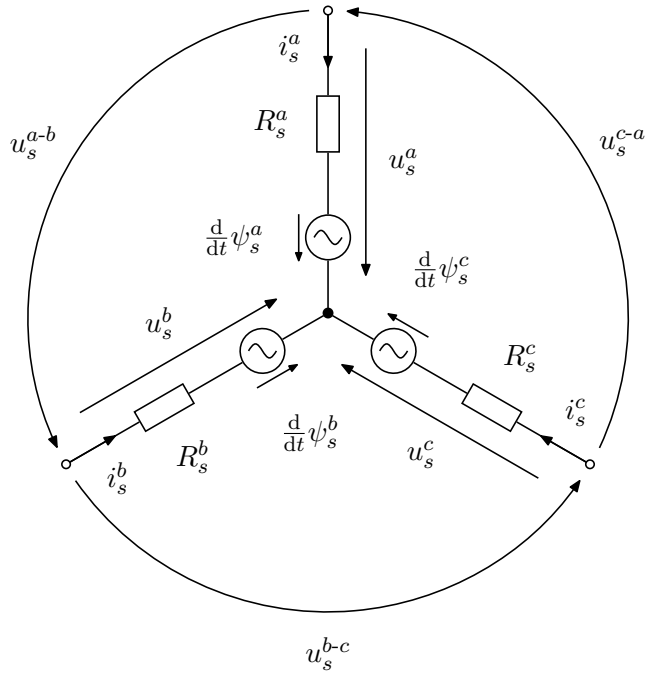

Figure 2.5: *Electric equivalent circuit of the stator of a PMSM.*

2.3.2.1 Nonlinear machine model

Figure 2.5 shows the electric equivalent circuit of the stator of a PMSM. The stator phase[10] voltages $\boldsymbol{u}_s^{abc} := (u_s^a, u_s^b, u_s^c)^\top$ (in V)^3 depend on the stator resistance matrix $\boldsymbol{R}_s^{abc} := \mathrm{diag}(R_s^a, R_s^b, R_s^c)$ (in Ω)$^{3\times3}$, the stator currents $\boldsymbol{i}_s^{abc} := (i_s^a, i_s^b, i_s^c)^\top$ (in A)^3, the stator flux linkages $\boldsymbol{\psi}_s^{abc} := (\psi_s^a, \psi_s^b, \psi_s^c)^\top$ (in V s)^3 and the electric angle φ_{pm} (in rad) of the permanent magnet (see Fig. 2.6). The stator voltage equation is given by

$$\boldsymbol{u}_s^{abc} = \boldsymbol{R}_s^{abc}\boldsymbol{i}_s^{abc} + \tfrac{\mathrm{d}}{\mathrm{d}t}\boldsymbol{\psi}_s^{abc}\left(\boldsymbol{i}_s^{abc}, \varphi_{\mathrm{pm}}\right). \tag{2.7}$$

The derivative of the flux linkage can be expressed as

$$\tfrac{\mathrm{d}}{\mathrm{d}t}\boldsymbol{\psi}_s^{abc}\left(\boldsymbol{i}_s^{abc}, \varphi_{\mathrm{pm}}\right) = \underbrace{\frac{\partial \boldsymbol{\psi}_s^{abc}\left(\boldsymbol{i}_s^{abc}, \varphi_{\mathrm{pm}}\right)}{\partial \boldsymbol{i}_s^{abc}}}_{=:\boldsymbol{L}_s^{abc}\left(\boldsymbol{i}_s^{abc}, \varphi_{\mathrm{pm}}\right)} \tfrac{\mathrm{d}}{\mathrm{d}t}\boldsymbol{i}_s^{abc} + \underbrace{\frac{\partial \boldsymbol{\psi}_s^{abc}\left(\boldsymbol{i}_s^{abc}, \varphi_{\mathrm{pm}}\right)}{\partial \varphi_{\mathrm{pm}}} \overbrace{\tfrac{\mathrm{d}}{\mathrm{d}t}\varphi_{\mathrm{pm}}}^{=:\omega_{\mathrm{pm}}}}_{=:\boldsymbol{\Gamma}_s^{abc}\left(\boldsymbol{i}_s^{abc}, \varphi_{\mathrm{pm}}\right)} \tag{2.8}$$

[9] This implies higher production costs, due to e.g. usage of more expensive materials. As the PMSM in the laboratory behaves linear throughout its whole operation range, the linear model will be used for this machine.

[10] The stator line-to-line voltages are denoted by $\boldsymbol{u}_s^{a\text{-}b\text{-}c} := (u_s^{a\text{-}b}, u_s^{b\text{-}c}, u_s^{c\text{-}a})^\top$ (in V)^3.

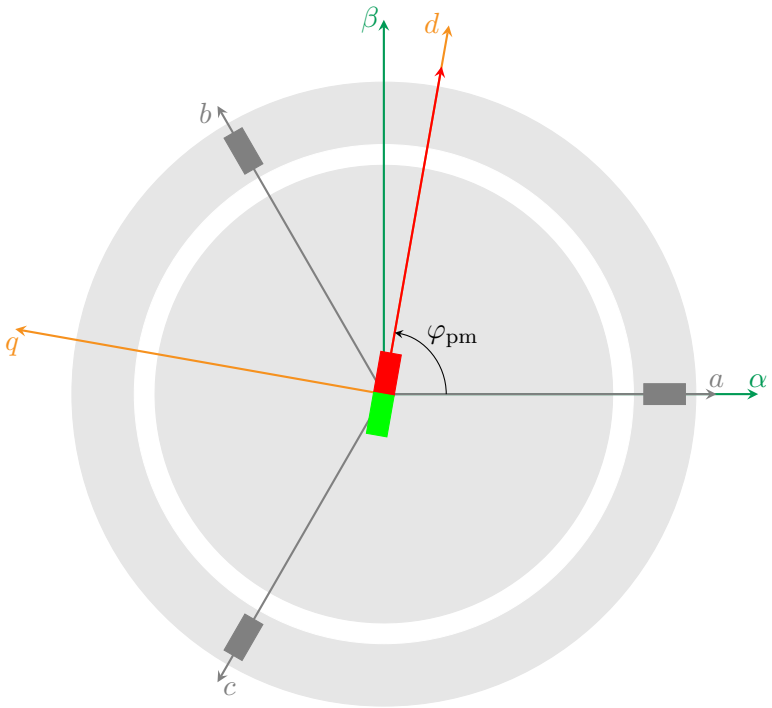

Figure 2.6: *Cross section of an isotropic PMSM (for one pole pair, i.e. $n_p = 1$) with:*

- *stator windings (a, b, c)*
- *stator-fixed coordinate system (α, β)*
- *permanent magnet oriented k-coordinate system (d, q)*

by using directional differentiation with differential stator inductance matrix $\boldsymbol{L}_s^{abc}$ (in $\frac{\mathrm{V\,s}}{\mathrm{A}}$)$^{3\times3}$, permanent magnet induced voltages $\boldsymbol{\Gamma}_s^{abc}$ (in V)^3 and angular velocity ω_{pm} (in $\frac{\mathrm{rad}}{\mathrm{s}}$) of the permanent magnet in the rotor.
The machine torque τ_m (in N m) calculates to (see [51])

$$\begin{aligned} \tau_m(\boldsymbol{i}_s^{abc}, \varphi_{\mathrm{pm}}) &= n_p \left(\boldsymbol{i}_s^{abc}\right)^\top \frac{1}{3} \begin{bmatrix} 1 & 1-\sqrt{3} & 1+\sqrt{3} \\ 1+\sqrt{3} & 1 & 1-\sqrt{3} \\ 1-\sqrt{3} & 1+\sqrt{3} & 1 \end{bmatrix} \boldsymbol{\psi}_s^{abc}(\boldsymbol{i}_s^{abc}, \varphi_{\mathrm{pm}}) \\ &\overset{[51]}{=} -n_p \hat{\psi}_{\mathrm{pm}} \begin{pmatrix} i_s^a \sin\left(\varphi_{\mathrm{pm}}\right) \\ i_s^b \sin\left(\varphi_{\mathrm{pm}} - \frac{2}{3}\pi\right) \\ i_s^c \sin\left(\varphi_{\mathrm{pm}} - \frac{4}{3}\pi\right) \end{pmatrix}, \end{aligned} \tag{2.9}$$

depending on stator currents $\boldsymbol{i}_s^{abc}$, pole pair number n_p, flux linkage amplitude $\hat{\psi}_{\mathrm{pm}}$ (in V s) of the permanent magnet and electric permanent magnet angle φ_{pm}.
Figure 2.6 shows the cross section of an isotropic PMSM with one pole pair. It shows the (three-phase) stator windings (a, b, c) and the permanent magnet. The stator-fixed abc-coordinate system is aligned with the three stator windings. The α-axis of the stator-fixed (orthogonal) $\alpha\beta$-coordinate system is aligned with the a-axis of the abc-coordinate system. The d-axis of the rotor-fixed (orthogonal) $k = dq$-coordinate system is aligned with the permanent magnet. Hence, the dq-coordinate system is rotating.
Transforming equations (2.7)-(2.9) into *permanent magnet flux linkage orientation* (commonly

known as *field orientation*), the $k = dq$-reference frame (see Fig. 2.6), using the reduced *Clarke* transformation and the reduced *Park* transformation (with reduced Clarke transformation matrix $\boldsymbol{T}_c$ and reduced Park transformation matrix $\boldsymbol{T}_p$, see Appendix A) and choosing the transformation angle to $\varphi_k = \varphi_{\mathrm{pm}}$ with its derivative $\omega_k = \frac{\mathrm{d}}{\mathrm{d}t}\varphi_k = \omega_{\mathrm{pm}}$ leads to (see [51, Example 14.24])

$$\boldsymbol{u}_s^{dq} = \boldsymbol{R}_s^{dq}(\varphi_k)\boldsymbol{i}_s^{dq} + \tfrac{\mathrm{d}}{\mathrm{d}t}\boldsymbol{\psi}_s^{dq}\left(\boldsymbol{i}_s^{dq}\right) + \omega_k \boldsymbol{J}\boldsymbol{\psi}_s^{dq}\left(\boldsymbol{i}_s^{dq}\right) \tag{2.10}$$

with transformed stator voltages $\boldsymbol{u}_s^{dq} := (u_s^d, u_s^q)^\top$ (in V)^2, stator currents $\boldsymbol{i}_s^{dq} := (i_s^d, i_s^q)^\top$ (in A)^2, flux linkages $\boldsymbol{\psi}_s^{dq} := (\psi_s^d, \psi_s^q)^\top$ (in V s)^2, rotation matrix[11] $\boldsymbol{J}$ and stator resistance matrix $\boldsymbol{R}_s^{dq}$ (in Ω)$^{2\times 2}$, which depends for different line resistances R_s^a, R_s^b, R_s^c on the transformation angle φ_k (see [103]).

Assumption (AS.7) *The stator resistances in each phase are equal and constant, i.e.*

$$R_s := R_s^a = R_s^b = R_s^c > 0 \quad \textit{(in } \Omega\textit{)}.$$

Expressing

$$\tfrac{\mathrm{d}}{\mathrm{d}t}\boldsymbol{\psi}_s^{dq}(\boldsymbol{i}_s^{dq}) = \underbrace{\frac{\partial \boldsymbol{\psi}_s^{dq}\left(\boldsymbol{i}_s^{dq}\right)}{\partial \boldsymbol{i}_s^{dq}}}_{=:\boldsymbol{L}_s^{dq}\left(\boldsymbol{i}_s^{dq}\right)} \tfrac{\mathrm{d}}{\mathrm{d}t}\boldsymbol{i}_s^{dq} = \begin{bmatrix} L_s^{dd}(\boldsymbol{i}_s^{dq}) & L_s^{dq}(\boldsymbol{i}_s^{dq}) \\ L_s^{qd}(\boldsymbol{i}_s^{dq}) & L_s^{qq}(\boldsymbol{i}_s^{dq}) \end{bmatrix} \tfrac{\mathrm{d}}{\mathrm{d}t}\boldsymbol{i}_s^{dq} \tag{2.11}$$

in terms of differential inductances and invoking (AS.7), (2.10) simplifies to

$$\boldsymbol{u}_s^{dq} = R_s\boldsymbol{i}_s^{dq} + \boldsymbol{L}_s^{dq}(\boldsymbol{i}_s^{dq})\tfrac{\mathrm{d}}{\mathrm{d}t}\boldsymbol{i}_s^{dq} + \omega_k \boldsymbol{J}\boldsymbol{\psi}_s^{dq}(\boldsymbol{i}_s^{dq}). \tag{2.12}$$

The machine torque τ_m (in N m) in dq-reference frame is given by

$$\tau_m(\boldsymbol{i}_s^{dq}) = \frac{2}{3\kappa^2} n_p \left(\boldsymbol{i}_s^{dq}\right)^\top \boldsymbol{J}\boldsymbol{\psi}_s^{dq}(\boldsymbol{i}_s^{dq}) \tag{2.13}$$

and depends on the scaling factor κ of the Clarke transformation, see Appendix A.

2.3.2.2 Linear machine model

For an isotropic PMSM with linear flux linkages (neglecting saturation), the stator flux linkages $\boldsymbol{\psi}_s^{dq}$ simplify to (see [51, Example 14.24])

$$\boldsymbol{\psi}_s^{dq}\left(\boldsymbol{i}_s^{dq}\right) = \underbrace{\begin{bmatrix} L_s & 0 \\ 0 & L_s \end{bmatrix}}_{=:\boldsymbol{L}_s^{dq}=L_s\boldsymbol{I}_2} \boldsymbol{i}_s^{dq} + \hat{\psi}_{\mathrm{pm}} \begin{pmatrix} 1 \\ 0 \end{pmatrix}, \tag{2.14}$$

with constant stator inductance L_s (in $\frac{\mathrm{V\,s}}{\mathrm{A}}$). Solving (2.10) for the derivative of the current $\boldsymbol{i}_s^{dq}$ and invoking Assumption (AS.7) leads to the current dynamics

$$\left.\begin{aligned} \tfrac{\mathrm{d}}{\mathrm{d}t}\boldsymbol{i}_s^{dq} &\overset{(2.10)}{\underset{(2.14)}{=}} \tfrac{1}{L_s}\left(\boldsymbol{u}_s^{dq} - R_s\boldsymbol{i}_s^{dq} - \omega_k L_s \boldsymbol{J}\boldsymbol{i}_s^{dq} - \omega_k \hat{\psi}_{\mathrm{pm}}\begin{pmatrix} 0 \\ 1 \end{pmatrix}\right) \\ \tau_m &\overset{(2.13)}{\underset{(2.14)}{=}} \tfrac{2}{3\kappa^2} n_p \hat{\psi}_{\mathrm{pm}} i_s^q, \end{aligned}\right\} \tag{2.15}$$

[11] For details on the *Park* transformation see Appendix A; $\boldsymbol{J} = \begin{bmatrix} 0 & -1 \\ 1 & 0 \end{bmatrix}$.

of an isotropic PMSM with linear flux linkages with initial currents $\boldsymbol{i}_s^{dq}(0) = \boldsymbol{T}_p^{-1}(\varphi_k(0))\boldsymbol{T}_c\boldsymbol{i}_{s,0}^{abc} := \boldsymbol{i}_{s,0}^{dq}$ (in A)[2].

2.3.3 Electrically excited synchronous machine (EESM)

The second machine type typically used in direct-drive WTS is the electrically excited synchronous machine. The modelling will at first be conducted for the most general case, an anisotropic (salient-pole) nonlinear EESM with damper windings. Afterwards the model will be reduced for an anisotropic nonlinear EESM without damper windings, usually used for speed-variable drives. The modelling of the EESM will be conducted in a similar manner as the modelling of the PMSM.

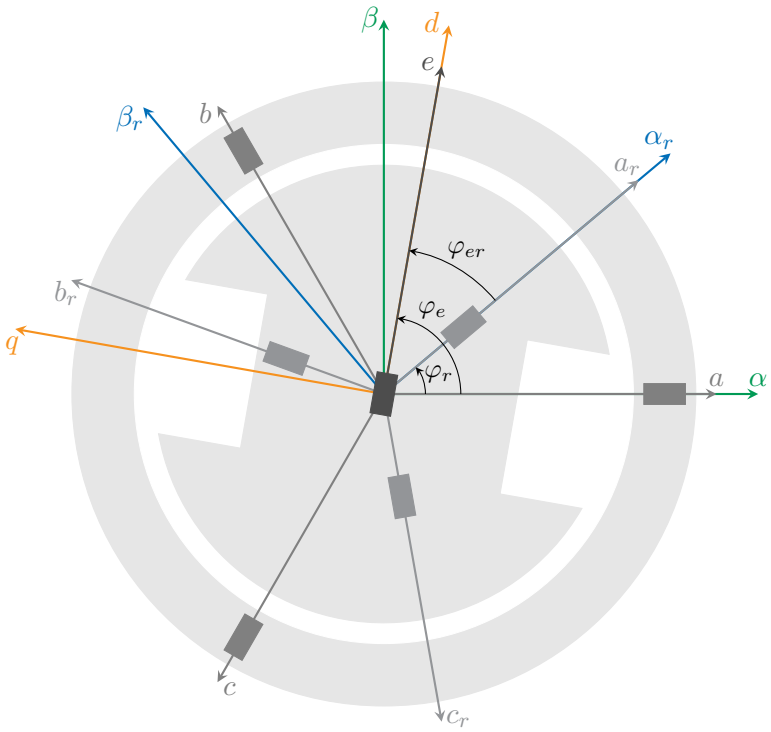

Figure 2.7: *Cross section of an anisotropic (salient-pole) EESM (for one pole pair, i.e. $n_p = 1$) with:*

- *stator windings (a, b, c)*
- *rotor windings (a_r, b_r, c_r)*
- *excitation winding (e)*
- *stator-fixed coordinate system (α, β)*
- *rotor-fixed coordinate system (α_r, β_r)*
- *excitation-oriented coordinate system (d, q)*

2.3.3.1 Nonlinear machine model with damper windings

Figure 2.7 shows the cross section for such an EESM with one pole pair. It shows the three winding sets, the (three-phase) stator windings (a, b, c), the (three-phase) rotor windings (a_r, b_r, c_r), and the excitation winding (e). For the stator-fixed (orthogonal) $\alpha\beta$-coordinate system, the α-axis is aligned with the a-axis of the stator. For the rotor-fixed (orthogonal) $\alpha_r\beta_r$-coordinate

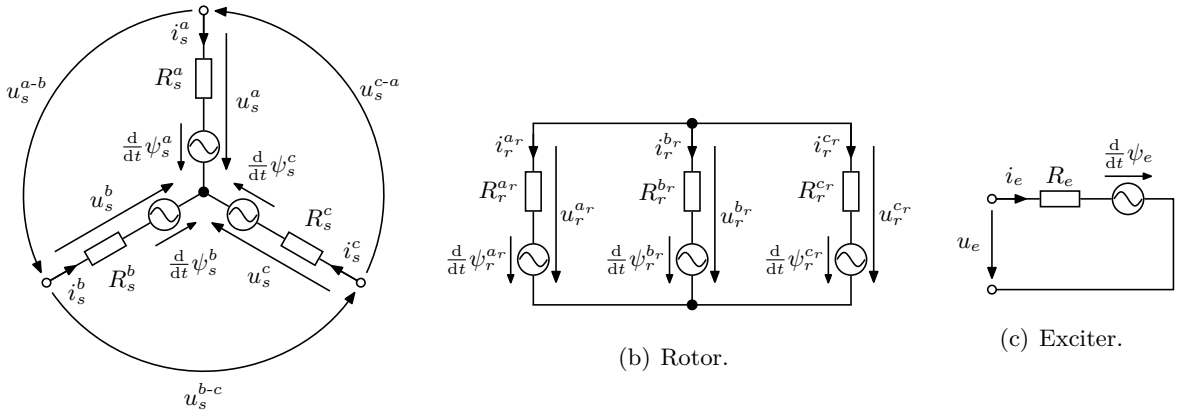

(a) Stator.

(b) Rotor.

(c) Exciter.

Figure 2.8: *Electric equivalent circuits of the EESM.*

system, the α_r-axis is aligned with the rotor a_r-axis. The d-axis of the excitation-oriented (orthogonal) dq-coordinate system is aligned with the excitation e-axis. The electric angle φ_r (in rad) is the angle between stator a-axis and rotor a_r-axis. The excitation angle φ_e (electric) is the angle between stator a-axis and excitation e-axis. The electric angle φ_{er} is defined as angle between rotor a_r-axis and excitation e-axis.

In Fig. 2.8 the electric equivalent circuits for stator, rotor and exciter are depicted. The stator of the EESM (see Fig. 2.8(a)) has the same equivalent circuit as the PMSM, see Fig. 2.6. The damper windings in the rotor (see Fig. 2.8(b)) are modelled as a short-circuited three-phase winding set. The excitation is a single-phase system (see Fig. 2.8(c)). Based on the electric equivalent circuits in Fig. 2.8, the basic equations for stator, rotor and excitation dynamics can be derived as follows

$$\left.\begin{aligned} \boldsymbol{u}_s^{abc} &= \boldsymbol{R}_s^{abc}\,\boldsymbol{i}_s^{abc} + \tfrac{\mathrm{d}}{\mathrm{d}t}\boldsymbol{\psi}_s^{abc}\Big(\boldsymbol{i}_s^{abc}, \boldsymbol{i}_r^{a_rb_rc_r}, i_e, \varphi_e\Big) \\ \boldsymbol{u}_r^{a_rb_rc_r} &= \boldsymbol{R}_r^{a_rb_rc_r}\,\boldsymbol{i}_r^{a_rb_rc_r} + \tfrac{\mathrm{d}}{\mathrm{d}t}\boldsymbol{\psi}_r^{a_rb_rc_r}\Big(\boldsymbol{i}_s^{abc}, \boldsymbol{i}_r^{a_rb_rc_r}, i_e, \varphi_e\Big) \\ u_e &= R_e(i_e)\,i_e + \tfrac{\mathrm{d}}{\mathrm{d}t}\psi_e\Big(\boldsymbol{i}_s^{abc}, \boldsymbol{i}_r^{a_rb_rc_r}, i_e, \varphi_e\Big), \end{aligned}\right\} \tag{2.16}$$

with stator voltages $\boldsymbol{u}_s^{abc} := (u_s^a, u_s^b, u_s^c)^\top$ (in V)^3, rotor voltages $\boldsymbol{u}_r^{a_rb_rc_r} := (u_r^{a_r}, u_r^{b_r}, u_r^{c_r})^\top$ (in V)^3, excitation voltage u_e (in V), stator resistance matrix $\boldsymbol{R}_s^{abc} := \mathrm{diag}(R_s^a, R_s^b, R_s^c)$ (in Ω)$^{3\times3}$, rotor resistance matrix $\boldsymbol{R}_r^{a_rb_rc_r} := \mathrm{diag}(R_r^{a_r}, R_r^{b_r}, R_r^{c_r})$ (in Ω)$^{3\times3}$, (excitation current i_e dependent) excitation resistance R_e (in Ω), stator currents $\boldsymbol{i}_s^{abc} := (i_s^a, i_s^b, i_s^c)^\top$ (in A)^3, rotor currents $\boldsymbol{i}_r^{a_rb_rc_r} := (i_r^{a_r}, i_r^{b_r}, i_r^{c_r})^\top$ (in A)^3, excitation current i_e (in A), stator flux linkages $\boldsymbol{\psi}_s^{abc} := (\psi_s^a, \psi_s^b, \psi_s^c)^\top$ (in V s)^3 with initial flux linkage values $\boldsymbol{\psi}_s^{abc}(0) = \boldsymbol{\psi}_{s,0}^{abc}$, rotor flux linkages $\boldsymbol{\psi}_r^{a_rb_rc_r} := (\psi_r^{a_r}, \psi_r^{b_r}, \psi_r^{c_r})^\top$ (in V s)^3 with initial values $\boldsymbol{\psi}_r^{a_rb_rc_r}(0) = \boldsymbol{\psi}_{r,0}^{a_rb_rc_r}$, excitation flux linkage ψ_e (in V s) with initial flux linkage value $\psi_e(0) = \psi_{e,0}$ and electric excitation angle φ_e (in rad). Based on the electric equivalent circuits in Fig. 2.8, the EESM in (2.16) has to fulfil the following constraints

$$\begin{aligned} \forall t \geq 0: \quad & i_s^a(t) + i_s^b(t) + i_s^c(t) = 0, \\ & i_r^{a_r}(t) + i_r^{b_r}(t) + i_r^{c_r}(t) = 0, \\ & u_r^{a_r}(t) = u_r^{b_r}(t) = u_r^{c_r}(t). \end{aligned} \tag{2.17}$$

Rewriting (2.16) in matrix-vector notation, by introducing the overall quantity vectors $\boldsymbol{i}^{abc} := (\boldsymbol{i}_s^{a_s b_s c_s}, \boldsymbol{i}_r^{a_r b_r c_r}, i_e)^\top$, $\boldsymbol{u}^{abc} := (\boldsymbol{u}_s^{a_s b_s c_s}, \boldsymbol{u}_r^{a_r b_r c_r}, u_e)^\top$, $\boldsymbol{\psi}^{abc} := (\boldsymbol{\psi}_s^{a_s b_s c_s}, \boldsymbol{\psi}_r^{a_r b_r c_r}, \psi_e)^\top$ and $\boldsymbol{R}^{abc} := \mathrm{diag}(\boldsymbol{R}_s^{a_s b_s c_s}, \boldsymbol{R}_r^{a_r b_r c_r}, R_e)$, leads to

$$\boldsymbol{u}^{abc} = \boldsymbol{R}^{abc}(i_e)\,\boldsymbol{i}^{abc} + \tfrac{\mathrm{d}}{\mathrm{d}t}\boldsymbol{\psi}^{abc}(\boldsymbol{i}^{abc}, \varphi_e). \tag{2.18}$$

Transforming (2.18) into the orthogonal $\alpha\beta\gamma$-reference frame, by using the extended Clarke transformation and its inverse (see Appendix A.1)

$$\boldsymbol{\mathcal{T}}_C := \begin{pmatrix} \boldsymbol{T}_C & \boldsymbol{0}_{3\times3} & \boldsymbol{0}_{3\times1} \\ \boldsymbol{0}_{3\times3} & \boldsymbol{T}_C & \boldsymbol{0}_{3\times1} \\ \boldsymbol{0}_{1\times3} & \boldsymbol{0}_{1\times3} & 1 \end{pmatrix}, \qquad \boldsymbol{\mathcal{T}}_C^{-1} := \begin{pmatrix} \boldsymbol{T}_C^{-1} & \boldsymbol{0}_{3\times3} & \boldsymbol{0}_{3\times1} \\ \boldsymbol{0}_{3\times3} & \boldsymbol{T}_C^{-1} & \boldsymbol{0}_{3\times1} \\ \boldsymbol{0}_{1\times3} & \boldsymbol{0}_{1\times3} & 1 \end{pmatrix}, \tag{2.19}$$

yields

$$\begin{aligned}
\boldsymbol{\mathcal{T}}_C\,\boldsymbol{u}^{abc} &= \boldsymbol{\mathcal{T}}_C\,\boldsymbol{R}^{abc}(i_e)\,\boldsymbol{i}^{abc} + \boldsymbol{\mathcal{T}}_C\,\tfrac{\mathrm{d}}{\mathrm{d}t}\boldsymbol{\psi}^{abc}(\boldsymbol{i}^{abc}, \varphi_e) \\
\Rightarrow\quad \boldsymbol{u}^{\alpha\beta\gamma} &\overset{\text{(A.1.2)}}{=} \underbrace{\boldsymbol{\mathcal{T}}_C\,\boldsymbol{R}^{abc}(i_e)\,\boldsymbol{\mathcal{T}}_C^{-1}}_{=:\boldsymbol{R}^{\alpha\beta\gamma}(i_e)}\boldsymbol{i}^{\alpha\beta\gamma} + \tfrac{\mathrm{d}}{\mathrm{d}t}\underbrace{\left(\boldsymbol{\mathcal{T}}_C\,\boldsymbol{\psi}^{abc}(\boldsymbol{\mathcal{T}}_C^{-1}\boldsymbol{i}^{\alpha\beta\gamma}, \varphi_e)\right)}_{=:\boldsymbol{\psi}^{\alpha\beta\gamma}(\boldsymbol{i}^{\alpha\beta\gamma}, \varphi_e)} \\
\Rightarrow\quad \boldsymbol{u}^{\alpha\beta\gamma} &= \boldsymbol{R}^{\alpha\beta\gamma}(i_e)\,\boldsymbol{i}^{\alpha\beta\gamma} + \tfrac{\mathrm{d}}{\mathrm{d}t}\boldsymbol{\psi}^{\alpha\beta\gamma}(\boldsymbol{i}^{\alpha\beta\gamma}, \varphi_e)\,.
\end{aligned} \tag{2.20}$$

In a next step the system will be transformed into the excitation oriented *dqo*-reference frame. While the excitation quantities do not have to be transformed at all, the stator quantities have to be rotated by the (time varying) angle φ_e (with its derivative $\omega_e = \frac{\mathrm{d}}{\mathrm{d}t}\varphi_e$ (in $\frac{\mathrm{rad}}{\mathrm{s}}$)) and the rotor quantities by the (constant) angle φ_{er} (see Fig. 2.7).

Applying the extended Park transformation matrix and its inverse (see Appendix A.2)

$$\boldsymbol{\mathcal{T}}_P(\varphi_e) := \begin{bmatrix} \boldsymbol{T}_P(\varphi_e) & \boldsymbol{0}_{3\times3} & \boldsymbol{0}_{3\times1} \\ \boldsymbol{0}_{3\times3} & \boldsymbol{T}_P(\varphi_{er}) & \boldsymbol{0}_{3\times1} \\ \boldsymbol{0}_{1\times3} & \boldsymbol{0}_{1\times3} & 1 \end{bmatrix}, \qquad \boldsymbol{\mathcal{T}}_P^{-1}(\varphi_e) := \begin{bmatrix} \boldsymbol{T}_P^{-1}(\varphi_e) & \boldsymbol{0}_{3\times3} & \boldsymbol{0}_{3\times1} \\ \boldsymbol{0}_{3\times3} & \boldsymbol{T}_P^{-1}(\varphi_{er}) & \boldsymbol{0}_{3\times1} \\ \boldsymbol{0}_{1\times3} & \boldsymbol{0}_{1\times3} & 1 \end{bmatrix} \tag{2.21}$$

to (2.20), leads to

$$\begin{aligned}
\boldsymbol{\mathcal{T}}_P^{-1}(\varphi_e)\,\boldsymbol{u}^{\alpha\beta\gamma} &= \boldsymbol{\mathcal{T}}_P^{-1}(\varphi_e)\,\boldsymbol{R}^{\alpha\beta\gamma}(i_e)\,\boldsymbol{i}^{\alpha\beta\gamma} + \boldsymbol{\mathcal{T}}_P^{-1}(\varphi_e)\,\tfrac{\mathrm{d}}{\mathrm{d}t}\boldsymbol{\psi}^{\alpha\beta\gamma}(\boldsymbol{i}^{\alpha\beta\gamma}, \varphi_e) \\
\Rightarrow\quad \boldsymbol{u}^{dqo} &\overset{\text{(A.2.15)}}{=} \underbrace{\boldsymbol{\mathcal{T}}_P^{-1}(\varphi_e)\,\boldsymbol{R}^{\alpha\beta\gamma}(i_e)\,\boldsymbol{\mathcal{T}}_P(\varphi_e)}_{=:\boldsymbol{R}^{dqo}(i_e, \varphi_e)}\boldsymbol{i}^{dqo} + \underbrace{\boldsymbol{\mathcal{T}}_P^{-1}(\varphi_e)\,\tfrac{\mathrm{d}}{\mathrm{d}t}\boldsymbol{\psi}^{\alpha\beta\gamma}\left(\boldsymbol{\mathcal{T}}_P(\varphi_e)\boldsymbol{i}^{dqo}, \varphi_e\right)}_{\overset{\text{(A.2.15)}}{=}\frac{\mathrm{d}}{\mathrm{d}t}\boldsymbol{\psi}^{dqo}(\boldsymbol{i}^{dqo}) - \frac{\mathrm{d}}{\mathrm{d}t}\left(\boldsymbol{\mathcal{T}}_P^{-1}(\varphi_e)\right)\boldsymbol{\psi}^{\alpha\beta\gamma}(\boldsymbol{i}^{\alpha\beta\gamma}, \varphi_e)} \\
&= \boldsymbol{R}^{dqo}(i_e, \varphi_e)\,\boldsymbol{i}^{dqo} + \tfrac{\mathrm{d}}{\mathrm{d}t}\boldsymbol{\psi}^{dqo}(\boldsymbol{i}^{dqo}) - \underbrace{\tfrac{\mathrm{d}}{\mathrm{d}t}\left(\boldsymbol{\mathcal{T}}_P^{-1}(\varphi_e)\right)}_{\overset{\text{(A.2.13)}}{=}-\omega_e\boldsymbol{\mathcal{J}}^{dqo}\boldsymbol{\mathcal{T}}_P^{-1}(\varphi_e)}\boldsymbol{\psi}^{\alpha\beta\gamma}(\boldsymbol{i}^{\alpha\beta\gamma}, \varphi_e) \\
&= \boldsymbol{R}^{dqo}(i_e, \varphi_e)\,\boldsymbol{i}^{dqo} + \tfrac{\mathrm{d}}{\mathrm{d}t}\boldsymbol{\psi}^{dqo}(\boldsymbol{i}^{dqo}) \\
&\qquad + \omega_e\boldsymbol{\mathcal{J}}^{dqo}\underbrace{\boldsymbol{\mathcal{T}}_P^{-1}(\varphi_e)\,\boldsymbol{\psi}^{\alpha\beta\gamma}\left(\boldsymbol{\mathcal{T}}_P^{-1}(\varphi_e)\boldsymbol{i}^{dqo}, \varphi_e\right)}_{=:\boldsymbol{\psi}^{dqo}(\boldsymbol{i}^{dqo})} \\
\Rightarrow\quad \boldsymbol{u}^{dqo} &= \boldsymbol{R}^{dqo}(i_e, \varphi_e)\,\boldsymbol{i}^{dqo} + \tfrac{\mathrm{d}}{\mathrm{d}t}\boldsymbol{\psi}^{dqo}(\boldsymbol{i}^{dqo}) + \omega_e\boldsymbol{\mathcal{J}}^{dqo}\,\boldsymbol{\psi}^{dqo}(\boldsymbol{i}^{dqo})
\end{aligned} \tag{2.22}$$

where

$$\boldsymbol{\mathcal{J}}^{dqo} := \begin{bmatrix} \boldsymbol{J}_{3\times 3} & \boldsymbol{0}_{3\times 4} \\ \boldsymbol{0}_{4\times 3} & \boldsymbol{0}_{4\times 4} \end{bmatrix} \tag{2.23}$$

and

$$\tfrac{\mathrm{d}}{\mathrm{d}t}\boldsymbol{\psi}^{dqo}(\boldsymbol{i}^{dqo}) = \underbrace{\frac{\partial \boldsymbol{\psi}^{dqo}(\boldsymbol{i}^{dqo})}{\partial \boldsymbol{i}^{dqo}}}_{=:\boldsymbol{L}^{dqo}(\boldsymbol{i}^{dqo})} \tfrac{\mathrm{d}}{\mathrm{d}t}\boldsymbol{i}^{dqo}. \tag{2.24}$$

Using additional knowledge about the EESM, the zero component in (2.22) is not necessary any longer and a reduced-order model can be derived. The following assumption is imposed:

Assumption (AS.8) *The resistances in each stator and rotor phase are equal and constant, respectively, i.e.*

$$R_s := R_s^a = R_s^b = R_s^c > 0 \quad \textit{and} \quad R_r := R_r^{a_r} = R_r^{b_r} = R_r^{c_r} > 0 \qquad \textit{(all in } \Omega\textit{)}.$$

Remark 2.3.1. *Assumption* (AS.8) *makes* $\boldsymbol{R}^{dqo}$ *independent of* φ_e*, i.e.*

$$\boldsymbol{R}^{dqo}(i_e) \overset{\text{(AS.8)}}{=} \boldsymbol{R}^{dqo}(i_e, \varphi_e) \tag{2.25}$$

Remark 2.3.2. *Assumption* (AS.2) *causes the flux linkage derivatives to sum up to zero, i.e.*

$$\forall t \geq 0: \qquad \tfrac{\mathrm{d}}{\mathrm{d}t}\psi_s^a(t) + \tfrac{\mathrm{d}}{\mathrm{d}t}\psi_s^b(t) + \tfrac{\mathrm{d}}{\mathrm{d}t}\psi_s^c(t) = 0, \qquad \tfrac{\mathrm{d}}{\mathrm{d}t}\psi_r^{a_r}(t) + \tfrac{\mathrm{d}}{\mathrm{d}t}\psi_r^{b_r}(t) + \tfrac{\mathrm{d}}{\mathrm{d}t}\psi_r^{c_r}(t) = 0. \tag{2.26}$$

Combining this with Assumption (AS.8) *leads to*

$$\forall t \geq 0: \qquad u_s^a(t) + u_s^b(t) + u_s^c(t) \overset{\substack{\text{(AS.2)} \\ \text{(AS.8)}}}{=} 0, \tag{2.27}$$

on the stator-side and to

$$\forall t \geq 0: \qquad u_r^{a_r}(t) + u_r^{b_r}(t) + u_r^{c_r}(t) \overset{\substack{\text{(AS.2)} \\ \text{(AS.8)}}}{=} 0, \tag{2.28}$$

on the rotor-side. So for the rotor voltages follows

$$\forall t \geq 0: \qquad u_r^{a_r}(t) = u_r^{b_r}(t) = u_r^{c_r}(t) \overset{(2.28)}{=} 0, \qquad \forall t \geq 0, \tag{2.29}$$

see [102, Chap. 1.8]. This leads to $\boldsymbol{u}_r^{dq}(t) = \boldsymbol{0}_2$ *for all* $t \geq 0$ *in the dq-reference frame.*

In view of Assumption (AS.2), Assumption (AS.8) and Remark 2.3.2, the zero components in (2.22) are not necessary any longer and can be neglected. Hence, (2.22) reduces to

$$\boldsymbol{u}^{dq} = \boldsymbol{R}^{dq}(i_e)\, \boldsymbol{i}^{dq} + \tfrac{\mathrm{d}}{\mathrm{d}t}\boldsymbol{\psi}^{dq}(\boldsymbol{i}^{dq}) + \omega_e \boldsymbol{\mathcal{J}}^{dq}\, \boldsymbol{\psi}^{dq}(\boldsymbol{i}^{dq}) \tag{2.30}$$

with reduced-order vectors and matrices

$$\begin{aligned} \boldsymbol{u}^{dq} &:= \begin{pmatrix} \boldsymbol{u}_s^{dq} \\ \boldsymbol{0}_2 \\ u_e \end{pmatrix}, \quad \boldsymbol{i}^{dq} := \begin{pmatrix} \boldsymbol{i}_s^{dq} \\ \boldsymbol{i}_r^{dq} \\ i_e \end{pmatrix}, \quad \boldsymbol{\psi}^{dq}(\boldsymbol{i}_s^{dq}) := \begin{pmatrix} \boldsymbol{\psi}_s^{dq}(\boldsymbol{i}^{dq}) \\ \boldsymbol{\psi}_r^{dq}(\boldsymbol{i}^{dq}) \\ \psi_e(\boldsymbol{i}^{dq}) \end{pmatrix}, \\ \boldsymbol{R}^{dq}(i_e) &:= \begin{bmatrix} R_s \boldsymbol{I}_2 & \boldsymbol{0}_{2\times 2} & \boldsymbol{0}_{2\times 1} \\ \boldsymbol{0}_{2\times 2} & R_r \boldsymbol{I}_2 & \boldsymbol{0}_{2\times 1} \\ \boldsymbol{0}_{1\times 2} & \boldsymbol{0}_{1\times 2} & R_e(i_e) \end{bmatrix}, \quad \boldsymbol{\mathcal{J}}^{dq} := \begin{bmatrix} \boldsymbol{J} & \boldsymbol{0}_{2\times 3} \\ \boldsymbol{0}_{3\times 2} & \boldsymbol{0}_{3\times 3} \end{bmatrix}. \end{aligned} \tag{2.31}$$

Replacing

$$\frac{\mathrm{d}}{\mathrm{d}t}\boldsymbol{\psi}^{dq}(\boldsymbol{i}^{dq}) = \underbrace{\frac{\partial \boldsymbol{\psi}^{dq}(\boldsymbol{i}^{dq})}{\partial \boldsymbol{i}^{dq}}}_{=:\boldsymbol{L}^{dq}(\boldsymbol{i}^{dq})} \frac{\mathrm{d}}{\mathrm{d}t}\boldsymbol{i}^{dq}, \tag{2.32}$$

by the representation with differential inductances, (2.30) can be written as

$$\boldsymbol{u}^{dq} = \boldsymbol{R}^{dq}(i_e)\boldsymbol{i}^{dq} + \boldsymbol{L}^{dq}(\boldsymbol{i}^{dq})\frac{\mathrm{d}}{\mathrm{d}t}\boldsymbol{i}^{dq} + \boldsymbol{\Gamma}^{dq}(\boldsymbol{i}^{dq}, \omega_e) \tag{2.33}$$

where

$$\begin{aligned}
\boldsymbol{L}^{dq}(\boldsymbol{i}^{dq}) &\overset{(2.32)}{=} \frac{\partial \boldsymbol{\psi}^{dq}(\boldsymbol{i}^{dq})}{\partial \boldsymbol{i}^{dq}} =: \begin{bmatrix} L_s^{dd}(\boldsymbol{i}^{dq}) & L_s^{dq}(\boldsymbol{i}^{dq}) & L_{sr}^{dd}(\boldsymbol{i}^{dq}) & L_{sr}^{dq}(\boldsymbol{i}^{dq}) & L_{se}^{d}(\boldsymbol{i}^{dq}) \\ L_s^{qd}(\boldsymbol{i}^{dq}) & L_s^{qq}(\boldsymbol{i}^{dq}) & L_{sr}^{qd}(\boldsymbol{i}^{dq}) & L_{sr}^{qq}(\boldsymbol{i}^{dq}) & L_{se}^{q}(\boldsymbol{i}^{dq}) \\ L_{rs}^{dd}(\boldsymbol{i}^{dq}) & L_{rs}^{dq}(\boldsymbol{i}^{dq}) & L_r^{dd}(\boldsymbol{i}^{dq}) & L_r^{dq}(\boldsymbol{i}^{dq}) & L_{re}^{d}(\boldsymbol{i}^{dq}) \\ L_{rs}^{qd}(\boldsymbol{i}^{dq}) & L_{rs}^{qq}(\boldsymbol{i}^{dq}) & L_r^{qd}(\boldsymbol{i}^{dq}) & L_r^{qq}(\boldsymbol{i}^{dq}) & L_{re}^{q}(\boldsymbol{i}^{dq}) \\ L_{es}^{d}(\boldsymbol{i}^{dq}) & L_{es}^{q}(\boldsymbol{i}^{dq}) & L_{er}^{d}(\boldsymbol{i}^{dq}) & L_{er}^{q}(\boldsymbol{i}^{dq}) & L_e(\boldsymbol{i}^{dq}) \end{bmatrix}, \\
\boldsymbol{\Gamma}^{dq}(\boldsymbol{i}^{dq}, \omega_e) &:= \omega_e \boldsymbol{\mathcal{J}}^{dq}\boldsymbol{\psi}^{dq}(\boldsymbol{i}^{dq}) \overset{(2.31)}{=} \omega_e \begin{bmatrix} \boldsymbol{J}\boldsymbol{\psi}_s^{dq}(\boldsymbol{i}^{dq}) & \boldsymbol{0}_{2\times 3} \\ \boldsymbol{0}_{3\times 2} & \boldsymbol{0}_{3\times 3} \end{bmatrix}
\end{aligned} \tag{2.34}$$

are the differential inductance matrix and the matrix of the flux linkage induced voltages, respectively. (2.33) now provides a relation between the voltages $\boldsymbol{u}^{dq}$ of the EESM, the currents $\boldsymbol{i}^{dq}$ in the EESM (states) and the rotational speed ω_e. The matrices $\boldsymbol{R}^{dq}$, $\boldsymbol{L}^{dq}$ and $\boldsymbol{\Gamma}^{dq}$ only depend on $\boldsymbol{i}^{dq}$ and ω_e, but do *not* depend on φ_e any longer.

The torque calculates to

$$\tau_m(\boldsymbol{i}^{dq}) = \tfrac{2}{3\kappa^2} n_p \left(\boldsymbol{i}_s^{dq}\right)^\top \boldsymbol{J}\boldsymbol{\psi}_s^{dq}(\boldsymbol{i}^{dq})\,. \tag{2.35}$$

2.3.3.2 Reduced-order model without damper windings

For variable-speed drives usually EESMs without damper windings are used. The reduced-order model for an EESM without damper windings can be derived from (2.33) by neglecting the damper/rotor entries in the vectors and matrices. The model can be written in a more compact form

$$\boldsymbol{u} = \boldsymbol{R}(i_e)\boldsymbol{i} + \tfrac{\mathrm{d}}{\mathrm{d}t}\boldsymbol{\psi}(\boldsymbol{i}) + \omega_e \boldsymbol{J}_{3\times 3}\boldsymbol{\psi}(\boldsymbol{i}), \tag{2.36}$$

with simplified vectors and matrices

$$\begin{aligned}
\boldsymbol{u} := \begin{pmatrix} \boldsymbol{u}_s^{dq} \\ u_e \end{pmatrix} = \begin{pmatrix} u_s^d \\ u_s^q \\ u_e \end{pmatrix}, \quad \boldsymbol{i} := \begin{pmatrix} \boldsymbol{i}_s^{dq} \\ i_e \end{pmatrix} = \begin{pmatrix} i_s^d \\ i_s^q \\ i_e \end{pmatrix}, \quad \boldsymbol{\psi}(\boldsymbol{i}) := \begin{pmatrix} \boldsymbol{\psi}_s^{dq}(\boldsymbol{i}) \\ \psi_e(\boldsymbol{i}) \end{pmatrix} = \begin{pmatrix} \psi_s^d(\boldsymbol{i}) \\ \psi_s^q(\boldsymbol{i}) \\ \psi_e(\boldsymbol{i}) \end{pmatrix}, \\
\boldsymbol{R}(i_e) := \begin{bmatrix} \boldsymbol{R}_s^{dq} & \boldsymbol{0}_2 \\ \boldsymbol{0}_2^\top & R_e(i_e) \end{bmatrix} = \begin{bmatrix} R_s^d & 0 & 0 \\ 0 & R_s^q & 0 \\ 0 & 0 & R_e(i_e) \end{bmatrix}.
\end{aligned} \tag{2.37}$$

Inserting

$$\frac{\mathrm{d}}{\mathrm{d}t}\boldsymbol{\psi}(\boldsymbol{i}) = \underbrace{\frac{\partial \boldsymbol{\psi}(\boldsymbol{i})}{\partial \boldsymbol{i}}}_{=:\boldsymbol{L}(\boldsymbol{i})} \frac{\mathrm{d}}{\mathrm{d}t}\boldsymbol{i}, \tag{2.38}$$

into (2.36), yields

$$\boldsymbol{u} = \boldsymbol{R}(i_e)\boldsymbol{i} + \boldsymbol{L}(\boldsymbol{i})\tfrac{\mathrm{d}}{\mathrm{d}t}\boldsymbol{i} + \boldsymbol{\Gamma}(\boldsymbol{i}, \omega_e) \tag{2.39}$$

where

$$\begin{aligned} \boldsymbol{L}(\boldsymbol{i}) \overset{(2.38)}{:=} \frac{\partial \boldsymbol{\psi}(\boldsymbol{i})}{\partial \boldsymbol{i}} =: \begin{bmatrix} \boldsymbol{L}_s^{dq}(\boldsymbol{i}) & \boldsymbol{l}_{se}^{dq}(\boldsymbol{i}) \\ \left(\boldsymbol{l}_{es}^{dq}(\boldsymbol{i})\right)^\top & L_e(\boldsymbol{i}) \end{bmatrix} =: \begin{bmatrix} L_s^{dd}(\boldsymbol{i}) & L_s^{dq}(\boldsymbol{i}) & L_{se}^{d}(\boldsymbol{i}) \\ L_s^{qd}(\boldsymbol{i}) & L_s^{qq}(\boldsymbol{i}) & L_{se}^{q}(\boldsymbol{i}) \\ L_{es}^{d}(\boldsymbol{i}) & L_{es}^{q}(\boldsymbol{i}) & L_e(\boldsymbol{i}) \end{bmatrix}, \\ \boldsymbol{\Gamma}(\boldsymbol{i}, \omega_e) := \begin{pmatrix} \omega_e \boldsymbol{J} \boldsymbol{\psi}_s^{dq}(\boldsymbol{i}) \\ 0 \end{pmatrix} = \omega_e \begin{pmatrix} -\psi_s^q(\boldsymbol{i}) \\ \psi_s^d(\boldsymbol{i}) \\ 0 \end{pmatrix}. \end{aligned} \tag{2.40}$$

The torque calculates to

$$\tau_m(\boldsymbol{i}) = \tfrac{2}{3\kappa^2} n_p \left(\boldsymbol{i}_s^{dq}\right)^\top \boldsymbol{J} \boldsymbol{\psi}_s^{dq}(\boldsymbol{i}). \tag{2.41}$$

A step-by-step explanation, how the parameters of model (2.39) with (2.40) can be estimated, is given in Appendix[12] B.

2.4 Power converters

Power converters are used in electric drive systems, to transform a dc-voltage into a three-phase ac-voltage with variable amplitude and frequency. The state-of-the-art 2-level voltage source converter (VSC) consists of six power switches and parallel diodes.

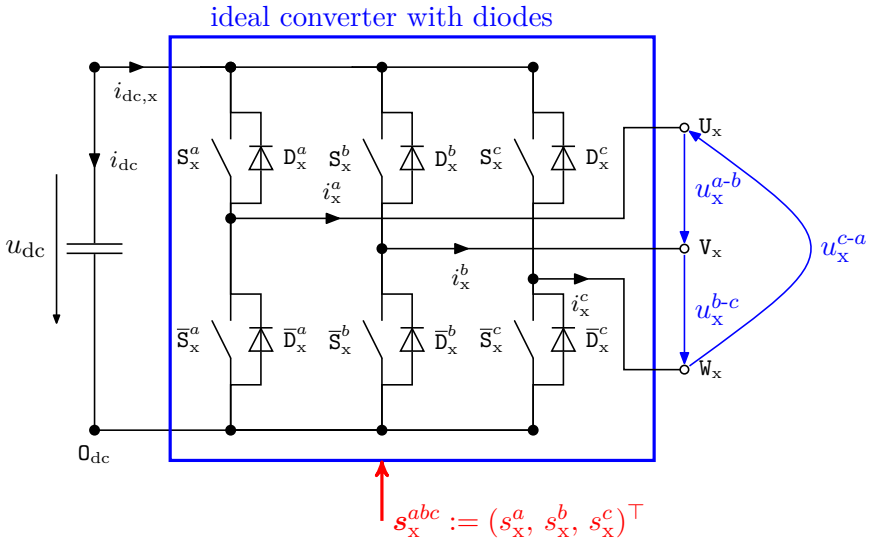

Figure 2.9: *Converter with ideal switches and parallel diodes.*

Figure 2.9 shows a converter with ideal switches and parallel diodes without connected load. The switches are denoted by S, the diodes by D. A bar above the symbol $\overline{\square}$ denotes an element (switch or diode) in the lower branch; an element without bar is in the upper branch. The superscripts a, b, c signify the branch of the switches and diodes. The "x" in the subscript

[12] Due to readability reasons, this is not explained here, but in the Appendix.

denotes the connected load and can be replaced e.g. by "s" when connected to the stator of an electric machine. The currents $i_{\mathrm{dc,x}}$, i_{x}^{a}, i_{x}^{b} and i_{x}^{c} are defined with positive direction towards the terminals $\mathtt{U}_{\mathrm{x}}$, $\mathtt{V}_{\mathrm{x}}$, $\mathtt{W}_{\mathrm{x}}$. $u_{\mathrm{x}}^{a\text{-}b}$, $u_{\mathrm{x}}^{b\text{-}c}$ and $u_{\mathrm{x}}^{c\text{-}a}$ are the voltages between the terminals $\mathtt{U}_{\mathrm{x}}$, $\mathtt{V}_{\mathrm{x}}$, $\mathtt{W}_{\mathrm{x}}$. The switching vector $\boldsymbol{s}_{\mathrm{x}}^{abc}$ provides the switching states of the converter. More details will be given in the following sections.

For the modelling of the VSC, following assumptions should hold.

Assumption (AS.9) *The load of the VSC is delta or star connected with floating neutral point, such that the sum of all currents is zero, i.e.* $i_{\mathrm{x}}^{a}(t) + i_{\mathrm{x}}^{b}(t) + i_{\mathrm{x}}^{c}(t) = 0$ *for all* $t \geq 0$.

Assumption (AS.10) *The switches and diodes are assumed to be ideal elements; e.g. on-resistance or threshold-voltage are neglected.*

Based on these assumptions, in the next sections, the diodes and switches are analysed separately as diode rectifier (only diodes) and ideal converter (only switches). For the fault-free converter, the diodes do not have to be modelled (see Sect. 2.4.2). But for a converter with open-switch fault, the diodes are relevant and have to be considered in the modelling (see Sect. 2.4.3.1). To simplify matters, the diode rectifier will at first be addressed separately.

2.4.1 Diode rectifier

For applications in electric drives, the diode rectifier is often used to supply a dc-link with power from the three-phase grid (see Fig. 2.10). Instead of state-of-the art modelling, where the line-to-line voltages $\boldsymbol{u}_{\mathrm{x}}^{a\text{-}b\text{-}c}$ are considered as input and u_{dc} as output, the modelling approach here applies this vice-versa. This is done in view of the converter modelling with open-switch fault in Sect. 2.4.3.1. For ideal diodes, the switching state of a diode (conducting ON or blocking OFF) only depends on the sign of the current in the respective branch (e.g. i_{x}^{a} for diodes $\mathtt{D}_{\mathrm{x}}^{a}$ and $\overline{\mathtt{D}}_{\mathrm{x}}^{a}$). For a positive current $i_{\mathrm{x}}^{a} > 0$, the diode $\overline{\mathtt{D}}_{\mathrm{x}}^{a}$ is conducting and $\mathtt{D}_{\mathrm{x}}^{a}$ is blocking. For a negative current $i_{\mathrm{x}}^{a} < 0$, the diode $\mathtt{D}_{\mathrm{x}}^{a}$ is conducting and for a zero current $i_{\mathrm{x}}^{a} = 0$, the diodes work as voltage divider[13].

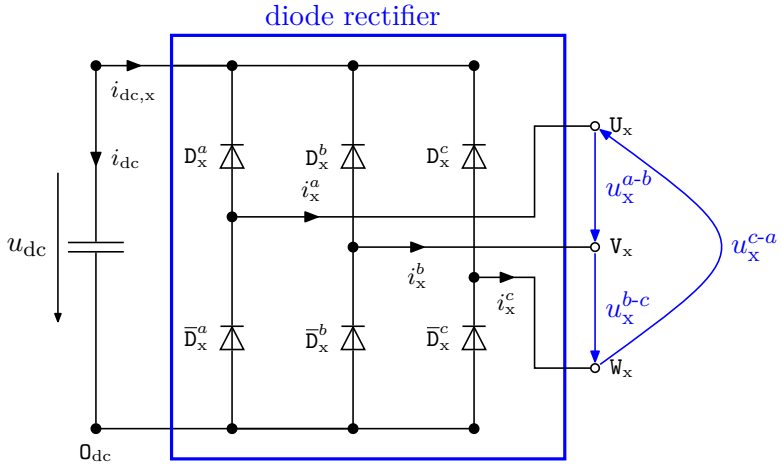

Figure 2.10: *Diode rectifier.*

[13]Details on this modelling for $i_{\mathrm{x}}^{a} = 0$, its validity and limitations will be discussed in Sect. 2.4.3.1.

Using the function

$$\left.\begin{aligned} \boldsymbol{f}_{<0}:\ \mathbb{R}^n \to \mathbb{R}^n,\quad \boldsymbol{x} := \begin{pmatrix} x_1 \\ \vdots \\ x_i \\ \vdots \\ x_n \end{pmatrix} \mapsto \boldsymbol{f}_{<0}(\boldsymbol{x}) := \begin{pmatrix} f_{<0,1}(x_1) \\ \vdots \\ f_{<0,i}(x_i) \\ \vdots \\ f_{<0,n}(x_n) \end{pmatrix} \\ \text{where} \qquad f_{<0,i}(x_i) = \begin{cases} 1 & ,x_i < 0 \\ \frac{1}{2} & ,x_i = 0 \\ 0 & ,x_i > 0. \end{cases} \quad ,\quad i \in \{1,\cdots,n\} \end{aligned}\right\}, \tag{2.42}$$

the dc-link current $i_{\mathrm{dc,x}}$ can be calculated to

$$i_{\mathrm{dc,x}} = \left(\boldsymbol{i}_{\mathrm{x}}^{abc}\right)^{\top} \boldsymbol{f}_{<0}\left(\boldsymbol{i}_{\mathrm{x}}^{abc}\right). \tag{2.43}$$

Introducing the voltage $u_{\mathtt{O}_{\mathrm{dc}}}$ (in V) at the potential $\mathtt{O}_{\mathrm{dc}}$ of the dc-link capacitor, the dc-link voltage u_{dc} (in V), the voltage u_w (in V) with $w \in \{\mathtt{U}_{\mathrm{x}}, \mathtt{V}_{\mathrm{x}}, \mathtt{W}_{\mathrm{x}}\}$ at the terminals $\mathtt{U}_{\mathrm{x}}$, $\mathtt{V}_{\mathrm{x}}$, $\mathtt{W}_{\mathrm{x}}$ for each phase $z \in \{a,b,c\}$ can be calculated[14] to

$$u_w = \begin{cases} u_{\mathrm{dc}} + u_{\mathtt{O}_{\mathrm{dc}}} & ,i^z < 0 \\ \frac{1}{2}u_{\mathrm{dc}} + u_{\mathtt{O}_{\mathrm{dc}}} & ,i^z = 0 \\ u_{\mathtt{O}_{\mathrm{dc}}} & ,i^z > 0. \end{cases} \tag{2.44}$$

Invoking matrix-vector notation and using $\boldsymbol{f}_{<0}$, yields

$$\boldsymbol{u}_{\mathtt{U}_{\mathrm{x}}\mathtt{V}_{\mathrm{x}}\mathtt{W}_{\mathrm{x}}} := \begin{pmatrix} u_{\mathtt{U}_{\mathrm{x}}} \\ u_{\mathtt{V}_{\mathrm{x}}} \\ u_{\mathtt{W}_{\mathrm{x}}} \end{pmatrix} = u_{\mathrm{dc}} \boldsymbol{f}_{<0}\left(\boldsymbol{i}_{\mathrm{x}}^{abc}\right) + \mathbf{1}_3 u_{\mathtt{O}_{\mathrm{dc}}}. \tag{2.45}$$

The line-to-line voltages are then given by

$$\begin{aligned} \boldsymbol{u}_{\mathrm{x}}^{a\text{-}b\text{-}c} := \begin{pmatrix} u_{\mathrm{x}}^{a\text{-}b} \\ u_{\mathrm{x}}^{b\text{-}c} \\ u_{\mathrm{x}}^{c\text{-}a} \end{pmatrix} &\overset{(A.3.22)}{=} \boldsymbol{T}_{\mathrm{ltl}}\, \boldsymbol{u}_{\mathtt{U}_{\mathrm{x}}\mathtt{V}_{\mathrm{x}}\mathtt{W}_{\mathrm{x}}} \\ &\overset{\substack{(A.3.22)\\(2.45)}}{=} \begin{bmatrix} 1 & -1 & 0 \\ 0 & 1 & -1 \\ -1 & 0 & 1 \end{bmatrix} \left(u_{\mathrm{dc}} \boldsymbol{f}_{<0}\left(\boldsymbol{i}_{\mathrm{x}}^{abc}\right) + \mathbf{1}_3 u_{\mathtt{O}_{\mathrm{dc}}}\right) \\ &= u_{\mathrm{dc}} \begin{bmatrix} 1 & -1 & 0 \\ 0 & 1 & -1 \\ -1 & 0 & 1 \end{bmatrix} \boldsymbol{f}_{<0}\left(\boldsymbol{i}_{\mathrm{x}}^{abc}\right). \end{aligned} \tag{2.46}$$

As usually an electric grid or an electric machine is connected to the terminals $\mathtt{U}_{\mathrm{x}}$, $\mathtt{V}_{\mathrm{x}}$, $\mathtt{W}_{\mathrm{x}}$, the following assumption is made:

Assumption (AS.11) *The load of the converter is symmetric, i.e.* $u_{\mathrm{x}}^a(t) + u_{\mathrm{x}}^b(t) + u_{\mathrm{x}}^c(t) = 0$ *for all* $t \geq 0$.

[14] According to Assumption (AS.10), the forward threshold voltage is neglected. u_{dc} and the amplitudes of $\boldsymbol{u}_{\mathrm{x}}^{a\text{-}b\text{-}c}$ are for electric drive applications usually much bigger than the threshold voltage.

Assumption (AS.11) allows to transform the line-to-line voltages into phase voltages as follows

$$\begin{aligned}\boldsymbol{u}_{\mathrm{x}}^{abc} &\overset{(A.3.24)}{=} (\boldsymbol{T}_{\mathrm{ltl}}^{\star})^{-1}\,\boldsymbol{u}_{\mathrm{x}}^{a\text{-}b\text{-}c} \overset{(AS.11)}{\underset{(2.46)}{=}} (\boldsymbol{T}_{\mathrm{ltl}}^{\star})^{-1}\,\boldsymbol{T}_{\mathrm{ltl}}\,\boldsymbol{u}_{\mathtt{U_x V_x W_x}} \\ &\overset{(A.3.22)}{\underset{(A.3.23)}{=}} \begin{bmatrix} \frac{2}{3} & -\frac{1}{3} & -\frac{1}{3} \\ -\frac{1}{3} & \frac{2}{3} & -\frac{1}{3} \\ -\frac{1}{3} & -\frac{1}{3} & \frac{2}{3} \end{bmatrix} \boldsymbol{u}_{\mathtt{U_x V_x W_x}} \\ &\overset{(2.45)}{=} \frac{u_{\mathrm{dc}}}{3} \begin{bmatrix} 2 & -1 & -1 \\ -1 & 2 & -1 \\ -1 & -1 & 2 \end{bmatrix} \boldsymbol{f}_{<0}\left(\boldsymbol{i}_{\mathrm{x}}^{abc}\right).\end{aligned} \tag{2.47}$$

The validation of this modelling approach will be provided implicitly by validating the open-switch fault converter model in Sect. 2.4.3.2.

2.4.2 Converter

Figure 2.11 shows an ideal converter. In the fault-free case for a star-connected (see Assumption (AS.9)), symmetrical load (see Assumption (AS.11)), the output voltages of the converter $\boldsymbol{u}_{\mathrm{x}}^{a\text{-}b\text{-}c}$ depend only on the switching vector $\boldsymbol{s}_{\mathrm{x}}^{abc} = (s_{\mathrm{x}}^{a}, s_{\mathrm{x}}^{b}, s_{\mathrm{x}}^{c})^{\top}$ and the dc-link voltage u_{dc} [4]. A "1" in the switching vector $\boldsymbol{s}_{\mathrm{x}}^{abc}$ means the upper switch is closed. A "0" represents a closed lower switch. For example, the switching vector $\boldsymbol{s}_{\mathrm{x}}^{abc} = (1, 1, 0)^{\top}$ yields closed switches $\mathtt{S}_{\mathrm{x}}^{a}$, $\mathtt{S}_{\mathrm{x}}^{b}$ and $\overline{\mathtt{S}}_{\mathrm{x}}^{c}$. The negated switching vector is given by

$$\overline{\boldsymbol{s}}_{\mathrm{x}}^{abc} = \mathbf{1}_3 - \boldsymbol{s}_{\mathrm{x}}^{abc}. \tag{2.48}$$

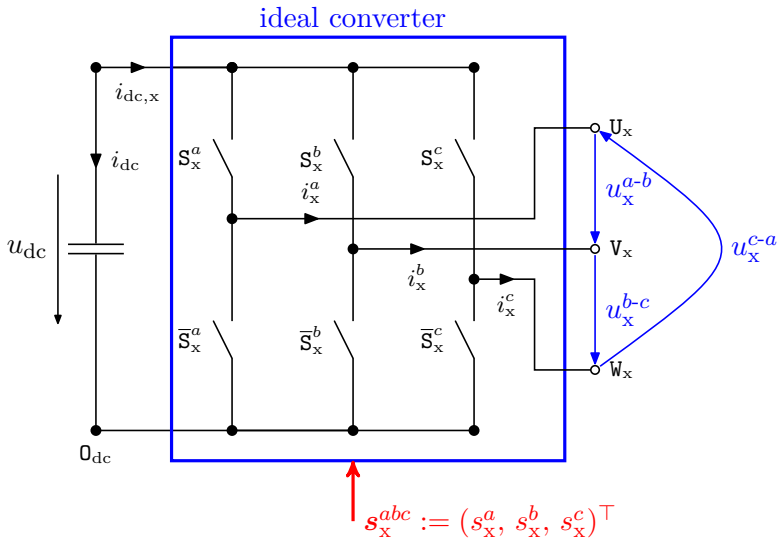

Figure 2.11: *Converter with ideal switches.*

The line-to-line output voltages can be calculated as follows (see [4])

$$\boldsymbol{u}_{\mathrm{x}}^{a\text{-}b\text{-}c} = u_{\mathrm{dc}} \begin{bmatrix} 1 & -1 & 0 \\ 0 & 1 & -1 \\ -1 & 0 & 1 \end{bmatrix} \boldsymbol{s}_{\mathrm{x}}^{abc}. \tag{2.49}$$

Using Assumption (AS.11), the phase voltages $\boldsymbol{u}_{\mathrm{x}}^{abc} = (u_{\mathrm{x}}^{a}, u_{\mathrm{x}}^{b}, u_{\mathrm{x}}^{c})^{\top}$ can be derived from the

line-to-line voltages as

$$\boldsymbol{u}_{\mathrm{x}}^{abc} \overset{\substack{(\mathrm{AS.11})\\(\mathrm{A.3.24})}}{=} \left(\boldsymbol{T}_{\mathrm{ltl}}^{\star}\right)^{-1} \boldsymbol{u}_{\mathrm{x}}^{a\text{-}b\text{-}c} \tag{2.50}$$

$$\overset{\substack{(\mathrm{A.3.23})\\(2.49)}}{=} \frac{u_{\mathrm{dc}}}{3} \begin{bmatrix} 2 & -1 & -1 \\ -1 & 2 & -1 \\ -1 & -1 & 2 \end{bmatrix} \boldsymbol{s}_{\mathrm{x}}^{abc} \overset{(2.48)}{=} \frac{u_{\mathrm{dc}}}{3} \begin{bmatrix} -2 & 1 & 1 \\ 1 & -2 & 1 \\ 1 & 1 & -2 \end{bmatrix} \overline{\boldsymbol{s}}_{\mathrm{x}}^{abc}. \tag{2.51}$$

The dc-current is given by (see [4])

$$i_{\mathrm{dc,x}} = \left(\boldsymbol{i}_{\mathrm{x}}^{abc}\right)^{\top} \boldsymbol{s}_{\mathrm{x}}^{abc} \overset{\substack{(\mathrm{AS.9})\\(2.48)}}{=} \left(-\boldsymbol{i}_{\mathrm{x}}^{abc}\right)^{\top} \overline{\boldsymbol{s}}_{\mathrm{x}}^{abc}. \tag{2.52}$$

2.4.3 Converter with open-switch fault

The basic idea of the presented modelling of a power converter with open-switch fault, was already published in the article [2]. For the relevance of this fault recall Sect. 1.1.
To analyse the impact of open-switch faults on electric machines and drives, a model of a faulty converter is needed. In [104–107] such models are proposed. However, these models are only given for a fault in only one specific switch and the models determine the phase voltages of the electric machine connected to the faulty converter by using so called "*pole voltages*" of the converter. If there is an open-switch fault in one of the switching devices, a deviation in the pole voltage of the respective phase occurs which affects all three phase voltages. The pole voltages are, however, a rather unintuitive quantity compared to, for example, the *switching state* of the power electronic devices or the *phase voltages* of the machine. Moreover, the use of pole voltages in simulations makes the converter model complicated. Additionally, the computation of the dc-current $i_{\mathrm{dc,x}}$ at the dc-link capacitor is neglected (see Fig. 2.9). Therefore, a more comprehensive model of converters with open-switch faults is needed which:

- computes line-to-line voltages $\boldsymbol{u}_{\mathrm{x}}^{a\text{-}b\text{-}c}$ and phase voltages $\boldsymbol{u}_{\mathrm{x}}^{abc}$,
- depends on switching state $\boldsymbol{s}_{\mathrm{x}}^{abc}$,
- allows for faults in each switch and
- considers the calculation of the dc-current $i_{\mathrm{dc,x}}$.

Such a model will be derived in the following section. It will be based on the following two assumptions:
Assumption (AS.12) *It is assumed that only one switch is faulty at a time. The switch does not close, regardless of the corresponding switching signal (open-switch fault).*
Assumption (AS.13) *The corresponding diode to the faulty switch is undamaged and still works properly*[15].

2.4.3.1 Switching model

The idea of modelling a converter with open-switch fault will first be explained for a fault in $\mathtt{S}_{\mathrm{x}}^{a}$ and afterwards a general model will be presented.
Figure 2.12 shows an ideal converter including free-wheeling diodes and a three-phase load consisting of resistances, inductances and voltage sources (e.g. an electric machine). For an open-switch fault in $\mathtt{S}_{\mathrm{x}}^{a}$, the only remaining path for the current in the upper branch is using

[15] This assumption is reasonable according to [50].

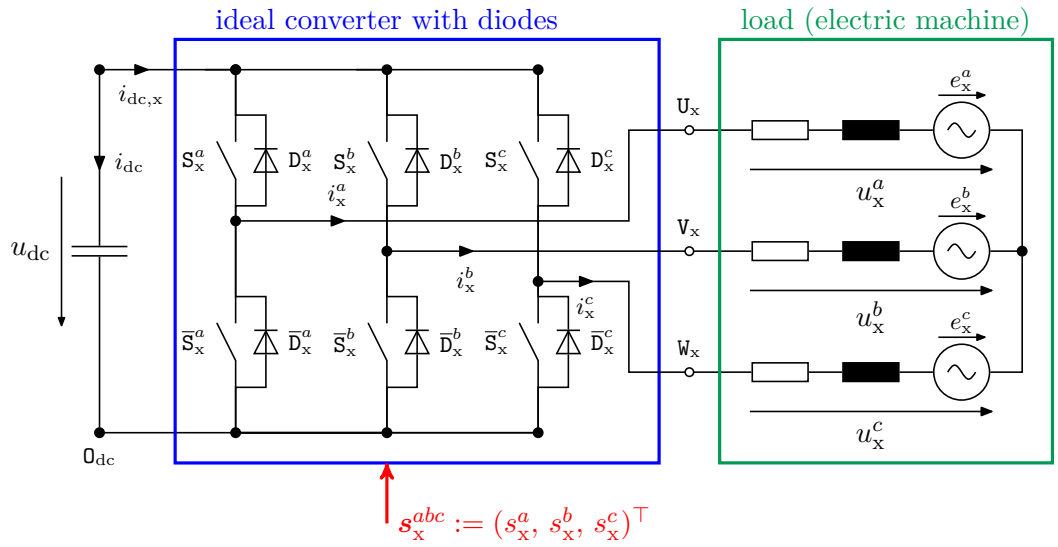

Figure 2.12: *Converter with ideal switches, parallel diodes and load (e.g. electric machine).*

diode $\mathtt{D}_{\mathrm{x}}^{a}$. As the conducting behaviour of the diode depends on the sign of the current i_{x}^{a} (see Sect. 2.4.1), the output voltages of the faulty converter also depend on it. There are three cases, (i) $i_{\mathrm{x}}^{a} < 0$, (ii) $i_{\mathrm{x}}^{a} = 0$ and (iii) $i_{\mathrm{x}}^{a} > 0$. Figure 2.13 shows the equivalent circuits for each case (i)-(iii) for an open-switch fault in $\mathtt{S}_{\mathrm{x}}^{a}$ and switching vector $\boldsymbol{s}_{\mathrm{x}}^{abc} := (\mathtt{1},\, \mathtt{1},\, \mathtt{0})^{\top}$. Conducting devices (switches and diodes) are omitted and displayed as conducting paths. Hence, only blocking devices are depicted. Converter and load were redrawn and differ from the presentation in Fig. 2.12 to emphasize the voltage drops at the branches of the load. For simplification, the load is just represented by inductances. It can be observed, that for $i_{\mathrm{x}}^{a} < 0$, the converter shows the same behaviour as without fault. For $i_{\mathrm{x}}^{a} = 0$ and $i_{\mathrm{x}}^{a} > 0$, the behaviour deviates from the fault-free case. For a fault in $\mathtt{S}_{\mathrm{x}}^{a}$ and a switching vector $\boldsymbol{s}_{\mathrm{x}}^{abc} := (\mathtt{1},\, \mathtt{1},\, \mathtt{0})^{\top}$, the output voltages[16] become (see Fig. 2.13)

$$\boldsymbol{u}_{\mathrm{x}}^{abc} = \begin{cases} \left(\frac{u_{\mathrm{dc}}}{3},\ \frac{u_{\mathrm{dc}}}{3},\ \frac{-2u_{\mathrm{dc}}}{3}\right)^{\top}, & \text{for } i_{\mathrm{x}}^{a} < 0 \\ \left(0,\ \frac{u_{\mathrm{dc}}}{2},\ \frac{-u_{\mathrm{dc}}}{2}\right)^{\top}, & \text{for } i_{\mathrm{x}}^{a} = 0 \\ \left(\frac{-u_{\mathrm{dc}}}{3},\ \frac{2u_{\mathrm{dc}}}{3},\ \frac{-u_{\mathrm{dc}}}{3}\right)^{\top}, & \text{for } i_{\mathrm{x}}^{a} > 0. \end{cases} \tag{2.53}$$

Generalizing this insight for all admissible switching vectors $\boldsymbol{s}_{\mathrm{x}}^{abc} \in \left\{(\mathtt{0},\, \mathtt{0},\, \mathtt{0})^{\top},\ \ldots\ ,(\mathtt{1},\, \mathtt{1},\, \mathtt{1})^{\top}\right\}$, for an open-switch fault in $\mathtt{S}_{\mathrm{x}}^{a}$, the relation in (2.51) has to be extended. The converter output

[16]The load can be imagined to act as voltage divider. For $i_{\mathrm{x}}^{a} = 0$ the potential of the star-point of the load and the potential of terminal $\mathtt{U}_{\mathrm{x}}$ are equal. For the connected load in Fig. 2.12, this holds for $e_{\mathrm{x}}^{a} = 0$ and $\frac{\mathrm{d}}{\mathrm{d}t} i_{\mathrm{x}}^{a} = 0$ (i.e. no voltage drop over the inductance). Depending on state and kind of the connected load, also cases of $i_{\mathrm{x}}^{a} = 0$ and $u_{\mathrm{x}}^{a} \neq 0$ are possible. Hence, the imagination of the voltage divider does not hold any longer. But for these cases the model stays only for an infinitely small time instance at $i_{\mathrm{x}}^{a} = 0$. Before and afterwards, the current is $i_{\mathrm{x}}^{a} < 0$ or $i_{\mathrm{x}}^{a} > 0$. For these currents, the modelling holds in any case. Hence, a possibly incorrect simulated voltage $\boldsymbol{u}_{\mathrm{x}}^{abc}$ for $i_{\mathrm{x}}^{a} = 0$ has no impact on the overall current evolution. So this modelling approach secures a simple and modular modelling of a converter with open-switch fault for investigations on the system level (e.g. converter and electric machine), see agreement of simulation and measurement results in Sect. 2.4.3.2. For a detailed modelling of the switching transitions of an converter with open-switch fault, this model should not be used. But in this case also Assumption (AS.10) does not hold.

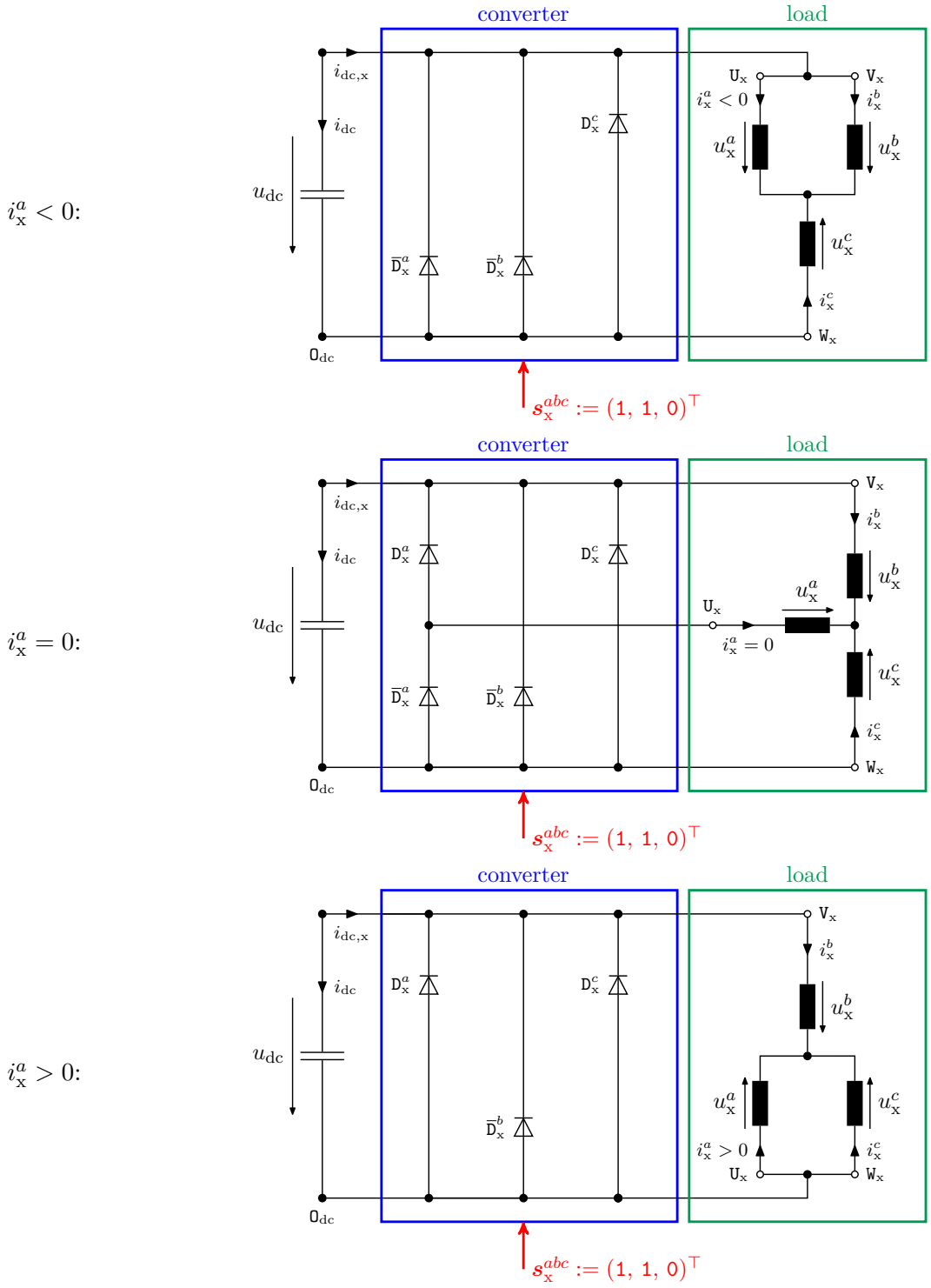

Figure 2.13: *Impact of an open-switch fault in S^a_x on the equivalent circuit of a symmetric electric three-phase load when switching vector $s^{abc}_x := (1, 1, 0)^\top$ is applied for $i^a_x < 0$ (top), $i^a_x = 0$ (middle) and $i^a_x > 0$ (bottom); conducting diodes and switches are displayed as conducting path.*

voltages are then given by [2]

$$\boldsymbol{u}_{\mathrm{x}}^{abc} = \frac{u_{\mathrm{dc}}}{3} \underbrace{\left(\begin{bmatrix} 2 & -1 & -1 \\ -1 & 2 & -1 \\ -1 & -1 & 2 \end{bmatrix} + \left\{ \begin{array}{ll} \mathbf{0}_{3\times 3}, & \text{for } i_{\mathrm{x}}^{a} < 0 \\ \begin{bmatrix} -1 & 0 & 0 \\ \frac{1}{2} & 0 & 0 \\ \frac{1}{2} & 0 & 0 \end{bmatrix}, & \text{for } i_{\mathrm{x}}^{a} = 0 \\ \begin{bmatrix} -2 & 0 & 0 \\ 1 & 0 & 0 \\ 1 & 0 & 0 \end{bmatrix}, & \text{for } i_{\mathrm{x}}^{a} > 0 \end{array} \right\} \right)}_{=:\boldsymbol{S}_{\mathtt{S}_{\mathrm{x}}^{a}}(i_{\mathrm{x}}^{a})} \boldsymbol{s}_{\mathrm{x}}^{abc}. \tag{2.54}$$

Like the relation between output voltage $\boldsymbol{u}_{\mathrm{x}}^{abc}$ and dc-link voltage u_{dc} depends in the faulty case on i_{x}^{a}, the same holds for the relation between $\boldsymbol{i}_{\mathrm{x}}^{abc}$ and $i_{\mathrm{dc,x}}$. For an open-switch fault in $\mathtt{S}_{\mathrm{x}}^{a}$ and e.g. switching vector $\boldsymbol{s}_{\mathrm{x}}^{abc} := (\mathtt{1},\ \mathtt{1},\ \mathtt{0})^{\top}$, the dc-link current is given by (see Fig. 2.13)

$$i_{\mathrm{dc,x}} = \begin{cases} i_{\mathrm{x}}^{a} + i_{\mathrm{x}}^{b}, & \text{for } i_{\mathrm{x}}^{a} \leq 0 \\ i_{\mathrm{x}}^{b}, & \text{for } i_{\mathrm{x}}^{a} > 0\,. \end{cases} \tag{2.55}$$

Generalizing this for all possible switching vectors, extends the relation given in (2.52) to

$$i_{\mathrm{dc,x}} = \left(\boldsymbol{i}_{\mathrm{x}}^{abc}\right)^{\top} \underbrace{\left(\begin{bmatrix} 1 & 0 & 0 \\ 0 & 1 & 0 \\ 0 & 0 & 1 \end{bmatrix} + \left\{ \begin{array}{ll} \mathbf{0}_{3\times 3}, & \text{for } i_{\mathrm{x}}^{a} \leq 0 \\ \begin{bmatrix} -1 & 0 & 0 \\ 0 & 0 & 0 \\ 0 & 0 & 0 \end{bmatrix}, & \text{for } i_{\mathrm{x}}^{a} > 0 \end{array} \right\} \right)}_{=:\boldsymbol{R}_{\mathtt{S}_{\mathrm{x}}^{a}}(i_{\mathrm{x}}^{a})} \boldsymbol{s}_{\mathrm{x}}^{abc}. \tag{2.56}$$

Generalizing all these relations for faults in all switches and all possible switching states, leads to the comprehensive model

$$\boldsymbol{u}_{\mathrm{x}}^{a\text{-}b\text{-}c} = \begin{cases} u_{\mathrm{dc}}\, \boldsymbol{Q}_{y}(i_{\mathrm{x}}^{z})\, \boldsymbol{s}_{\mathrm{x}}^{abc} & \text{for fault in upper switch} \\ u_{\mathrm{dc}}\, \boldsymbol{Q}_{y}(i_{\mathrm{x}}^{z})\, \overline{\boldsymbol{s}}_{\mathrm{x}}^{abc} & \text{for fault in lower switch} \end{cases} \tag{2.57}$$

$$\boldsymbol{u}_{\mathrm{x}}^{abc} = \begin{cases} \frac{u_{\mathrm{dc}}}{3}\, \boldsymbol{S}_{y}(i_{\mathrm{x}}^{z})\, \boldsymbol{s}_{\mathrm{x}}^{abc} & \text{for fault in upper switch} \\ \frac{u_{\mathrm{dc}}}{3}\, \boldsymbol{S}_{y}(i_{\mathrm{x}}^{z})\, \overline{\boldsymbol{s}}_{\mathrm{x}}^{abc} & \text{for fault in lower switch} \end{cases} \tag{2.58}$$

$$i_{\mathrm{dc,x}} = \begin{cases} \left(\boldsymbol{i}_{\mathrm{x}}^{abc}\right)^{\top} \boldsymbol{R}_{y}(i_{\mathrm{x}}^{z})\, \boldsymbol{s}_{\mathrm{x}}^{abc} & \text{for fault in upper switch} \\ \left(\boldsymbol{i}_{\mathrm{x}}^{abc}\right)^{\top} \boldsymbol{R}_{y}(i_{\mathrm{x}}^{z})\, \overline{\boldsymbol{s}}_{\mathrm{x}}^{abc} & \text{for fault in lower switch} \end{cases} \tag{2.59}$$

with $y \in \left\{\mathtt{S}_{\mathrm{x}}^{a}, \mathtt{S}_{\mathrm{x}}^{b}, \mathtt{S}_{\mathrm{x}}^{c}, \overline{\mathtt{S}}_{\mathrm{x}}^{a}, \overline{\mathtt{S}}_{\mathrm{x}}^{b}, \overline{\mathtt{S}}_{\mathrm{x}}^{c}\right\}$ and $z \in \{a, b, c\}$. The matrices $\boldsymbol{Q}_{y}$ for calculating line-to-line voltages and $\boldsymbol{S}_{y}$ for phase voltages are listed in Tab. 2.1. The matrices $\boldsymbol{R}_{y}$ to calculate the dc-current $i_{\mathrm{dc,x}}$ are listed in Tab. 2.2.

Remark 2.4.1. *The model of the faulty converter is derived for an amplitude correct scaling of the Clarke transformation (i.e. $\kappa = \frac{2}{3}$). For details and impacts of this choice see Sect. 3.2.1.1 and Appendix A.1.*

Table 2.1: *Voltage model of a faulty converter with switching matrices $\boldsymbol{Q}_y$ (for calculating the line-to-line voltages) and $\boldsymbol{S}_y$ (for calculating the phase voltages) for faulty switches $\mathtt{S}_{\mathrm{x}}^a$, $\mathtt{S}_{\mathrm{x}}^b$, $\mathtt{S}_{\mathrm{x}}^c$ or $\overline{\mathtt{S}}_{\mathrm{x}}^a$, $\overline{\mathtt{S}}_{\mathrm{x}}^b$, $\overline{\mathtt{S}}_{\mathrm{x}}^c$.*

$\boldsymbol{u}_{\mathrm{x}}^{a\text{-}b\text{-}c} = u_{\mathrm{dc}} \boldsymbol{Q}_y(i_{\mathrm{x}}^z)\, \boldsymbol{s}_{\mathrm{x}}^{abc}$			
	$y = \mathtt{S}_{\mathrm{x}}^a, z = a$	$y = \mathtt{S}_{\mathrm{x}}^b, z = b$	$y = \mathtt{S}_{\mathrm{x}}^c, z = c$
$\boldsymbol{Q}_y\,(i_{\mathrm{x}}^z < 0)$	$\begin{bmatrix} 1 & -1 & 0 \\ 0 & 1 & -1 \\ -1 & 0 & 1 \end{bmatrix}$	$\begin{bmatrix} 1 & -1 & 0 \\ 0 & 1 & -1 \\ -1 & 0 & 1 \end{bmatrix}$	$\begin{bmatrix} 1 & -1 & 0 \\ 0 & 1 & -1 \\ -1 & 0 & 1 \end{bmatrix}$
$\boldsymbol{Q}_y\,(i_{\mathrm{x}}^z = 0)$	$\begin{bmatrix} \frac{1}{2} & -1 & 0 \\ 0 & 1 & -1 \\ -\frac{1}{2} & 0 & 1 \end{bmatrix}$	$\begin{bmatrix} 1 & -\frac{1}{2} & 0 \\ 0 & \frac{1}{2} & -1 \\ -1 & 0 & 1 \end{bmatrix}$	$\begin{bmatrix} 1 & -1 & 0 \\ 0 & 1 & -\frac{1}{2} \\ -1 & 0 & \frac{1}{2} \end{bmatrix}$
$\boldsymbol{Q}_y\,(i_{\mathrm{x}}^z > 0)$	$\begin{bmatrix} 0 & -1 & 0 \\ 0 & 1 & -1 \\ 0 & 0 & 1 \end{bmatrix}$	$\begin{bmatrix} 1 & 0 & 0 \\ 0 & 0 & -1 \\ -1 & 0 & 1 \end{bmatrix}$	$\begin{bmatrix} 1 & -1 & 0 \\ 0 & 1 & 0 \\ -1 & 0 & 0 \end{bmatrix}$
$\boldsymbol{u}_{\mathrm{x}}^{a\text{-}b\text{-}c} = u_{\mathrm{dc}} \boldsymbol{Q}_y(i_{\mathrm{x}}^z)\, \overline{\boldsymbol{s}}_{\mathrm{x}}^{abc}$			
	$y = \overline{\mathtt{S}}_{\mathrm{x}}^a, z = a$	$y = \overline{\mathtt{S}}_{\mathrm{x}}^b, z = b$	$y = \overline{\mathtt{S}}_{\mathrm{x}}^c, z = c$
$\boldsymbol{Q}_y\,(i_{\mathrm{x}}^z < 0)$	$\begin{bmatrix} 0 & 1 & 0 \\ 0 & -1 & 1 \\ 0 & 0 & -1 \end{bmatrix}$	$\begin{bmatrix} -1 & 0 & 0 \\ 0 & 0 & 1 \\ 1 & 0 & -1 \end{bmatrix}$	$\begin{bmatrix} -1 & 1 & 0 \\ 0 & -1 & 0 \\ 1 & 0 & 0 \end{bmatrix}$
$\boldsymbol{Q}_y\,(i_{\mathrm{x}}^z = 0)$	$\begin{bmatrix} -\frac{1}{2} & 1 & 0 \\ 0 & -1 & 1 \\ \frac{1}{2} & 0 & -1 \end{bmatrix}$	$\begin{bmatrix} -1 & \frac{1}{2} & 0 \\ 0 & -\frac{1}{2} & 1 \\ 1 & 0 & -1 \end{bmatrix}$	$\begin{bmatrix} -1 & 1 & 0 \\ 0 & -1 & \frac{1}{2} \\ 1 & 0 & -\frac{1}{2} \end{bmatrix}$
$\boldsymbol{Q}_y\,(i_{\mathrm{x}}^z > 0)$	$\begin{bmatrix} -1 & 1 & 0 \\ 0 & -1 & 1 \\ 1 & 0 & -1 \end{bmatrix}$	$\begin{bmatrix} -1 & 1 & 0 \\ 0 & -1 & 1 \\ 1 & 0 & -1 \end{bmatrix}$	$\begin{bmatrix} -1 & 1 & 0 \\ 0 & -1 & 1 \\ 1 & 0 & -1 \end{bmatrix}$
$\boldsymbol{u}_{\mathrm{x}}^{abc} \overset{\text{(AS.11)}}{=} u_{\mathrm{dc}} \left(\boldsymbol{T}_{\mathrm{ltl}}^{\star}\right)^{-1} \boldsymbol{Q}_y(i_{\mathrm{x}}^z)\, \boldsymbol{s}_{\mathrm{x}}^{abc} = \frac{u_{\mathrm{dc}}}{3} \boldsymbol{S}_y(i_{\mathrm{x}}^z)\, \boldsymbol{s}_{\mathrm{x}}^{abc}$			
	$y = \mathtt{S}_{\mathrm{x}}^a, z = a$	$y = \mathtt{S}_{\mathrm{x}}^b, z = b$	$y = \mathtt{S}_{\mathrm{x}}^c, z = c$
$\boldsymbol{S}_y\,(i_{\mathrm{x}}^z < 0)$	$\begin{bmatrix} 2 & -1 & -1 \\ -1 & 2 & -1 \\ -1 & -1 & 2 \end{bmatrix}$	$\begin{bmatrix} 2 & -1 & -1 \\ -1 & 2 & -1 \\ -1 & -1 & 2 \end{bmatrix}$	$\begin{bmatrix} 2 & -1 & -1 \\ -1 & 2 & -1 \\ -1 & -1 & 2 \end{bmatrix}$
$\boldsymbol{S}_y\,(i_{\mathrm{x}}^z = 0)$	$\begin{bmatrix} 1 & -1 & -1 \\ -\frac{1}{2} & 2 & -1 \\ -\frac{1}{2} & -1 & 2 \end{bmatrix}$	$\begin{bmatrix} 2 & -\frac{1}{2} & -1 \\ -1 & 1 & -1 \\ -1 & -\frac{1}{2} & 2 \end{bmatrix}$	$\begin{bmatrix} 2 & -1 & -\frac{1}{2} \\ -1 & 2 & -\frac{1}{2} \\ -1 & -1 & 1 \end{bmatrix}$
$\boldsymbol{S}_y\,(i_{\mathrm{x}}^z > 0)$	$\begin{bmatrix} 0 & -1 & -1 \\ 0 & 2 & -1 \\ 0 & -1 & 2 \end{bmatrix}$	$\begin{bmatrix} 2 & 0 & -1 \\ -1 & 0 & -1 \\ -1 & 0 & 2 \end{bmatrix}$	$\begin{bmatrix} 2 & -1 & 0 \\ -1 & 2 & 0 \\ -1 & -1 & 0 \end{bmatrix}$
$\boldsymbol{u}_{\mathrm{x}}^{abc} \overset{\text{(AS.11)}}{=} u_{\mathrm{dc}} \left(\boldsymbol{T}_{\mathrm{ltl}}^{\star}\right)^{-1} \boldsymbol{Q}_y(i_{\mathrm{x}}^z)\, \overline{\boldsymbol{s}}_{\mathrm{x}}^{abc} = \frac{u_{\mathrm{dc}}}{3} \boldsymbol{S}_y(i_{\mathrm{x}}^z)\, \overline{\boldsymbol{s}}_{\mathrm{x}}^{abc}$			
	$y = \overline{\mathtt{S}}_{\mathrm{x}}^a, z = a$	$y = \overline{\mathtt{S}}_{\mathrm{x}}^b, z = b$	$y = \overline{\mathtt{S}}_{\mathrm{x}}^c, z = c$
$\boldsymbol{S}_y\,(i_{\mathrm{x}}^z < 0)$	$\begin{bmatrix} 0 & 1 & 1 \\ 0 & -2 & 1 \\ 0 & 1 & -2 \end{bmatrix}$	$\begin{bmatrix} -2 & 0 & 1 \\ 1 & 0 & 1 \\ 1 & 0 & -2 \end{bmatrix}$	$\begin{bmatrix} -2 & 1 & 0 \\ 1 & -2 & 0 \\ 1 & 1 & 0 \end{bmatrix}$
$\boldsymbol{S}_y\,(i_{\mathrm{x}}^z = 0)$	$\begin{bmatrix} -1 & 1 & 1 \\ \frac{1}{2} & -2 & 1 \\ \frac{1}{2} & 1 & -2 \end{bmatrix}$	$\begin{bmatrix} -2 & \frac{1}{2} & 1 \\ 1 & -1 & 1 \\ 1 & \frac{1}{2} & -2 \end{bmatrix}$	$\begin{bmatrix} -2 & 1 & \frac{1}{2} \\ 1 & -2 & \frac{1}{2} \\ 1 & 1 & -1 \end{bmatrix}$
$\boldsymbol{S}_y\,(i_{\mathrm{x}}^z > 0)$	$\begin{bmatrix} -2 & 1 & 1 \\ 1 & -2 & 1 \\ 1 & 1 & -2 \end{bmatrix}$	$\begin{bmatrix} -2 & 1 & 1 \\ 1 & -2 & 1 \\ 1 & 1 & -2 \end{bmatrix}$	$\begin{bmatrix} -2 & 1 & 1 \\ 1 & -2 & 1 \\ 1 & 1 & -2 \end{bmatrix}$

Table 2.2: *Dc-link current model of a faulty converter with switching matrices* $\boldsymbol{R}_y$ *for faulty switches* $\mathtt{S}_\mathrm{x}^a,\ \mathtt{S}_\mathrm{x}^b,\ \mathtt{S}_\mathrm{x}^c$ *or* $\overline{\mathtt{S}}_\mathrm{x}^a,\ \overline{\mathtt{S}}_\mathrm{x}^b,\ \overline{\mathtt{S}}_\mathrm{x}^c$.

	$i_{\mathrm{dc,x}} = \left(\boldsymbol{i}_\mathrm{x}^{abc}\right)^\top \boldsymbol{R}_y(i_\mathrm{x}^z)\, \boldsymbol{s}_\mathrm{x}^{abc}$		
	$y = \mathtt{S}_\mathrm{x}^a, z = a$	$y = \mathtt{S}_\mathrm{x}^b, z = b$	$y = \mathtt{S}_\mathrm{x}^c, z = c$
$\boldsymbol{R}_y\,(i_\mathrm{x}^z \le 0)$	$\begin{bmatrix}1&0&0\\0&1&0\\0&0&1\end{bmatrix}$	$\begin{bmatrix}1&0&0\\0&1&0\\0&0&1\end{bmatrix}$	$\begin{bmatrix}1&0&0\\0&1&0\\0&0&1\end{bmatrix}$
$\boldsymbol{R}_y\,(i_\mathrm{x}^z > 0)$	$\begin{bmatrix}0&0&0\\0&1&0\\0&0&1\end{bmatrix}$	$\begin{bmatrix}1&0&0\\0&0&0\\0&0&1\end{bmatrix}$	$\begin{bmatrix}1&0&0\\0&1&0\\0&0&0\end{bmatrix}$
	$i_{\mathrm{dc,x}} = \left(\boldsymbol{i}_\mathrm{x}^{abc}\right)^\top \boldsymbol{R}_y(i_\mathrm{x}^z)\, \overline{\boldsymbol{s}}_\mathrm{x}^{abc}$		
	$y = \overline{\mathtt{S}}_\mathrm{x}^a, z = a$	$y = \overline{\mathtt{S}}_\mathrm{x}^b, z = b$	$y = \overline{\mathtt{S}}_\mathrm{x}^c, z = c$
$\boldsymbol{R}_y\,(i_\mathrm{x}^z < 0)$	$\begin{bmatrix}0&0&0\\0&-1&0\\0&0&-1\end{bmatrix}$	$\begin{bmatrix}-1&0&0\\0&0&0\\0&0&-1\end{bmatrix}$	$\begin{bmatrix}-1&0&0\\0&-1&0\\0&0&0\end{bmatrix}$
$\boldsymbol{R}_y\,(i_\mathrm{x}^z \ge 0)$	$\begin{bmatrix}-1&0&0\\0&-1&0\\0&0&-1\end{bmatrix}$	$\begin{bmatrix}-1&0&0\\0&-1&0\\0&0&-1\end{bmatrix}$	$\begin{bmatrix}-1&0&0\\0&-1&0\\0&0&-1\end{bmatrix}$

2.4.3.2 Model verification

For the verification of the mathematical model of a converter with open-switch fault, simulation results (using the model derived in Sect. 2.4.3.1) are compared with measurement results. The converter is connected to the stator[17] of a PMSM that is current controlled (see Fig. 2.12). The PMSM is connected to a speed controlled reluctance synchronous machine (RSM) (for details see Sect. 4.1.2). Three simulation and measurement experiments have been conducted:

($\mathrm{E}_{2.1}$) Open-switch fault in $\mathtt{S}_s^a$ for a PMSM in motor mode.

($\mathrm{E}_{2.2}$) Open-switch fault in $\mathtt{S}_s^a$ for a PMSM in generator mode.

($\mathrm{E}_{2.3}$) Open-switch fault in $\overline{\mathtt{S}}_s^a$ for a PMSM in generator mode.

Figures 2.14–2.16 show results for open-switch faults comparing simulation and measurement results. In Fig. 2.14 (Experiment ($\mathrm{E}_{2.1}$)) and Fig. 2.15 (Experiment ($\mathrm{E}_{2.2}$)), switch $\mathtt{S}_s^a$ of the upper branch is faulty during motor and generator mode of an electric drive, respectively. In Fig. 2.16 (Experiment ($\mathrm{E}_{2.3}$)), switch $\overline{\mathtt{S}}_s^a$ of the lower branch of the converter has a fault (see Fig. 2.12). In each figure, the first subplot shows the mechanical speed ω_m. The speed varies, due to the varying torque of the PMSM due to the open-switch fault. The second subplot shows the currents i_s^d and i_s^q and their references. The lower subplot shows the currents i_s^a, i_s^b, i_s^c.
Experiment ($\mathrm{E}_{2.1}$): The lower subplot of Fig. 2.14 (motor mode) shows, that only the negative half-wave of i_s^a is feasible; i_s^a cannot become positive. Due to the star connection of the PMSM (i.e. $i_s^a + i_s^b + i_s^c = 0$, see Assumption (AS.3)), also the currents i_s^b and i_s^c are affected by an open-switch fault in phase a. Hence, also the sinusoidal waveforms of i_s^b and i_s^c are distorted. The second subplot shows the machine currents in the dq-reference frame. Both currents do not follow their reference values and do oscillate. While the currents oscillate during the expected positive half-wave of i_s^a, their values are almost constant during the negative half-wave of i_s^a. But

[17] Hence, the index "x" for naming switches, diodes, voltages and currents will be changed to "s".

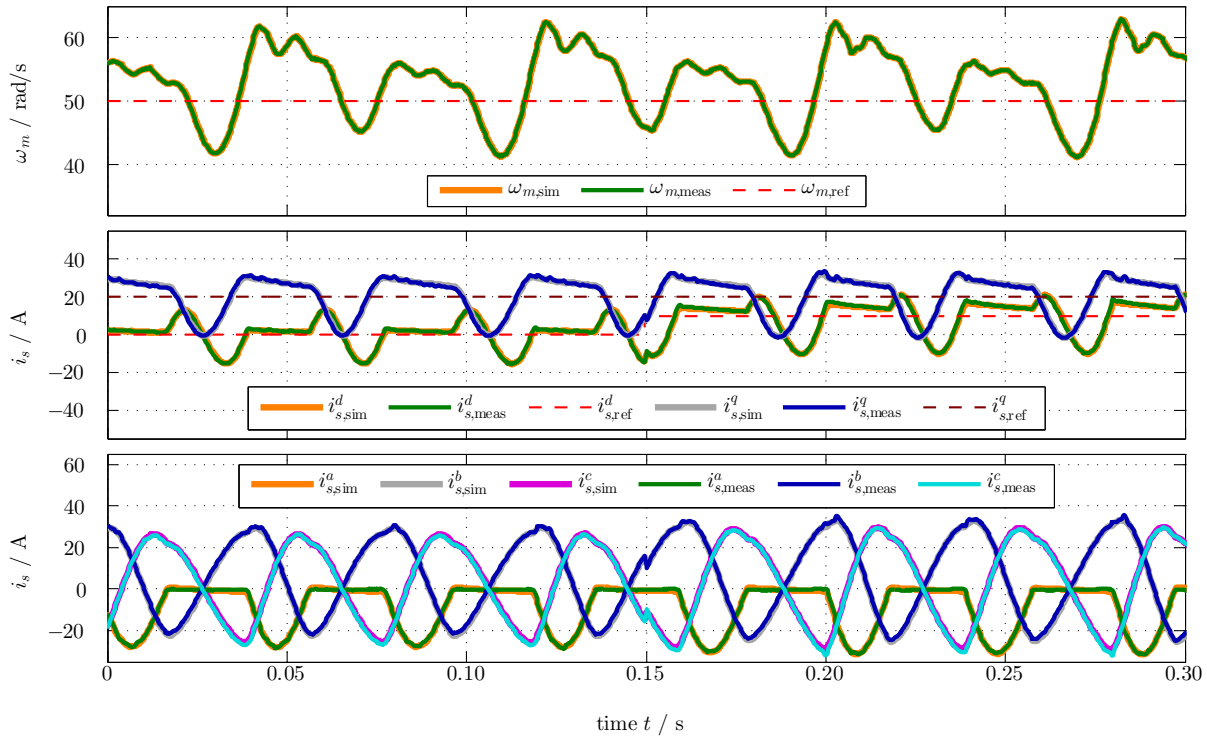

Figure 2.14: *Experiment* ($\mathrm{E}_{2.1}$)*: Comparison of simulation and measurement results for an open-switch fault in* $\mathtt{S}^a_s$ *for a PMSM in motor mode.*

still, both currents cannot track their reference values during the not fault-affected (negative) half-wave of i^a_s.
Experiment ($\mathrm{E}_{2.2}$): In Fig. 2.15, i^q_s is negative and the PMSM is operated as generator. In the lower subplot, it can be seen, that i^a_s is not zero anymore during its positive half-wave. This is due to the induced voltage in phase a of the machine operated in generator mode (a detailed explanation for this will be given in Sect. 3.3.1.4). Although the waveform of i^a_s is now slightly improved compared to motor mode, i^d_s and i^q_s still oscillate and deviate from their reference values even during the negative half-wave of i^a_s.
Experiment ($\mathrm{E}_{2.3}$): Figure 2.16 shows the behaviour of the system for an open-switch fault in $\overline{\mathtt{S}}^a_s$. The speed is increased to $\omega_{m,\mathrm{ref}} = 100\,\frac{\mathrm{rad}}{\mathrm{s}}$. Hence, the frequency of the currents is also increased. As expected for a fault in $\overline{\mathtt{S}}^a_s$, the negative half-wave of i^a_s is not feasible. Also for this case oscillations in i^d_s and i^q_s occur during the not feasible half-wave of i^a_s and deviations from the references for the feasible half-wave are still present.
For all three experiments, as shown in Fig. 2.14–2.16, simulation and measurement results do coincide, which underpins that the mathematical model derived in Sect. 2.4.3.1 is capable of describing the physical behaviour of a converter with open-switch fault with sufficient precision.

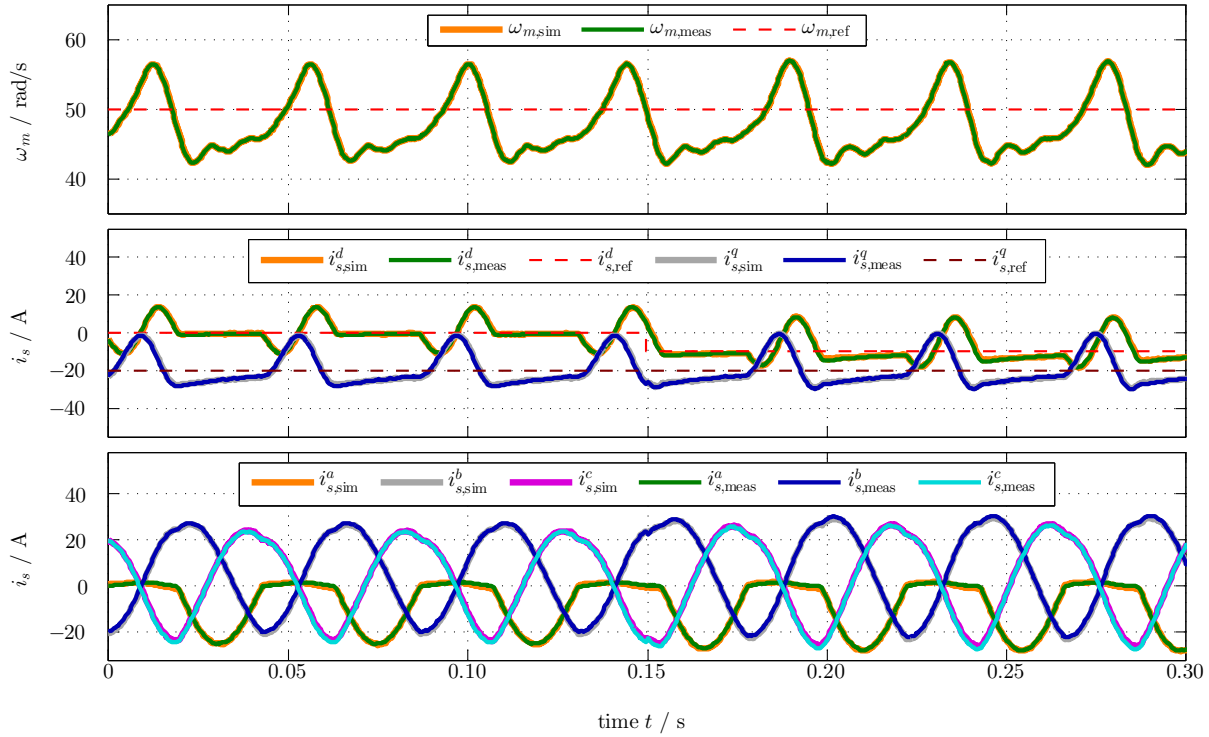

Figure 2.15: *Experiment* ($\mathrm{E}_{2.2}$)*: Comparison of simulation and measurement results for an open-switch fault in* $\mathtt{S}^a_s$ *for a PMSM in generator mode.*

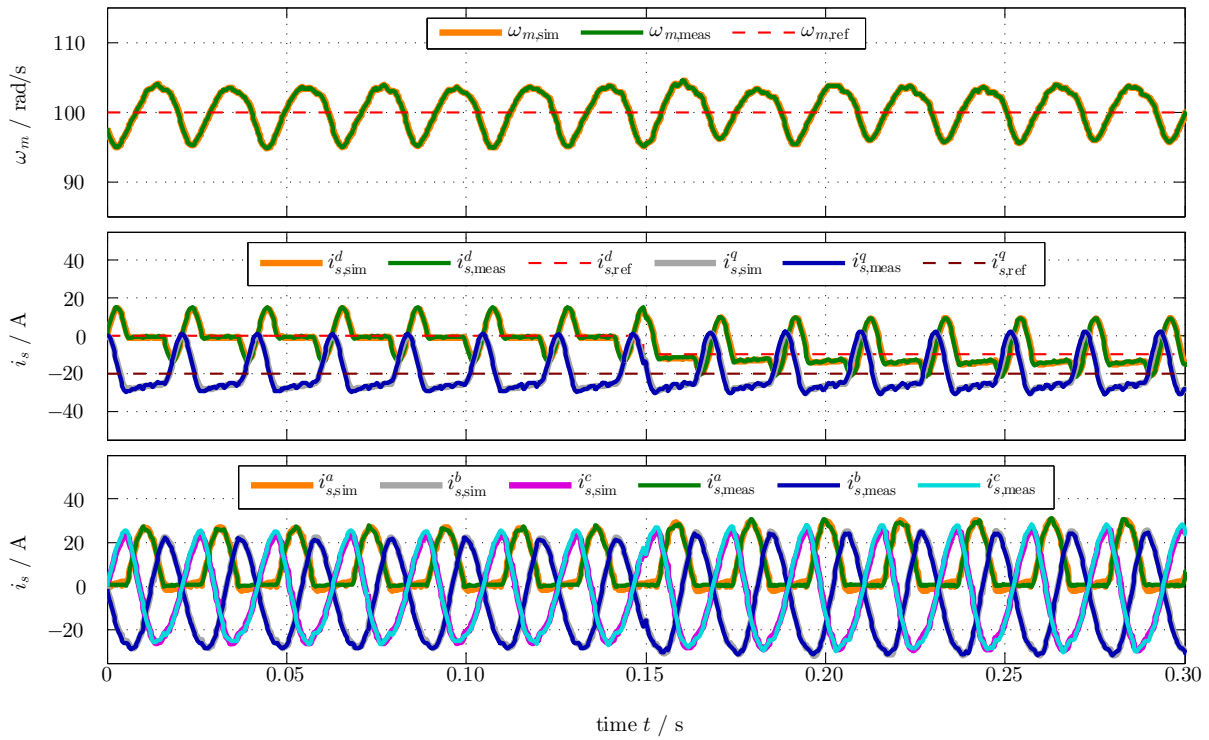

Figure 2.16: *Experiment* ($\mathrm{E}_{2.3}$)*: Comparison of simulation and measurement results for an open-switch fault in* $\overline{\mathtt{S}}^a_s$ *for a PMSM in generator mode.*

Chapter 3

Control of large-scale direct-drive wind turbine systems

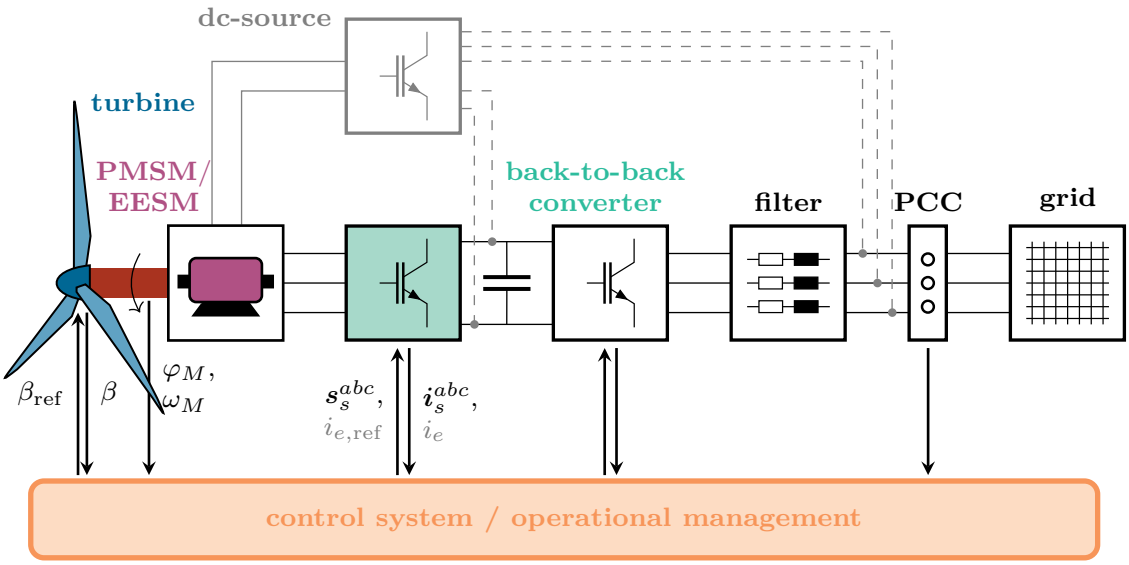

Figure 3.1: *Overview of the components of a wind turbine system with PMSM or EESM including control system and operational management.*

This chapter is partially based on [2–4] where parts were already published. Figure 3.1 illustrates the core components of a wind turbine system with its control system and operational management. For control of the turbine, pitch angle β is measured and can be controlled by changing its reference β_{ref}. For the mechanical system, machine angle φ_M and rotational speed ω_M are measured[18]. The electric machine can be controlled by the switching vector $\boldsymbol{s}_s^{abc}$ of the machine-side converter and the reference excitation current $i_{e,\text{ref}}$ (only for EESMs). The available measurement signals are the stator currents $\boldsymbol{i}_s^{abc}$ and the excitation current i_e (only for EESMs).

In the following sections, the control systems of wind turbine and electric machines (PMSM and EESM) without and with open-switch fault in the machine-side converter are explained.

[18] Note that for direct-drive WTS with rigid shaft holds $\varphi_M = \varphi_T$, $\omega_M = \omega_T$.

3.1 Wind turbine control

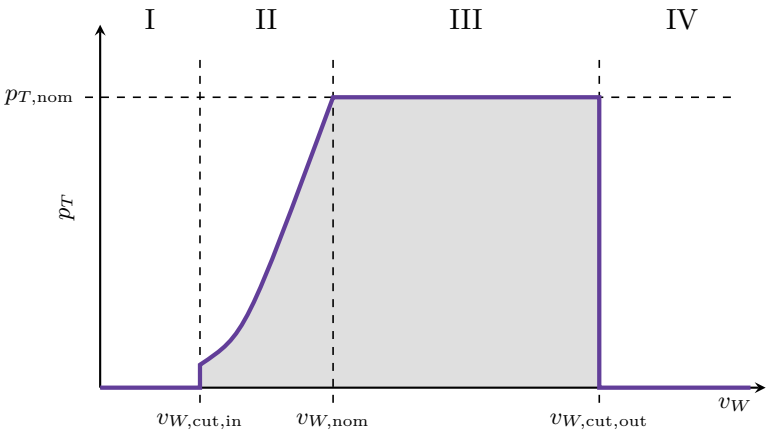

Figure 3.2: *Wind turbine operation regimes.*

Depending on the wind speed v_W (see Fig. 3.2), the wind turbine system operates in one of at least four *regimes of operation*.

- **Regime I ($v_W < v_{W,\text{cut,in}}$):** For a wind speed v_W smaller than the cut-in wind speed $v_{W,\text{cut,in}}$ (in $\frac{\text{m}}{\text{s}}$) no power is produced.
- **Regime II ($v_{W,\text{cut,in}} \leq v_W < v_{W,\text{nom}}$):** The turbine power p_T is smaller than its rated value $p_{T,\text{nom}}$ (in W) and the control objective is to extract the maximum power.
- **Regime III ($v_{W,\text{nom}} \leq v_W < v_{W,\text{cut,out}}$):** The turbine power is at least the rated value of the turbine (i.e. $p_T \geq p_{T,\text{nom}}$). The control objective in this regime is to limit the turbine power to its rated value.
- **Regime IV ($v_{W,\text{cut,out}} \leq v_W$):** For a wind speed v_W larger than the cut-out wind speed $v_{W,\text{cut,out}}$ (in $\frac{\text{m}}{\text{s}}$) no power is produced.

In both active regimes (regime II and regime III) the control objectives are fulfilled by a combination of controlling the pitch angle β and the machine torque τ_M. Figure 3.3 depicts the control strategies for regime II and regime III:

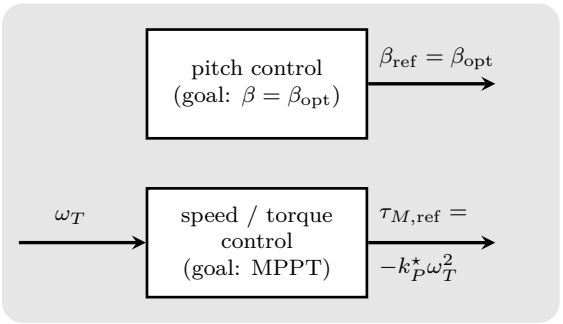

(a) Control strategy for regime II.

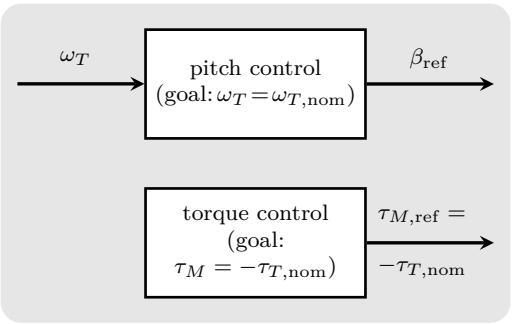

(b) Control strategy for regime III.

Figure 3.3: *Control strategies for* (a) regime II and (b) regime III (based on Fig. 4 in [7]).

Regime II: The control objective is to extract the maximal power i.e. maximum power point tracking (MPPT). The pitch angle is controlled to its optimal value, i.e. $\beta_{\text{ref}} = \beta_{\text{opt}}$. The rotational speed of the turbine is controlled by the nonlinear control law $\tau_{M,\text{ref}} = -k_P^\star \omega_T^2$ (in N m) to achieve convergence to the optimal tip speed ratio λ_{opt}, where the power coefficient c_P has its maximal value $c_{P,\text{opt}}$ (see graph of the power coefficient in Fig. 2.2). For more details on the nonlinear controller, its derivation and a stability analysis see [4], [96, Ch. 8], [108] and [109], respectively.
Regime III: The control objective in this regime is to limit the extracted turbine power to its rated value. The speed control problem is shifted to the pitch controller. If the turbine rotational speed exceeds its nominal value, i.e. $\omega_T > \omega_{T,\text{nom}}$, the pitch angle β must be increased to decrease the power coefficient c_P (see graph of the power coefficient in Fig. 2.2). The machine torque is kept constant at the rated turbine torque, i.e. $\tau_{M,\text{ref}} = -\tau_{T,\text{nom}}$, by a proper torque feedforward controller (see e.g. [52]).
Pitch and torque controller—as illustrated in Fig. 3.3—fulfil the control objectives for both regimes intrinsically and will be described in more detail in the upcoming sections.

Remark 3.1.1. *For some WTS two additional regimes, regime II.5 (between regime II and regime III) and regime III.5 (between regime III and regime IV) are introduced. For details see e.g. [96, Sect. 8.3], [110] and [111].*

3.1.1 Pitch control

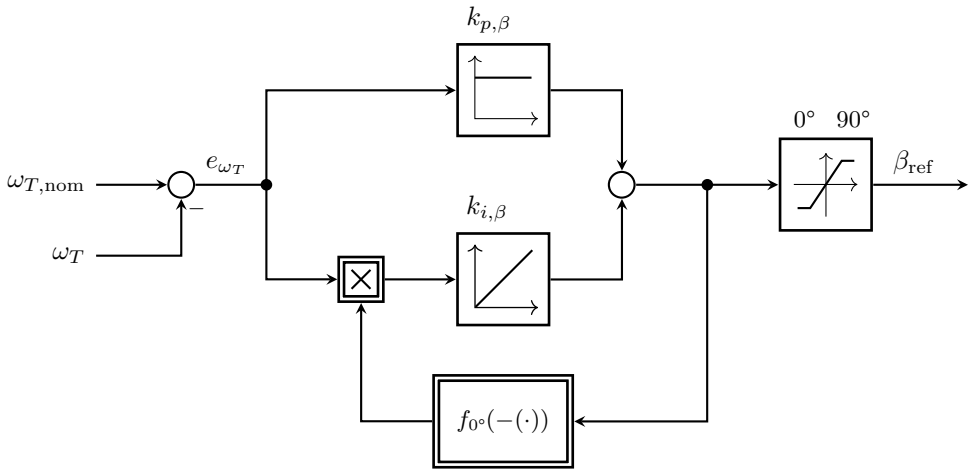

Figure 3.4: *Block diagram of pitch controller with output saturation and anti-windup (conditional integration).*

The output saturated PI-controller with anti-windup strategy [3] is given by

$$\left.\begin{aligned} \tfrac{\mathrm{d}}{\mathrm{d}t}\xi_\beta &= f_{0^\circ}\Big(- k_{p,\beta}\big(\overbrace{\omega_{T,\text{nom}} - \omega_T}^{=:e_{\omega_T}}\big) - k_{i,\beta}\xi_\beta\Big)\, e_{\omega_T}, \\ \beta_{\text{ref}} &= \operatorname{sat}_{0^\circ}^{90^\circ}[k_{p,\beta}e_{\omega_T} + k_{i,\beta}\xi_\beta] \end{aligned}\right\} \tag{3.1}$$

and generates the pitch angle reference β_{ref} for the underlying position control system of the rotor blades. The PI-controller dynamics in (3.1) depend on turbine rotational speed ω_T as input (or rather the rotational speed error e_{ω_T} (in $\frac{\text{rad}}{\text{s}}$), depending on the rated rotational speed $\omega_{T,\text{nom}}$ of the turbine), proportional gain $k_{p,\beta}$ (in $\frac{^\circ\text{s}}{\text{rad}}$) and integral gain $k_{i,\beta}$ (in $\frac{^\circ}{\text{rad}}$). The output

β_{ref} is saturated to remain within physically reasonable bounds (i.e. $0° \leq \beta_{\text{ref}} \leq 90°$). Figure 3.4 shows a block diagram of the pitch controller.

3.1.2 Torque control

The nonlinear torque controller

$$\tau_{M,\text{ref}} = -\operatorname{sat}_0^{\tau_{T,\text{nom}}}\left[k_P^\star\,\omega_T^2\right] \text{ where } k_P^\star := \frac{\varrho\pi r_T^5}{2}\frac{c_P(\lambda_{\text{opt}},\beta_{\text{opt}})}{(\lambda_{\text{opt}})^3}, \tag{3.2}$$

outputs the torque for MPPT in regime II and the rated (nominal) torque $\tau_{T,\text{nom}}$ in regime III. The torque controller only depends on known values of the WTS; such as air density ρ, turbine radius r_T, optimal tip speed ratio λ_{opt} and optimal pitch angle β_{opt} and measured turbine speed ω_T. A measurement of the wind speed is not required for MPPT[19].

3.2 Electric drive control

As this work focuses on the control of the machine-side of a WTS, the control of the grid-side is not discussed. Details on the control of the grid-side of a WTS with similar nomenclature can be found in [3–5, 8, 9, 91].

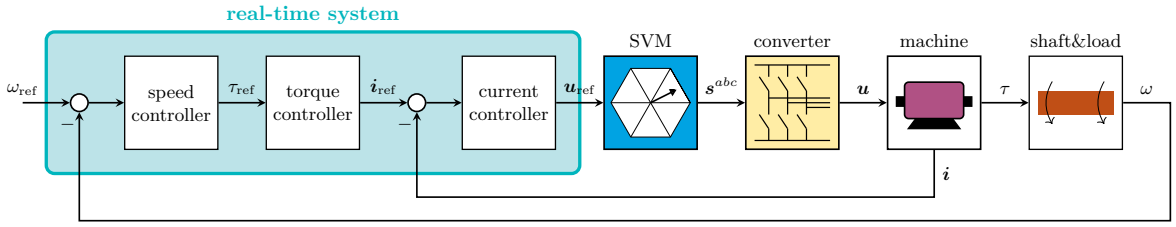

Figure 3.5: *Cascade control structure for a speed-controlled drive.*

Before starting with the electric drive control, an overview on the principle design of a drive control system is given. Figure 3.5 shows the cascade control structure for a speed-controlled drive. The controllers are implemented on a real-time system. The speed controller input is the difference[20] $\omega_{\text{ref}} - \omega$ between demanded speed and actual speed. The controller output is a torque demand τ_{ref} to control this difference to zero. Standard drives are *not* equipped with a torque sensor. Hence, only feedforward torque control is possible, which is sensitive towards parameter variations and insufficient modelling of the torque–current relationship. The output of the torque controller is a reference current vector $\boldsymbol{i}_{\text{ref}}$, which is supposed to cause the machine to produce the demanded torque τ_{ref}. As the currents of the machine are measured, feedback current control using the difference $\boldsymbol{i}_{\text{ref}} - \boldsymbol{i}$ to create the voltage reference vector $\boldsymbol{u}_{\text{ref}}$ is possible. The space-vector modulation (SVM) is usually implemented outside the real-time system with a much faster sampling rate. The SVM creates the switching signals $\boldsymbol{s}^{abc}$ for the converter. Applying $\boldsymbol{s}^{abc}$, the converter creates the output voltage vector $\boldsymbol{u}$, and for a fault-free converter on average holds $\boldsymbol{u} \approx \boldsymbol{u}_{\text{ref}}$. The voltage vector $\boldsymbol{u}$ causes the machine to produce the torque τ, which influences speed ω of shaft and load.
Details on the torque and current controllers and their specifics for PMSM and EESM are given in the following sections. But before starting with the actual controller design, the switching signal generation for a converter will be explained in detail.

[19] This implies a perfectly working torque control. If this assumption does not hold, efficiency and power production of the WTS are deteriorated (see [7]).

[20] The nonlinear turbine controller (3.2) does not use the difference $\omega_{\text{ref}} - \omega$, but just ω.

3.2.1 Control of converter

The output of a converter are switched voltages. Their average value over one switching period T_{sw} (in s) should equal the demanded reference. For that, appropriate switching signals $\boldsymbol{s}_{\mathrm{x}}^{abc}$ have to be created (see Fig. 3.5 and Sect. 2.4.2, modelling of an ideal converter and Fig. 2.11). To do so, there exists a huge variety of methods (for more details see [53, Chap. 14]). One of the most common methods is called *space-vector modulation*. For the fault-free converter a symmetrical space-vector modulation will be used in this work (see [54, Sect. 2.4.1], [112, Sect. 8.4.10], [113, Sect. 6.1.1]).

3.2.1.1 Space-vector modulation (SVM)

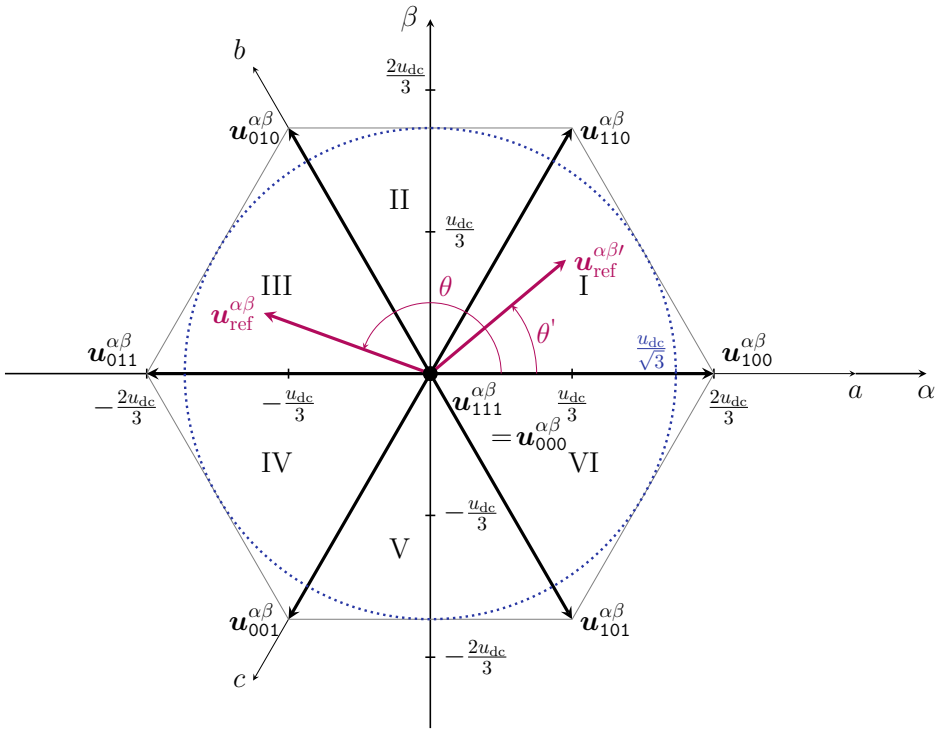

Figure 3.6: *Voltage hexagon for a voltage source converter with space-vector scaling* $\kappa = \frac{2}{3}$*, reference voltage vector* $\boldsymbol{u}_{\mathrm{ref}}^{\alpha\beta}$ *in sector III and auxiliary reference voltage vector* $\boldsymbol{u}_{\mathrm{ref}}^{\alpha\beta\prime}$ *in sector I.*

Figure 3.6 shows the hexagon of feasible output voltages $\boldsymbol{u}^{\alpha\beta} = (u^{\alpha}, u^{\beta})^{\top}$ for the eight possible (active) switching states of a 2-level converter. There are two zero switching states $\{\mathtt{000}, \mathtt{111}\}$ and six active switching states $\{\mathtt{100}, \mathtt{110}, \mathtt{010}, \mathtt{011}, \mathtt{001}, \mathtt{101}\}$. The boundary (adjacent) space-vectors of the respective sector (e.g. for sector III: $\boldsymbol{u}_{\mathtt{010}}^{\alpha\beta}$ and $\boldsymbol{u}_{\mathtt{011}}^{\alpha\beta}$), and, usually, both zero vectors $\boldsymbol{u}_{\mathtt{000}}^{\alpha\beta}$ and $\boldsymbol{u}_{\mathtt{111}}^{\alpha\beta}$ are applied to approximate the reference voltage vector $\boldsymbol{u}_{\mathrm{ref}}^{\alpha\beta}$ over one switching period $T_{\mathrm{sw}} = 1/f_{\mathrm{sw}}$ (inverse of the switching frequency f_{sw} (in $\frac{1}{\mathrm{s}}$)), i.e.

$$\begin{aligned}\boldsymbol{u}_{\mathrm{ref}}^{\alpha\beta} &= \frac{1}{T_{\mathrm{sw}}}\left(\int_{t}^{t+\frac{T_0}{2}} \boldsymbol{u}_{\mathtt{000}}^{\alpha\beta}\mathrm{d}\tau + \int_{t+\frac{T_0}{2}}^{t+T_0} \boldsymbol{u}_{\mathtt{111}}^{\alpha\beta}\mathrm{d}\tau + \int_{t+T_0}^{t+T_0+T_1} \boldsymbol{u}_{\mathtt{010}}^{\alpha\beta}\mathrm{d}\tau + \int_{t+T_0+T_1}^{t+T_0+T_1+T_2} \boldsymbol{u}_{\mathtt{011}}^{\alpha\beta}\mathrm{d}\tau\right) \\ &= \frac{1}{T_{\mathrm{sw}}}\left(\tfrac{T_0}{2}\boldsymbol{u}_{\mathtt{000}}^{\alpha\beta} + \tfrac{T_0}{2}\boldsymbol{u}_{\mathtt{111}}^{\alpha\beta} + T_1\boldsymbol{u}_{\mathtt{010}}^{\alpha\beta} + T_2\boldsymbol{u}_{\mathtt{011}}^{\alpha\beta}\right).\end{aligned} \tag{3.3}$$

To do so, T_{sw} is divided into three time intervals: T_1 (in s) for the first non-zero vector, T_2 (in

s) for the second non-zero vector and T_0 (in s) for the zero vectors such that $T_1 + T_2 + T_0 = T_{\mathrm{sw}}$ (see Fig. 3.6 and Fig. 3.7). Based on the amplitude $\widehat{u}_{\mathrm{ref}}$ (in V) and the angle θ (in °/rad) of the reference voltage vector

$$\boldsymbol{u}_{\mathrm{ref}}^{\alpha\beta} = \begin{pmatrix} u_{\mathrm{ref}}^{\alpha} \\ u_{\mathrm{ref}}^{\beta} \end{pmatrix} = \widehat{u}_{\mathrm{ref}} \begin{pmatrix} \cos(\theta) \\ \sin(\theta) \end{pmatrix}, \tag{3.4}$$

the time intervals T_1, T_2 and T_0 can be calculated as follows [112, p. 699], [114]

$$T_1 := \sqrt{3}\frac{\widehat{u}_{\mathrm{ref}}}{u_{\mathrm{dc}}} \sin\left(\tfrac{\pi}{3} - \theta^{'}\right) T_{\mathrm{sw}} \tag{3.5}$$

$$T_2 := \sqrt{3}\frac{\widehat{u}_{\mathrm{ref}}}{u_{\mathrm{dc}}} \sin\left(\theta^{'}\right) T_{\mathrm{sw}} \tag{3.6}$$

$$T_0 := T_{\mathrm{sw}} - T_1 - T_2, \tag{3.7}$$

where

$$\widehat{u}_{\mathrm{ref}} := \sqrt{\left(u_{\mathrm{ref}}^{\alpha}\right)^2 + \left(u_{\mathrm{ref}}^{\beta}\right)^2} \qquad \text{and} \tag{3.8}$$

$$\theta^{'} := \mathrm{mod}(\underbrace{\mathrm{atan2}(u_{\mathrm{ref}}^{\beta}, u_{\mathrm{ref}}^{\alpha})}_{=:\theta}, \tfrac{\pi}{3}) \in [0, \tfrac{\pi}{3}). \tag{3.9}$$

The angle $\theta^{'}$ (in °/rad) is the shifted angle of the angle θ as in sector I (see Fig. 3.6). If the voltage reference vector is not limited to its maximum feasible value (see Sect. 3.2.2.1),

$$\widehat{u}(u_{\mathrm{dc}}, \theta^{'}) := \underbrace{\frac{\sqrt{3}}{\sin(\theta^{'}) + \sqrt{3}\cos(\theta^{'})}}_{\frac{\sqrt{3}}{2} \leq \,\cdot\, \leq 1} \cdot \tfrac{2}{3} u_{\mathrm{dc}} \leq \tfrac{2}{3} u_{\mathrm{dc}} \quad \text{(in V)} \tag{3.10}$$

within the full (fault-free) voltage hexagon (see Fig. 3.6), depending on the implementation of the SVM, a negative time T_0 could occur deteriorating the SVM output. The maximally available amplitude $\widehat{u}$ of the converter depends on the voltage reference angle θ and the dc-link voltage. Note that $\hat{u}_{\max}$ varies inside the voltage hexagon. It is larger for $\theta = 0°$ or $\theta = 60°$ (maximum voltage amplitude $\widehat{u}(u_{\mathrm{dc}}, 0) = \frac{2}{3}u_{\mathrm{dc}}$) than for $\theta = 30°$ (minimum voltage amplitude $\widehat{u}(u_{\mathrm{dc}}, \pi/6) = \frac{1}{\sqrt{3}}u_{\mathrm{dc}}$). Invoking trigonometric identities leads to the expression of $\widehat{u}$ in (3.10) by only considering the first sector of the voltage hexagon, i.e. $\theta = \theta^{'} \in [0°, 60°)$. Note that, in sector I, $\theta^{'}$ coincides with θ. Then, by using the auxiliary phase angle $\theta^{'}$ as defined in (3.9), the generalized formula for the available amplitude $\widehat{u}$ is obtained for all other sectors of the voltage hexagon.

Figure 3.7 shows the switching pattern for a voltage reference vector in sector III. The switching pattern is symmetric towards $t = \frac{T_{\mathrm{sw}}}{2}$. First the zero switching vector $\boldsymbol{u}_{000}^{\alpha\beta}$ is applied for $\frac{T_0}{4}$. Afterwards the first non-zero vector $\boldsymbol{u}_{010}^{\alpha\beta}$ is applied for $\frac{T_1}{2}$. It is that vector, where only one switching state needs to be changed. The second non-zero vector $\boldsymbol{u}_{011}^{\alpha\beta}$ is applied for $\frac{T_2}{2}$ and than the second zero vector $\boldsymbol{u}_{111}^{\alpha\beta}$ for $\frac{T_0}{4}$. After that, the whole switching process runs in reverse until $t = T_{\mathrm{sw}}$. With this type of SVM, it is secured, that only one switching state changes at every switching transition.

Remark 3.2.1 (Relationship between scaling of space-vectors and voltage hexagon.)**.** *The maximum feasible voltage in the voltage hexagon (see Fig. 3.6), depends on the scaling factor κ of the Clarke transformation matrix (see* (A.1.4)*,* (A.1.5) *and [51, Chap. 14]).*

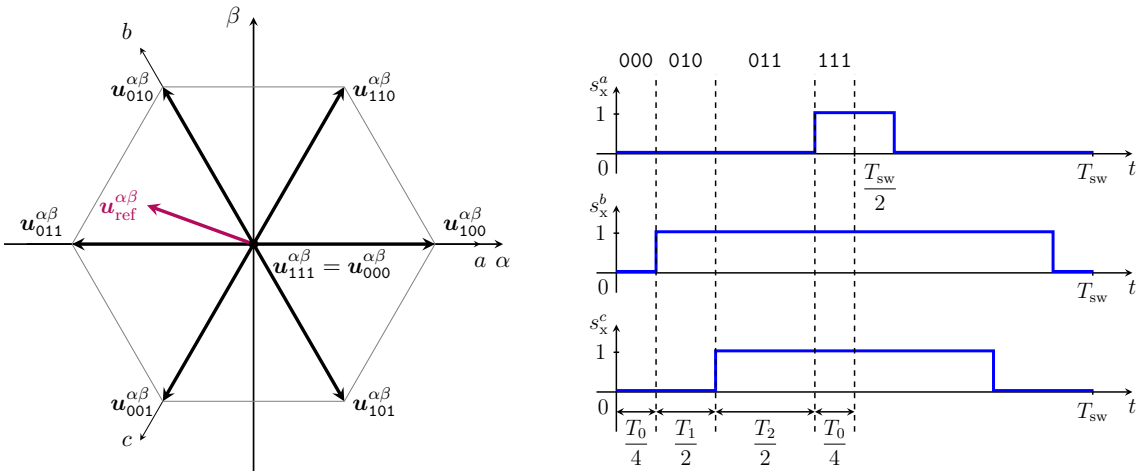

(a) Voltage hexagon with voltage reference $\boldsymbol{u}^{\alpha\beta}_{\text{ref}}$ in sector III.

(b) Switching pattern for generation of $\boldsymbol{u}^{\alpha\beta}_{\text{ref}}$.

Figure 3.7: *Switching pattern* (b) *to generate a voltage reference* $\boldsymbol{u}^{\alpha\beta}_{\text{ref}}$ *in sector III* (a) *by a linear combination of the voltage vectors* $\boldsymbol{u}^{\alpha\beta}_{000}$, $\boldsymbol{u}^{\alpha\beta}_{010}$, $\boldsymbol{u}^{\alpha\beta}_{011}$ *and* $\boldsymbol{u}^{\alpha\beta}_{111}$.

3.2.1.2 Converter dynamics approximation

For the current controller design, the delay between applying reference voltages $\boldsymbol{u}_{\text{ref}}$ to the SVM and the actual appearance of $\boldsymbol{u}$ at the output must be considered (see [53, Sect. 14.6]). The converter dynamics can be approximated by

$$\frac{\mathrm{d}}{\mathrm{d}t}\boldsymbol{u} = \frac{1}{T_{\text{avg}}}\left(-\boldsymbol{u} + \boldsymbol{u}_{\text{ref}}\right) \tag{3.11}$$

as first order lag system with converter time delay T_{avg} (in s), see [51, Sect. 14.3]. Depending on the used type of SVM and its implementation, the converter time delay varies within the interval [51, p. 520]

$$T_{\text{avg}} \in \left[\frac{T_{\text{sw}}}{2}, \frac{3T_{\text{sw}}}{2}\right]. \tag{3.12}$$

3.2.2 Control of PMSM

In this section, the control of the PMSM will be explained. As shown in Fig. 3.5, the feedforward torque controller creates a current reference vector $\boldsymbol{i}_{\text{ref}}$ based on the torque reference τ_{ref}. The feedback current control creates reference voltages $\boldsymbol{u}_{\text{ref}}$ based on the difference $\boldsymbol{i}_{\text{ref}} - \boldsymbol{i}$ between demanded currents and actual currents. First the current controller and subsequently the torque controller design will be presented in detail.

3.2.2.1 Current control

Figure 3.8 shows the current control system consisting of PI-controllers with anti-windup, cross-coupling feedforward compensation and reference voltage saturation. Each part will be explained in the following in more detail.
The controller design will be discussed for the nonlinear machine (2.12) with differential inductances, but can easily be adapted to the linear machine (2.15). For that $\boldsymbol{L}_s^{dq}$ and $\boldsymbol{\psi}_s^{dq}$ have to be replaced accordingly. Recalling the machine dynamics in (2.12), i.e.

$$\boldsymbol{u}_s^{dq} = \boldsymbol{R}_s^{dq}\boldsymbol{i}_s^{dq} + \boldsymbol{L}_s^{dq}(\boldsymbol{i}_s^{dq})\tfrac{\mathrm{d}}{\mathrm{d}t}\boldsymbol{i}_s^{dq} + \omega_k \boldsymbol{J}\boldsymbol{\psi}_s^{dq}(\boldsymbol{i}_s^{dq}) \tag{3.13}$$

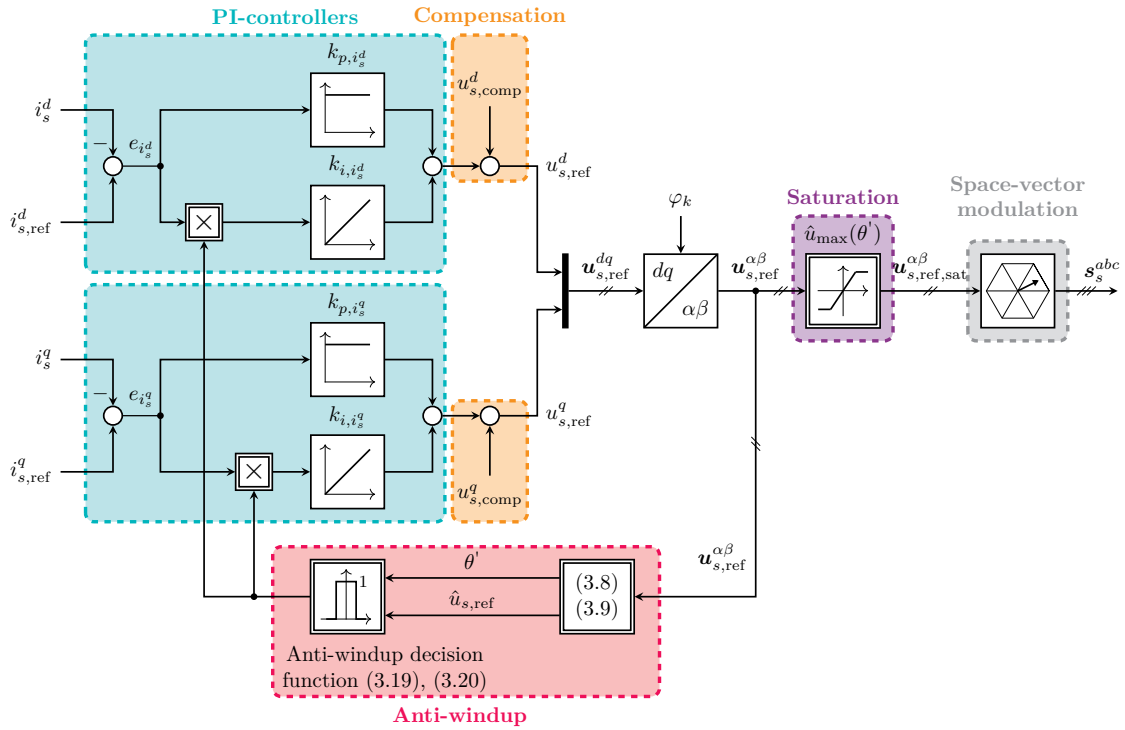

Figure 3.8: *Standard control system for PMSM (field-oriented control): PI-controllers with anti-windup, cross-coupling feedforward compensation and reference voltage saturation.*

with vectors and matrices

$$\boldsymbol{u}_s^{dq} := \begin{pmatrix} u_s^d \\ u_s^q \end{pmatrix}, \quad \boldsymbol{i}_s^{dq} := \begin{pmatrix} i_s^d \\ i_s^q \end{pmatrix}, \quad \boldsymbol{R}_s^{dq} := \begin{bmatrix} R_s^d & 0 \\ 0 & R_s^q \end{bmatrix}, \quad \boldsymbol{L}_s^{dq} := \begin{bmatrix} L_s^{dd} & L_s^{dq} \\ L_s^{qd} & L_s^{qq} \end{bmatrix} =: \begin{bmatrix} l_{11} & l_{12} \\ l_{21} & l_{22} \end{bmatrix}. \tag{3.14}$$

and assuming the existence of the inverse $(\boldsymbol{L}_s^{dq})^{-1}$ of the inductance matrix $\boldsymbol{L}_s^{dq}$ (for details and conditions see [51, Sect. 14.3.2]), (3.13) can be rearranged to obtain the current dynamics

$$\tfrac{\mathrm{d}}{\mathrm{d}t}\boldsymbol{i}_s^{dq} = \left(\boldsymbol{L}_s^{dq}(\boldsymbol{i}_s^{dq})\right)^{-1}\left(\boldsymbol{u}_s^{dq} - \boldsymbol{R}_s^{dq}\boldsymbol{i}_s^{dq} - \omega_k \boldsymbol{J}\boldsymbol{\psi}_s^{dq}(\boldsymbol{i}_s^{dq})\right) \tag{3.15}$$

where

$$\left(\boldsymbol{L}_s^{dq}\right)^{-1} = \frac{1}{\det\left(\boldsymbol{L}_s^{dq}\right)}\begin{bmatrix} l_{22} & -l_{12} \\ -l_{21} & l_{11} \end{bmatrix} = \frac{1}{l_{11}l_{22} - l_{12}l_{21}}\begin{bmatrix} l_{22} & -l_{12} \\ -l_{21} & l_{11} \end{bmatrix} =: \begin{bmatrix} l_{11}^{-1} & l_{12}^{-1} \\ l_{21}^{-1} & l_{22}^{-1} \end{bmatrix}. \tag{3.16}$$

So the d- and q-component dynamics become

$$\left.\begin{aligned} \tfrac{\mathrm{d}}{\mathrm{d}t} i_s^d &= l_{11}^{-1}\Big[u_s^d - R_s^d i_s^d + \underbrace{\omega_k\psi_s^q + \tfrac{l_{12}^{-1}}{l_{11}^{-1}}\left(u_s^q - R_s^q i_s^q - \omega_k\psi_s^d\right)}_{=:u_{s,\mathrm{dist}}^d}\Big] \\ \tfrac{\mathrm{d}}{\mathrm{d}t} i_s^q &= l_{22}^{-1}\Big[u_s^q - R_s^q i_s^q \underbrace{-\omega_k\psi_s^d + \tfrac{l_{21}^{-1}}{l_{22}^{-1}}\left(u_s^d - R_s^d i_s^d + \omega_k\psi_s^q\right)}_{=:u_{s,\mathrm{dist}}^q}\Big]. \end{aligned}\right\} \tag{3.17}$$

To control the currents i_s^d and i_s^q of the PMSM, PI-controllers and feedforward disturbance com-

pensation are used (see Fig. 3.8). The demanded reference voltages consist of two components and are given by

$$\boldsymbol{u}_{s,\mathrm{ref}}^{dq} = \underbrace{\boldsymbol{u}_{s,\mathrm{pi}}^{dq}}_{\text{PI-controller output}} + \underbrace{\boldsymbol{u}_{s,\mathrm{comp}}^{dq}}_{\text{disturbance compensation}} \tag{3.18}$$

with reference voltage vector $\boldsymbol{u}_{s,\mathrm{ref}}^{dq} := (u_{s,\mathrm{ref}}^{d}, u_{s,\mathrm{ref}}^{q})^{\top}$ (in V)^2, output voltage vector $\boldsymbol{u}_{s,\mathrm{pi}}^{dq} := (u_{s,\mathrm{pi}}^{d}, u_{s,\mathrm{pi}}^{q})^{\top}$ (in V)^2 of the PI-controllers and disturbance compensation vector $\boldsymbol{u}_{s,\mathrm{comp}}^{dq} := (u_{s,\mathrm{comp}}^{d}, u_{s,\mathrm{comp}}^{q})^{\top}$ (in V)^2. For *static* disturbance compensation, $\boldsymbol{u}_{s,\mathrm{comp}}^{dq} = -(u_{s,\mathrm{dist}}^{d}, u_{s,\mathrm{dist}}^{q})^{\top}$ is chosen. Details can be found in [4] or [53, Sect. 7.1.1]. The PI-controllers are equipped with an anti-windup strategy to limit the reference voltages (see Sect. 3.2.1.1). The dynamics of the PI-controllers are

$$\left.\begin{aligned} \tfrac{\mathrm{d}}{\mathrm{d}t}\boldsymbol{\xi} &= f_{\mathrm{aw}}(\boldsymbol{u}_{s,\mathrm{ref}}^{dq}, \hat{u}_s)\boldsymbol{e} \\ \boldsymbol{u}_{\mathrm{pi}} &= \boldsymbol{K}_{p,\boldsymbol{i}}\boldsymbol{e} + \boldsymbol{K}_{i,\boldsymbol{i}}\boldsymbol{\xi} \end{aligned}\right\} \tag{3.19}$$

with current tracking error $\boldsymbol{e} := \boldsymbol{i}_{s,\mathrm{ref}}^{dq} - \boldsymbol{i}_{s}^{dq}$ (in V)^2, initial value $\boldsymbol{\xi}(0) = \mathbf{0}_2$, anti-windup decision function[21]

$$f_{\mathrm{aw}}(\boldsymbol{u}_{s,\mathrm{ref}}^{dq}, \hat{u}_s) = f_{\hat{u}_s}\left(\left\|(u_{s,\mathrm{ref}}^{d}, u_{s,\mathrm{ref}}^{q})^{\top}\right\|\right) \tag{3.20}$$

and proportional and integral gain matrices

$$\boldsymbol{K}_{p,\boldsymbol{i}_s^{dq}} = \mathrm{diag}\left(k_{p,i_s^d}, k_{p,i_s^q}\right) = \mathrm{diag}\left(\tfrac{1}{2T_{\mathrm{avg}}l_{11}^{-1}}, \tfrac{1}{2T_{\mathrm{avg}}l_{22}^{-1}}\right) \qquad \text{and} \tag{3.21}$$

$$\boldsymbol{K}_{i,\boldsymbol{i}_s^{dq}} = \mathrm{diag}\left(k_{i,i_s^d}, k_{i,i_s^q}\right) = \mathrm{diag}\left(\tfrac{R_s^d}{2T_{\mathrm{avg}}}, \tfrac{R_s^q}{2T_{\mathrm{avg}}}\right). \tag{3.22}$$

The current PI-controllers are tuned according to the *"Magnitude Optimum"* (see [4]). Using T_{avg} as in (3.12) assures to include the time delay of the converter into the current controller design.
To avoid physically not feasible reference values and possibly unpredictable behaviour of the switching signal generation (see Sect. 3.2.1), the reference voltages are saturated to

$$\boldsymbol{u}_{s,\mathrm{ref,sat}}^{dq} = \mathbf{sat}_{\hat{u}_s}(\boldsymbol{u}_{s,\mathrm{ref}}^{dq}), \tag{3.23}$$

such that the amplitude of $\boldsymbol{u}_{s,\mathrm{ref,sat}}^{dq}$ is limited to the maximally feasible value $\hat{u}_s$, i.e.

$$\forall t \geq 0: \qquad \left\|\boldsymbol{u}_{s,\mathrm{ref,sat}}^{dq}(t)\right\| \leq \hat{u}_s, \tag{3.24}$$

whereas the angle is *not* changed.

3.2.2.2 Torque control

The term *torque control* is usually used for the generation of reference currents based on a reference torque (see Fig. 3.10). As common drive trains mostly lack a torque sensor (due to its high costs), torque control is implemented as feedforward control. So the quality of this control is highly dependent on a proper knowledge of the physics of the electric machine (see [52], [53, Sect. 16.7], [54, Chap. 7], [55, Chap. 5], [59, Chap. 6]). Since the same torque can be produced by different combinations of currents[22], there is some degree of freedom in choosing

[21] Recall the definition of $f_{\hat{u}_s}$ in the Nomenclature section and (3.10).

[22] E.g. for an isotropic PMSM, see (2.15), for every physically feasible combination of different i_s^d-values and one value of i_s^q the same torque is produced

these reference currents. The usage of these degrees of freedom can be summarized in four[23] commonly used control strategies [52]:

- *maximum torque per current* (MTPC): Usage of the shortest current vector that produces the demanded torque. Hence, the ohmic losses are minimal.
- *maximum current* (MC): Production of the maximally feasible torque, only considering current and voltage limitations.
- *field weakening* (FW): For increased rotational speeds, the MTPC strategy is not feasible anymore due to voltage limitations. For that the optimal currents use the maximally available voltage and produce the demanded torque.
- *maximum torque per voltage* (MTPV): When the demanded torque exceeds the admissible torque of the FW strategy, the MTPV strategy chooses the currents that produce the maximally feasible torque considering the voltage constraints.

Assumption (AS.14) *Since wind turbine systems rotate rather slowly and the drive train is designed for maximum power output, it is assumed that the machine will never reach its voltage limit.*

In view of Assumption (AS.14), only the MTPC control strategy is of interest in this thesis. For a linear isotropic PMSM, as given in (2.15), the MTPC torque control strategy is easily achieved by controlling $i^d_{s,\mathrm{ref}} = i^d_s = 0$ and choosing

$$i^q_{s,\mathrm{ref}} = \frac{3\kappa^2 \tau_{m,\mathrm{ref}}}{2 n_p \hat{\psi}_{\mathrm{pm}}}. \tag{3.25}$$

Remark 3.2.2. *For nonlinear PMSMs, the relation between torque τ_m and $\boldsymbol{i}_s^{dq}$ is not linear anymore (see* (2.13)*). For these machines, the MTPC control strategy that will be presented in Sect. 3.2.3.2 for an EESM can be used.*

3.2.3 Control of EESM

In this section, the control of the EESM will be explained. The principle control structure is similar to the PMSM. The feedforward torque controller creates a current reference vector $\boldsymbol{i}_{\mathrm{ref}}$ based on the torque reference τ_{ref} and the feedback current control creates reference voltages $\boldsymbol{u}_{\mathrm{ref}}$ based on the difference $\boldsymbol{i}_{\mathrm{ref}} - \boldsymbol{i}$ between demanded currents and actual currents (see Fig. 3.5). But for the EESM an additional current, the excitation current i_e, has to be controlled and can be utilized to create the demanded torque τ_{ref}. How this is done and the advantages of this additional degree of freedom will be explained in detail in the following sections. First the current controller and subsequently the torque controller design will be presented. For the control of the EESM the reduced-order machine model (2.39) without damper will be used.

3.2.3.1 Current control

Figure 3.9 shows the current control system. Again PI-controllers with anti-windup, cross-coupling feedforward compensation and reference voltage saturation are implemented. Each component will be explained in more detail.

[23] Here the definitions as in [52] are used. Unfortunately, there is no commonly accepted definition for these terms. Other definitions can be found in [53, Sect. 16.7], [54, Chap. 7], [55, Chap. 5], [59, Chap. 6].

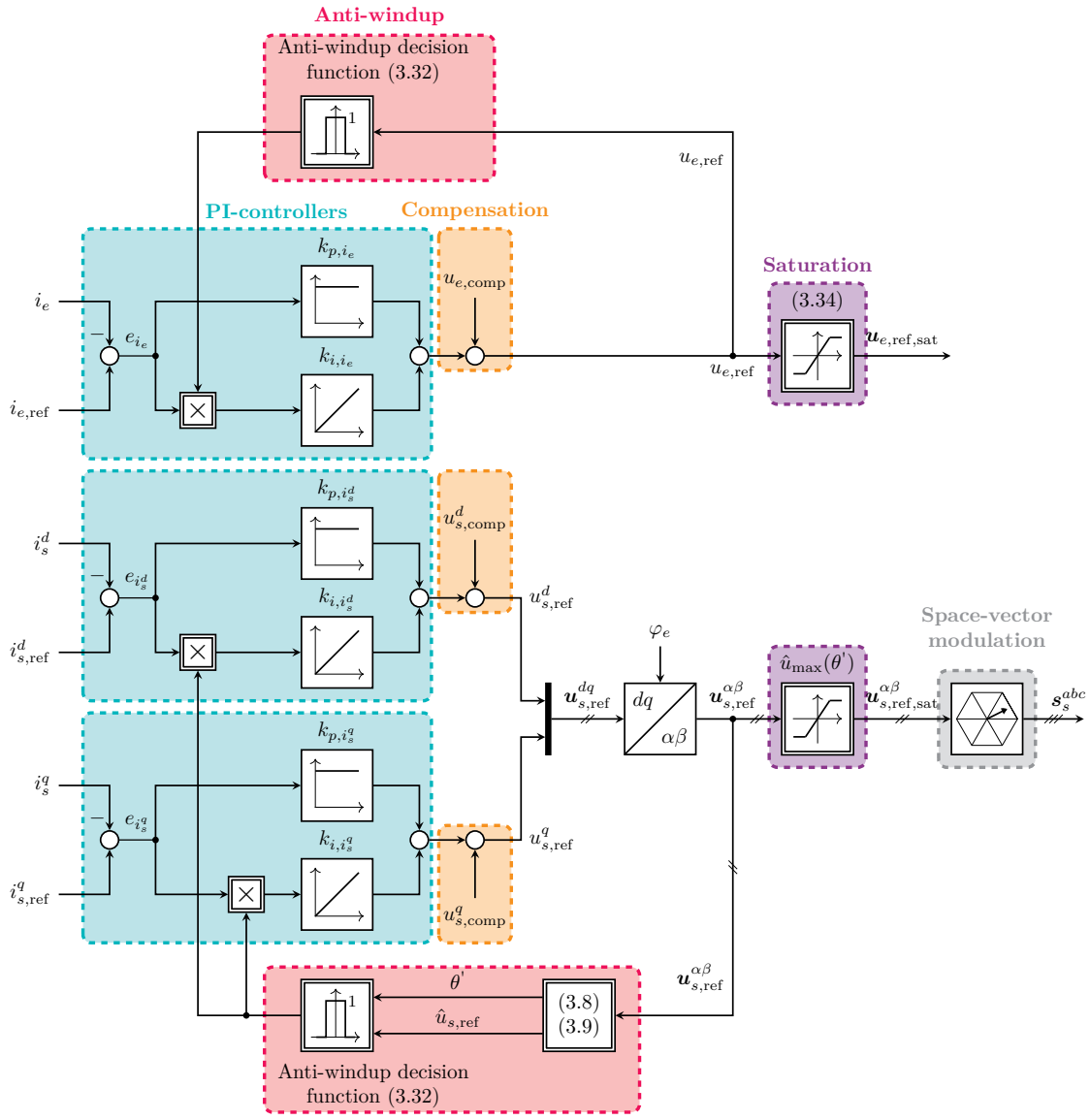

Figure 3.9: *Standard control system for EESM (field-oriented control): PI-controllers with anti-windup, cross-coupling feedforward compensation and reference voltage saturation.*

Recalling the electric dynamics (2.39) of the EESM, given by

$$\boldsymbol{u} = \boldsymbol{R}(i_e)\boldsymbol{i} + \boldsymbol{L}(\boldsymbol{i})\tfrac{\mathrm{d}}{\mathrm{d}t}\boldsymbol{i} + \boldsymbol{\Gamma}(\boldsymbol{i}, \omega_e), \tag{3.26}$$

and assuming the existence of the inverse $\boldsymbol{L}^{-1}$ of the inductance matrix $\boldsymbol{L}$ (for all relevant current vectors $\boldsymbol{i}$), (3.26) can be written in state-space form of the current dynamics

$$\tfrac{\mathrm{d}}{\mathrm{d}t}\boldsymbol{i} = (\boldsymbol{L}(\boldsymbol{i}))^{-1}\left(\boldsymbol{u} - \boldsymbol{R}(i_e)\boldsymbol{i} - \boldsymbol{\Gamma}(\boldsymbol{i}, \omega_e)\right) \tag{3.27}$$

of the EESM, where

$$\boldsymbol{L}^{-1} = \tfrac{1}{\det(\boldsymbol{L})}\begin{bmatrix} l_{22}l_{33} - l_{23}l_{32} & l_{13}l_{32} - l_{12}l_{33} & l_{12}l_{23} - l_{13}l_{22} \\ l_{23}l_{31} - l_{21}l_{33} & l_{11}l_{33} - l_{13}l_{31} & l_{13}l_{21} - l_{11}l_{23} \\ l_{21}l_{32} - l_{22}l_{31} & l_{12}l_{31} - l_{11}l_{32} & l_{11}l_{22} - l_{12}l_{21} \end{bmatrix} =: \begin{bmatrix} l_{11}^{-1} & l_{12}^{-1} & l_{13}^{-1} \\ l_{21}^{-1} & l_{22}^{-1} & l_{23}^{-1} \\ l_{31}^{-1} & l_{32}^{-1} & l_{33}^{-1} \end{bmatrix} \tag{3.28}$$

with

$$\det(\boldsymbol{L}) = l_{11}l_{22}l_{33} + l_{12}l_{23}l_{31} + l_{13}l_{21}l_{32} - l_{11}l_{23}l_{32} - l_{12}l_{21}l_{33} - l_{13}l_{22}l_{31}. \tag{3.29}$$

Concluding, the current dynamics can be stated element wise as follows

$$\left.\begin{aligned}
\tfrac{\mathrm{d}}{\mathrm{d}t} i_s^d &= l_{11}^{-1}\Big[u_s^d - R_s^d i_s^d + \underbrace{\omega_e\psi_s^q + \tfrac{l_{12}^{-1}}{l_{11}^{-1}}\left(u_s^q - R_s^q i_s^q - \omega_e\psi_s^d\right) + \tfrac{l_{13}^{-1}}{l_{11}^{-1}}\left(u_e - R_e i_e\right)}_{=:u_{s,\mathrm{dist}}^d}\Big] \\
\tfrac{\mathrm{d}}{\mathrm{d}t} i_s^q &= l_{22}^{-1}\Big[u_s^q - R_s^q i_s^q \underbrace{-\omega_e\psi_s^d + \tfrac{l_{21}^{-1}}{l_{22}^{-1}}\left(u_s^d - R_s^d i_s^d + \omega_e\psi_s^q\right) + \tfrac{l_{23}^{-1}}{l_{22}^{-1}}\left(u_e - R_e i_e\right)}_{=:u_{s,\mathrm{dist}}^q}\Big] \\
\tfrac{\mathrm{d}}{\mathrm{d}t} i_e &= l_{33}^{-1}\Big[u_e - R_e i_e + \underbrace{\tfrac{l_{31}^{-1}}{l_{33}^{-1}}\left(u_s^d - R_s^d i_s^d + \omega_e\psi_s^q\right) + \tfrac{l_{32}^{-1}}{l_{33}^{-1}}\left(u_s^q - R_s^q i_s^q - \omega_e\psi_s^d\right)}_{=:u_{e,\mathrm{dist}}}\Big].
\end{aligned}\right\} \tag{3.30}$$

To control the currents of the EESM, PI-controllers and feedforward disturbance compensation are used. The demanded reference voltage consists of two components, i.e.

$$\boldsymbol{u}_{\mathrm{ref}} = \underbrace{\boldsymbol{u}_{\mathrm{pi}}}_{\text{PI-controller output}} + \underbrace{\boldsymbol{u}_{\mathrm{comp}}}_{\text{disturbance compensation}} \tag{3.31}$$

with reference voltage vector $\boldsymbol{u}_{\mathrm{ref}} := (u_{s,\mathrm{ref}}^d, u_{s,\mathrm{ref}}^q, u_{e,\mathrm{ref}})^\top$ (in V)^3, PI-controller output voltage vector $\boldsymbol{u}_{\mathrm{pi}} := (u_{s,\mathrm{pi}}^d, u_{s,\mathrm{pi}}^q, u_{e,\mathrm{pi}})^\top$ (in V)^3 and disturbance compensation voltage vector $\boldsymbol{u}_{\mathrm{comp}} := (u_{s,\mathrm{comp}}^d, u_{s,\mathrm{comp}}^q, u_{e,\mathrm{comp}})^\top$ (in V)^3. For *static* disturbance compensation the compensation vector is chosen to $\boldsymbol{u}_{\mathrm{comp}} = -(u_{s,\mathrm{dist}}^d, u_{s,\mathrm{dist}}^q, u_{e,\mathrm{dist}})^\top$ (in V)^3. More details can be found in [4], [53, Sect. 7.1.1] or [115]. The PI-controllers are equipped with anti-windup for reference voltages outside of the feasible range (see Sect. 3.2.1). The dynamics of the PI-controllers is given by[24]

$$\left.\begin{aligned}
\tfrac{\mathrm{d}}{\mathrm{d}t}\boldsymbol{\xi} &= \begin{bmatrix} f_{\hat{u}_s}\left(\left\|(u_{s,\mathrm{ref}}^d, u_{s,\mathrm{ref}}^q)^\top\right\|\right)\mathbf{1}_2 \\ f_{u_{e,\min},u_{e,\max}}(u_{e,\mathrm{ref}}, e_{i_e}) \end{bmatrix}\boldsymbol{e} \\
\boldsymbol{u}_{\mathrm{pi}} &= \boldsymbol{K}_{p,\boldsymbol{i}}\boldsymbol{e} + \boldsymbol{K}_{i,\boldsymbol{i}}\boldsymbol{\xi}
\end{aligned}\right\} \tag{3.32}$$

with current tracking error $\boldsymbol{e} := (e_{i_s^d}, e_{i_s^q}, e_{i_e})^\top := \boldsymbol{i}_{\mathrm{ref}} - \boldsymbol{i}$ (in A)^3, initial value $\boldsymbol{\xi}(0) = \mathbf{0}_3$ and proportional and integral gain matrices[25]

$$\left.\begin{aligned}
\boldsymbol{K}_{p,\boldsymbol{i}} &= \mathrm{diag}\left(k_{p,i_s^d}, k_{p,i_s^q}, k_{p,i_e}\right) = \mathrm{diag}\left(\tfrac{1}{6T_{\mathrm{sw}}l_{11}^{-1}}, \tfrac{1}{6T_{\mathrm{sw}}l_{22}^{-1}}, \tfrac{1}{2T_{\mathrm{avg,e}}l_{33}^{-1}}\right) \\
\boldsymbol{K}_{i,\boldsymbol{i}} &= \mathrm{diag}\left(k_{p,i_s^d}, k_{p,i_s^q}, k_{p,i_e}\right) = \mathrm{diag}\left(\tfrac{R_s^d}{6T_{\mathrm{sw}}}, \tfrac{R_s^q}{6T_{\mathrm{sw}}}, \tfrac{R_e}{2T_{\mathrm{avg,e}}}\right).
\end{aligned}\right\} \tag{3.33}$$

Again, as for the PMSM (see (3.23)) the output of the controller is saturated

$$\boldsymbol{u}_{\mathrm{ref,sat}} = \begin{pmatrix} \mathbf{sat}_{\hat{u}_s}(\boldsymbol{u}_{s,\mathrm{ref}}^{dq}) \\ \mathrm{sat}_{u_{e,\min}}^{u_{e,\max}}(u_{e,\mathrm{ref}}) \end{pmatrix}. \tag{3.34}$$

The saturation for the stator of the EESM is the same as for the PMSM. As the excitation voltage is a dc-value, the reference voltage $u_{e,\mathrm{ref}}$ is saturated between $u_{e,\min}$ and $u_{e,\max}$.

[24] Recall the definitions of $f_{\hat{u}_s}$ and $f_{u_{e,\min},u_{e,\max}}(u_{e,\mathrm{ref}}, e_{i_e})$ in the Nomenclature section and (3.10).

[25] The time constant $T_{\mathrm{avg,e}}$ of the dc-source for the excitation voltage u_e was experimentally determined and is $T_{\mathrm{avg,e}} = 17.5\,\mathrm{ms}$ for the laboratory setup (see Sect. 4.1).

Remark 3.2.3. *The used EESM in the laboratory is equipped with damper windings (see Sect. 4.1.3). As the model used for controller design and the real machine do differ during transients, the proposed compensation will not be used, i.e.* $\boldsymbol{u}_{\mathrm{comp}} = \mathbf{0}_3$*, and* (3.31) *reduces to*

$$\boldsymbol{u}_{\mathrm{ref}} = \boldsymbol{u}_{\mathrm{pi}}\,. \tag{3.35}$$

Remark 3.2.4. *While the controller gains in* (3.33) *vary with the current* $\boldsymbol{i}$*, the gains will in certain cases be chosen constant in the ongoing work. For an open-switch fault in the converter, which causes strong current ripples, it is beneficial not to change the controller gains for an EESM with damper winding. Hence, the inductance, flux linkage and resistance values for* $i_s^d = 0\,\mathrm{A}$*,* $i_s^q = 0\,\mathrm{A}$ *and* $i_e = 10\,\mathrm{A}$ *will be used and* $\boldsymbol{K}_{p,\boldsymbol{i}}$ *and* $\boldsymbol{K}_{i,\boldsymbol{i}}$ *are replaced by*

$$\left.\begin{aligned} \boldsymbol{K}_{p,\boldsymbol{i},L} &= \operatorname{diag}\left(\frac{1}{6T_{\mathrm{sw}}l_{11}^{-1}(0{,}0{,}10)}, \frac{1}{6T_{\mathrm{sw}}l_{22}^{-1}(0{,}0{,}10)}, \frac{1}{2T_{\mathrm{avg,e}}l_{33}^{-1}(0{,}0{,}10)}\right) \\ \boldsymbol{K}_{i,\boldsymbol{i},L} &= \operatorname{diag}\left(\frac{R_s^d}{6T_{\mathrm{sw}}}, \frac{R_s^q}{6T_{\mathrm{sw}}}, \frac{R_e(0{,}0{,}10)}{2T_{\mathrm{avg,e}}}\right). \end{aligned}\right\} \tag{3.36}$$

3.2.3.2 Torque control

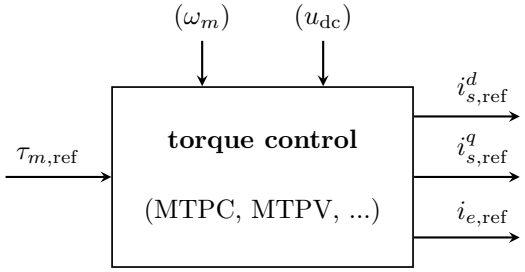

Figure 3.10: *Feedforward torque control for EESM.*

The torque of an EESM depends on the three currents i_s^d, i_s^q and i_e. Figure 3.10 shows the feedforward torque control. The reference currents $i_{s,\mathrm{ref}}^d$, $i_{s,\mathrm{ref}}^q$ and $i_{e,\mathrm{ref}}$ are created based on the torque reference $\tau_{m,\mathrm{ref}}$ and—depending on the applied control strategies (MTPC, MTPV, etc., see Sect. 3.2.2.2)—also based on rotational speed[26] ω_m and dc-link voltage u_{dc}. As i_s^d and i_s^q are applied in the stator and i_e in the exciter, the ohmic losses of stator and exciter have to be summed up to the total ohmic loss

$$p_{R,\mathrm{loss}} = \tfrac{2}{3\kappa^2}R_s\left((i_s^d)^2 + (i_s^q)^2\right) + R_e(i_e)i_e^2 \qquad (\text{in W}) \tag{3.37}$$

to have a measure of the optimality of an operation point. The MTPC trajectory can be calculated offline using measured data (see Appendix B). Due to the nonlinear machine behaviour, an analytical calculation is not possible and the MTPC trajectory is determined numerically. If a torque sensor is available, the measured torque[27] can be used for the calculation of the optimal MTPC trajectory. Otherwise or additionally, the torque can be calculated using (2.41), i.e.

$$\tau_m(\boldsymbol{i}) = \tfrac{2}{3\kappa^2}n_p\left(\boldsymbol{i}_s^{dq}\right)^{\top}\boldsymbol{J}\boldsymbol{\psi}_s^{dq}(\boldsymbol{i})\,. \tag{3.38}$$

[26] This is here not the case, recall Assumption (AS.14).

[27] If the measured torque is used for calculating the MTPC trajectory, disturbing influences like friction (see Fig. B.3), "breaking torque" τ_{i_e} due to i_e and ω_m (see Fig. 4.6), etc. have to be known and taken into account accordingly.

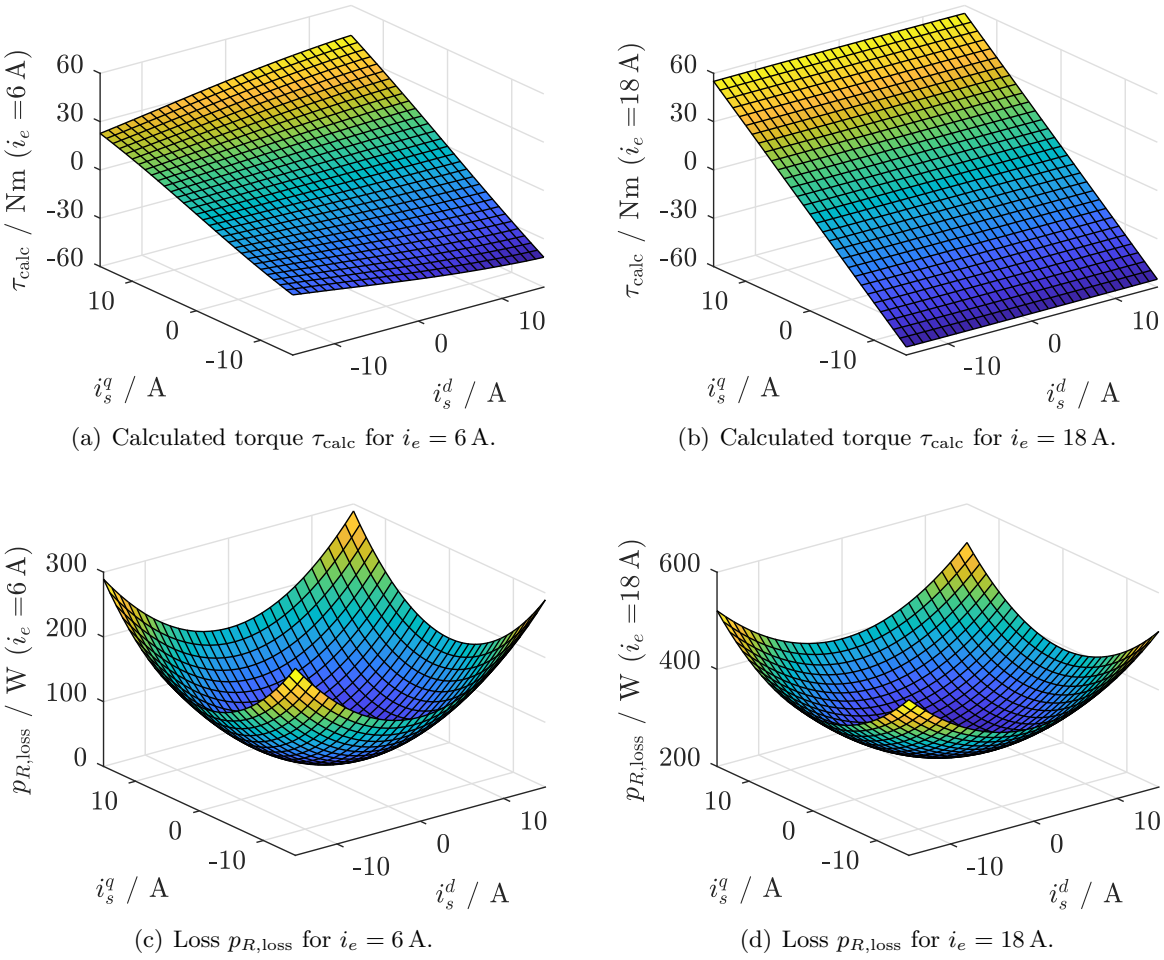

(a) Calculated torque τ_{calc} for $i_e = 6\,\text{A}$.

(b) Calculated torque τ_{calc} for $i_e = 18\,\text{A}$.

(c) Loss $p_{R,\text{loss}}$ for $i_e = 6\,\text{A}$.

(d) Loss $p_{R,\text{loss}}$ for $i_e = 18\,\text{A}$.

Figure 3.11: *Torque τ_{calc} and loss $p_{R,\text{loss}}$ for the EESM for $i_e = 6\,\text{A}$ and $i_e = 18\,\text{A}$.*

Figure 3.11 shows in the upper plots the calculated torque over i_s^d and i_s^q for constant $i_e = 6\,\text{A}$ and $i_e = 18\,\text{A}$. The lower plots show the corresponding ohmic losses $p_{R,\text{loss}}$. Comparing left and right column shows, that the same torque can be produced using different current triples $\boldsymbol{i} = (i_s^d, i_s^q, i_e)^\top$ and with different ohmic losses. Searching for the current triple $\boldsymbol{i} = (i_s^d, i_s^q, i_e)^\top$ with minimal losses for each torque value leads to the MTPC trajectory for feedforward torque control. Figure 3.12 shows the MTPC trajectory and the trendline. The torque increases from its minimal value to its maximal value in positive i_s^q-direction. In Fig. 3.12(b) and Fig. 3.12(c) the lateral and the top view of Fig. 3.12(a) are shown, respectively. As Figure 3.11 already showed, it is not loss-optimal to use high values of i_e for small torque values.

3.2.3.3 Control performance

To investigate the control performance and to further validate the machine model of the EESM (see Sect. B.3), changes in current references and speed were conducted[28]. Four different experiments were performed:

($\text{E}_{3.1,\text{EESM}}$) Reference change in $i_{e,\text{ref}}$ for $\omega_m = 50\,\frac{\text{rad}}{\text{s}}$.

[28] For the reference signals, ramps are used to limit the gradient and thereby reduce the influence of the damper windings.

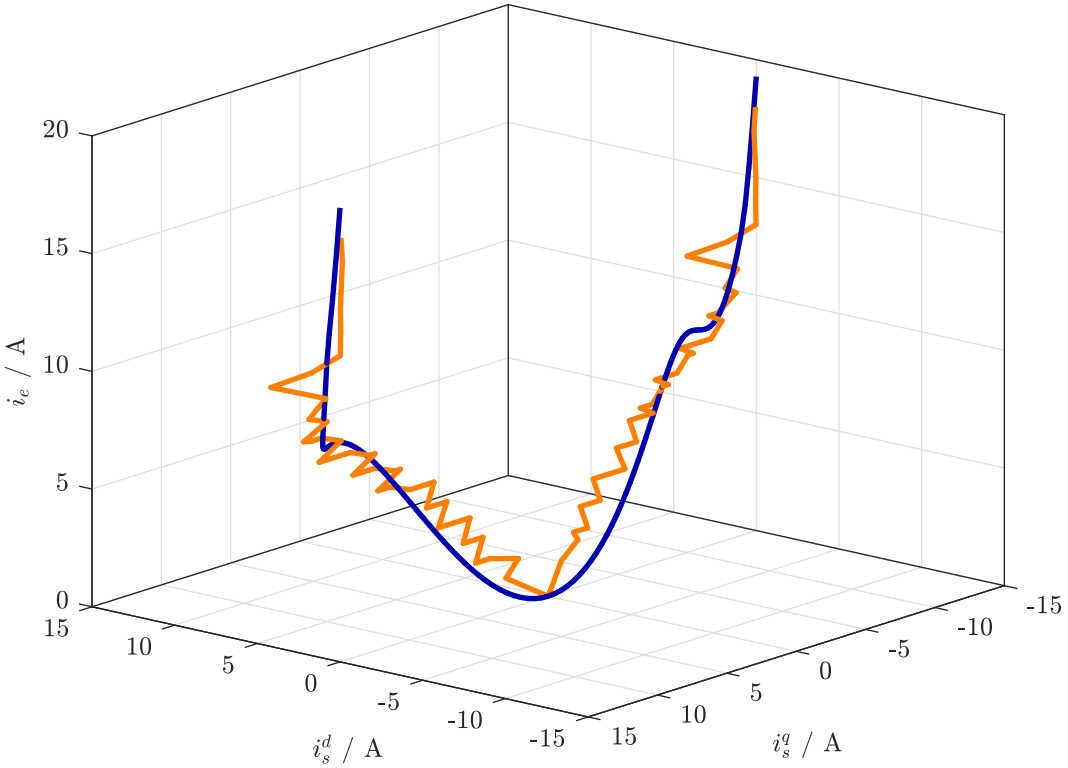

(a) MTPC trajectory for EESM.

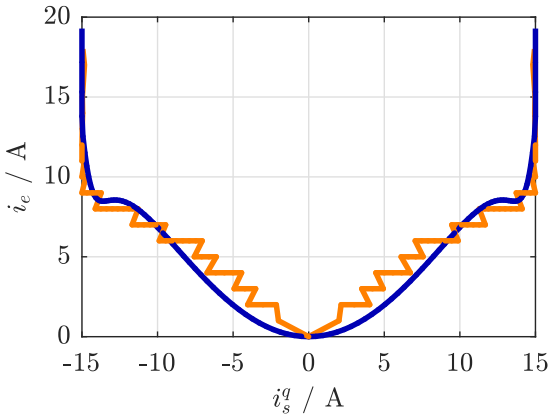

(b) MTPC trajectory for EESM (view: i_s^q-i_e-plain).

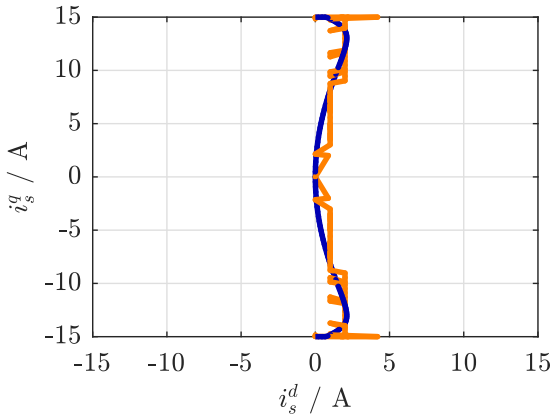

(c) MTPC trajectory for EESM (view: i_s^d-i_s^q-plain).

Figure 3.12: *Calculated MTPC* — *trajectory and* — *trendline for EESM.*

($E_{3.2,EESM}$) Reference change in $i^q_{s,ref}$ for $\omega_m = 50\,\frac{rad}{s}$.

($E_{3.3,EESM}$) Reference change in $i^d_{s,ref}$ for $\omega_m = 100\,\frac{rad}{s}$.

($E_{3.4,EESM}$) Reference changes in $\omega_{m,ref}$.

The following figures compare measurement and simulation results. The EESM for the simulation is modelled using the nonlinear flux linkage maps as described in Appendix B. In both cases, the PI-controller (3.35) with gain matrices (3.36) is used. Figures 3.13-3.15 are all structured the same. The upper subplot shows the rotational speed ω_m and its reference. Subplots two until four depict the currents i_s^d, i_s^q, i_e and their references, respectively. In the fifth subplot,

the measurement and simulation results for phase current i_s^a is shown. The last subplot shows the machine torque τ_m.
Figure 3.13 shows a reference change in $i_{e,\mathrm{ref}}$ (Experiment ($\mathrm{E}_{3.1,\mathrm{EESM}}$)). Measurement and simulation do increase simultaneously and track the increased reference. Due to the magnetic cross-coupling deviations in i_s^d and i_s^q from their reference values appear, but the controllers do compensate for that. Measurement and simulation results for current i_s^a and torque τ_m are very similar, even during transients. The measured signals of q-current and torque τ_m show significantly higher oscillations than those in the simulation.

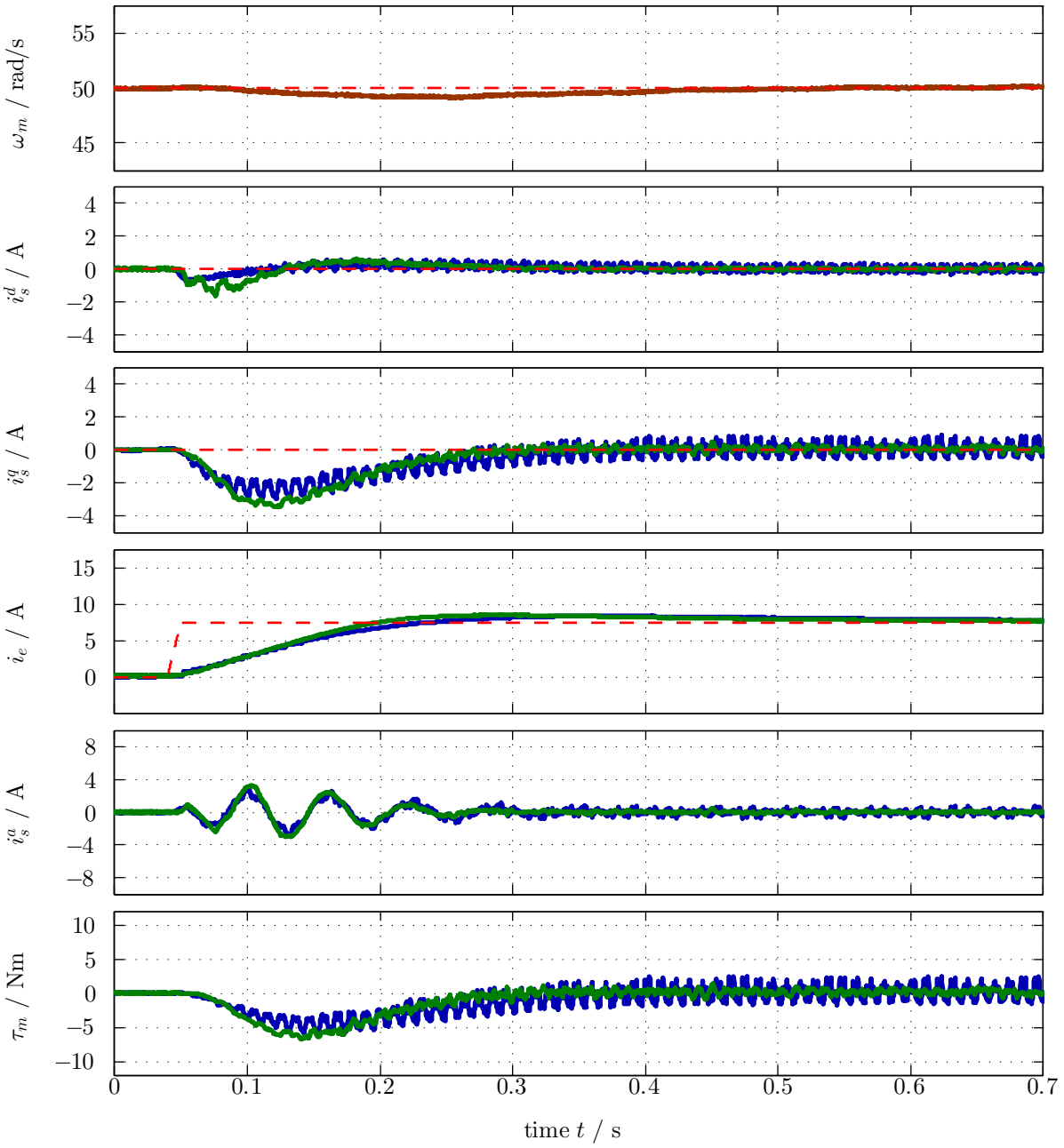

Figure 3.13: *Experiment* ($\mathrm{E}_{3.1,\mathrm{EESM}}$)*: Comparison of measurement and simulation results with* — *measured quantity,* — *simulated quantity and* - - - *reference value for EESM.*

In Fig. 3.14, a reference change in i_s^q is shown (Experiment ($\mathrm{E}_{3.2,\mathrm{EESM}}$)). Measurement and simulation do track the reference reliably and (almost) instantaneously. The cross-coupling

to i_s^d and i_e is stronger in the simulation results than in the measurement results. But it is compensated for by their controllers. For i_s^a, measurement and simulation results do match throughout the whole experiment. Measured and simulated torque signal τ_m do match on average. But due to higher oscillations in the measured i_s^q also the measured τ_m shows stronger oscillations than the simulated signal. Because of the quickly increasing torque τ_m, the rotational speed ω_m increases. From $t = 0.25\,\mathrm{s}$ on, ω_m decreases and the speed controller of the DFIM is successfully counteracting.

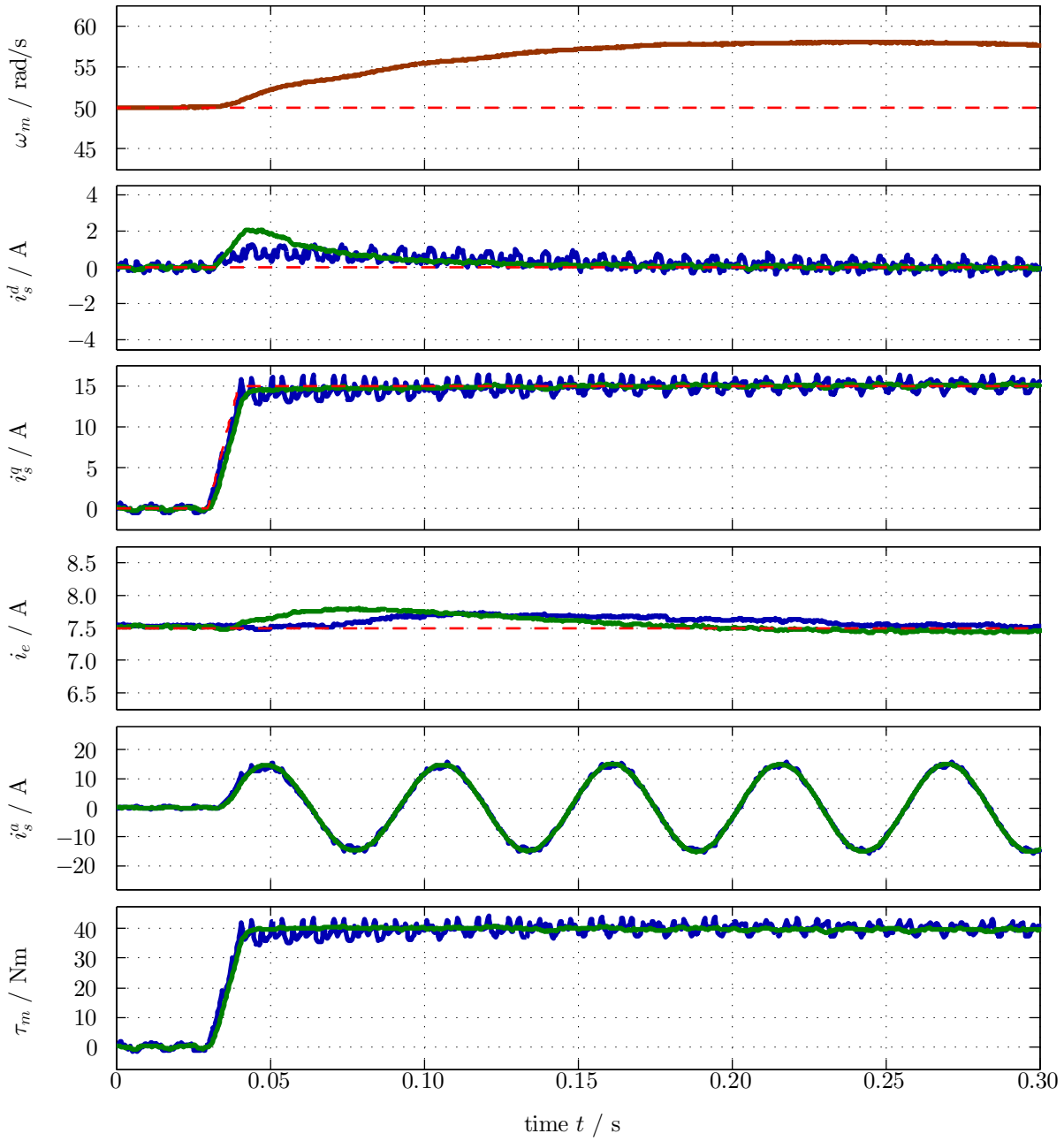

Figure 3.14: *Experiment* ($\mathrm{E}_{3.2,\mathrm{EESM}}$)*: Comparison of measurement and simulation results with* —— *measured quantity,* —— *simulated quantity and* - - - *reference value for EESM.*

In Fig. 3.15, the rotational speed reference is increased to $\omega_{m,\mathrm{ref}} = 100\,\frac{\mathrm{rad}}{\mathrm{s}}$ (while it was $\omega_{m,\mathrm{ref}} = 50\,\frac{\mathrm{rad}}{\mathrm{s}}$ before). The reference change of $i_{s,\mathrm{ref}}^d$ (Experiment ($\mathrm{E}_{3.3,\mathrm{EESM}}$)) is tracked slightly faster in the measurement than in the simulation. The simulation signal of i_s^q deviates a bit more

from its reference value than the measurement signal. For i_e, it is vice versa. But for both currents measurement, simulation and reference values do match shortly after. Except for the short transient period, no difference between measurement and simulation is visible for i_s^a. For the torque τ_m, measurement and simulations do match on average except for the short transient time. Overall the measurement signals of stator currents and the resulting torque show small oscillations, which the simulation does not replicate.

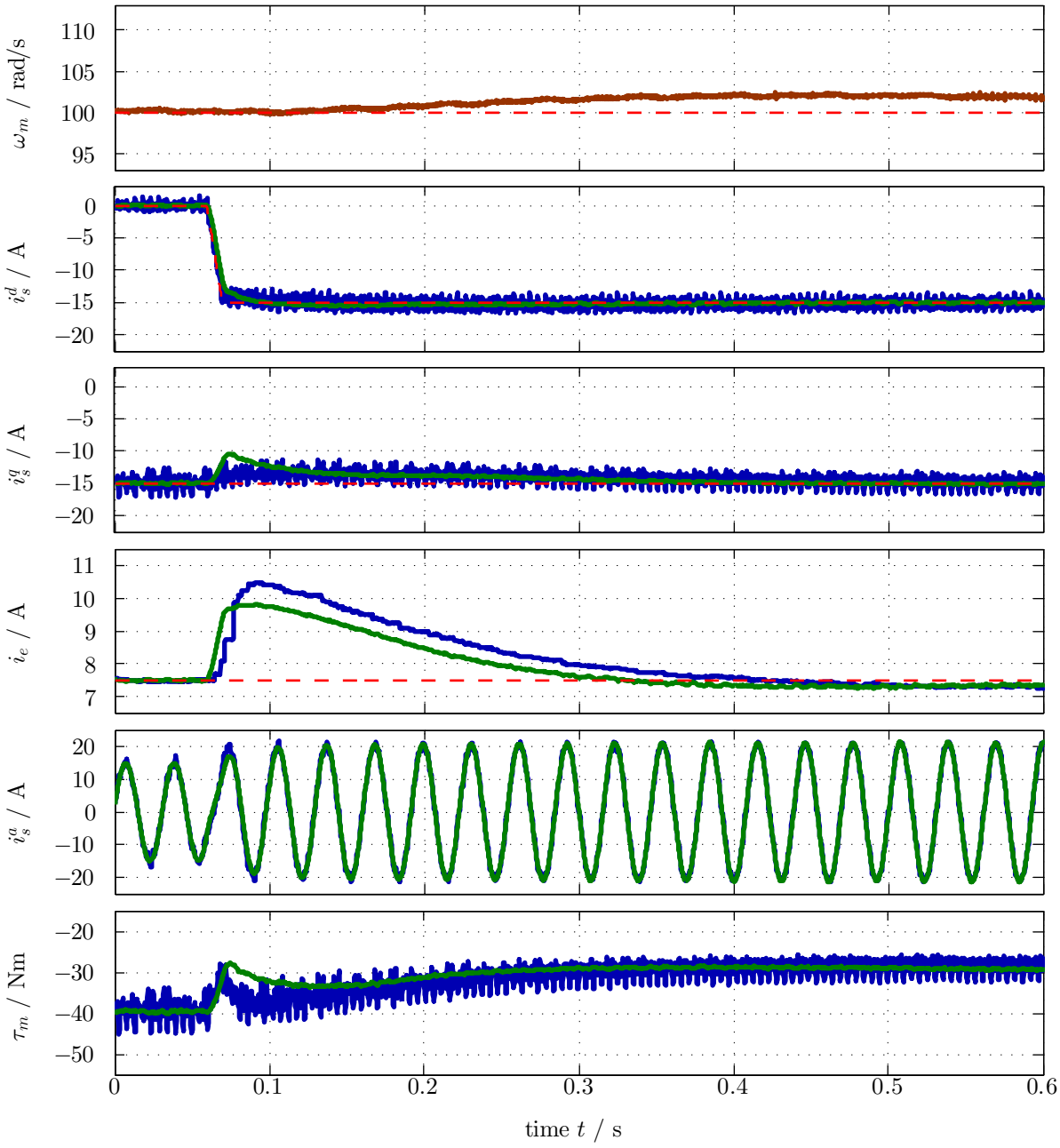

Figure 3.15: *Experiment* ($E_{3.3,EESM}$)*: Comparison of measurement and simulation results* —— *measured quantity,* —— *simulated quantity and* - - - *reference value for EESM.*

Figure 3.16 investigates the disturbance rejection capability of the current controllers (Experiment ($E_{3.4,EESM}$)). The upper subplot shows the rotational speed ω_m, which changes over time. Due to the quite large inertia of the drive train, the DFIM (for details see description of laboratory setup in Sect. 4.1.3) can follow its speed reference $\omega_{m,ref}$ only slowly. In the current

signals—shown in subplots two to four—only small deviations from the reference are visible. The deviations are corrected by the respective controllers quickly and without offset. In subplot five, one sees the increased frequency of the oscillations of i_s^a for increased ω_m. The increased band of the measured stator currents for increased ω_m is also visible in the torque in the lower subplot. Also for this investigation, measurement and simulation results do match and show almost identical behaviour.

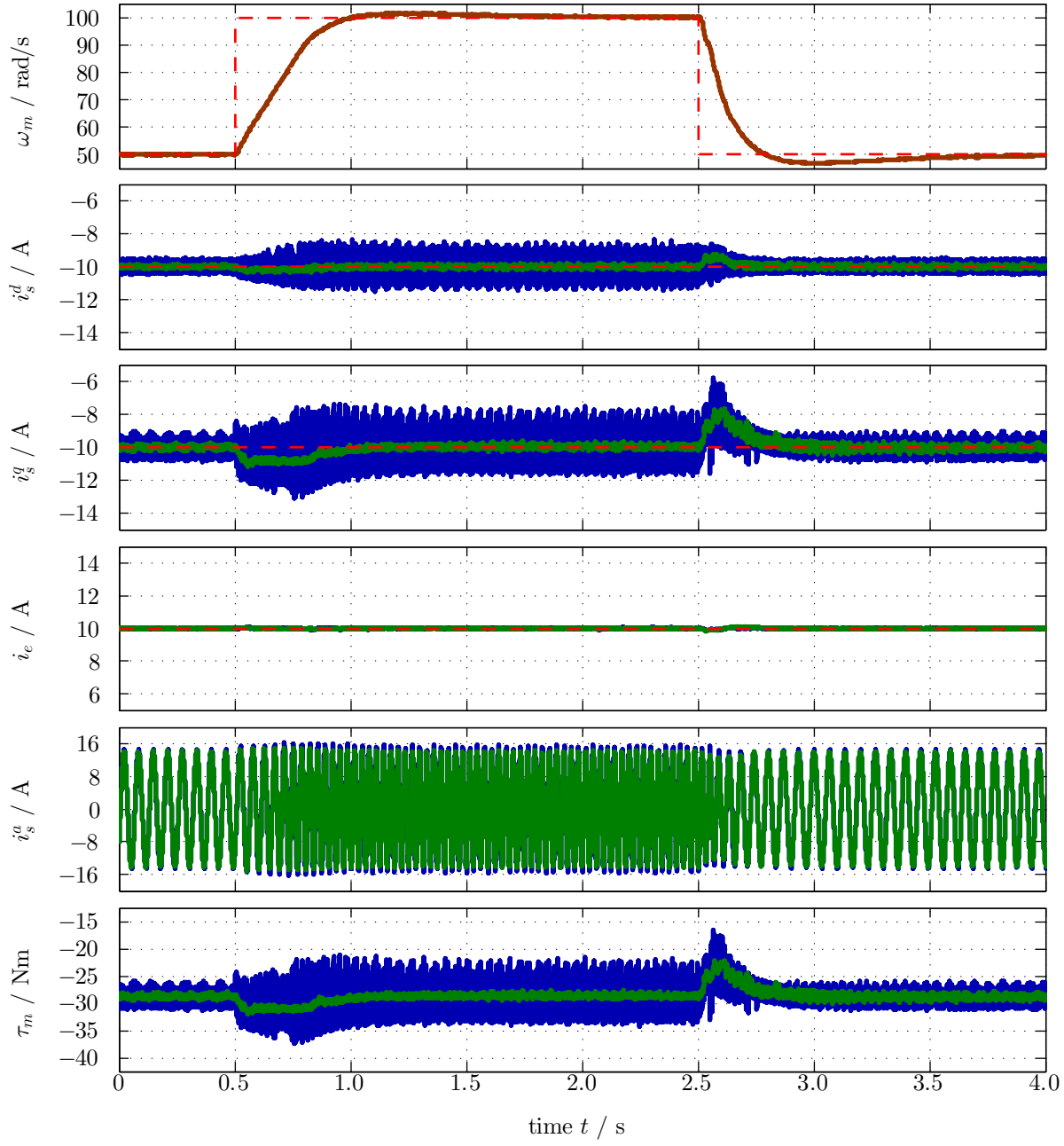

Figure 3.16: *Experiment* ($E_{3.4,EESM}$)*: Comparison of measurement and simulation results with* —— *measured quantity,* —— *simulated quantity and* - - - *reference value for EESM.*

Summarizing, measurement and simulation results do match for steady state and are similar for transients. The controllers do reliably track their references and are robust against cross-coupling and disturbances. Noise in the measurement of the stator currents and small oscillations due to the damper windings of the EESM are not replicated by the simulation (since not modelled).

3.3 Electric drive control under open-switch faults

This section will derive several methods to improve the control performance under open-switch converter faults. These methods require not only the detection of the presence of a fault, but also the identification of the type of the fault. It is necessary to know which switch is constantly open. For this task already several methods are proposed and used. The literature review in Sect. 1.1 states references. The state-of-the-art post-fault control approaches are discussed in Sect. 1.2.1. The impacts of the faults will be analysed for each machine separately. But the basic problem is, that open-switch faults cause ripples in the machine currents, which cause ripples in the torque, which is problematic for the mechanic of the overall drive train. Hence, the goal is to reduce the ripples in the currents, make the *abc*-currents sinusoidal again and thereby make the produced torque smoother. The necessary modifications are first discussed for PMSMs and afterwards for EESMs.

3.3.1 Post-fault control of PMSM

Some parts of this section were already published in [2]. The proposed post-fault control of a PMSM is based on the standard control system with three modifications:

($\mathrm{M}_{3.1,\mathrm{PMSM}}$) Improvement of anti-windup strategy.

($\mathrm{M}_{3.2,\mathrm{PMSM}}$) Modification of SVM.

($\mathrm{M}_{3.3,\mathrm{PMSM}}$) Injection of optimal d-axis current.

In Fig. 3.17, the standard control system, as shown in Fig. 3.8, is extended by these three modifications. The modifications for the improved and fault-tolerant control systems are highlighted in blue. But before the three modifications are described in detail in Sect. 3.3.1.2-3.3.1.4, a measure for the impact of the fault has to be defined. Such a measure is necessary to evaluate the effectiveness of the proposed post-fault strategies in limiting the impact of the fault to the overall system.

3.3.1.1 Fault impact analysis

To find a suitable measure for the impact of an open-switch fault on the overall system, the impacts of such a fault are first investigated more thoroughly. Figure 3.18 shows in the upper subplot the mechanical speed ω_m for a PMSM drive under open-switch fault in $\mathtt{S}_s^a$. The second subplot shows the currents i_s^d and i_s^q and their reference values. The third subplot shows the three phase currents i_s^a, i_s^b and i_s^c. In each plot the simulation and measurement results are depicted. The current i_s^q is oscillating and constantly deviates from its reference value. As the torque of the PMSM is linearly dependent on i_s^q (recall (2.15), i.e. $\tau_m = \frac{2}{3k^2} n_p \hat{\psi}_{\mathrm{pm}} i_s^q$), also the torque τ_m is oscillating. Due to the high and fast fluctuations in the torque of the PMSM, the coupled machine, a speed controlled RSM (for details see description of the laboratory setup in Sect. 4.1.2), is not able to secure a constant rotational speed (see upper subplot in Fig. 3.18). As the ripples in the q-current/torque not only cause oscillations in the speed, but also cause a lot of stress to the mechanical subsystem of the whole drive train (see [23]), this stress should be reflected in the choice of the measure.
To do so, the square root of the quadratic deviation of i_s^q from its reference value over at least one[29] electric revolution of the PMSM is chosen as measure. More precisely, the PMSM fault

[29] To minimize the impact of fluctuations and measurement errors, the average over 10 revolutions is used for the square root.

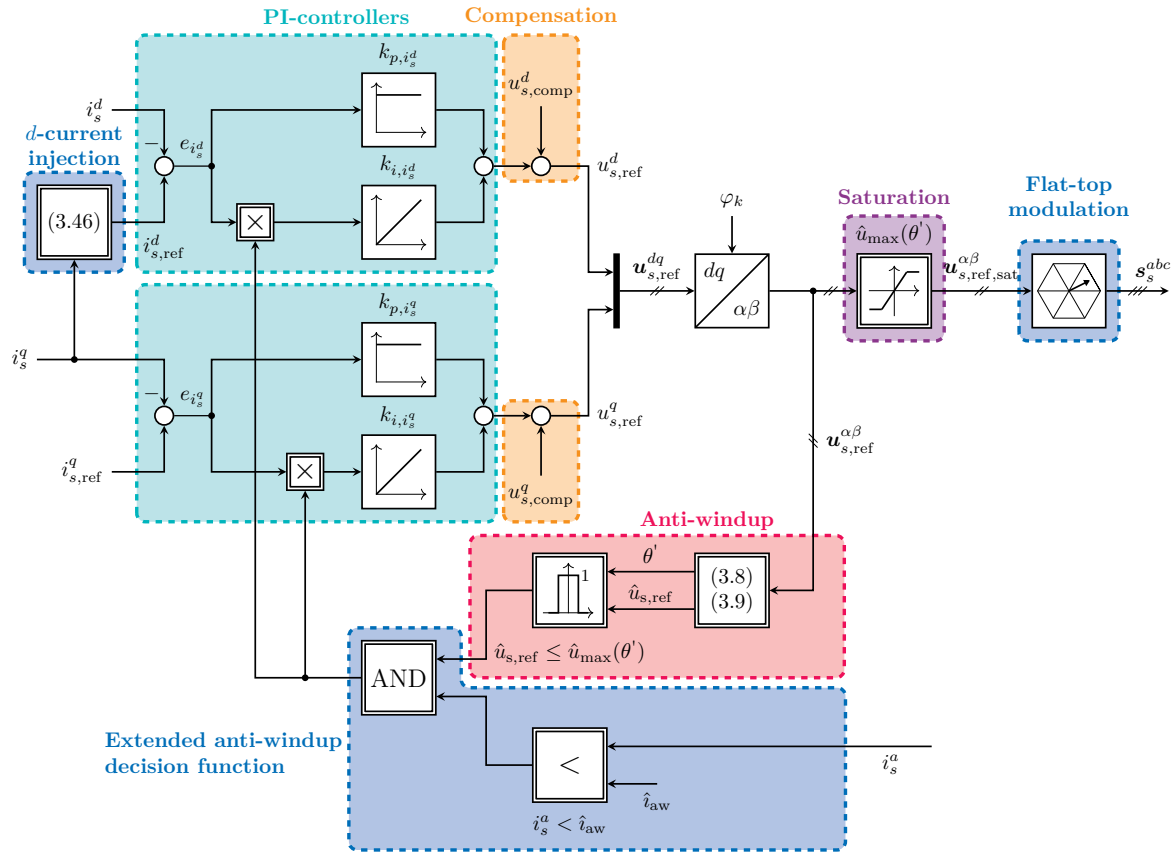

Figure 3.17: *Fault-tolerant control system for a PMSM for an open-switch fault in* $\mathtt{S}_s^a$*: PI-controllers with improved anti-windup, cross-coupling feedforward compensation and reference voltage saturation (Modifications* ($\mathrm{M}_{3.1,\mathrm{PMSM}}$)-($\mathrm{M}_{3.3,\mathrm{PMSM}}$) *compared to field-oriented control are highlighted in blue).*

impact measure is defined as follows

$$\mathfrak{E}_{i_s^q} = \sqrt{\frac{1}{10} \sum_{l=1}^{10 n_{\mathrm{sample}}} \left(i_{s,\mathrm{ref}}^q - i_s^q[l] \right)^2 \frac{T_{\mathrm{sw}}}{1\,\mathrm{s}}} \qquad (\text{in A}), \tag{3.39}$$

where the (sampled at each switching period T_{sw}) sampled current $i_s^q[l] \approx i_s^q(lT_{\mathrm{sw}})$ is averaged over

$$n_{\mathrm{sample}} = \mathrm{round}\left(\frac{2\pi}{n_p \omega_{m,\mathrm{ref}} T_{\mathrm{sw}}} \right) \tag{3.40}$$

samples for one electric rotation of the PMSM. To be able to compare the measure for different currents, the error $\mathfrak{E}_{i_s^q}$ is normalized with respect to the absolute value of its reference, i.e.

$$\mathfrak{e}_{i_s^q} = \frac{\mathfrak{E}_{i_s^q}}{\left| i_{s,\mathrm{ref}}^q \right|}. \tag{3.41}$$

Remark 3.3.1. *To obtain meaningful results for* $\mathfrak{E}_{i_s^q}$ *and* $\mathfrak{e}_{i_s^q}$*, the system is evaluated in steady state (as far as possible) and the references* $i_{s,\mathrm{ref}}^q$ *and* $\omega_{m,\mathrm{ref}}$ *should be constant and not zero.*

To investigate the impact of an open-switch fault in $\mathtt{S}_s^a$ and the three post-fault Modifications

($M_{3.1,PMSM}$)-($M_{3.3,PMSM}$) on the PMSM step-by-step, six different experiments are conducted:

($E_{3.5,PMSM}$) Open-switch fault in $\mathtt{S}_s^a$, standard controller, see Fig. 3.8.

($E_{3.6,PMSM}$) Open-switch fault in $\mathtt{S}_s^a$, controller with improved AWU strategy (Modification ($M_{3.1,PMSM}$)).

($E_{3.7,PMSM}$) Experiment ($E_{3.6,PMSM}$) + modification of SVM / flat-top modulation (Modifications ($M_{3.1,PMSM}$) + ($M_{3.2,PMSM}$)).

($E_{3.8,PMSM}$) Experiment ($E_{3.7,PMSM}$) + phase shift angle $\varphi_0 = 150°$.

($E_{3.9,PMSM}$) Experiment ($E_{3.7,PMSM}$) + phase shift angle $\varphi_0 = 210°$.

($E_{3.10,PMSM}$) Experiment ($E_{3.7,PMSM}$) + fault-optimal d-axis current injection (Modifications ($M_{3.1,PMSM}$) + ($M_{3.2,PMSM}$) + ($M_{3.3,PMSM}$)); control structure, see Fig. 3.17.

Table 3.1: *Comparison of measures $\mathfrak{E}_{i_s^q}$ and $\mathfrak{e}_{i_s^q}$ for improved post-fault control.*

control strategy	$\mathfrak{E}_{i_s^q,\mathrm{sim}}$	$\mathfrak{e}_{i_s^q,\mathrm{sim}}$	$\mathfrak{E}_{i_s^q,\mathrm{meas}}$	$\mathfrak{e}_{i_s^q,\mathrm{meas}}$
($E_{3.5,PMSM}$): standard control	1.674 A	0.084	1.666 A	0.083
($E_{3.6,PMSM}$): improved AWU	1.563 A	0.078	1.554 A	0.078
($E_{3.7,PMSM}$): improved AWU + flat-top	0.362 A	0.018	0.480 A	0.024
($E_{3.6,PMSM}$): improved AWU + flat-top + $\varphi_0 = 150°$	0.635 A	0.032	0.730 A	0.036
($E_{3.9,PMSM}$): improved AWU + flat-top + $\varphi_0 = 210°$	0.193 A	0.010	0.156 A	0.008
($E_{3.10,PMSM}$): improved AWU + flat-top + optimal d-current injection	0.078 A	0.004	0.143 A	0.007

Table 3.1 summarizes the errors $\mathfrak{E}_{i_s^q}$ and relative errors $\mathfrak{e}_{i_s^q}$ for simulation and measurement results of Experiments ($E_{3.5,PMSM}$)-($E_{3.10,PMSM}$). The different strategies will be explained in detail in the following sections. But it can already be seen here, that combining Modifications ($M_{3.1,PMSM}$)-($M_{3.3,PMSM}$) in Experiment ($E_{3.10,PMSM}$) (last row of Tab. 3.1) reduces $\mathfrak{E}_{i_s^q}$ and $\mathfrak{e}_{i_s^q}$ for simulation *and* measurement drastically.
Figure 3.18 shows simulation and measurement results for an open-switch fault in $\mathtt{S}_s^a$ without any modification to the control system (Experiment ($E_{3.5,PMSM}$)). The upper plot shows the oscillating mechanical speed ω_m. The oscillations in ω_m are due to the oscillating torque of the PMSM in the faulty case. The currents i_s^d and i_s^q, shown in subplot two, are oscillating throughout the positive half-wave of i_s^a (shown in the lower subplot). i_s^q also deviates from its reference in the "healthy" negative half-wave. The measures are $\mathfrak{E}_{i_s^q,\mathrm{sim}} = 1.674\,\mathrm{A}$ & $\mathfrak{e}_{i_s^q,\mathrm{sim}} = 0.084$ for simulation and $\mathfrak{E}_{i_s^q,\mathrm{meas}} = 1.666\,\mathrm{A}$ & $\mathfrak{e}_{i_s^q,\mathrm{meas}} = 0.083$ for measurement.
Being equipped with a measure for the impact of the fault, the following sections will describe the three proposed Modifications ($M_{3.1,PMSM}$)-($M_{3.3,PMSM}$) to improve the post-fault control in detail.

3.3.1.2 Improved anti-windup strategy

As a first step, the anti-windup strategy of the PI-current controllers (3.19) is modified. The overshoots in the q-current during the "healthy" negative half-wave of i_s^a for an open-switch fault in $\mathtt{S}_s^a$ (recall Fig. 3.18) are—at least partly—due to windup of the integral control action of the PI-controllers during the positive (almost zero) half-wave of i_s^a because the available voltage is reduced. To avoid this windup, an additional condition considering the current direction and

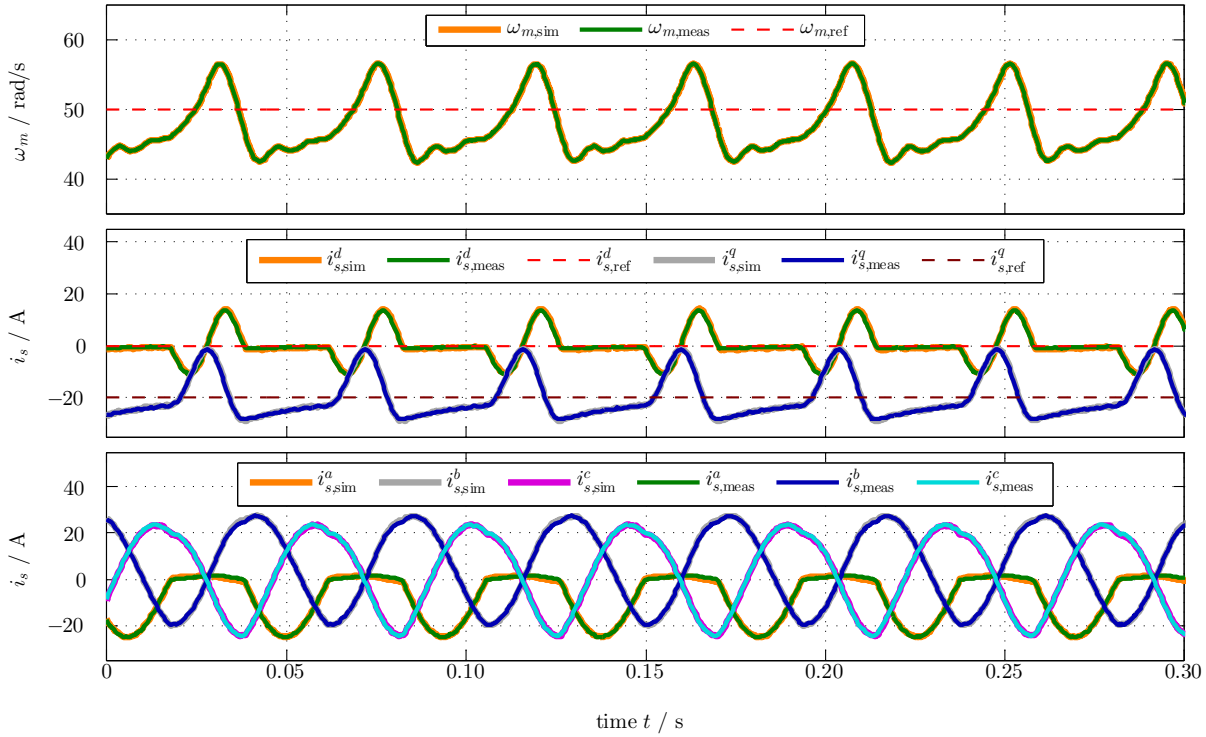

Figure 3.18: *Experiment* ($\mathrm{E}_{3.5,\mathrm{PMSM}}$)*: Comparison of simulation and measurement results for an open-switch fault in* $\mathtt{S}_s^a$ *using standard control for PMSM (*$\mathfrak{E}_{i_s^q,\mathrm{sim}} = 1.674\,\mathrm{A}$ *and* $\mathfrak{E}_{i_s^q,\mathrm{meas}} = 1.666\,\mathrm{A}$*).*

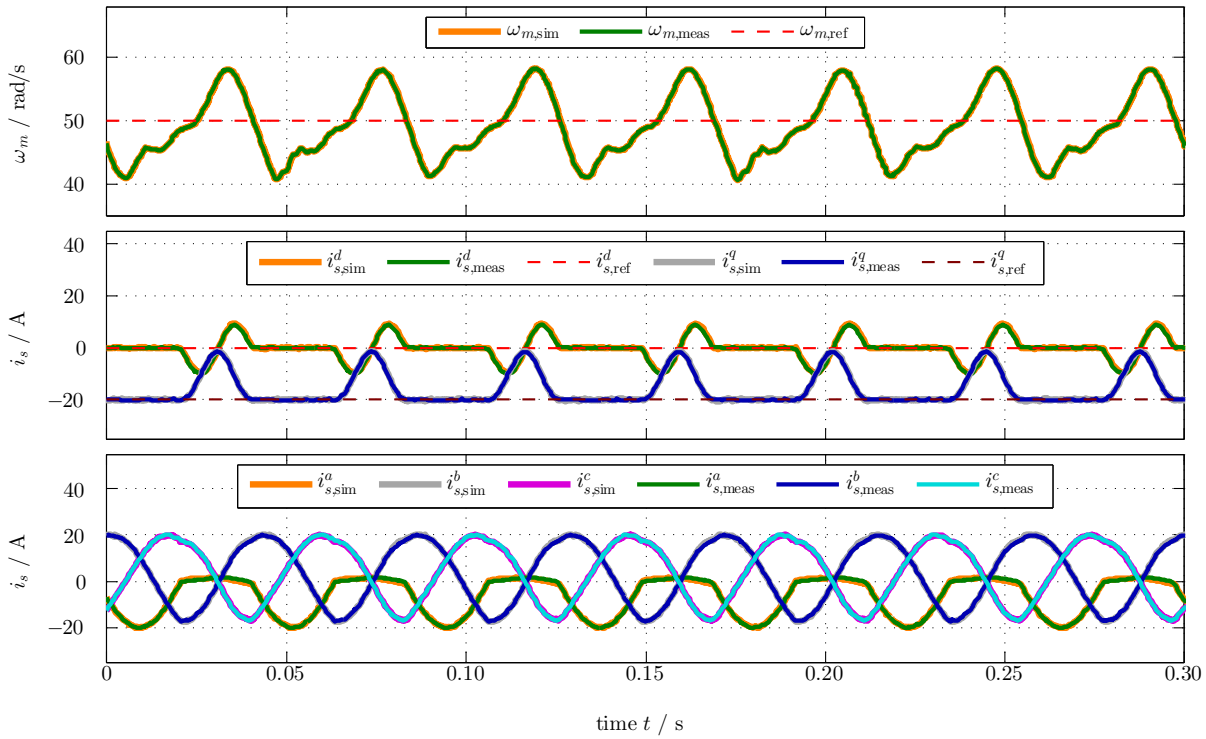

Figure 3.19: *Experiment* ($\mathrm{E}_{3.6,\mathrm{PMSM}}$)*: Comparison of simulation and measurement results for an open-switch fault in* $\mathtt{S}_s^a$ *using improved AWU for PMSM (*$\mathfrak{E}_{i_s^q,\mathrm{sim}} = 1.563\,\mathrm{A}$ *and* $\mathfrak{E}_{i_s^q,\mathrm{meas}} = 1.554\,\mathrm{A}$*).*

the available voltage (see Fig. 3.17) must be introduced which leads to the extended anti-windup decision function[30]

$$f_{\mathrm{aw}}^{\star}(\boldsymbol{u}_{s,\mathrm{ref}}^{dq}, \hat{u}_s, i_s^a) := \begin{cases} 1 & \text{, if } f_{\hat{u}_s}\left(\|(u_{s,\mathrm{ref}}^d, u_{s,\mathrm{ref}}^q)^\top\|\right) \quad \text{AND} \quad i_s^a < \hat{\imath}_{\mathrm{aw}} < 0 \\ 0 & \text{, else} \end{cases} \tag{3.42}$$

for open-switch faults in $\mathtt{S}_s^a$ (phase a), which replaces $f_{\mathrm{aw}}(\cdot)$ in (3.19). The constant $\hat{\imath}_{\mathrm{aw}} < 0$ (in A) represents the maximally admissible anti-windup current and should be chosen negative to account for the chattering of the phase current i_s^a around zero (recall Fig. 3.18). Note that, for any other faulty phase with open-switch fault in $\mathtt{S}_s^b$ or $\mathtt{S}_s^c$, the respective phase current direction of i_s^b or i_s^c must be considered in (3.42) instead of i_s^a. For a fault in a lower switch ($\overline{\mathtt{S}}_s^a$, $\overline{\mathtt{S}}_s^b$ or $\overline{\mathtt{S}}_s^c$), the threshold has to be positive and "<" in (3.42) has to be replaced by ">".
In Fig. 3.19, the improved control performance due to the extended anti-windup strategy (3.42) is shown (Experiment ($\mathrm{E}_{3.6,\mathrm{PMSM}}$)). The *abc*-currents (lower subplot) do not alter much (almost no improvement regarding Fig. 3.18 is visible). The absolute measures reduce slightly to $\mathfrak{E}_{i_s^q,\mathrm{sim}} = 1.563\,\mathrm{A}$ and $\mathfrak{E}_{i_s^q,\mathrm{meas}} = 1.554\,\mathrm{A}$. But the tracking performance of the currents i_s^d and, in particular, i_s^q is improved substantially. During the positive (almost zero) half-wave of i_s^a, both currents still do not perfectly track their references; but during the negative half-wave of i_s^a, both currents are capable of (almost) asymptotic set-point tracking. Especially, the current ripple in the q-current is drastically reduced during the negative half-wave of i_s^a.

Remark 3.3.2 (Choosing the threshold $\hat{\imath}_{\mathrm{aw}}$)**.** *In Section 4.1.2, the threshold $\hat{\imath}_{\mathrm{aw}} = -1\,\mathrm{A}$ was chosen which corresponds to approximately 2 % of the nominal machine current (see Tab. 4.1). Note that this threshold depends on and has to be adjusted for the considered electric drive system with respect to e.g. measurement noise, sensor precision, and switching frequency of the converter.*

3.3.1.3 Modified SVM

The second step to improve the control performance during open-switch faults is the modification of the space-vector modulation. Note that any open-switch fault in one of the *upper* switches (i.e. $\mathtt{S}_s^a$, $\mathtt{S}_s^b$ or $\mathtt{S}_s^c$) leads to a shifted zero vector $\boldsymbol{u}_{\mathtt{111}}^{\alpha\beta}$ (for fault in $\mathtt{S}_s^a$, $i_s^a \geq 0$ and $i_s^a = 0$, see Fig. 3.20); whereas any open-switch fault in one of the *lower* switches (i.e. $\overline{\mathtt{S}}_s^a$, $\overline{\mathtt{S}}_s^b$ or $\overline{\mathtt{S}}_s^c$) shifts the other zero vector $\boldsymbol{u}_{\mathtt{000}}^{\alpha\beta}$. Hence, one of the zero vectors is not zero any more. Figure 3.20 summarizes the shift of the voltage vectors for an open-switch fault in $\mathtt{S}_s^a$ along the negative a-axis. The following observations can be made:

- For $i_s^a < 0$, the voltage vectors (see Fig. 3.20(a)) are *not* shifted (see e.g. $\boldsymbol{u}_{\mathtt{110},i_s^a<0}^{\alpha\beta}$ or $\boldsymbol{u}_{\mathtt{101},i_s^a<0}^{\alpha\beta}$ in Fig. 3.20(a)). Normal operation is feasible.

- For $i_s^a = 0$, the voltage vectors (see Fig. 3.20(b)) with a "1" for $\mathtt{S}_s^a$ are shifted by $\boldsymbol{\Delta u}_{i_s^a=0}^{\alpha\beta} = -\frac{1}{3}u_{\mathrm{dc}}$ in negative a-direction (see e.g. $\boldsymbol{u}_{\mathtt{110},i_s^a=0}^{\alpha\beta}$ or $\boldsymbol{u}_{\mathtt{101},i_s^a=0}^{\alpha\beta}$ in Fig. 3.20(b)). Normal operation is *not* feasible.

- For $i_s^a > 0$, the voltage vectors (see Fig. 3.20(c)) with a "1" for $\mathtt{S}_s^a$ are shifted by $\boldsymbol{\Delta u}_{i_s^a>0}^{\alpha\beta} = -\frac{2}{3}u_{\mathrm{dc}}$ in negative a-direction (see e.g. $\boldsymbol{u}_{\mathtt{110},i_s^a>0}^{\alpha\beta}$ or $\boldsymbol{u}_{\mathtt{101},i_s^a>0}^{\alpha\beta}$ in Fig. 3.20(c)). Normal operation is *not* feasible.

[30] Recall the definition of $f_{\hat{u}_s}$ in the Nomenclature section and (3.10).

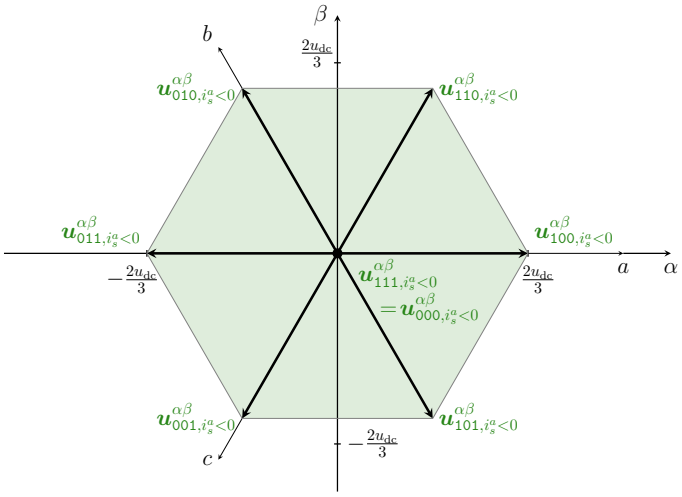

(a) Voltage hexagon for $i_s^a < 0$.

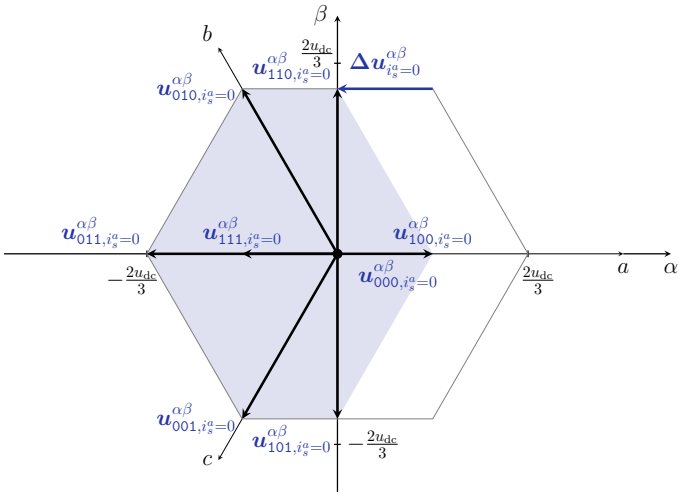

(b) Voltage hexagon for $i_s^a = 0$.

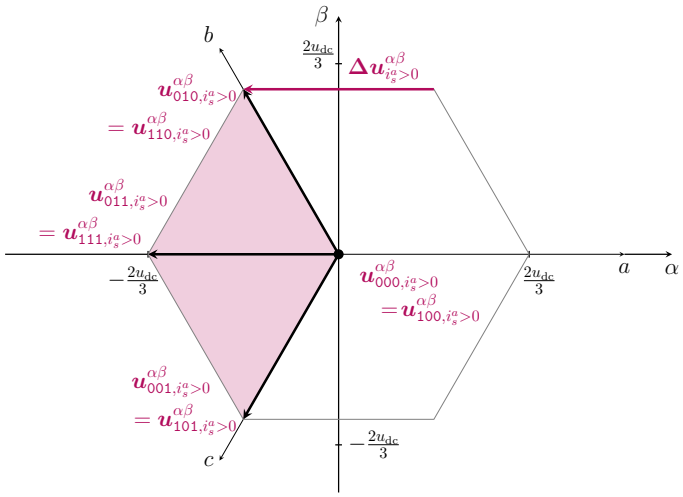

(c) Voltage hexagon for $i_s^a > 0$.

Figure 3.20: *Voltage hexagon with shifted voltage vectors* $\boldsymbol{u}_s^{\alpha\beta}$ *and feasible sectors for a fault in* $\mathtt{S}_s^a$*: The shifted vectors are shown for all three cases* (a) $i_s^a < 0$, (b) $i_s^a = 0$, (c) $i_s^a > 0$ *and all possible switching vectors* $\boldsymbol{s}_s^{abc}$.

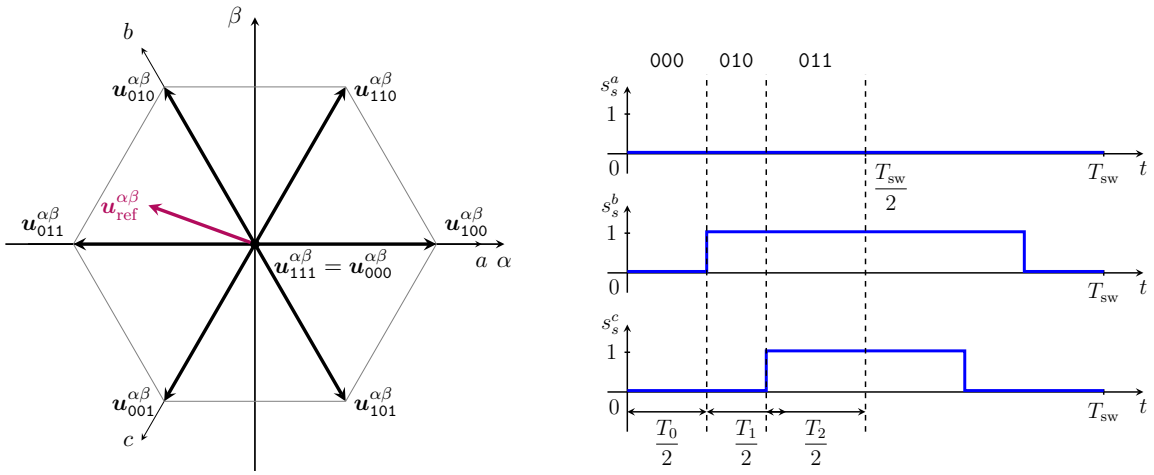

(a) Voltage hexagon with voltage reference $\boldsymbol{u}^{\alpha\beta}_{\text{ref}}$ in sector III.

(b) Flat-top switching pattern for generation of $\boldsymbol{u}^{\alpha\beta}_{\text{ref}}$.

Figure 3.21: *Flat-top switching pattern* (b) *to generate a voltage reference* $\boldsymbol{u}^{\alpha\beta}_{\text{ref}}$ *in sector III* (a) *by a linear combination of the space-vectors* $\boldsymbol{u}^{\alpha\beta}_{000}$, $\boldsymbol{u}^{\alpha\beta}_{010}$ *and* $\boldsymbol{u}^{\alpha\beta}_{011}$ *avoiding the vector* $\boldsymbol{u}^{\alpha\beta}_{111}$.

In Fig. 3.20, also the feasible voltage areas in the voltage hexagon for an open-switch fault in $\mathtt{S}^a_s$ are shown depending on the direction of current i^a_s. For $i^a_s < 0$, the full voltage hexagon can be used (see Fig. 3.20(a)). For $i^a_s = 0$ or $i^a_s > 0$, the feasible areas in the voltage hexagon become smaller (see Fig. 3.20(b) and Fig. 3.20(c), respectively). Most critical case occurs for $i^a_s > 0$, where only the sectors III and IV are feasible.
Then, using *flat-top* modulation allows to use only the non-shifted zero vector (see [53, Chap. 14.6], [116]). For example, for an open-switch fault in $\mathtt{S}^a_s$, $\mathtt{S}^b_s$ or $\mathtt{S}^c_s$, only the non-shifted zero vector $\boldsymbol{u}^{\alpha\beta}_{000}$ is applied (see Fig. 3.21 in comparison to the standard SVM shown in Fig. 3.7). For faults in $\overline{\mathtt{S}}^a_s$, $\overline{\mathtt{S}}^b_s$ or $\overline{\mathtt{S}}^c_s$ only the non-shifted zero vector $\boldsymbol{u}^{\alpha\beta}_{111}$ is used.
In Fig. 3.22 the positive effect of the flat-top modulation on the control performance and the error $\mathfrak{E}_{i^q_s}$ is illustrated (Experiment ($\text{E}_{3.7,\text{PMSM}}$)). As before, the upper subplot shows the rotational speed ω_m, the second subplot the currents i^d_s and i^q_s with their reference values and the lower subplot depicts the *abc*-currents for the modified control system with extended anti-windup *and* modified SVM. Clearly, the intervals where $i^a_s \approx 0\,\text{A}$ are significantly shortened. Moreover, positive and almost sinusoidal i^a_s currents are again feasible due to the modified SVM. Hence, the absolute error values are drastically reduced to $\mathfrak{E}_{i^q_s,\text{sim}} = 0.362\,\text{A}$ and $\mathfrak{E}_{i^q_s,\text{meas}} = 0.480\,\text{A}$ and the tracking control performances of the currents i^d_s and i^q_s are improved as well.

Remark 3.3.3 (Small switching time for the zero vectors)**.** *If the time* T_0 *of the zero vector is very small (i.e. the zero vector is applied only for a very short period of time), the proposed modification of the SVM only has a minor impact on the control performance, as the shifted zero vector is almost never used.*

3.3.1.4 Fault-optimal *d*-axis current injection

The last improvement is to inject an optimal (additional) *d*-current to minimize the error $\mathfrak{E}_{i^q_s}$ even further. In the following, an open-switch fault in $\mathtt{S}^a_s$ is considered. For other open-switch faults, the modifications are straight forward. As discussed in Sect. 2.4.3.1 and Sect. 3.3.1.3, for a fault in $\mathtt{S}^a_s$ and $i^a_s \geq 0$, the output voltages that can be provided by the faulty converter are limited (see Fig. 3.20). For e.g. $i^a_s > 0$, only voltage vectors from the sectors III and IV are feasible (recall Fig. 3.20(c)). The principle idea of the optimal *d*-current injection is to generate

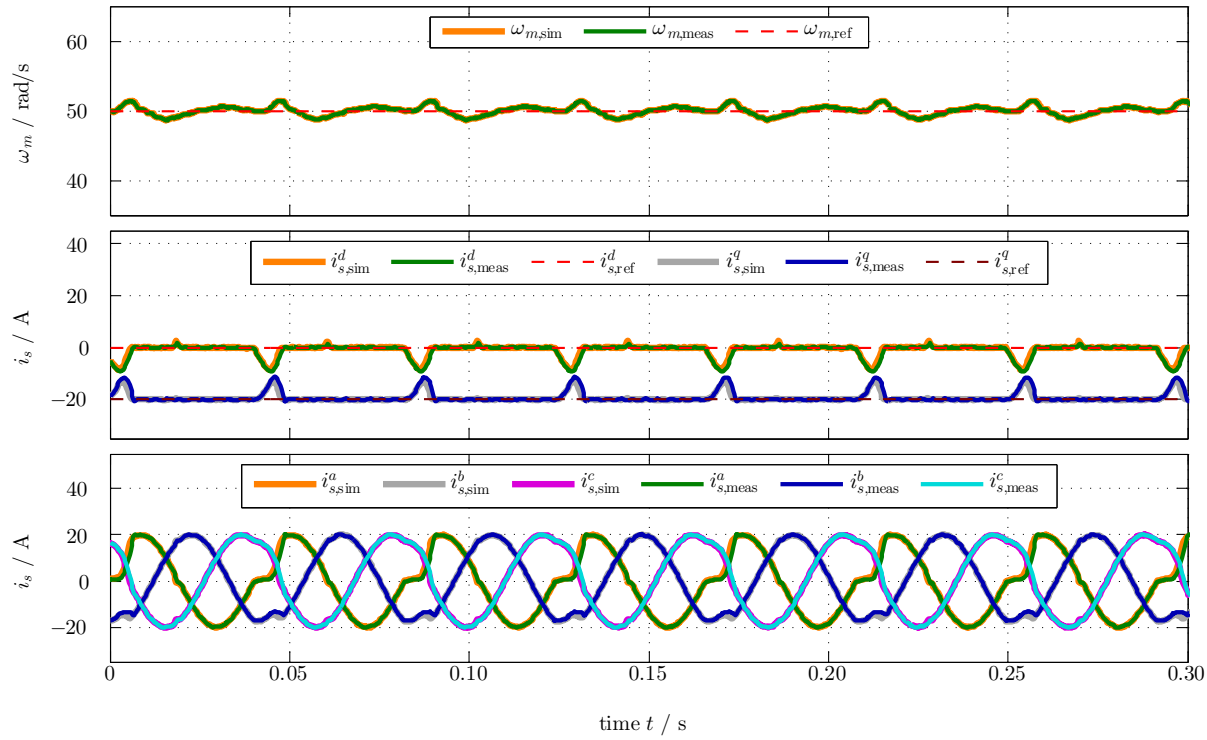

Figure 3.22: *Experiment* ($\mathrm{E}_{3.7,\mathrm{PMSM}}$)*: Comparison of simulation and measurement results for an open-switch fault in* $\mathtt{S}_s^a$ *using improved AWU and modified SVM for PMSM (*$\mathfrak{E}_{i_s^q,\mathrm{sim}} = 0.362\,\mathrm{A}$ *and* $\mathfrak{E}_{i_s^q,\mathrm{meas}} = 0.480\,\mathrm{A}$*).*

auxiliary reference voltage vectors within those two feasible sectors as long as possible. The goal is to determine an optimal *phase shift* φ_0 (in rad or °) between stator current $\boldsymbol{i}_s^{\alpha\beta}$ and reference voltage $\boldsymbol{u}_{s,\mathrm{ref}}^{\alpha\beta}$.

To illustrate the idea, in Fig. 3.23, the phase shifts $\varphi_0 = 150°$ and $\varphi_0 = 210°$ are shown for two time instants t_0 and t_1 where $\boldsymbol{i}_s^{\alpha\beta}(t_0)$ and $\boldsymbol{i}_s^{\alpha\beta}(t_1)$ are located on the negative and positive β-axis, respectively. Note that, if the phase current i_s^a is non-negative, the stator current space-vector $\boldsymbol{i}_s^{\alpha\beta}$ is located in the *right* half-plane (see Fig. 3.23). More precisely, at t_0 with $i_s^a(t_0) = 0$ (i_s^a becomes positive thereafter), $\boldsymbol{i}_s^{\alpha\beta}$ lies on the negative β-axis; whereas, at t_1 with $i_s^a(t_1) = 0$ (i_s^a becomes negative afterwards), $\boldsymbol{i}_s^{\alpha\beta}$ is aligned with the positive β-axis. Clearly, within the interval $[t_0, t_1]$, the current vector rotates by 180° and, optimally, the corresponding stator voltage reference space-vector $\boldsymbol{u}_{s,\mathrm{ref}}^{\alpha\beta}$ should be within the sectors III and IV as long as possible in order to apply feasible and correct voltages to the generator. However, as these two sectors span only over 120°, it is not possible to apply the correct voltages during the whole non-negative half-wave of i_s^a during an open-switch fault in $\mathtt{S}_s^a$. During the remaining 60°, incorrect voltages will be applied by the faulty converter which affect the shape of the currents and cause deviations from the desired sinusoidal waveform.

Depending on the phase shift φ_0 between stator current and reference voltage, different parts of the non-negative half-wave of i_s^a are affected by the fault. For $\varphi_0 = 150°$ (see Fig. 3.23(a)), $\boldsymbol{u}_{s,\mathrm{ref}}^{\alpha\beta}$ starts in sector II at time t_0. So, for the first 60° of the current half-wave, incorrect voltages are applied to the generator. As soon as $\boldsymbol{u}_{s,\mathrm{ref}}^{\alpha\beta}$ enters sector III, the correct voltages can be provided (even) by the faulty converter. When $\boldsymbol{u}_{s,\mathrm{ref}}^{\alpha\beta}$ lies in the sectors III and IV, the correct voltages lead to a sinusoidal current. For $\varphi_0 = 210°$ (see Fig. 3.23(b)), the behaviour is flipped: At time t_0, $\boldsymbol{u}_{s,\mathrm{ref}}^{\alpha\beta}$ starts already in the feasible sector III and, hence, during the first

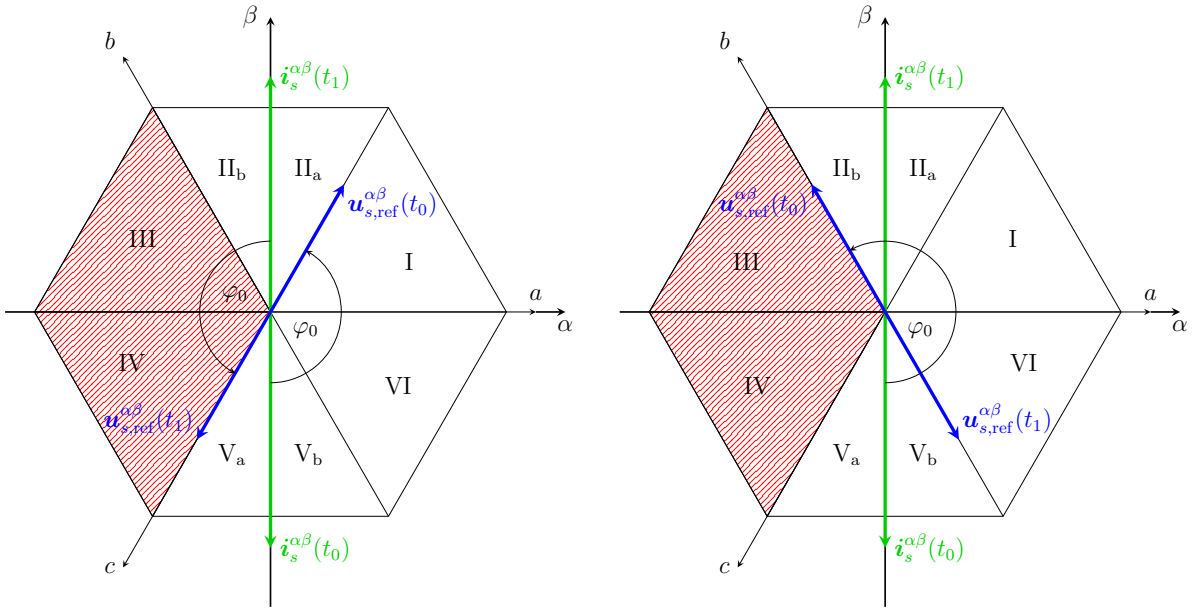

(a) $\varphi_0 = 150°$. (b) $\varphi_0 = 210°$.

Figure 3.23: *Stator current vector* $\boldsymbol{i}_s^{\alpha\beta}$ *and voltage reference vector* $\boldsymbol{u}_{s,\mathrm{ref}}^{\alpha\beta}$ *at time* t_0 *and* t_1 *for* (a) $\varphi_0 = 150°$ *and* (b) $\varphi_0 = 210°$.

120° of the non-negative current half-wave, the correct voltages are applied. But, as soon as $\boldsymbol{u}_{s,\mathrm{ref}}^{\alpha\beta}$ enters sector V, incorrect voltages are generated by the converter for the rest of the half-wave until time t_1. Concluding, in order to fully benefit from the two feasible voltage sectors III and IV, where the correct voltages can be generated for $i_s^a > 0$, the phase shift must be within the interval $\varphi_0 \in [150°, 210°]$. The observations above are also validated by simulation and measurement results: For $\varphi_0 = 150°$ (see Fig. 3.24, Experiment ($\mathrm{E}_{3.8,\mathrm{PMSM}}$)), during the first 60°, the phase current i_s^a jitters around zero. In contrast to the last 120°, where the desired sinusoidal characteristic is achieved. For $\varphi_0 = 210°$ (see Fig. 3.25, Experiment ($\mathrm{E}_{3.9,\mathrm{PMSM}}$)), the phase current i_s^a exhibits a sinusoidal characteristic during the first 120°, whereas, for the last 60°, it is deteriorated.

The phase shift φ_0 can be altered by the injection of a d-current which also changes the ratio between active power p (in W) and reactive power q (in var), since

$$q = p \cdot \tan(\varphi_0) \quad \text{where} \quad p = \tfrac{2}{3\kappa^2}(\boldsymbol{u}_s^{dq})^\top \boldsymbol{i}_s^{dq} \quad \text{and} \quad q = \tfrac{2}{3\kappa^2}(\boldsymbol{u}_s^{dq})^\top \boldsymbol{J}\boldsymbol{i}_s^{dq} \qquad \text{(see e.g. [4])}. \tag{3.43}$$

Moreover, note that, due to (2.13), i_s^d can be chosen independently of the desired torque ($\tau_m = \frac{2}{3\kappa^2} n_p \hat{\psi}_{\mathrm{pm}} i_s^q$). In order to derive an analytical expression for the reference current $i_{s,\mathrm{ref}}^d$ of the to-be-injected current i_s^d, the following assumption is imposed:

Assumption (AS.15) *The copper losses in the PMSM are negligible and its current dynamics are in steady state, i.e.*

$$R_s \approx 0\,\Omega \quad \textit{and} \quad \tfrac{\mathrm{d}}{\mathrm{d}t}\boldsymbol{i}_s^{dq} = \boldsymbol{0}_2. \tag{3.44}$$

Solving (2.15) (in steady state) for $\boldsymbol{u}_s^{dq}$ and inserting the result into (3.43) gives

$$\underbrace{n_p\omega_m}_{\omega_k}\left[L_s(i_s^d)^2 + L_s(i_s^q)^2 + \hat{\psi}_{\mathrm{pm}} i_s^d\right] = \left[R_s(i_s^d)^2 + R_s(i_s^q)^2 + n_p\omega_m\hat{\psi}_{\mathrm{pm}} i_s^q\right]\tan(\varphi_0),$$

which is a second-order polynomial in i_s^d. Its root with the smaller amplitude is used as d-current

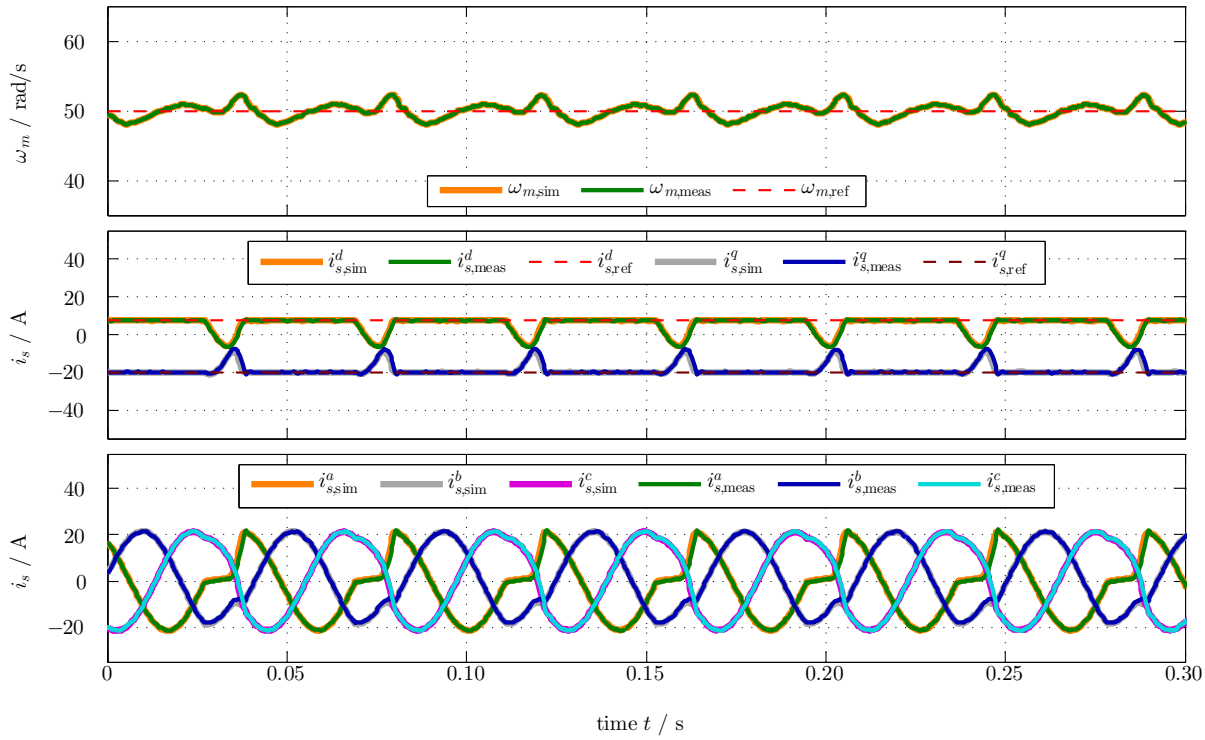

Figure 3.24: *Experiment* ($\mathrm{E}_{3.8,\mathrm{PMSM}}$)*: Simulation and measurement results for currents* $\boldsymbol{i}_s^{dq}$ *(with references) and* $\boldsymbol{i}_s^{abc}$ *for phase shift angle* $\varphi_0 = 150°$ *for PMSM (*$\mathfrak{E}_{i_s^q,\mathrm{sim}} = 0.635\,\mathrm{A}$ *and* $\mathfrak{E}_{i_s^q,\mathrm{meas}} = 0.730\,\mathrm{A}$*).*

reference[31], i.e.

$$i_s^d(i_s^q) = -\frac{n_p\omega_m\hat{\psi}_{\mathrm{pm}}}{2\big(n_p\omega_m L_s - R_s\tan(\varphi_0)\big)} + \sqrt{\frac{(n_p\omega_m\hat{\psi}_{\mathrm{pm}})^2}{4\big(n_p\omega_m L_s - R_s\tan(\varphi_0)\big)^2} - (i_s^q)^2 + \frac{n_p\omega_m\hat{\psi}_{\mathrm{pm}}\, i_s^q\,\tan(\varphi_0)}{\big(n_p\omega_m L_s - R_s\tan(\varphi_0)\big)}}$$

$$\overset{(\mathrm{AS}.15)}{=} -\frac{\hat{\psi}_{\mathrm{pm}}}{2\,L_s} + \sqrt{\underbrace{(\tfrac{\hat{\psi}_{\mathrm{pm}}}{2\,L_s})^2 - (i_s^q)^2 + \tfrac{\hat{\psi}_{\mathrm{pm}}}{L_s}\, i_s^q\,\tan(\varphi_0)}_{=:\varkappa}}. \tag{3.45}$$

For several combinations of i_s^q and φ_0, the term $\varkappa$ inside the root becomes negative leading to a complex, hence not feasible i_s^d-current and, for the machine used for measurements only the green area in Fig. 3.26 is admissible. For q-currents $i_s^q < -32.44\,\mathrm{A}$ the maximum possible angle φ_0 becomes smaller than 210°. So for very small q-currents, only a fraction of the voltage sectors III and IV (i.e. $\varphi_0 \in [150°, 210°]$), is feasible. To account for that, the d-current reference is determined by

$$i_{s,\mathrm{ref}}^d(i_s^q) := \begin{cases} -\frac{\hat{\psi}_{\mathrm{pm}}}{2\,L_s} + \sqrt{(\frac{\hat{\psi}_{\mathrm{pm}}}{2\,L_s})^2 - (i_s^q)^2 + \frac{\hat{\psi}_{\mathrm{pm}}}{L_s}\, i_s^q\,\tan(\varphi_0)} & \text{if } \varkappa \geq 0 \\ 0 & \text{else.} \end{cases} \tag{3.46}$$

Summarizing, for large machines with $R_s \approx 0$, the reference current $i_{s,\mathrm{ref}}^d$ depends on the machine parameters L_s and $\hat{\psi}_{\mathrm{pm}}$, the current i_s^q (or its reference $i_{s,\mathrm{ref}}^q$) and the desired phase angle φ_0. There exists an optimal value for φ_0 to minimize the error $\mathfrak{E}_{i_s^q}$. For the considered machine, the

[31] The solution with "−" in front of the root would lead to a higher current magnitude.

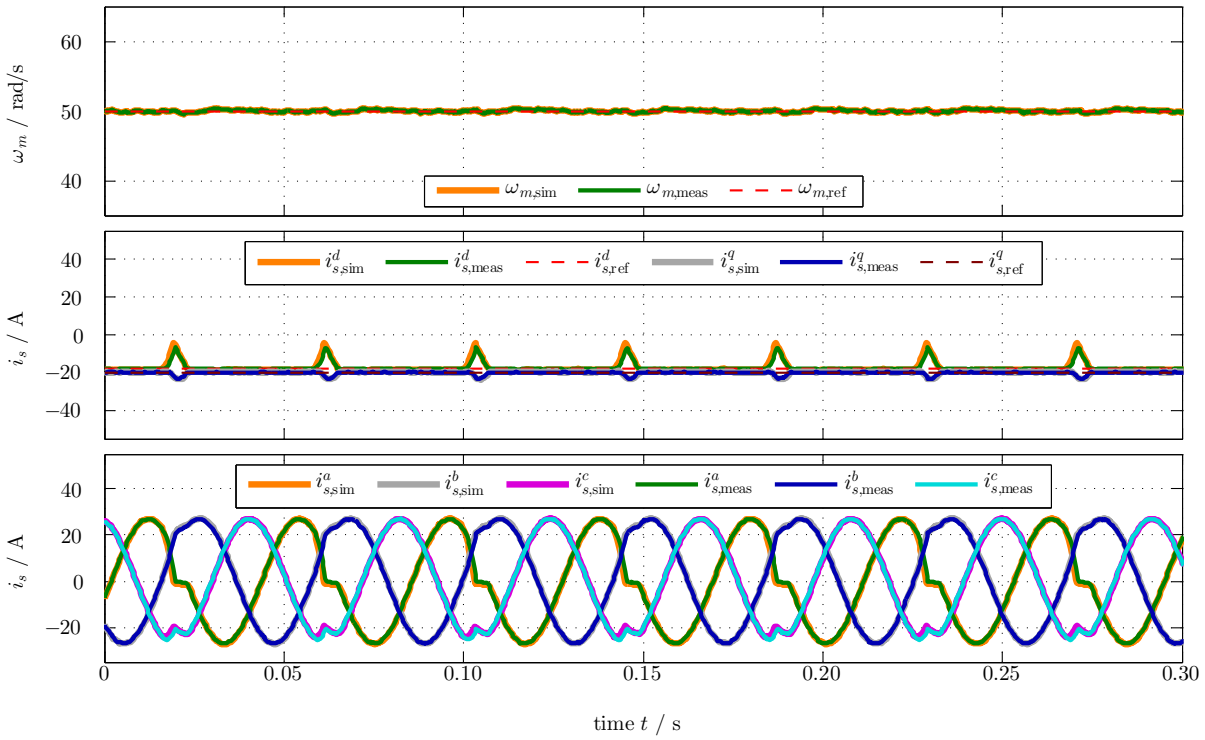

Figure 3.25: *Experiment* ($\mathrm{E}_{3.9,\mathrm{PMSM}}$)*: Simulation and measurement results for currents* $\boldsymbol{i}_s^{dq}$ *(with references) and* $\boldsymbol{i}_s^{abc}$ *for phase shift angle* $\varphi_0 = 210°$ *for PMSM* ($\mathfrak{E}_{i_s^q,\mathrm{sim}} = 0.193\,\mathrm{A}$ *and* $\mathfrak{E}_{i_s^q,\mathrm{meas}} = 0.156\,\mathrm{A}$*).*

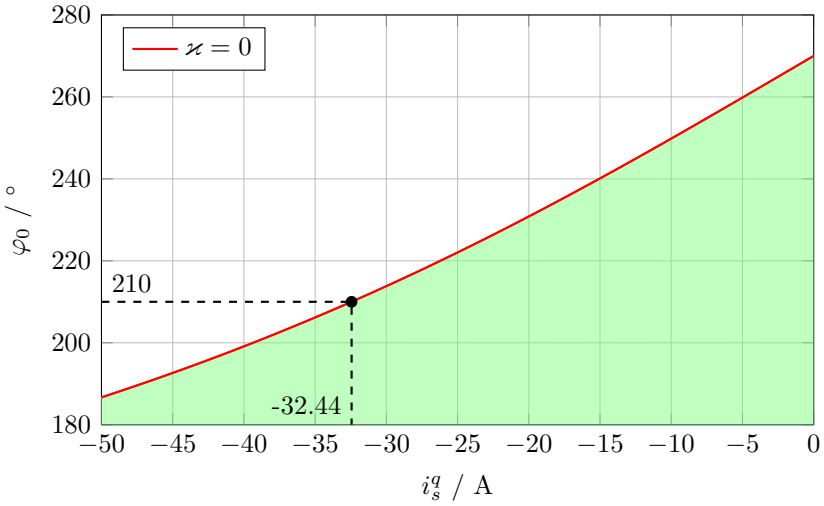

Figure 3.26: *Maximum possible angle* φ_0 *over current* i_s^q *(green area).*

optimal value was found by iterative simulations: These results are depicted in Fig. 3.27. The error $\mathfrak{E}_{i_s^q}$ is plotted over i_s^q and φ_0 and the optimal trajectory $\varphi_0^\star$ is displayed in red. Clearly, for other machines, the optimal values might be different. For increasing values of i_s^q, the optimal curve increases from $\varphi_0 = 190°$. For i_s^q values close to zero, $\varphi_0^\star$ decreases again. The valley for $\varphi_0^\star$ of the error $\mathfrak{E}_{i_s^q}$-map is flat, so that choosing an angle close to $\varphi_0^\star$ has only a limited impact on the value of $\mathfrak{E}_{i_s^q}$.

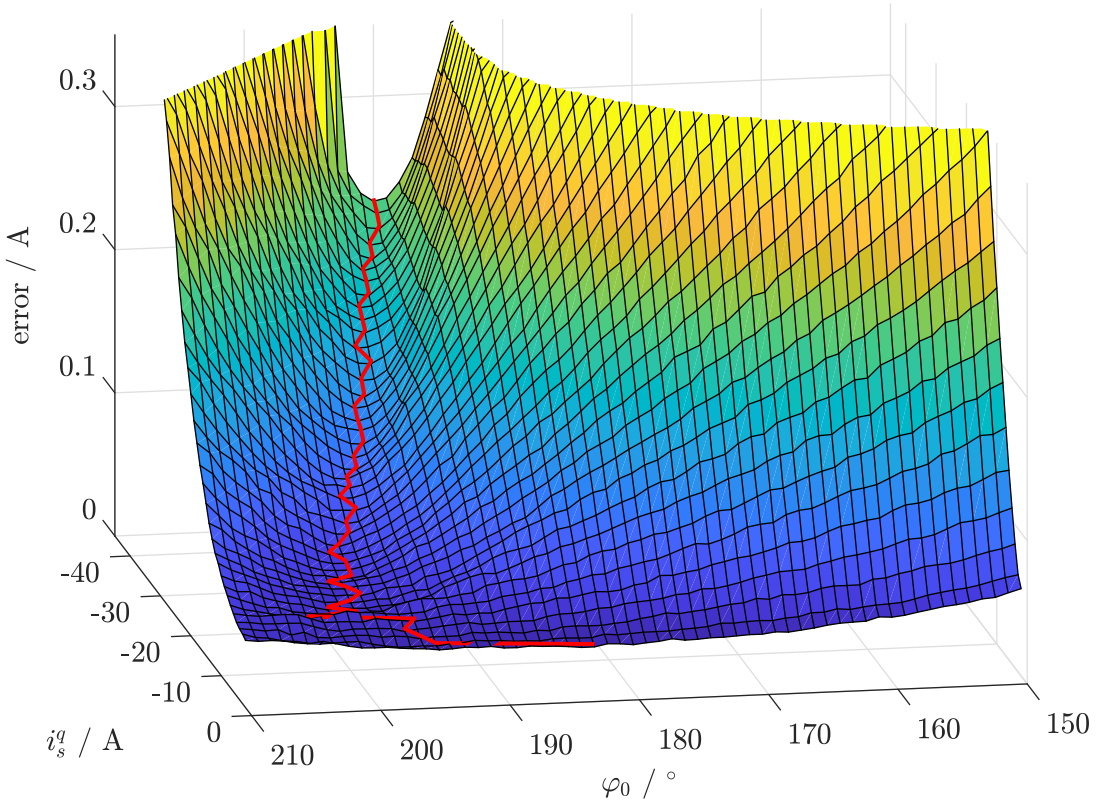

Figure 3.27: *Quadratic error $\mathfrak{E}_{i_s^q}$ depending on i_s^q and φ_0 for $\omega_m = 50\,\frac{\text{rad}}{\text{s}}$ with optimal angle $\varphi_0^\star$-curve in red.*

Figure 3.28 shows the topview of Fig. 3.27 for the optimal trajectory $\varphi_0^\star$ for different rotational speeds $\omega_m \in \{50, 100, 150\}\,\frac{\text{rad}}{\text{s}}$. It shows, the optimal trajectory is for high currents (almost) identical. For bigger i_s^q values, the optimal values $\varphi_0^\star$ are different, but as Fig. 3.27 indicates, the error $\mathfrak{E}_{i_s^q}$ is also small. Hence, using the optimal trajectory determined at one rotational speed for the whole speed range of the machine might not cause big differences in the overall result.
Finally, in Fig. 3.29, simulation and measurement results for the overall fault-tolerant control system with extended anti-windup, modified SVM (flat-top modulation) *and* optimally injected *d*-current are presented (Experiment ($\text{E}_{3.10,\text{PMSM}}$)). The upper subplot shows the rotational speed ω_m. The second subplot depicts the currents i_s^d and i_s^q and their reference values, whereas the lower subplot illustrates the shape of the *abc*-currents. The error values for this scenario are $\mathfrak{E}_{i_s^q,\text{sim}} = 0.078\,\text{A}$ and $\mathfrak{E}_{i_s^q,\text{meas}} = 0.143\,\text{A}$, which are clearly the lowest values compared to the other results in Figures 3.18, 3.19 and 3.22. Looking at the relative errors, $\mathfrak{e}_{i_s^q,\text{sim}} = 0.004$ and $\mathfrak{e}_{i_s^q,\text{meas}} = 0.007$ shows that the deviation is below 1 %. Moreover, the reference tracking capability, in particular, of i_s^q is the best which implies that the torque ripples[32] are also minimized (recall (2.13)) leading to less stress on the mechanical drive train.

[32]Note that, if the produced generator torque in wind turbine systems does not equal its reference value, wind turbine efficiency and power production are reduced [7].

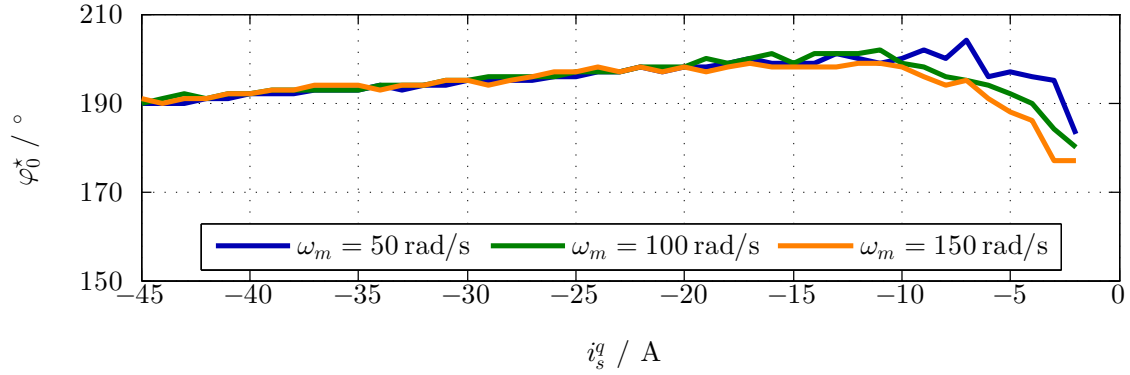

Figure 3.28: *Comparison of optimal angles $\varphi_0^\star$ over currents i_s^q for different rotational speeds ω_m.*

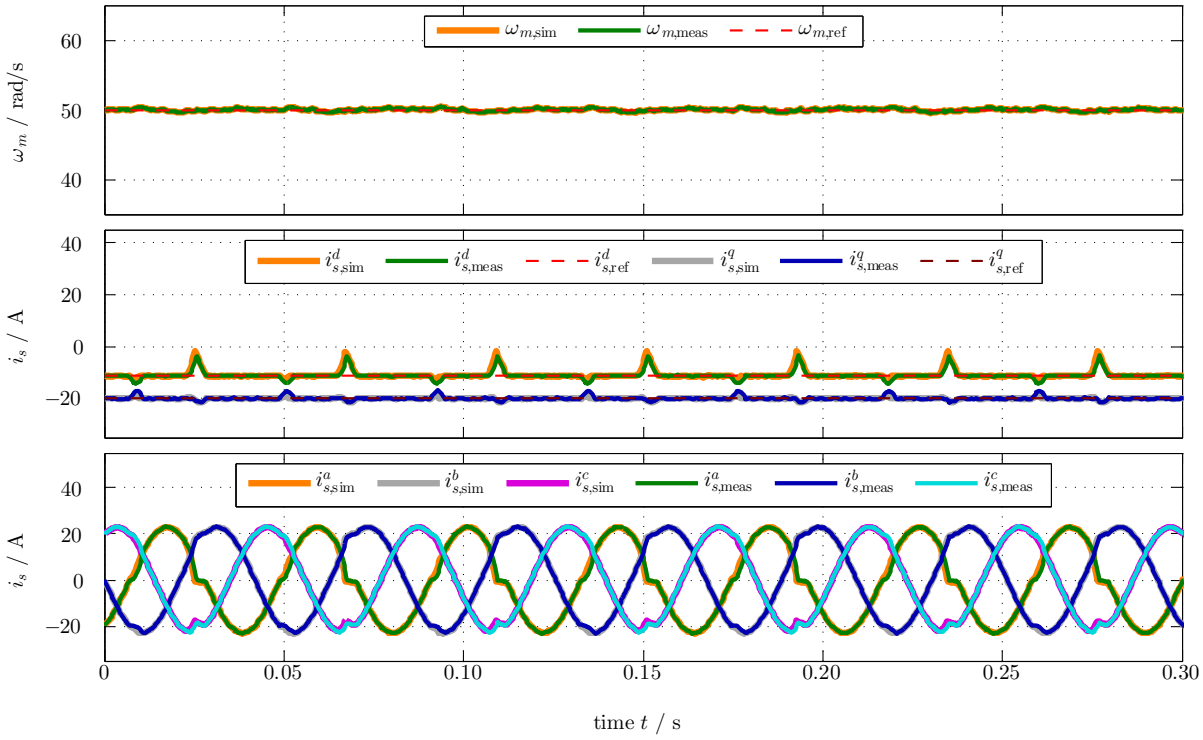

Figure 3.29: *Experiment* ($\mathrm{E}_{3.10,\mathrm{PMSM}}$)*: Comparison of simulation and measurement results for an open-switch fault in $\mathbb{S}_s^a$ using improved AWU, modified SVM and optimal d-current injection for PMSM ($\mathfrak{E}_{i_s^q,\mathrm{sim}} = 0.078\,\mathrm{A}$ and $\mathfrak{E}_{i_s^q,\mathrm{meas}} = 0.143\,\mathrm{A}$).*

The positive effects of the three modifications to obtain the post-fault current control system of the PMSM were already summarized and compared in Tab. 3.1 where error $\mathfrak{E}_{i_s^q}$ and relative error $\mathfrak{e}_{i_s^q}$ are listed for each case. Figure 3.30 shows measurement results for an experiment with several scenarios: (i) the fault-free case (for the first second), (ii) an open-switch fault (from 1 s until the end of the measurement) in $\mathbb{S}_s^a$ with standard control, (iii) with improved AWU, (iv) with improved AWU and flat-top modulation and (v) with improved AWU, flat-top modulation and optimal *d*-current injection. The upper subplot shows the rotational speed ω_m of the drive train, the second subplot shows the measured torque τ_{meas}. In the third subplot the currents i_s^d and i_s^q and their references are shown. The lower subplot shows the *abc*-phase currents. Due to the high oscillations in the torque of the PMSM—due to the fault—the rotational speed is also strongly oscillating between 1 s and 3 s. After that the torque ripples decrease and so do

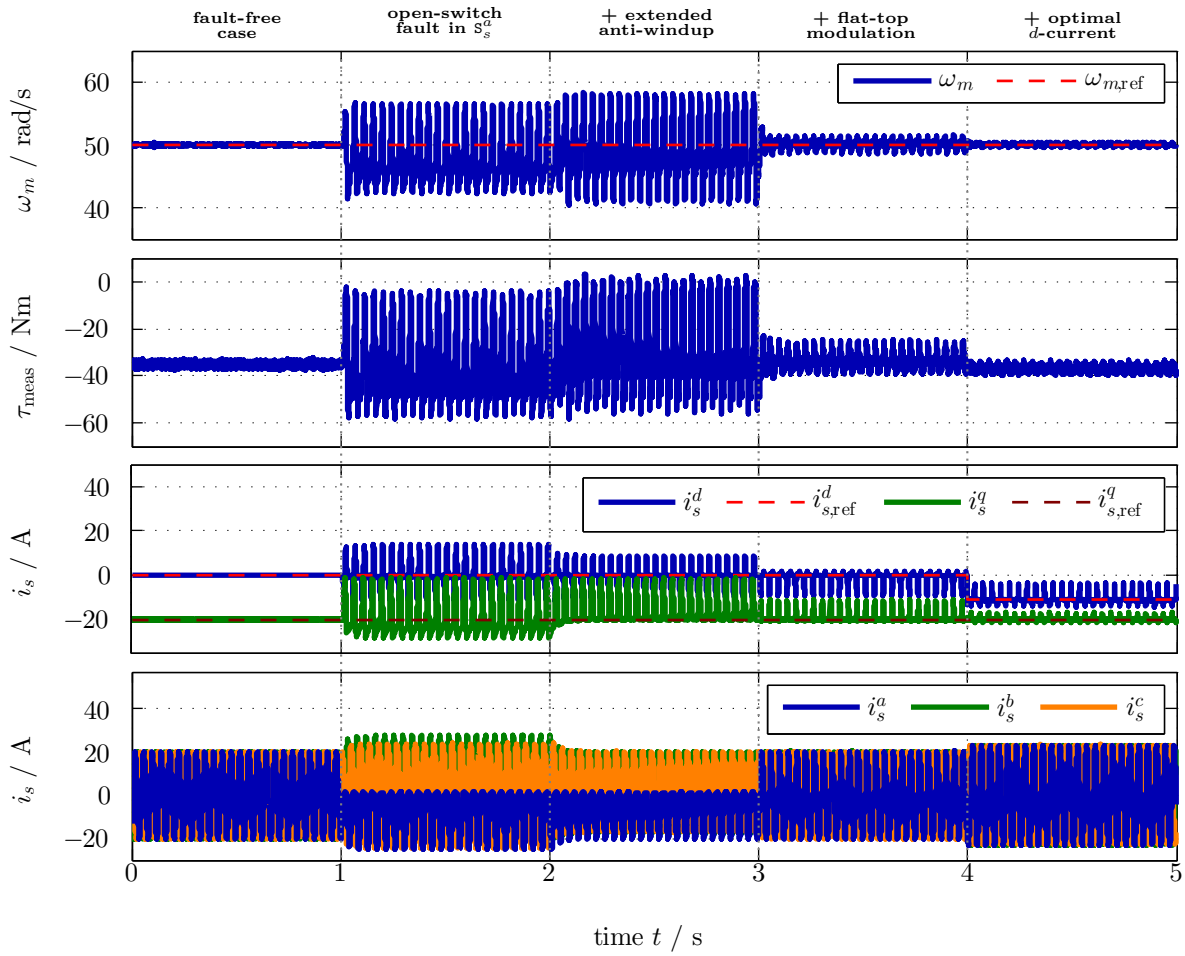

Figure 3.30: *Measurement results for current control performance during five different scenarios: (i) fault-free case, (ii) open-switch fault in* S_s^a ($\mathrm{E}_{3.5,\mathrm{PMSM}}$)*, (iii) with extended AWU* ($\mathrm{E}_{3.6,\mathrm{PMSM}}$)*, (iv) additionally with modified SVM* ($\mathrm{E}_{3.7,\mathrm{PMSM}}$) *and (v) additionally with optimal d-current injection* ($\mathrm{E}_{3.10,\mathrm{PMSM}}$) *for PMSM.*

the ripples in the speed. While the improved AWU shows only slight improvements on the control performance, the flat-top modulation makes a big difference ($\mathfrak{E}_{i_s^q,\mathrm{meas}}$ reduces about 70 %). Finally the optimal q-current injection reduces the relative error $\mathfrak{e}_{i_s^q,\mathrm{meas}}$ below 1 % (see Tab. 3.1).
Summarizing, although an open-switch fault is present, the PMSM can be controlled to track an i_s^q reference and only small differences between fault free case ([0 s, 1 s]) and complete post-fault control ([4 s, 5 s]) are visible in ω_m, τ_{meas} and i_s^q.

Remark 3.3.4 (Possible limitation of the d-current injection in wind turbine systems)**.** *Due to the current rating/limitation of the machine-side converter, the additional injection of a d-current might not be feasible up to the rated torque of the isotropic generator in wind turbine systems. Only current vector magnitudes smaller than a maximal value* $\hat{i}_{\max} \geq \sqrt{(i_s^d)^2 + (i_s^q)^2}$ *(in* A*) are admissible. Hence, not all currents* i_s^q *can be realized to obtain a desired machine torque* $\tau_m \sim i_s^q$ *(recall* (2.13)*). Therefore, the uninterrupted operation of the wind turbine system under open-switch faults might not be possible for all wind speeds unless the pitch control system is incorporated into the fault-tolerant control system. The turbine torque (proportional to the wind speed cubed and the pitch angle) must be decreased by changing the pitch angle such that the*

current rating of the machine-side converter is not exceeded (for details see [4], [96, Chap. 8]). The proposed pitch controller in Sect. 3.1.1 fulfils this condition. Experiments (E_3) in Sect. 4.3.1 and Sect. 4.3.2 investigate the impacts of this limitation.

Remark 3.3.5 (Validity of results for faults in other switches)**.** *Since the voltage hexagon is symmetrical, the optimal phase angle trajectory (for this particular machine, see Fig. 3.27) is identical for an open-switch fault in any other switch. For a fault in e.g.* $\mathtt{S}_s^b$ *and* $i_s^b > 0\,\mathrm{A}$*, only voltage vectors within the sectors V and VI are feasible (instead of sectors III and IV for a fault in* $\mathtt{S}_s^a$*). Therefore, the feasible sectors are obtained by a simple rotation by* $120°$ *(see Fig. 3.23). Summarizing, all conclusions made for* $\mathtt{S}_s^a$ *do also hold for open-switch faults in the other switches simply by considering the respective (rotated) feasible sectors.*

Remark 3.3.6 (Motor mode)**.** *For a converter outputting power, e.g. for PMSMs in motor mode or for grid-side converters in wind turbine systems, solely phase shifts of* $\varphi_0 \in (-90°, 90°)$ *are feasible (for* $\varphi_0 \in (90°, 270°)$ *the converter drags power). Hence, it is not possible to fully benefit from the sectors III and IV, as a* $\varphi_0 \in (150°, 210°)$ *is necessary for that (see Fig. 3.23). For* $\varphi_0 \in (-30°, 30°)$ *the voltage reference vector* $\boldsymbol{u}_{s,\mathrm{ref}}^{\alpha\beta}$ *is never in the sectors III and IV for positive* i_s^a*. So only for up to* $60°$ *of the* $180°$ *during a positive* i_s^a*,* $\boldsymbol{u}_{s,\mathrm{ref}}^{\alpha\beta}$ *can be in the feasible sectors III and IV in motor mode. For* $\varphi_0 = 90°$*,* $\boldsymbol{u}_{s,\mathrm{ref}}^{\alpha\beta}$ *is for* $60°$ *in the feasible sectors III and IV. For* $\varphi_0 = 45°$*,* $\boldsymbol{u}_{s,\mathrm{ref}}^{\alpha\beta}$ *is only for* $15°$ *in the feasible sectors III and IV. Note that, for* $\varphi_0 = -90°$ *or* $\varphi_0 = 90°$ *only reactive power is exchanged with the device connected to the converter (see* (3.43)*).*

3.3.2 Post-fault control of EESM

For the post-fault control of EESMs similar strategies as for PMSMs are used. In Fig. 3.31 the standard control system—as shown in Fig. 3.9—is extended. The modifications for the improved and fault-tolerant control systems are highlighted in blue. After defining a measure for the impact of the fault on the EESMs current/torque control performance, again three modifications to the standard current control system are proposed:

($\mathrm{M}_{3.1,\mathrm{EESM}}$) Improvement of anti-windup strategy.

($\mathrm{M}_{3.2,\mathrm{EESM}}$) Modification of SVM.

($\mathrm{M}_{3.3,\mathrm{EESM}}$) Fault-optimal current reference generation.

3.3.2.1 Fault impact analysis

The torque of a nonlinear EESM depends on all three currents i_s^d, i_s^q, i_e (see (2.41)). So instead of the q-current as for the PMSM[33], the deviations in the torque τ_m are used as measure for the impact of an open-switch fault. Hence, the square root of the quadratic deviation of τ_m from its reference value $\tau_{m,\mathrm{ref}}$ over one[34] electric revolution of the EESM is chosen as measure, i.e.

$$\mathfrak{E}_{\tau_m} = \sqrt{\frac{1}{10} \sum_{l=1}^{10 n_{\mathrm{sample}}} \left(\tau_{m,\mathrm{ref}} - \tau_m[l]\right)^2 \frac{T_{\mathrm{sw}}}{1\,\mathrm{s}}} \qquad (\text{in N m}) \tag{3.47}$$

[33]The torque of the linear isotropic PMSM only depends on i_s^q (see (2.15))

[34]To minimize the impact of fluctuations and measurement errors, the average over 10 revolutions is used for the square root.

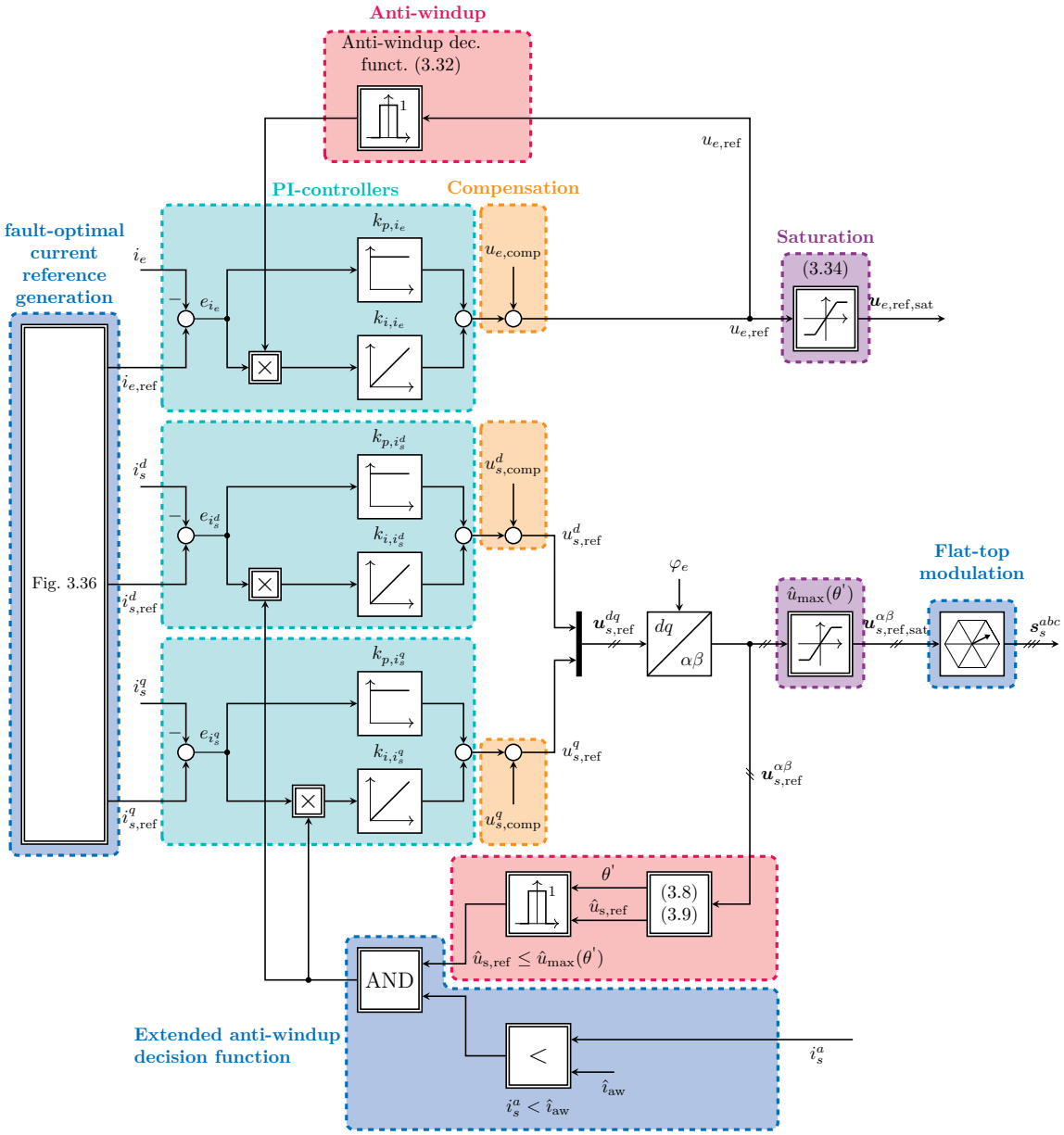

Figure 3.31: *Fault-tolerant control system for an EESM for an open-switch fault in* $\mathtt{S}_s^a$*: PI-controllers with improved anti-windup, cross-coupling feedforward compensation and reference voltage saturation (Modifications* ($\mathrm{M}_{3.1,\mathrm{EESM}}$)-($\mathrm{M}_{3.3,\mathrm{EESM}}$) *compared to standard field-oriented control are highlighted in blue).*

where the (sampled at each switching period T_{sw}) sampled torque $\tau_m[l] \approx \tau_m(lT_{\mathrm{sw}})$ is averaged over n_{sample} samples (as defined in (3.40)) for one electric revolution of the EESM. To be able to compare the deviation for different torques, the measure $\mathfrak{E}_{\tau_m}$ is normalized with respect to the absolute value of its reference leading to the relative error

$$\mathfrak{e}_{\tau_m} = \frac{\mathfrak{E}_{\tau_m}}{|\tau_{m,\mathrm{ref}}|}. \tag{3.48}$$

To investigate the impact of an open-switch fault in $\mathtt{S}_s^a$ and the three post-fault Modifications ($\mathrm{M}_{3.1,\mathrm{EESM}}$)-($\mathrm{M}_{3.3,\mathrm{EESM}}$) on the EESM step-by-step, four different experiments will be

conducted:

($E_{3.5,EESM}$) Open-switch fault in $\mathtt{S}_s^a$, standard controller, see Fig. 3.9.

($E_{3.6,EESM}$) Open-switch fault in $\mathtt{S}_s^a$, controller with improved AWU strategy (Modification ($M_{3.1,EESM}$)).

($E_{3.7,EESM}$) Experiment ($E_{3.6,EESM}$) + modification of SVM / flat-top modulation (Modifications ($M_{3.1,EESM}$) + ($M_{3.2,EESM}$)).

($E_{3.8,EESM}$) Experiment ($E_{3.7,EESM}$) + fault-optimal current reference generation (Modifications ($M_{3.1,EESM}$) + ($M_{3.2,EESM}$) + ($M_{3.3,EESM}$)); control structure, see Fig. 3.31.

Table 3.2 summarizes the errors $\mathfrak{E}_{\tau_m}$ and relative errors $\mathfrak{e}_{\tau_m}$ for simulation and measurement results of Experiments ($E_{3.5,EESM}$)-($E_{3.8,EESM}$). The different strategies will be explained in detail in the following sections. But it can already be seen here, that combining Modifications ($M_{3.1,EESM}$)-($M_{3.3,EESM}$) in Experiment ($E_{3.8,EESM}$) (last row of Tab. 3.2) reduces $\mathfrak{E}_{\tau_m}$ and $\mathfrak{e}_{\tau_m}$ for simulation *and* measurement drastically.

Table 3.2: *Comparison of error $\mathfrak{E}_{\tau_m}$ and relative error $\mathfrak{e}_{\tau_m}$ for improved post-fault control.*

control strategy	$\mathfrak{E}_{\tau_m,\mathrm{sim}}$	$\mathfrak{e}_{\tau_m,\mathrm{sim}}$	$\mathfrak{E}_{\tau_m,\mathrm{meas}}$	$\mathfrak{e}_{\tau_m,\mathrm{meas}}$
($E_{3.5,EESM}$): standard control	3.674 N m	0.122	2.853 N m	0.095
($E_{3.6,EESM}$): improved AWU	3.257 N m	0.109	2.928 N m	0.098
($E_{3.7,EESM}$): improved AWU + flat-top	1.026 N m	0.034	0.815 N m	0.027
($E_{3.8,EESM}$): improved AWU + flat-top + optimal current reference	0.179 N m	0.006	0.479 N m	0.016

Figure 3.32 exemplifies the impact of an open-switch fault in $\mathtt{S}_s^a$ on the EESM[35] current/torque control performance with standard controllers (Experiment ($E_{3.5,EESM}$)). In this figure, measurement and simulation results are compared. The first subplot shows the rotational speed ω_m and its reference. The speed is oscillating around $\omega_{m,\mathrm{ref}} = 50\,\frac{\mathrm{rad}}{\mathrm{s}}$. This is due to the speed control of the load machine (DFIM, see Sect. 4.1.3), which cannot instantaneously counteract the torque ripples of the EESM induced by the open-switch fault. The torque of the EESM is shown in the second subplot. Measurement and simulation never track the reference torque of $\tau_{m,\mathrm{ref}} = -30\,\mathrm{N\,m}$. The torque of the simulation oscillates a bit more than the measured torque. The stator d-current is depicted in the third subplot. During the negative half-wave of i_s^a, i_s^d tracks its reference. Measurement and simulation results do match. Subplot four shows the stator q-current. As the torque in subplot two, it does never track its reference value and the simulation results are oscillating a bit more than the measurement results. The excitation current i_e and its reference is shown in the fifth subplot. During the negative half-wave of i_s^a, measurement and simulation results do track their references. During the (expected) positive half-wave of i_s^a, both signals oscillate around the reference and differ from it. The difference between measurement and simulation results are caused by the low time resolution of the dc-source for the excitation. The last subplot shows $\boldsymbol{i}_s^{abc}$ of measurement and simulation. Simulation and measurement results do match during the negative half-wave of i_s^a and are very similar for the (expected) positive half-wave. As already observed for the PMSM (see Sect. 3.3.1) for an open-switch fault in $\mathtt{S}_s^a$, the positive half-wave of i_s^a is also missing for an EESM.

[35]Details on the implementation and parameters for the drive train will be given in Sect. 4.1.3.

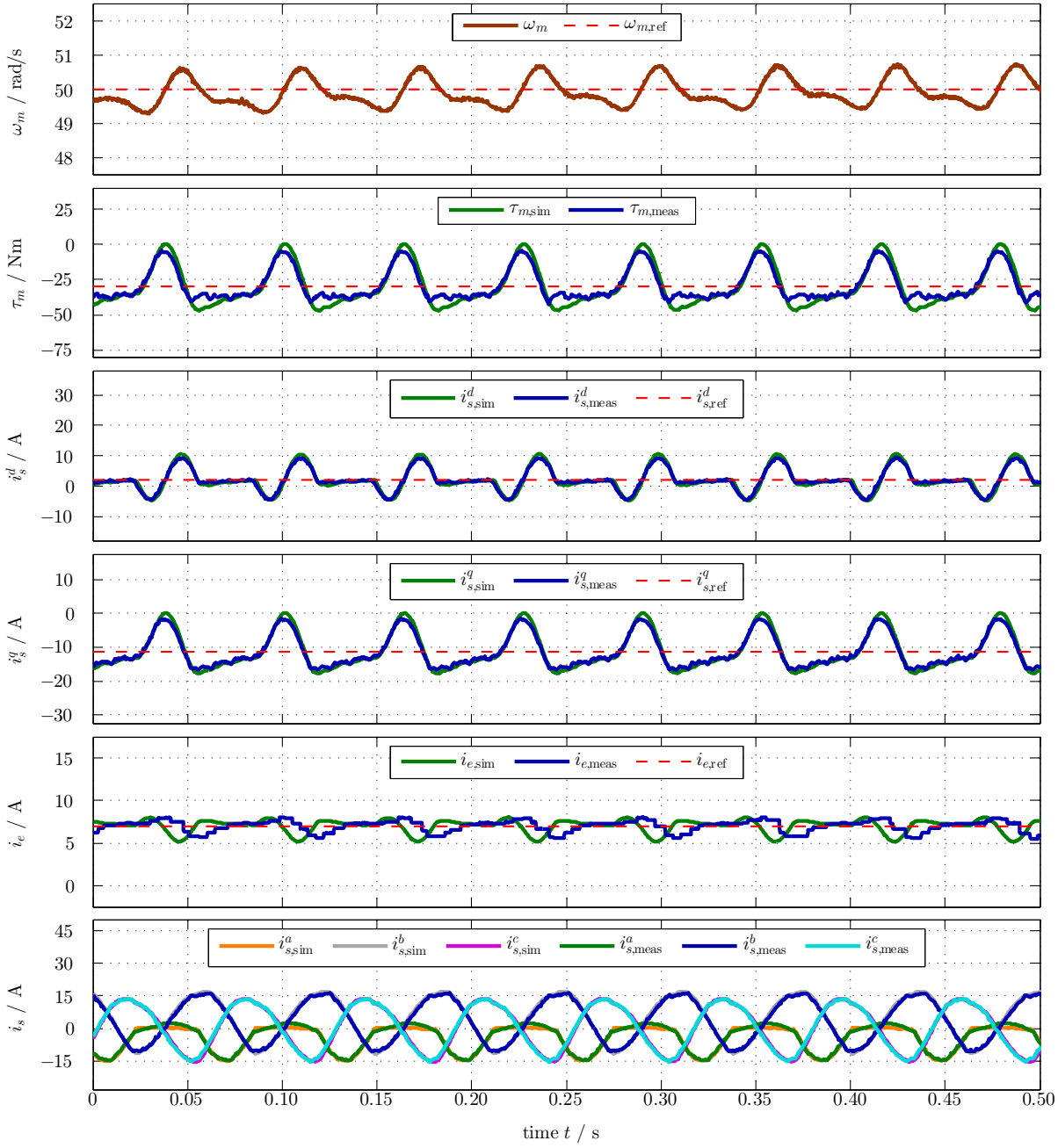

Figure 3.32: *Experiment* ($\mathrm{E}_{3.5,\mathrm{EESM}}$)*: Comparison of simulation and measurement results for an open-switch fault in* $\mathtt{S}^a_s$ *for EESM (*$\mathfrak{E}_{\tau_m,\mathrm{sim}} = 3.674\,\mathrm{N\,m}$ *and* $\mathfrak{E}_{\tau_m,\mathrm{meas}} = 2.853\,\mathrm{N\,m}$*).*

3.3.2.2 Improved anti-windup strategy

The used improved anti-windup strategy is identical to the strategy used for the PMSM (see (3.42) in Sect. 3.3.1.2). The anti-windup strategy for the excitation current i_e is not changed, as the dc-source for the excitation is not directly affected by an open-switch fault in the stator converter (see Fig. 3.31).

Figure 3.33 shows the results of the same scenario as in Fig. 3.32, but with the use of the improved anti-windup strategy (Experiment ($\mathrm{E}_{3.6,\mathrm{EESM}}$)). The signals are the same as in Fig. 3.32. The torque in subplot two is still oscillating, but in this case it tracks its reference for the negative half-wave of i^a_s. The same is true for i^d_s and i^q_s in subplots three and four, respectively. Besides

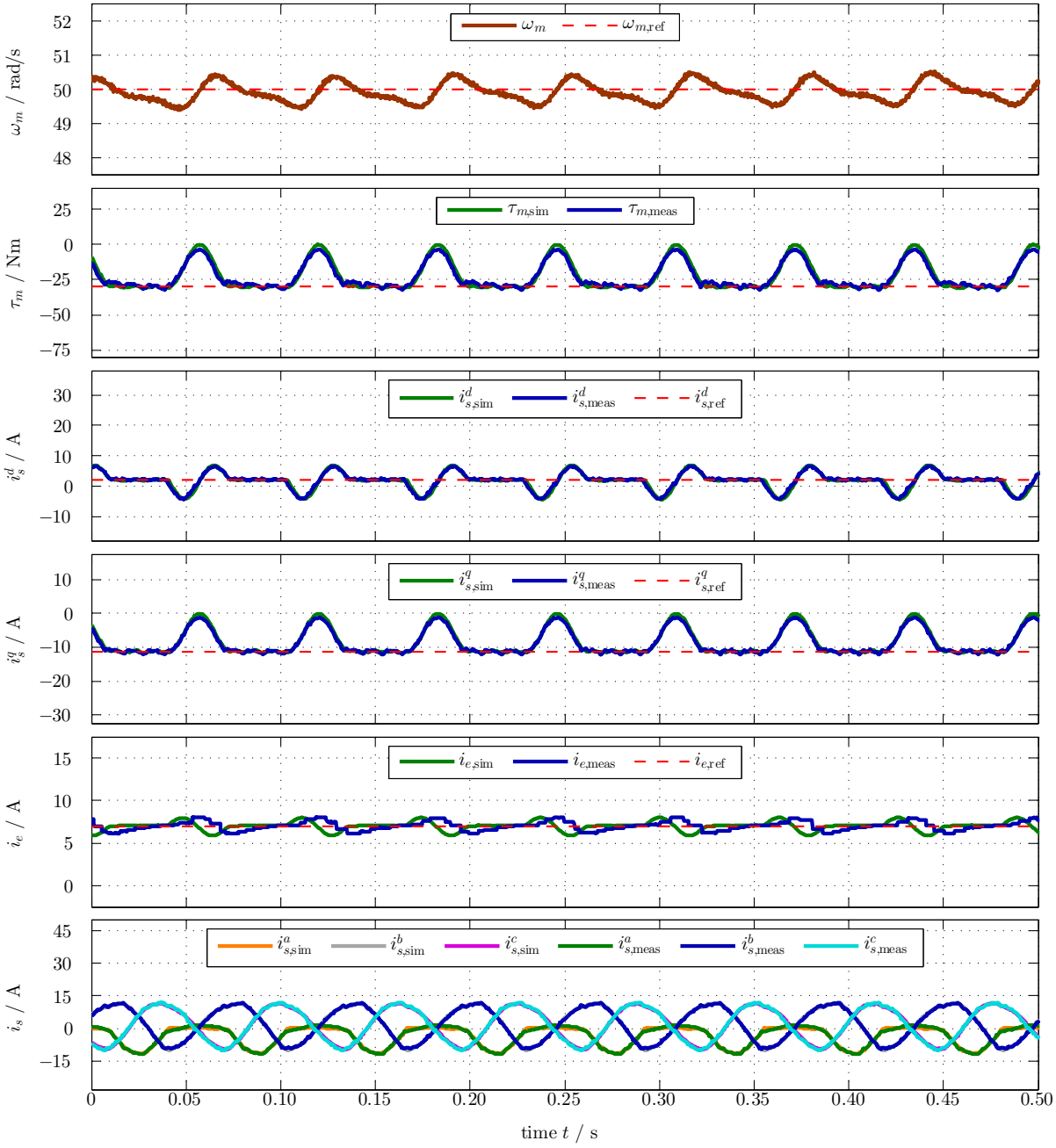

Figure 3.33: *Experiment* ($\mathrm{E}_{3.6,\mathrm{EESM}}$)*: Comparison of simulation and measurement results for an open-switch fault in* $\mathfrak{s}^a_s$ *using improved AWU for EESM (*$\mathfrak{E}_{\tau_m,\mathrm{sim}} = 3.257\,\mathrm{N\,m}$ *and* $\mathfrak{E}_{\tau_m,\mathrm{meas}} = 2.928\,\mathrm{N\,m}$*).*

of i_e, measurement and simulation results do match very closely. While the absolute error decreases to $\mathfrak{E}_{\tau_m,\mathrm{sim}} = 3.257\,\mathrm{N\,m}$ for the simulation (before $\mathfrak{E}_{\tau_m,\mathrm{sim}} = 3.674\,\mathrm{N\,m}$), the error for the measurement increases slightly to $\mathfrak{E}_{\tau_m,\mathrm{meas}} = 2.928\,\mathrm{N\,m}$ (before $\mathfrak{E}_{\tau_m,\mathrm{meas}} = 2.853\,\mathrm{N\,m}$). Hence, the improved anti-windup strategy does only show a minor improvement in the simulation results.

3.3.2.3 Modified SVM

As for the post-fault control of the PMSM (see Sect. 3.3.1.2), it is also beneficial for the post-fault control of an EESM to avoid the infeasible zero space-vector ($\boldsymbol{u}_{111}^{\alpha\beta}$ for a fault in an upper switch, $\boldsymbol{u}_{000}^{\alpha\beta}$ for a fault in a lower switch). The dc-source for the excitation current is not affected by this measure.

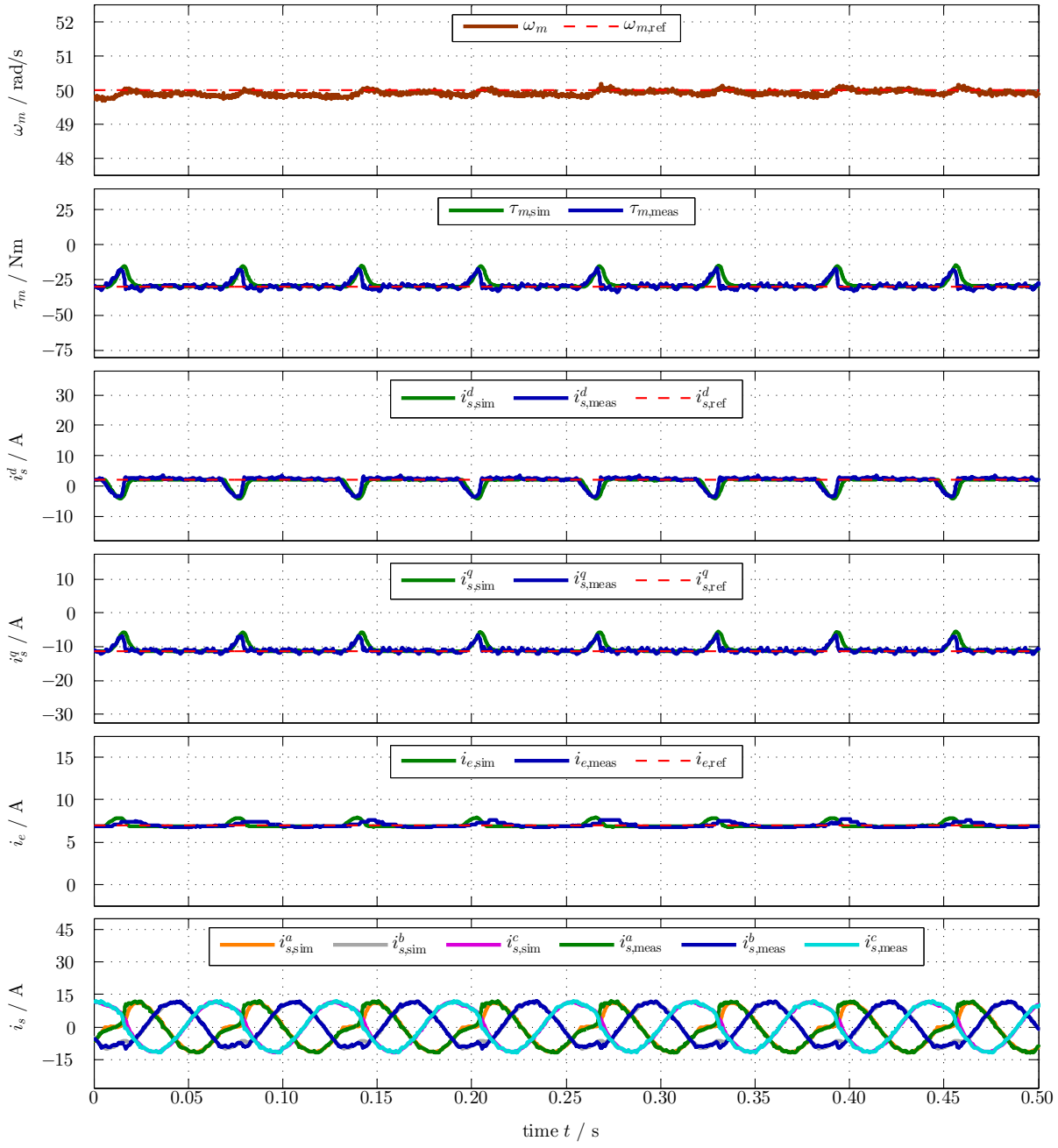

Figure 3.34: *Experiment* ($\mathrm{E}_{3.7,\mathrm{EESM}}$)*: Comparison of simulation and measurement results for an open-switch fault in* $\mathtt{S}_s^a$ *using improved AWU and modified SVM for EESM (*$\mathfrak{E}_{\tau_m,\mathrm{sim}} = 1.026\,\mathrm{N\,m}$ *and* $\mathfrak{E}_{\tau_m,\mathrm{meas}} = 0.815\,\mathrm{N\,m}$*).*

Figure 3.34 shows the comparison of simulation and measurement results for an open-switch fault in $\mathtt{S}_s^a$ using the improved anti-windup strategy and the modified SVM / flat-top modulation (Experiment ($\mathrm{E}_{3.7,\mathrm{EESM}}$)). Compared to Fig. 3.33 (Experiment ($\mathrm{E}_{3.6,\mathrm{EESM}}$)) where only the

improved anti-windup strategy is used, the results have significantly improved. The rotational speed ω_m (upper subplot) is now almost capable of tracking its reference. The amplitude of the torque deviation (subplot two) is much smaller and the torque tracks its reference for a longer time per revolution. The same is true for i_s^d, i_s^q and i_e in subplots three, four and five, respectively. The currents i_s^a do now have at least partly a positive half-wave. Measurements and simulations do match except for the beginning of the positive half-wave. The current i_s^a of the measurement becomes a bit earlier positive per revolution than that of the simulation. But for both the absolute error reduces drastically. The simulation error reduces to $\mathfrak{E}_{\tau_m,\mathrm{sim}} = 1.026\,\mathrm{N\,m}$ (before $\mathfrak{E}_{\tau_m,\mathrm{sim}} = 3.257\,\mathrm{N\,m}$) and the measurement error to $\mathfrak{E}_{\tau_m,\mathrm{meas}} = 0.815\,\mathrm{N\,m}$ (before $\mathfrak{E}_{\tau_m,\mathrm{meas}} = 2.928\,\mathrm{N\,m}$).

3.3.2.4 Fault-optimal current reference generation

The torque of a nonlinear EESM depends on all three currents i_s^d, i_s^q, i_e (see (2.41)). So instead of using the MTPC-trajectory (see Fig. 3.12), a new fault-optimal current reference trajectory for feedforward torque control has to be determined. For that simulations were conducted for $i_s^d \in [-15\,\mathrm{A}, 15\,\mathrm{A}]$, $i_s^q \in [-15\,\mathrm{A}, 15\,\mathrm{A}]$ and $i_e \in [0\,\mathrm{A}, 19\,\mathrm{A}]$ with a step size of 1 A. For the simulation, the improved anti-windup and the modified SVM were used. For each feasible negative torque (only for generator mode), the current triple (i_s^d, i_s^q, i_e) with minimum $\mathfrak{E}_{\tau_m}$ was searched for. Figure 3.35 shows the fault-optimal current references for negative torques for an open-switch fault in $\mathtt{S}_s^a$ for different angular velocities $\omega_m \in \{50, 75, 100\}\,\frac{\mathrm{rad}}{\mathrm{s}}$. While the MTPC curve for decreasing torque moves towards a positive i_s^d, the fault-optimal current references move towards a negative i_s^d and uses higher excitation currents i_e. The optimal trajectories for the different speeds are very similar, so the error caused by choosing one trajectory[36] for all speeds only is not significant (see Sect. 3.3.1.4).

Remark 3.3.7. *For faults in other switches than $\mathtt{S}_s^a$, the optimal trajectories are very similar. Figure 3.36 shows the fault-optimal current reference trajectories for feedforward torque control for open-switch faults in $\mathtt{S}_s^a$-$\overline{\mathtt{S}}_s^c$.*

In Fig. 3.37, the comparison of simulation and measurement results for an open-switch fault in $\mathtt{S}_s^a$ using improved AWU, modified SVM and fault-optimal current reference is shown (Experiment ($\mathrm{E}_{3.8,\mathrm{EESM}}$)). Compared to Fig. 3.34 (Experiment ($\mathrm{E}_{3.7,\mathrm{EESM}}$)), where only the improved AWU and the modified SVM were used, the rotational speed ω_m in the upper subplot is smother. ω_m now (almost) perfectly tracks its reference. The torque τ_m in subplot two tracks its reference throughout the whole time and almost no oscillations are visible. Because of the fault-optimal current reference generation another current triple (i_s^d, i_s^q, i_e) is chosen to create the reference torque, in contrast to Fig. 3.34 (where the MTPC-trajectory was used). $i_{s,\mathrm{ref}}^d$ has become negative, $i_{s,\mathrm{ref}}^q$ is slightly increased and $i_{e,\mathrm{ref}}$ is also increased. Besides in i_s^d, almost no oscillations in the currents are visible. In the current i_s^a, shown in the lower subplot, the period with zero current is now shifted to the end of the positive half-wave. Measurement and simulation results match very closely in all subplots for this scenario. The absolute error reduces significantly for the simulation to $\mathfrak{E}_{\tau_m,\mathrm{sim}} = 0.179\,\mathrm{N\,m}$ (before $\mathfrak{E}_{\tau_m,\mathrm{sim}} = 1.026\,\mathrm{N\,m}$) and the measurement error was almost cut in half to $\mathfrak{E}_{\tau_m,\mathrm{meas}} = 0.479\,\mathrm{N\,m}$ (before $\mathfrak{E}_{\tau_m,\mathrm{meas}} = 0.815\,\mathrm{N\,m}$).
In Tab. 3.2 the absolute and relative errors for all the investigated scenarios were already summarized (Experiments ($\mathrm{E}_{3.5,\mathrm{EESM}}$)-($\mathrm{E}_{3.8,\mathrm{EESM}}$)). Figure 3.38 shows measurement results for an experiment with five scenarios: (i) the fault-free case (for the first two seconds), (ii) an open-switch fault (from 2 s until the end of the measurement) in $\mathtt{S}_s^a$ with standard control (Experiment ($\mathrm{E}_{3.5,\mathrm{EESM}}$)), (iii) with improved AWU (Experiment ($\mathrm{E}_{3.6,\mathrm{EESM}}$)), (iv) with improved

[36] In this thesis, the trajectory for $\omega_m = 50\,\frac{\mathrm{rad}}{\mathrm{s}}$ is chosen.

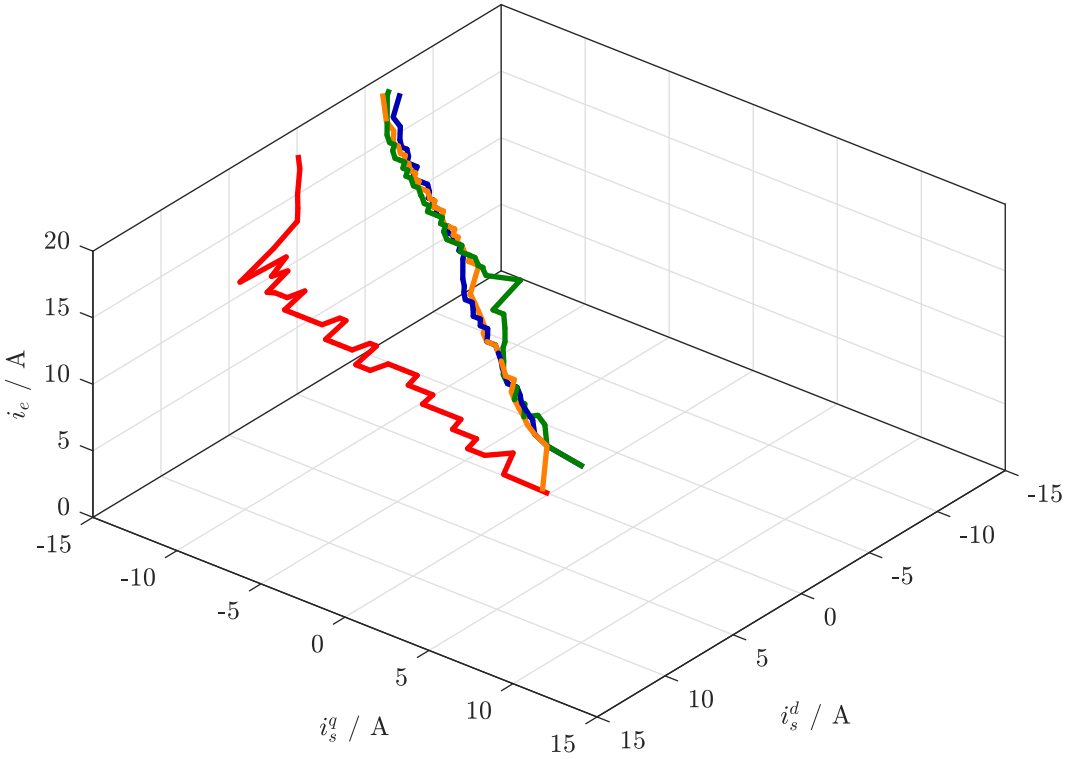

(a) Trajectories of fault-optimal current references for EESM.

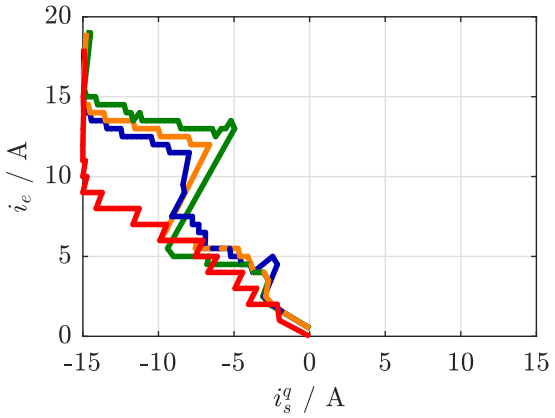

(b) Trajectories of fault-optimal current references for EESM (view: i_s^q-i_e-plain).

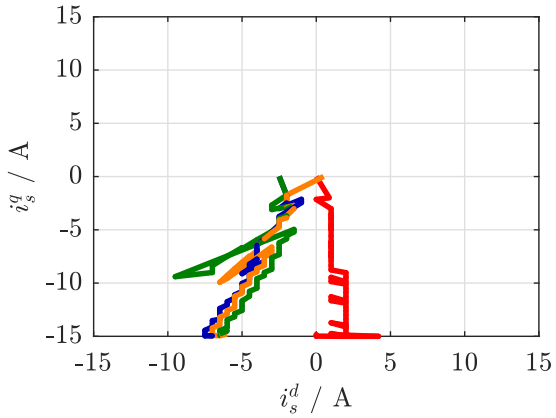

(c) Trajectories of fault-optimal current references for EESM (view: i_s^d-i_s^q-plain).

Figure 3.35: *Comparison of fault-optimal current references for feedforward torque control for open-switch fault in* $\mathtt{S}_s^a$ *for* — $\omega_m = 50\,\frac{\text{rad}}{\text{s}}$, — $\omega_m = 75\,\frac{\text{rad}}{\text{s}}$, — $\omega_m = 100\,\frac{\text{rad}}{\text{s}}$, *and* — *MTPC reference for EESMs in generator mode, i.e. negative torque.*

AWU and flat-top modulation (Experiment ($\text{E}_{3.7,\text{EESM}}$)) and (v) with improved AWU, flat-top modulation and fault-optimal current reference generation (Experiment ($\text{E}_{3.8,\text{EESM}}$)). The upper subplot shows the rotational speed ω_m of the drive train and its reference $\omega_{m,\text{ref}}$. The second subplot shows the torque τ_m. In the third, fourth and fifth subplot, the currents i_s^d, i_s^q and i_e and their references are shown, respectively. The lower subplot shows the *abc*-phase currents. Due to the open-switch fault, high oscillations in the torque of the EESM occur leading to high oscillations in the rotational speed between 2 s and 6 s. After that the torque ripples decrease

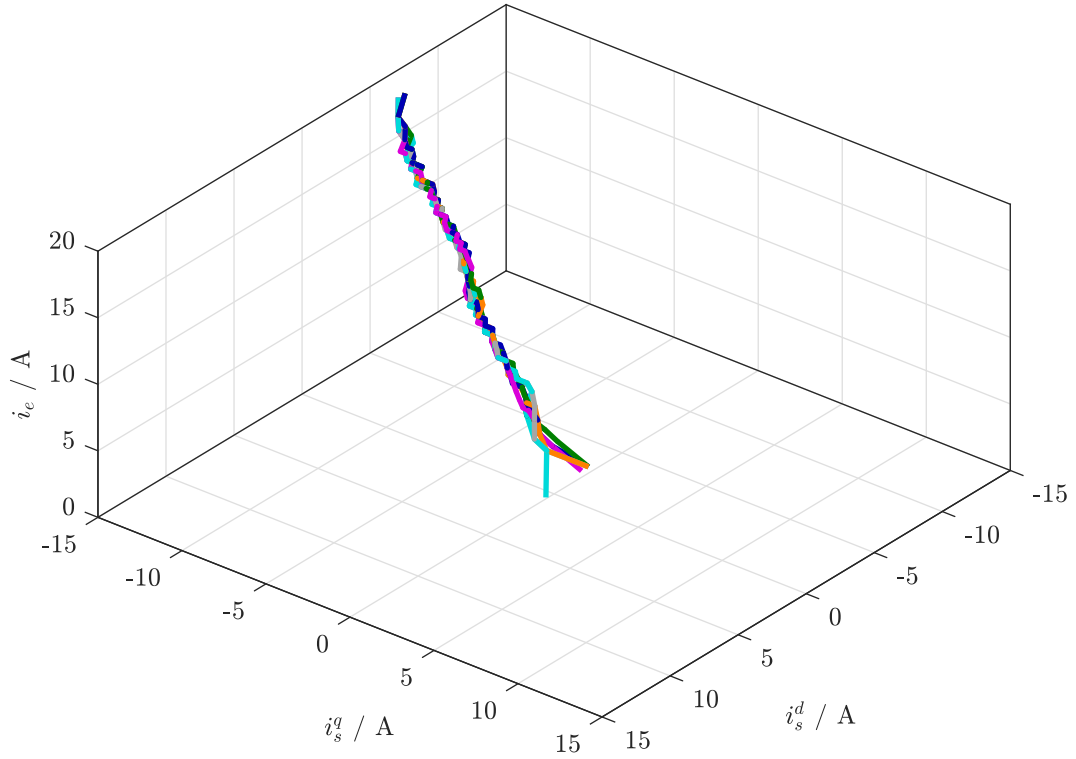

(a) Trajectory for EESM.

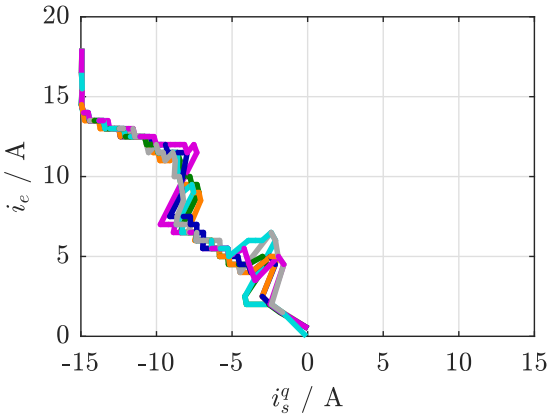

(b) Trajectory for EESM (view: i_s^q-i_e-plain).

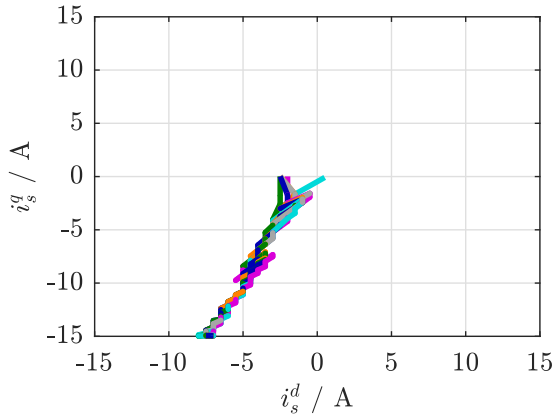

(c) Trajectory for EESM (view: i_s^d-i_s^q-plain).

Figure 3.36: *Comparison of fault-optimal current references for feedforward torque control for open-switch fault in* $\mathfrak{S}_s^a$, $\mathfrak{S}_s^b$, $\mathfrak{S}_s^c$, $\overline{\mathfrak{S}}_s^a$, $\overline{\mathfrak{S}}_s^b$ *or* $\overline{\mathfrak{S}}_s^c$ *for* $\omega_m = 50\,\frac{\text{rad}}{\text{s}}$ *and EESMs in generator mode, i.e. negative torque.*

and so do the ripples in speed. While the improved AWU shows only slight improvements on the control performance, the flat-top modulation makes a big difference ($\mathfrak{E}_{\tau_m,\text{meas}}$ reduces about 70 %). Finally, the fault-optimal current references reduce the relative error $\mathfrak{e}_{\tau_m,\text{meas}}$ below values of 2 %.

Summarizing, the EESM can be—although an open-switch fault is present—controlled to track a torque reference. Only small differences between fault free ([0 s, 2 s]) and faulty ([8 s, 10 s]) case are visible in ω_m and τ_m when the proposed post-fault control strategy is used.

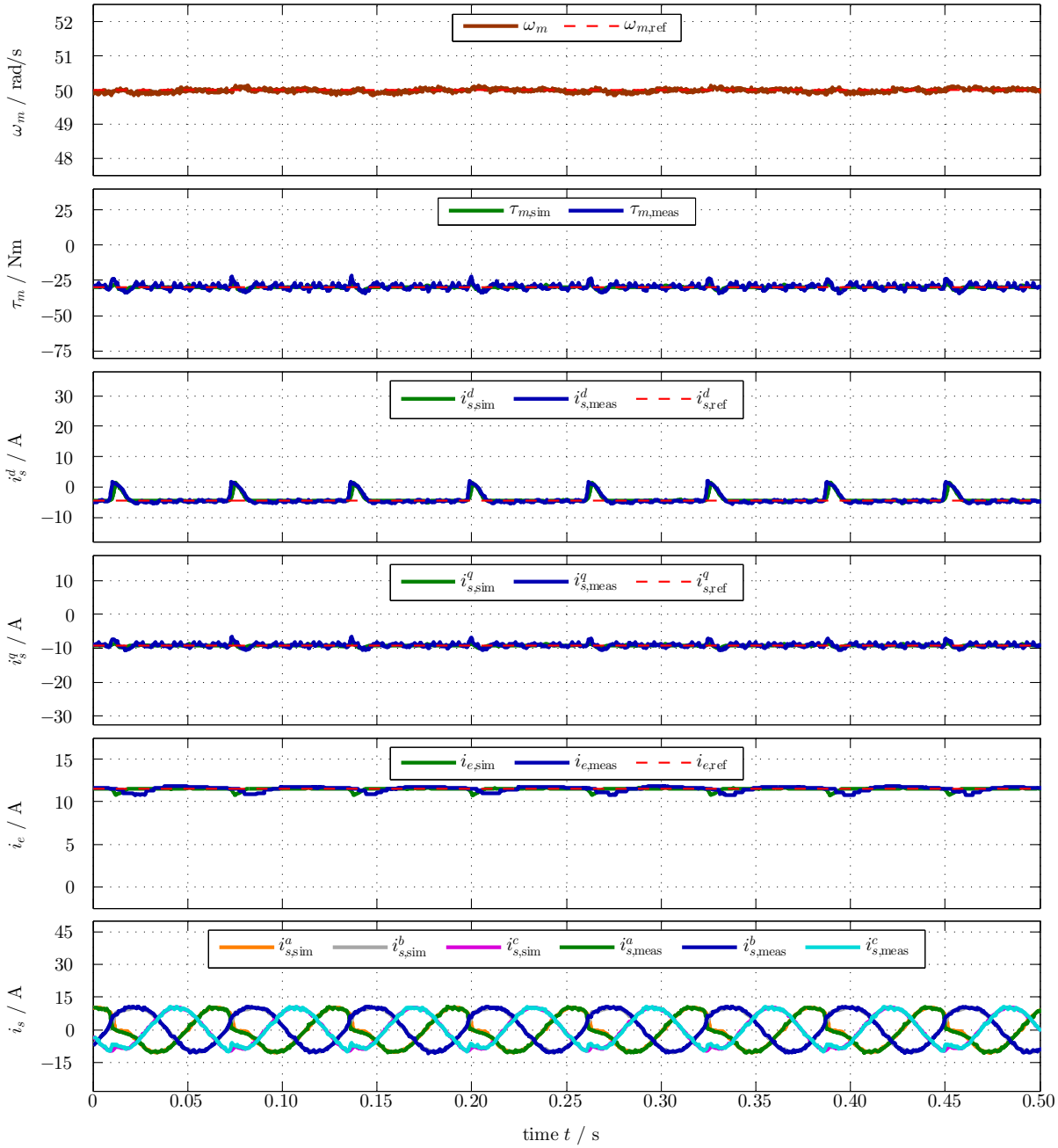

Figure 3.37: *Experiment* ($\mathrm{E}_{3.8,\mathrm{EESM}}$)*: Comparison of simulation and measurement results for an open-switch fault in* $\mathtt{S}_s^a$ *using improved AWU, modified SVM and fault-optimal current reference for EESM (*$\mathfrak{E}_{\tau_m,\mathrm{sim}} = 0.179\,\mathrm{N\,m}$ *and* $\mathfrak{E}_{\tau_m,\mathrm{meas}} = 0.479\,\mathrm{N\,m}$*).*

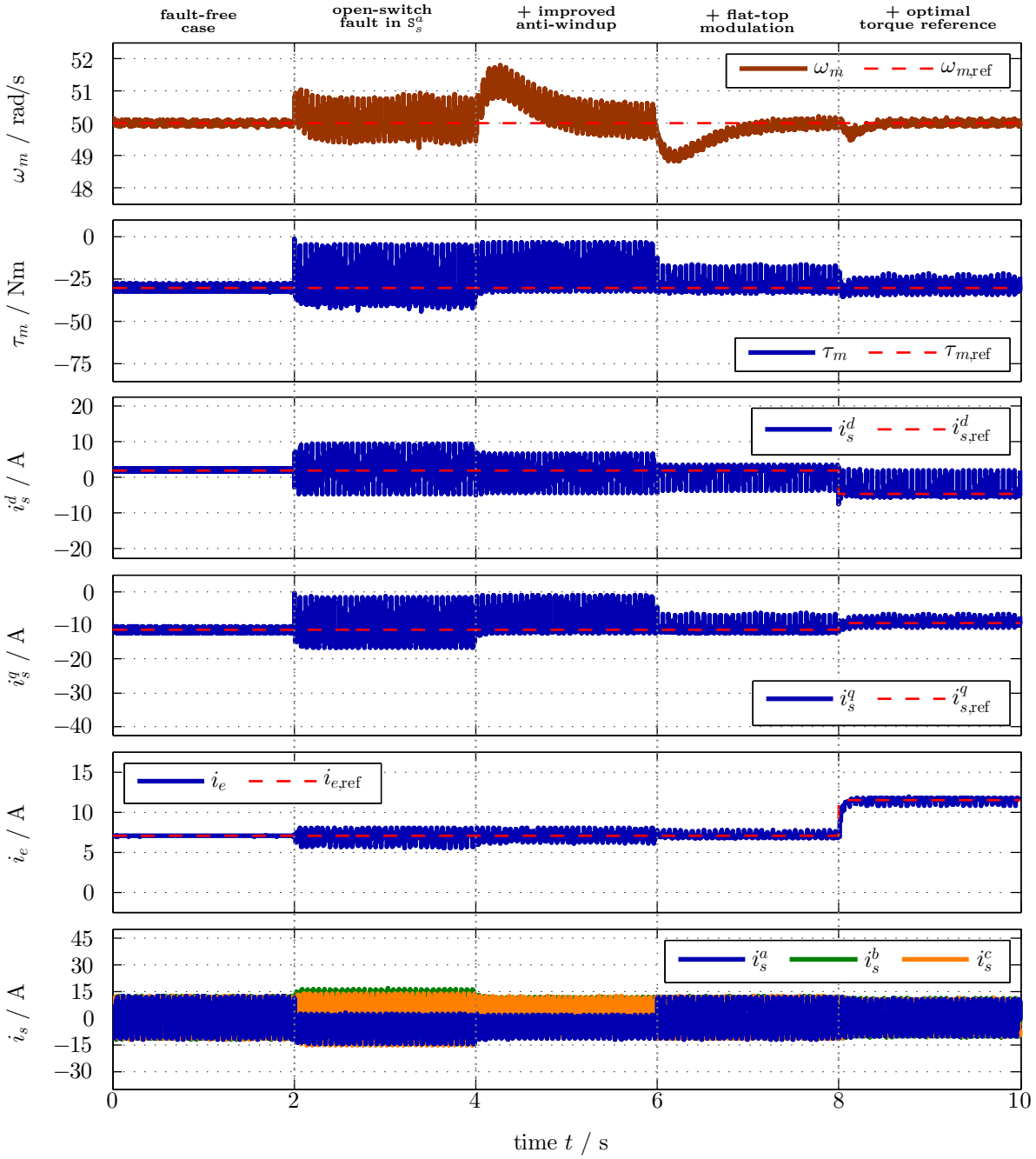

Figure 3.38: *Measurement results for current control performance during five different scenarios: (i) fault-free case, (ii) open-switch fault in* $\mathtt{S}_s^a$ ($\mathrm{E}_{3.5,\mathrm{EESM}}$)*, (iii) with extended AWU* ($\mathrm{E}_{3.6,\mathrm{EESM}}$)*, (iv) additionally with modified SVM* ($\mathrm{E}_{3.7,\mathrm{EESM}}$) *and (v) additionally with fault-optimal current reference* ($\mathrm{E}_{3.8,\mathrm{EESM}}$) *for EESM.*

Chapter 4

Post-fault control of wind turbine systems with open-switch converter faults

In this chapter, the positive impact of the proposed post-fault control strategy on the overall wind turbine system under an open-switch converter fault is illustrated by measurements. To be able to analyse this impact, the large-scale wind turbine system dynamics have to be scaled to the small-scale laboratory setup. Hence, after describing the overall laboratory setup, the scaling procedure is explained. The impacts of the post-fault control strategy on the overall WTS are discussed for PMSM and EESM, respectively.

4.1 Laboratory setup

To be able to understand the scaling process and all the adjustments for the specifics of the laboratory setup, it is necessary to introduce the available laboratory setup first. After giving an overview of the overall system, the setups for measurements with the PMSM and for measurements with the EESM are explained in detail.

4.1.1 Overview

The basic components of the laboratory setup are shown in Fig. 4.1:

- **Host-PC:** The Host-PC controls the real-time system and logs the measurement data (see Fig. 4.1, C).
- **dSPACE real-time system:** The real-time system evaluates the sensor signals, runs the control algorithms and outputs the switching signal $\boldsymbol{s}^{abc}$ to the converters (see Fig. 4.1, A).
- **Converter:** The converter applies the switching signals and produces an output voltage. The output is connected to an electric machine. The converter measures the output currents $\boldsymbol{i}^{abc}$ and the dc-link voltage u_{dc} (see Fig. 4.1, B1 and B2) and provides the data to the real-time system.
- **DC-source:** The dc-source is connected to the exciter of the EESM and applies the excitation voltage u_e. The measurements of the excitation voltage u_e and the excitation current i_e are made available to the real-time system.

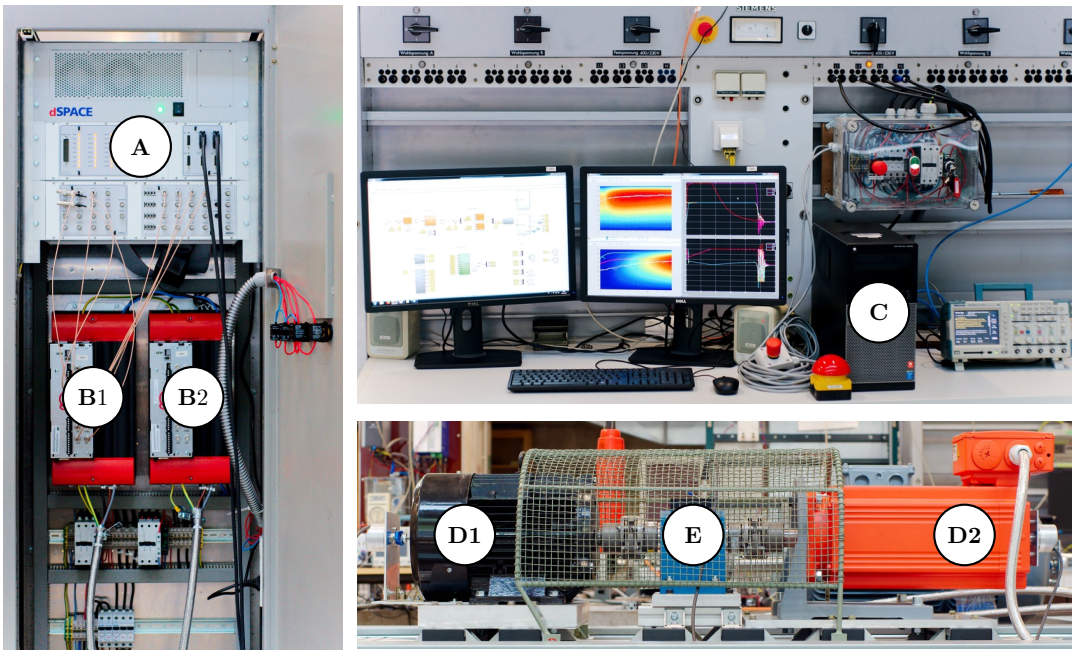

Figure 4.1: *Laboratory test-bench with dSPACE real-time system (A), voltage-source converter (B1) and (B2) connected back-to-back, Host-PC (C), reluctance synchronous machine (RSM; D1) and permanent magnet synchronous machine (PMSM; D2), and torque sensor (E).*

- **Drive trains:** There are two drive trains in the laboratory, that can be connected to the converters and the real-time system separately. In one drive train, a PMSM (see Fig. 4.1, D2) is coupled to a reluctance synchronous machine (RSM) (see Fig. 4.1, D1; for details see Sect. 4.1.2). At the other drive train, an EESM is coupled to a doubly-fed synchronous machine (DFIM) (for details see Sect. 4.1.3).

- **Torque sensor:** Each shaft, mechanically connecting two electric machines, is equipped with a torque sensor. The measured torque τ_{meas} is made available to the real-time system (see Fig. 4.1, E).

- **Encoder:** Each electric machine is equipped with an encoder. The measurement of angle φ_m of the position of the rotor and the angular velocity ω_m are made available to the real-time system.

The dSPACE real-time system is a time discrete, sampled system. The sample period of the processor of the real-time system is the switching period T_{sw} of the SVM (i.e. for $f_{\text{sw}} = 4\,\text{kHz} \rightarrow T_{\text{sw}} = 250\,\mu\text{s}$, see Sect. 3.2.1). The system executes the following steps in each sample period: (i) capturing of measurement signals, (ii) executing the control algorithms, (iii) making the output signals available to the connected devices. The reference voltages $\boldsymbol{u}_{\text{ref}}$ are handed over from the processor to the *Digital Waveform Output Board* (DS5101) of the dSPACE real-time system. The DS5101 has a faster sampling period (25 ns, see [117, p. 560]) to calculate and directly output the switching signals $\boldsymbol{s}^{abc}$ for the converter using the SVM algorithm derived in Sect. 3.2.1.1.

4.1.2 Power train with PMSM-RSM

A picture of the drive train, comprising PMSM and RSM, is shown on the lower right of Fig 4.1. Figure 4.2 depicts the electric connection of the drive train to the real-time system. Currents, angles, rotational speeds and the shaft torque are measured. The real-time system outputs reference voltages to the SVMs, that provide the switching signals to the converters.

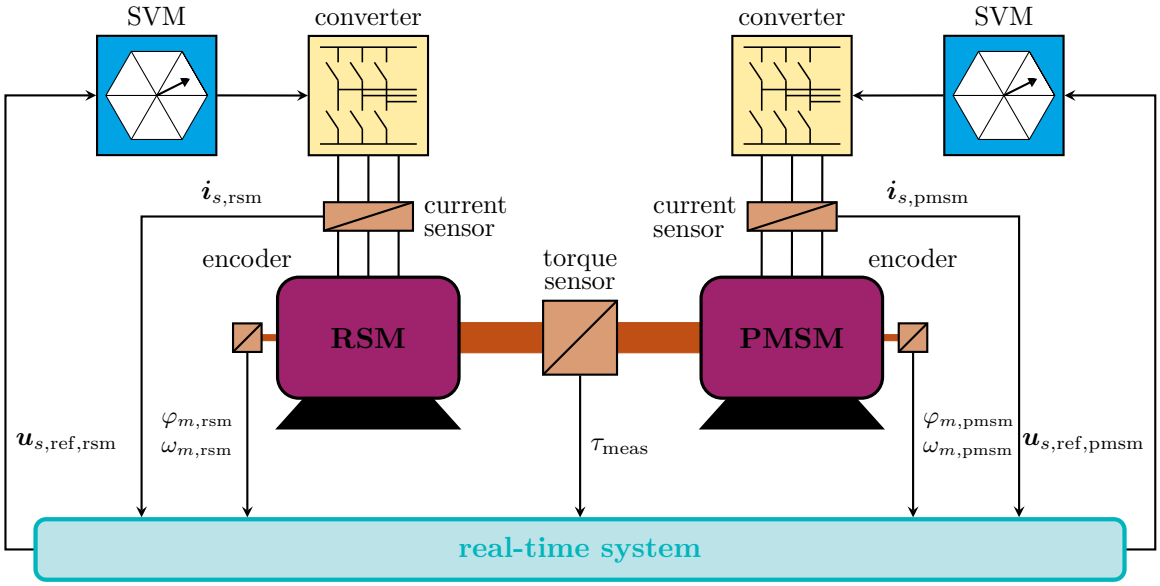

Figure 4.2: *Illustration of laboratory setup and connection with the real-time system for drive train PMSM-RSM.*

The drive train is affected by friction. For example for an accurate feedforward torque control, it is necessary to know the friction to be able to compensate for it (see Sect. 2.2). The friction of the drive train PMSM-RSM is depicted in Fig. 4.3. The total friction $\tau_{\mathrm{fric,tot}} := \tau_{\mathrm{fric,rsm}} + \tau_{\mathrm{fric,pmsm}}$ is the sum of the friction $\tau_{\mathrm{fric,rsm}}$ of the RSM and the friction $\tau_{\mathrm{fric,pmsm}}$ of the PMSM (all in N m). The parameters of the electric machines are shown in Table 4.1.

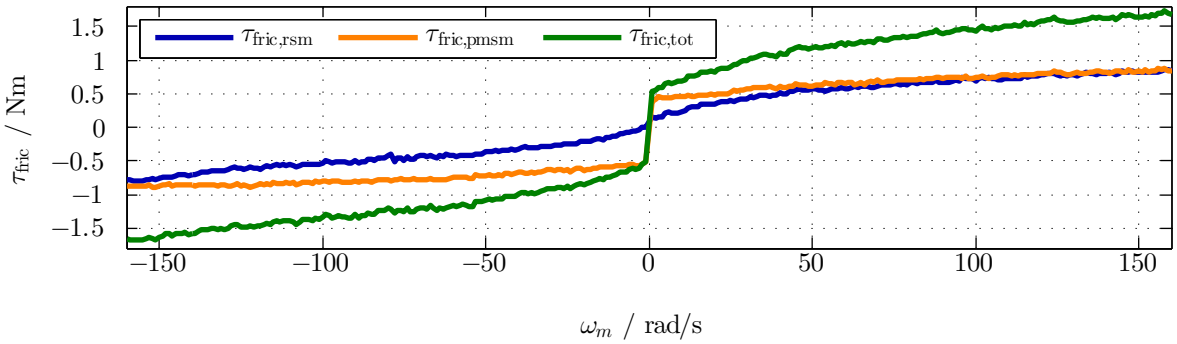

Figure 4.3: *Measured friction of laboratory drive train PMSM-RSM.*

4.1.3 Power train with EESM-DFIM

Figure 4.4 shows the drive train EESM-DFIM. Both machines are coupled with a torque sensor. Figure 4.5 depicts the electric connection of the drive train with the real-time system. Currents, angles, rotational speeds and the shaft torque are measured. The real-time system outputs

Table 4.1: *Parameters of PMSM and RSM.*

description	**symbol=value**
isotropic PMSM	
pole pairs	$n_p = 3$
stator resistance	$R_s = 0.15\,\Omega$
stator inductance	$L_s^d = L_s^q = 3.35 \cdot 10^{-3}\,\mathrm{H}$
PM-flux linkage	$\psi_{\mathrm{pm}} = 0.376\,5\,\mathrm{V\,s}$
machine inertia	$\Theta = 1.630 \cdot 10^{-2}\,\mathrm{kg\,m^2}$
nominal speed	$\omega_{\mathrm{nom}} = 209.4\,\frac{\mathrm{rad}}{\mathrm{s}}$
nominal machine power	$p_{\mathrm{nom}} = 14.5 \cdot 10^3\,\mathrm{W}$
nominal stator current	$\hat{i}_{s,\mathrm{nom}} = 46.7\,\mathrm{A}$
anisotropic RSM	
pole pairs	$n_p = 2$
stator resistance	$R_s = 0.4\,\Omega$
stator inductances	nonlinear (see [118, Fig. 2])
machine inertia	$\Theta = 1.890 \cdot 10^{-2}\,\mathrm{kg\,m^2}$
nominal speed	$\omega_{\mathrm{nom}} = 157.1\,\frac{\mathrm{rad}}{\mathrm{s}}$
nominal machine power	$p_{\mathrm{nom}} = 9.4 \cdot 10^3\,\mathrm{W}$
nominal stator current	$\hat{i}_{s,\mathrm{nom}} = 29.7\,\mathrm{A}$

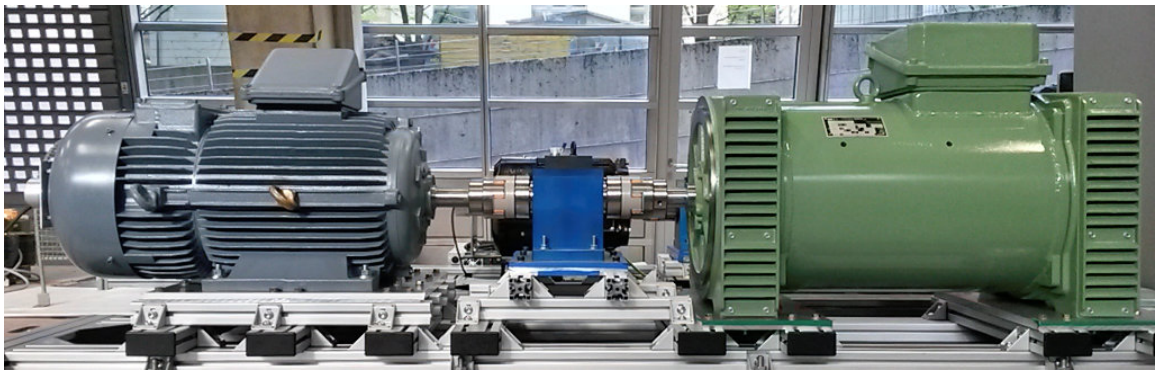

Figure 4.4: *Drive train with DFIM (left side) and EESM (right side) and torque sensor.*

reference voltages to the SVMs, that provide the switching signals for the converters and the dc-source, that outputs the excitation voltage. In the laboratory, rotor *and* stator of the DFIM are connected to a converter. Usually, the stator of a DFIM is directly connected to the grid. For the WTS emulation, the configuration with two converters is chosen in order to be able to use a wider speed-range as for direct grid connection.

Also this drive train is affected by friction. The friction of the EESM-DFIM drive train is depicted in Fig. 4.7. The total friction $\tau_{\mathrm{fric,tot}} := \tau_{\mathrm{fric,dfim}} + \tau_{\mathrm{fric,eesm}}$ is the sum of the friction $\tau_{\mathrm{fric,dfim}}$ of the DFIM and the friction $\tau_{\mathrm{fric,eesm}}$ of the EESM (all in N m). The "breaking torque" τ_{i_e} of the EESM is shown in Fig. 4.6. The parameters of these two electric machines are shown in Table 4.2.

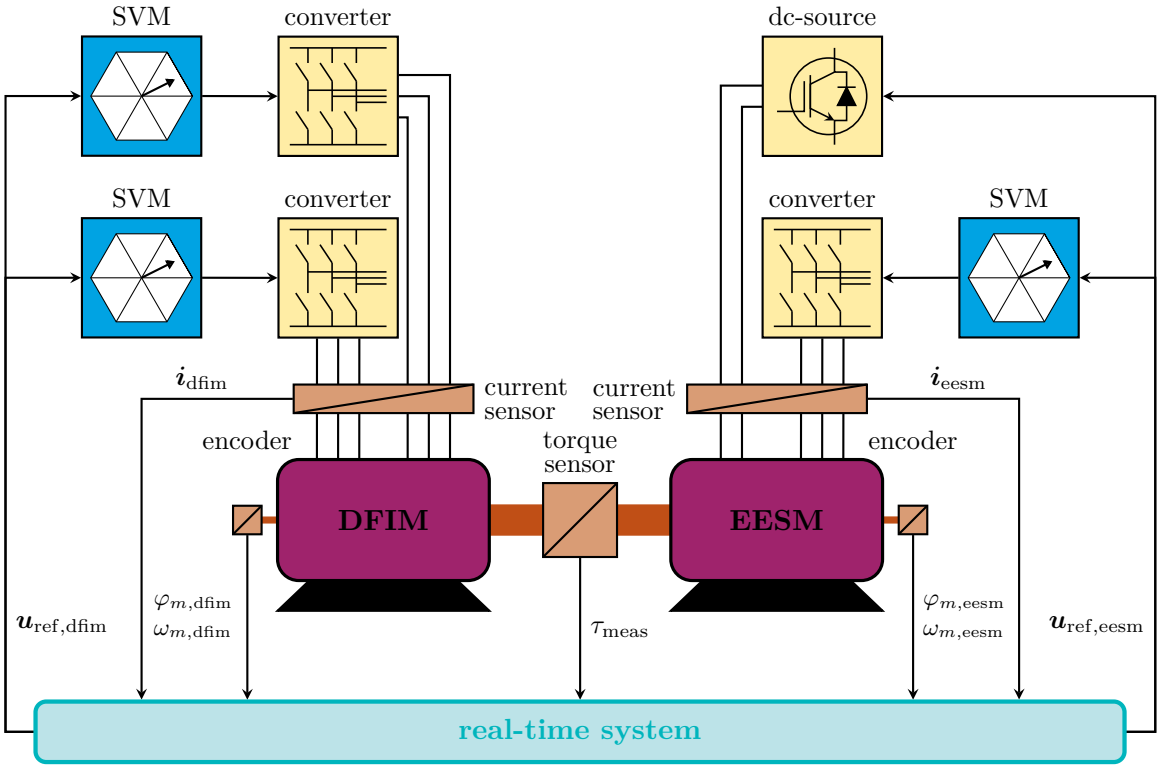

Figure 4.5: *Illustration of laboratory setup and connection with the real-time system for drive train EESM-DFIM.*

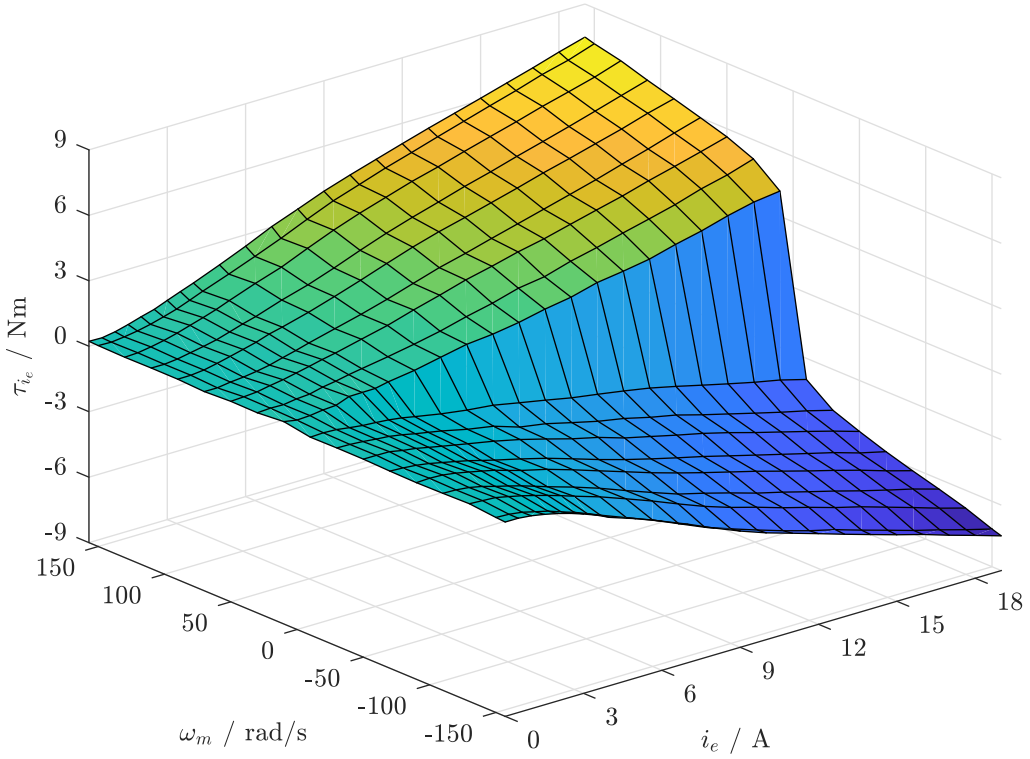

Figure 4.6: *"Breaking torque" τ_{i_e} depending on the rotational speed ω_m and the excitation current i_e.*

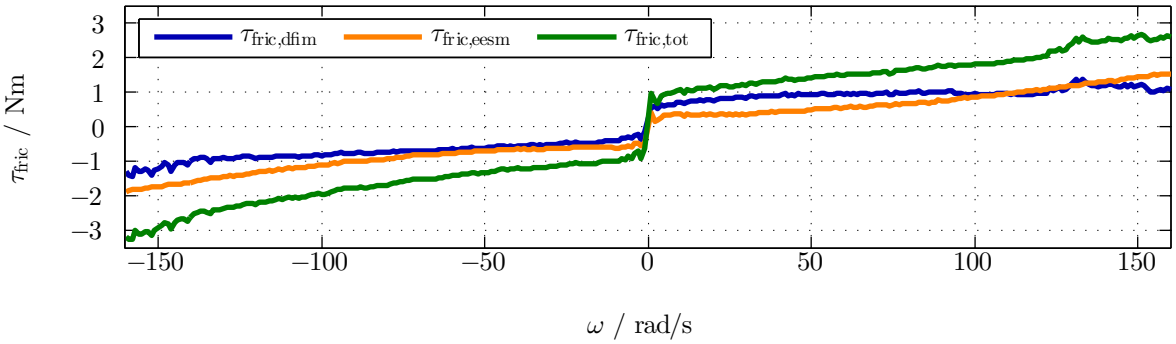

Figure 4.7: *Measured friction of laboratory drive train EESM-DFIM.*

Table 4.2: *Parameters of EESM and DFIM.*

description	**symbol=value**
anisotropic EESM	
pole pairs	$n_p = 2$
stator resistance	$R_s = 0.38\,\Omega$
excitation resistance	R_e nonlinear (see Fig. B.3)
inductances	nonlinear (see Sect. B)
machine inertia	$\Theta = 0.273\,\text{kg}\,\text{m}^2$
nominal speed	$\omega_{\text{nom}} = 157.1\,\frac{\text{rad}}{\text{s}}$
nominal machine power	$p_{\text{nom}} = 10 \cdot 10^3\,\text{W}$
nominal stator current	$\hat{i}_{s,\text{nom}} = 29.7\,\text{A}$
nominal excitation current	$i_{e,\text{nom}} = 19\,\text{A}$
isotropic DFIM	
pole pairs	$n_p = 2$
stator resistance	$R_s = 0.72\,\Omega$
excitation resistance	$R_r = 0.55\,\Omega$
inductances	nonlinear
machine inertia	$\Theta = 9.37 \cdot 10^{-2}\,\text{kg}\,\text{m}^2$
nominal speed	$\omega_{\text{nom}} = 157.1\,\frac{\text{rad}}{\text{s}}$
nominal machine power	$p_{\text{nom}} = 10 \cdot 10^3\,\text{W}$
nominal stator current	$\hat{i}_{s,\text{nom}} = 29.6\,\text{A}$
nominal rotor current	$\hat{i}_{r,\text{nom}} = 24.0\,\text{A}$

4.2 Scaling of wind turbine system dynamics to small-scale laboratory setups

This section is partially based on [1] where the scaling method is already validated for wind turbine systems. In [1], a turbine with flexible shaft and gear box is investigated. Here, as the focus is on direct-drive WTS, the turbine shaft is modelled rigid and without gear box (see Sect. 2.2). The objective is to emulate a large-scale WTS at a small-scale laboratory setup, by using two mechanically coupled machines. One laboratory machine is used to emulate the turbine behaviour (subscript $\square_{m_t}$); the other laboratory machine emulates the machine/generator of a WTS (subscript $\square_{m_m}$), see Fig 4.8.
To explain the scaling process, first the state-space model of the large-scale WTS is presented. After that, the scaling process is explained step-by-step. The scaling based on the ratios of phy-

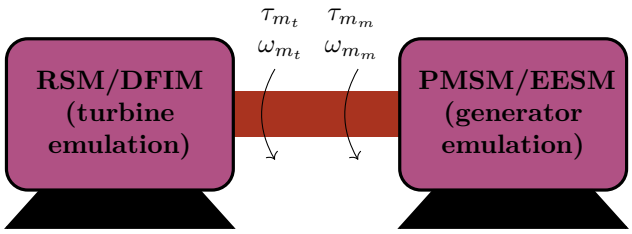

Figure 4.8: *Laboratory test-bench for emulation of the WTS by using a scaled WTS model.*

sical SI-units is introduced and the necessity and the design of the virtual gear box is explained. The SI-unit scaling and the relations of the virtual gear box are summarized in the scaling of the state-space model of the WTS drive train. At the end of this section, necessary adaptations regarding the laboratory setup are discussed.

4.2.1 Modelling of the power train of the large-scale WTS

The dynamics of the drive train of the large-scale direct-drive WTS, as introduced in (2.6), can be written compactly as state-space model

$$\left.\begin{aligned} \tfrac{\mathrm{d}}{\mathrm{d}t}\boldsymbol{x}_K &= \boldsymbol{A}_K\,\boldsymbol{x}_K + \boldsymbol{b}_K\,u_K + \boldsymbol{h}_K\,w_K \\ \boldsymbol{y}_K &= \boldsymbol{x}_K \end{aligned}\right\} \tag{4.1}$$

where

$$\left.\begin{aligned} \boldsymbol{x}_K &= \begin{pmatrix} \omega_T \\ \varphi_T \end{pmatrix}, \quad u_K = \tau_M, \\ w_K &:= \tau_T(v_W, \omega_T, \beta) - f_T(\omega_T), \\ \boldsymbol{A}_K &= \begin{bmatrix} -\frac{\nu_T}{\Theta_T+\Theta_M} & 0 \\ 1 & 0 \end{bmatrix}, \\ \boldsymbol{b}_K &= \begin{pmatrix} \frac{1}{\Theta_T+\Theta_M} \\ 0 \end{pmatrix}, \; \boldsymbol{h}_K = \begin{pmatrix} \frac{1}{\Theta_T+\Theta_M} \\ 0 \end{pmatrix}, \end{aligned}\right\} \tag{4.2}$$

are the state vector, the system input (machine/generator torque), the disturbance (including turbine torque τ_T and nonlinear friction $f_T(\omega_T)$), the system matrix, the input vector and the disturbance-input vector, respectively. The initial values of the state vector are given by $\boldsymbol{x}_K(0) = (\omega_{T,0},\, \varphi_{T,0})^\top$. The physical quantities in (4.2) represent turbine inertia Θ_T and machine inertia Θ_M (both in $\mathrm{kg\,m^2}$), turbine viscous friction coefficient ν_T, turbine angular velocity ω_T, turbine torque τ_T and machine/generator torque τ_M. The overall friction torque $\tau_{T,\mathrm{fric}} := \nu_T\omega_T + f_T(\omega_T)$ (in $\mathrm{N\,m}$) comprises linear viscous friction and nonlinear friction, respectively (more details on nonlinear friction modelling can be found in [51, Sect. 11.1.5]).

4.2.2 Scaling based on ratios of SI-units

The steps of the scaling process are shown in Fig. 4.9 and will be explained below in detail. The scaling can be divided into for layers (with four types of quantities):

(i) the *large-scale turbine system*, denoted by the index written as capital letter, e.g. $\square_K$ (e.g. large-scale turbine inertia Θ_T or large-scale turbine torque τ_T),

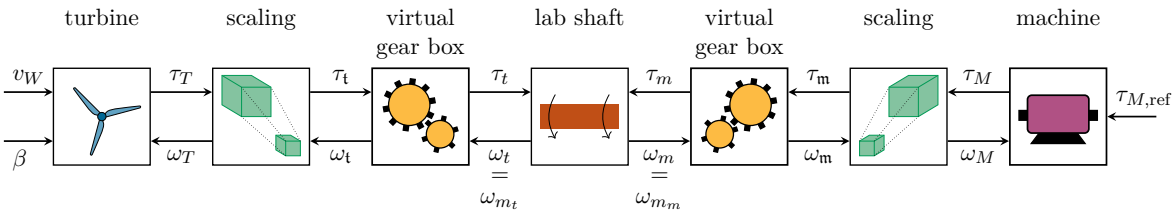

Figure 4.9: *Overview of the scaling of the wind turbine system for the implementation in the laboratory.*

(ii) the *small-scale turbine without referring*[37], denoted by the index written as a black letter minuscule, e.g. $\square_\mathfrak{t}$ (e.g. small-scale turbine inertia $\Theta_\mathfrak{t}$ without referring[38] or small-scale turbine torque $\tau_\mathfrak{t}$ without referring),

(iii) the *small-scale turbine system*, denoted by the index written as minuscule, e.g. $\square_k$ (e.g. small-scale turbine inertia Θ_t or small-scale turbine torque τ_t) and

(iv) the *laboratory setup*, denoted by the index written as minuscule with subscript, e.g. $\square_{k_y}$ (e.g. inertia Θ_{m_t} of the laboratory machine emulating the turbine or torque τ_{m_t} of the laboratory machine emulating the turbine).

Remark 4.2.1. *It is necessary to distinguish between layer (iii) and layer (iv), as the down-scaled turbine inertia Θ_t does not necessarily equal the inertia Θ_{m_t} of the laboratory machine emulating the turbine (e.g. for the drive train PMSM-RSM $\Theta_t = 3.24\,\mathrm{kg\,m^2}$ does not equal $\Theta_{m_t} = 1.89 \cdot 10^{-2}\,\mathrm{kg\,m^2}$). Also the torques τ_t and τ_{m_t} are different. For a proper WTS emulation in the laboratory, the torque τ_{m_t} of the laboratory machine emulating the turbine must, among other things, compensate for the friction of the laboratory drive train. Details on these necessary adaptations will be given in Sect. 4.2.5.*

Figure 4.9 shows the overview of the overall scaling process. The output quantities of the large-scale WTS model, turbine torque τ_T and machine torque τ_M are down-scaled to the small-scale WTS emulation. The down-scaled torques τ_t and τ_m are applied to the laboratory shaft[39]. The resulting rotational speeds ω_t and ω_m are up-scaled to the large-scale WTS and fed into the turbine model and machine model, respectively. Details on each step of the scaling process, the derivation of the scaling factors and the design of the virtual gear box are given in the following paragraphs. First the scaling based on the ratios of physical SI-units is explained in detail.
In [119], the principle idea of scaling of physically similar systems based on the ratios of physical SI-units is introduced. In [79], this method is adapted for the scaling of the aerodynamics of wind turbines for small-scale experiments in the wind tunnel.
The basic idea of scaling to a physically similar system is:

(i) Deriving scaling factors for the three SI-units *meter* m, *kilogram* kg, *second* s based on the desired scaling of (in this case) the *air density* ρ, *time* t and *power* p.

(ii) Using the resulting scaling factors for the SI-units to scale all the other physical quantities (based on their units, as a combination of three basic SI-units).

[37] This intermediate layer is only introduced to ease understanding by allowing for a step-by-step explanation of the scaling process. The necessity of the virtual gear box will be explained in detail in Sect. 4.2.3

[38] The "referred" quantity describes the value of the quantity on the other side of a gear box.

[39] More precisely, τ_{m_t} and τ_{m_m} are applied to the laboratory shaft and include τ_t and τ_m, respectively. But also necessary compensation torques and emulation torques are included in τ_{m_t} and τ_{m_m} (for details see Sect. 4.2.5 or Fig. 4.11 for the PMSM-RSM drive train or Fig. 4.14 for the EESM-DFIM drive train).

For the following, three assumptions[40] are imposed:

Assumption (AS.16) *To be able to use the c_P-curve of the large-scale WTS also for the small-scale system, the air density ρ_K of the large-scale turbine and the air density $\rho_\mathfrak{k}$ (both in $\frac{\mathrm{kg}}{\mathrm{m}^3}$) of the small-scale version have to be identical, i.e.*

$$\rho_K = \rho_\mathfrak{k} = \rho_k \quad \Rightarrow \quad \mu_\rho := \frac{\rho_\mathfrak{k}}{\rho_K} = \frac{\rho_k}{\rho_K} = 1\,. \tag{4.3}$$

Assumption (AS.17) *To keep the available computational time for the controller of the small-scale model the same as for the controller of the large-scale turbine, the time t_K of the large-scale turbine and the time $t_\mathfrak{k}$ (both in* s*) of the small-scale counterpart have to be identical, i.e.*

$$t_K = t_\mathfrak{k} = t_k \quad \Rightarrow \quad \mu_{\mathrm{time}} := \frac{t_\mathfrak{k}}{t_K} = \frac{t_k}{t_K} = 1\,. \tag{4.4}$$

Assumption (AS.18) *The power scaling factor μ_p is defined as the relation between the nominal power $p_{T,\mathrm{nom}}$ of the large-scale turbine and the nominal power $p_{\mathfrak{t},\mathrm{nom}}$ (both in $\frac{\mathrm{kg\,m^2}}{\mathrm{s}^3}$) of the small-scale model, i.e.*

$$\mu_p := \frac{p_{\mathfrak{t},\mathrm{nom}}}{p_{T,\mathrm{nom}}} = \frac{p_{t,\mathrm{nom}}}{p_{T,\mathrm{nom}}}. \tag{4.5}$$

All relevant mechanical parameters can be expressed as a combination of the three SI-units *meter* m, *kilogram* kg, *second* s. Taking this and Assumptions (AS.16)-(AS.18) into account, the scaling factors for these three units can be computed as follows

$$\mu_\mathrm{m} := \frac{\mathrm{m}_\mathfrak{k}}{\mathrm{m}_K}, \quad \mu_\mathrm{kg} := \frac{\mathrm{kg}_\mathfrak{k}}{\mathrm{kg}_K}, \quad \mu_\mathrm{s} := \frac{\mathrm{s}_\mathfrak{k}}{\mathrm{s}_K}. \tag{4.6}$$

The three scaling factors in (4.6) are *meter* scaling factor μ_m, *kilogram* scaling factor μ_kg and *second* scaling factor μ_s and allow to relate the physical quantities of large-scale and small-scale system as will be shown next.

Expressing the scaling factors of Assumptions (AS.16)-(AS.18), density scaling factor μ_ρ, time scaling factor μ_{time} and power scaling factor μ_p by the scaling factors of the SI-units

$$\mu_\rho = \frac{\mu_\mathrm{kg}}{\mu_\mathrm{m}^3} \overset{\text{(AS.16)}}{=} 1, \quad \mu_{\mathrm{time}} = \mu_\mathrm{s} \overset{\text{(AS.17)}}{=} 1, \quad \mu_p = \frac{\mu_\mathrm{kg}\mu_\mathrm{m}^2}{\mu_\mathrm{s}^3} \tag{4.7}$$

leads to

$$\mu_\mathrm{kg} = \mu_\mathrm{m}^3 \quad \text{and} \quad \mu_\mathrm{s} = 1 \tag{4.8}$$

and the scaling factors of the SI-units are related as follows

$$\mu_\mathrm{m} = (\mu_p)^{\frac{1}{5}}\,, \quad \mu_\mathrm{kg} = (\mu_p)^{\frac{3}{5}}\,, \quad \mu_\mathrm{s} = 1, \tag{4.9}$$

and depend only on the power scaling factor μ_p.

Combining all this information allows to scale the relevant physical quantities based on their SI-units:

[40] As the virtual gear box is invariant regarding air density, time and power, the small-scale values $\square_\mathfrak{k}$ without referring or the small-scale values $\square_k$ can be used for the scaling process.

- angle φ (in rad)
$$\mu_\varphi := \frac{\varphi_{\mathfrak{k}}}{\varphi_K} \overset{(4.9)}{=} 1 \tag{4.10}$$

- rotational speed ω (in $\frac{\text{rad}}{\text{s}}$)
$$\mu_\omega := \frac{\omega_{\mathfrak{k}}}{\omega_K} = \frac{1}{\mu_\text{s}} \overset{(4.9)}{=} 1 \tag{4.11}$$

- velocity v (in $\frac{\text{m}}{\text{s}}$)
$$\mu_v := \frac{v_{\mathfrak{k}}}{v_K} = \frac{\mu_\text{m}}{\mu_\text{s}} \overset{(4.9)}{=} (\mu_p)^{\frac{1}{5}} \tag{4.12}$$

- torque τ (in $\frac{\text{kg}\,\text{m}^2}{\text{s}^2}$)
$$\mu_\tau := \frac{\tau_{\mathfrak{k}}}{\tau_K} = \frac{\mu_\text{kg}\mu_\text{m}^2}{\mu_\text{s}^2} \overset{(4.9)}{=} \mu_p \tag{4.13}$$

- inertia Θ (in $\text{kg}\,\text{m}^2$)
$$\mu_\Theta := \frac{\Theta_{\mathfrak{k}}}{\Theta_K} = \mu_\text{kg}\mu_\text{m}^2 \overset{(4.9)}{=} \mu_p \tag{4.14}$$

- length l (in m)
$$\mu_l := \frac{l_{\mathfrak{k}}}{l_K} = \mu_\text{m} \overset{(4.9)}{=} (\mu_p)^{\frac{1}{5}} \tag{4.15}$$

- time t (in s)
$$\mu_\text{time} := \frac{t_{\mathfrak{k}}}{t_K} = \mu_\text{s} \overset{(4.9)}{=} 1, \tag{4.16}$$

with angle scaling factor μ_φ, angular velocity scaling factor μ_ω, velocity scaling factor μ_v, torque scaling factor μ_τ, inertia scaling factor μ_Θ, length scaling factor μ_l and time scaling factor μ_time, respectively.

4.2.3 Virtual gear box

The electric machines used as generators in wind turbines are designed according to the nominal values of the wind turbine. To account for that[41] in the small-scale model, a "virtual" machine gear ratio

$$\begin{aligned} g_\text{virt} := \frac{\omega_{m_t,\text{nom}}}{\omega_{\mathfrak{t},\text{nom}}} = \frac{\varphi_t}{\varphi_{\mathfrak{t}}} = \frac{\omega_t}{\omega_{\mathfrak{t}}} = \frac{\tau_{\mathfrak{t}}}{\tau_t} = \sqrt{\frac{\Theta_{\mathfrak{t}}}{\Theta_t}} \\ = \frac{\varphi_m}{\varphi_{\mathfrak{m}}} = \frac{\omega_m}{\omega_{\mathfrak{m}}} = \frac{\tau_{\mathfrak{m}}}{\tau_m} = \sqrt{\frac{\Theta_{\mathfrak{m}}}{\Theta_m}} \end{aligned} \tag{4.17}$$

must be introduced to fit nominal speed $\omega_{\mathfrak{t},\text{nom}}$ (in $\frac{\text{rad}}{\text{s}}$) of the scaled turbine and nominal speed $\omega_{m_t,\text{nom}}$ (in $\frac{\text{rad}}{\text{s}}$) of the turbine emulating electric machines[42] in the laboratory (see Fig. 4.8 and Fig. 4.9). The virtual gear box ratio g_virt achieves, that the generator of the large-scale WTS and the machines emulating the WTS in the laboratory setup operate at the same relative speed with respect to their nominal speed. E.g. if the turbine of the large-scale model operates

[41] The number $n_p = 48$ of pole pairs of the PMSM in the large-scale WTS differs significantly from the number $n_p = 3$ of pole pairs of the PMSM in the laboratory. So a proper referring is inevitable.

[42] Here, both nominal speeds ω_{m_t} or ω_{m_m} can be used. For reasonable results, always the value for the machine with the least nominal speed should be chosen. In the laboratory setup, for the drive train RSM-PMSM, the nominal speed of the turbine emulating machine (RSM, see Fig. 4.8) is the limiting quantity. Hence, the virtual gear ratio is chosen accordingly by using this parameter (see Tab. 4.4). So for the given setup, the RSM operates at e.g. 95 % of its nominal speed whereas the PMSM operates at 71 % of its nominal speed.

at 95 % nominal speed, the electric machines emulating the WTS in the small-scale laboratory setup operate at the utmost at 95 % of their nominal speed.

Hence, the inertias, torques, angular speeds and angles of the wind turbine are scaled by the virtual gear box ratio g_{virt} to match all quantities to the small-scale setup (see Fig. 4.9) as follows

$$\Theta_t := \frac{1}{g_{\text{virt}}^2}\Theta_{\mathfrak{t}} \overset{(4.14)}{=} \frac{\mu_\Theta}{g_{\text{virt}}^2}\Theta_T \tag{4.18}$$

$$\tau_t := \frac{1}{g_{\text{virt}}}\tau_{\mathfrak{t}} \overset{(4.13)}{=} \frac{\mu_\tau}{g_{\text{virt}}}\tau_T \tag{4.19}$$

$$\omega_t := g_{\text{virt}}\omega_{\mathfrak{t}} \overset{(4.11)}{=} g_{\text{virt}}\mu_\omega\omega_T \tag{4.20}$$

$$\varphi_t := g_{\text{virt}}\varphi_{\mathfrak{t}} \overset{(4.10)}{=} g_{\text{virt}}\mu_\varphi\varphi_T \tag{4.21}$$

$$\Theta_m := \frac{1}{g_{\text{virt}}^2}\Theta_{\mathfrak{m}} \overset{(4.14)}{=} \frac{\mu_\Theta}{g_{\text{virt}}^2}\Theta_M \tag{4.22}$$

$$\tau_m := \frac{1}{g_{\text{virt}}}\tau_{\mathfrak{m}} \overset{(4.13)}{=} \frac{\mu_\tau}{g_{\text{virt}}}\tau_M \tag{4.23}$$

$$\omega_m := g_{\text{virt}}\omega_{\mathfrak{m}} \overset{(4.11)}{=} g_{\text{virt}}\mu_\omega\omega_M \tag{4.24}$$

$$\varphi_m := g_{\text{virt}}\varphi_{\mathfrak{m}} \overset{(4.10)}{=} g_{\text{virt}}\mu_\varphi\varphi_M \tag{4.25}$$

with virtual gear box ratio g_{virt}, small-scale turbine inertia Θ_t (in $\mathrm{kg\,m^2}$), small-scale turbine inertia $\Theta_{\mathfrak{t}}$ (in $\mathrm{kg\,m^2}$) without referring, large-scale turbine inertia Θ_T (in $\mathrm{kg\,m^2}$), small-scale turbine torque τ_t (in $\mathrm{N\,m}$), small-scale turbine torque $\tau_{\mathfrak{t}}$ (in $\mathrm{N\,m}$) without referring, large-scale turbine torque τ_T (in $\mathrm{N\,m}$), small-scale turbine speed ω_t (in $\frac{\mathrm{rad}}{\mathrm{s}}$), small-scale turbine speed $\omega_{\mathfrak{t}}$ (in $\frac{\mathrm{rad}}{\mathrm{s}}$) without referring, large-scale turbine speed ω_T (in $\frac{\mathrm{rad}}{\mathrm{s}}$), small-scale turbine angle φ_t (in rad), small-scale turbine angle $\varphi_{\mathfrak{t}}$ (in rad) without referring, large-scale turbine angle φ_T (in rad), small-scale machine inertia Θ_m (in $\mathrm{kg\,m^2}$), small-scale machine inertia $\Theta_{\mathfrak{m}}$ (in $\mathrm{kg\,m^2}$) without referring, large-scale machine inertia Θ_M (in $\mathrm{kg\,m^2}$), small-scale machine torque τ_m (in $\mathrm{N\,m}$), small-scale machine torque $\tau_{\mathfrak{m}}$ (in $\mathrm{N\,m}$) without referring, large-scale machine torque τ_M (in $\mathrm{N\,m}$), small-scale machine speed ω_m (in $\frac{\mathrm{rad}}{\mathrm{s}}$), small-scale machine speed $\omega_{\mathfrak{m}}$ (in $\frac{\mathrm{rad}}{\mathrm{s}}$) without referring, large-scale machine speed ω_M (in $\frac{\mathrm{rad}}{\mathrm{s}}$), small-scale machine angle φ_m (in rad), small-scale machine angle $\varphi_{\mathfrak{m}}$ (in rad) without referring, large-scale machine angle φ_M (in rad), inertia scaling factor μ_Θ, torque scaling factor μ_τ, angular velocity scaling factor μ_ω and angle scaling factor μ_φ.

Remark 4.2.2. *As example, the scaling of the turbine inertia Θ_T is performed for the PMSM-RSM drive train. The large-scale turbine inertia is $\Theta_T = 8.6 \cdot 10^6\,\mathrm{kg\,m^2}$ (see Tab. 4.3). The small-scale turbine inertia without referring calculates to $\Theta_{\mathfrak{t}} = \mu_\Theta\Theta_T = 21.5 \cdot 10^3\,\mathrm{kg\,m^2}$. Referring by the virtual gear box leads to the small-scale turbine inertia $\Theta_t = \frac{\Theta_{\mathfrak{t}}}{g_{\text{virt}}^2} = 3.24\,\mathrm{kg\,m^2}$. The inertia of the turbine emulating electrical machine in the laboratory (RSM) is $\Theta_{m_t} = 1.89 \cdot 10^{-2}\,\mathrm{kg\,m^2}$ (see Tab. 4.4).*

4.2.4 Scaling of the state-space drive train model

Using (4.10)-(4.25), the state-space model of the large-scale WTS drive train with state vector $\boldsymbol{x}_K$, system input u_K, system output $\boldsymbol{y}_K$ and disturbance w_K can be scaled to the state-space

model of the small-scale WTS drive train by the following linear transformation

$$\underbrace{\begin{pmatrix}\omega_t\\ \varphi_t\end{pmatrix}}_{:=\boldsymbol{x}_k} = \underbrace{\begin{bmatrix}\mu_\omega g_{\text{virt}} & 0\\ 0 & \mu_\varphi g_{\text{virt}}\end{bmatrix}}_{:=\boldsymbol{\Gamma}_1} \underbrace{\begin{pmatrix}\omega_T\\ \varphi_T\end{pmatrix}}_{:=\boldsymbol{x}_K} \tag{4.26}$$

$$\underbrace{\tau_m}_{:=u_k} = \underbrace{\frac{\mu_\tau}{g_{\text{virt}}}}_{:=\Gamma_2} \underbrace{\tau_M}_{:=u_K}, \quad w_k = \underbrace{\frac{\mu_\tau}{g_{\text{virt}}}}_{:=\Gamma_3} w_K \tag{4.27}$$

where

$$w_k := \tau_t(v_W, \omega_T, \beta) + f_t(\omega_T) \tag{4.28}$$

$$w_K := \tau_T(v_W, \omega_T, \beta) + f_T(\omega_T). \tag{4.29}$$

Inserting this into (4.1) results in the *small-scale* state-space representation

$$\left.\begin{aligned}\tfrac{\mathrm{d}}{\mathrm{d}t}\boldsymbol{x}_k &= \overbrace{\boldsymbol{\Gamma}_1\boldsymbol{A}_K\boldsymbol{\Gamma}_1^{-1}}^{\boldsymbol{A}_k}\boldsymbol{x}_k + \overbrace{\boldsymbol{\Gamma}_1\boldsymbol{b}_K\Gamma_2^{-1}}^{\boldsymbol{b}_k}u_k + \overbrace{\boldsymbol{\Gamma}_1\boldsymbol{h}_K\Gamma_3^{-1}}^{\boldsymbol{h}_k}w_k\\ \boldsymbol{y}_k &= \boldsymbol{x}_k.\end{aligned}\right\} \tag{4.30}$$

of the drive train with small-scale system matrix $\boldsymbol{A}_k$, small-scale input vector $\boldsymbol{b}_k$ and small-scale disturbance vector $\boldsymbol{h}_k$.

4.2.5 Adaptations for laboratory setup

Some parameters (inertias and friction) of the laboratory setup do *not* match the down-scaled WTS (4.30). Therefore, inertias, have to be emulated and friction must be compensated to obtain a fitting behaviour.
The machines in the laboratory setup, emulating the turbine and the wind turbine generator/machine, are denoted by subscripts $\square_{m_t}$ and $\square_{m_m}$, respectively. The rotational speed ω_{m_t} (in $\frac{\text{rad}}{\text{s}}$) of the turbine emulating machine and the rotational speed ω_{m_m} (in $\frac{\text{rad}}{\text{s}}$) of the generator emulating machine equal the rotational speeds of the small-scale WTS, i.e.

$$\omega_{m_t} = \omega_t \quad \text{and} \quad \omega_{m_m} = \omega_m\,. \tag{4.31}$$

4.2.5.1 Laboratory torque

The values τ_{m_t} and τ_{m_m} (both in N m) are applied by the emulating machines in the laboratory and calculated by

$$\tau_{m_t} = \tau_t - \tau_{\Theta_{\text{emu}}} + \tau_{\text{fric}} \quad \text{and} \tag{4.32}$$

$$\tau_{m_m} = \tau_m\,. \tag{4.33}$$

with inertia emulation torque $\tau_{\Theta_{\text{emu}}}$ and friction torque τ_{fric}. The determining of these two torques will be explained in the following sections.

Remark 4.2.3 (Drive train EESM-DFIM)**.** *For the EESM-DFIM drive train also the "breaking torque" τ_{i_e} has to be considered (see Fig. 4.6) and* (4.32) *changes to*

$$\tau_{m_t} = \tau_t - \tau_{\Theta_{\text{emu}}} + \tau_{\text{fric}} + \tau_{i_e}\,. \tag{4.34}$$

4.2.5.2 Inertia emulation

As already mentioned in the modelling of the drive train (see Sect. 2.2),

Assumption (AS.19) *it is assumed, that the inertias of the drive trains, in the laboratory and in the turbine, are concentrated (lumped masses).*

The small-scale turbine and machine inertias Θ_t and Θ_m are larger than the inertia Θ_{m_t} of the turbine emulating machine in the laboratory and the inertia Θ_{m_m} (both in $\mathrm{kg\,m^2}$) of the generator emulating machine in the laboratory, respectively. So their difference, the emulated inertia

$$\Theta_{\mathrm{emu}} := (\Theta_t + \Theta_m) - (\Theta_{m_t} + \Theta_{m_m}) \qquad (\text{in } \mathrm{kg\,m^2}) \tag{4.35}$$

has to be emulated by the laboratory machines. The torque $\tau_{\Theta_{\mathrm{emu}}}$ (in $\mathrm{N\,m}$), which achieves inertia emulation is given by

$$\tau_{\Theta_{\mathrm{emu}}} = \Theta_{\mathrm{emu}} \tfrac{\mathrm{d}}{\mathrm{d}t}\omega_{m_t}\,. \tag{4.36}$$

To emulate the inertia Θ_{emu}, the derivative $\frac{\mathrm{d}}{\mathrm{d}t}\omega_{m_t}$ of the rotational speed is needed. Because $\frac{\mathrm{d}}{\mathrm{d}t}\omega_{m_t}$ is not measured, a phase-locked loop (PLL) is used to estimate the derivative $\frac{\mathrm{d}}{\mathrm{d}t}\tilde{\omega}$ (in $\frac{\mathrm{rad}}{\mathrm{s}^2}$) based on the measured speed ω (see Fig. 4.10, where the block diagram is shown). The state-space representation of the PLL is given by

$$\left.\begin{aligned} \tfrac{\mathrm{d}}{\mathrm{d}t}\boldsymbol{x}_{\mathrm{pll}} &= \boldsymbol{A}_{\mathrm{pll}}\,\boldsymbol{x}_{\mathrm{pll}} + \boldsymbol{b}_{\mathrm{pll}}\,u_{\mathrm{pll}} \\ y_{\mathrm{pll}} &= \boldsymbol{c}_{\mathrm{pll}}^{\top}\boldsymbol{x}_{\mathrm{pll}} + d_{\mathrm{pll}}u_{\mathrm{pll}} \end{aligned}\right\} \tag{4.37}$$

where

$$\left.\begin{aligned} \boldsymbol{x}_{\mathrm{pll}} &= \begin{pmatrix} \xi_{\mathrm{pll}} \\ \tilde{\omega} \end{pmatrix}, \quad u_{\mathrm{pll}} = \omega, \\ \boldsymbol{A}_{\mathrm{pll}} &= \begin{bmatrix} 0 & -1 \\ k_{i,\mathrm{pll}} & -k_{p,\mathrm{pll}} \end{bmatrix},\ \boldsymbol{b}_{\mathrm{pll}} = \begin{pmatrix} 1 \\ k_{p,\mathrm{pll}} \end{pmatrix}, \\ \boldsymbol{c}_{\mathrm{pll}} &= \begin{pmatrix} k_{i,\mathrm{pll}} \\ -k_{p,\mathrm{pll}} \end{pmatrix},\ d_{\mathrm{pll}} = k_{p,\mathrm{pll}} \end{aligned}\right\} \tag{4.38}$$

are the state vector, the system input (rotational speed), the system matrix, the input vector, the output vector and the feedthrough, respectively. The initial values of the state vector are given by $\boldsymbol{x}_{\mathrm{pll}}(0) = (\xi_{\mathrm{pll},0},\, \tilde{\omega}_0)^{\top} \in \mathbb{R}^2$ (in rad and $\frac{\mathrm{rad}}{\mathrm{s}}$). The constants in (4.38) are the proportional gain $k_{p,\mathrm{pll}}$ (in $\frac{1}{\mathrm{s}}$) and the integral gain $k_{i,\mathrm{pll}}$ (in $\frac{1}{\mathrm{s}^2}$) of the PI-controller of the PLL (see Fig. 4.10).

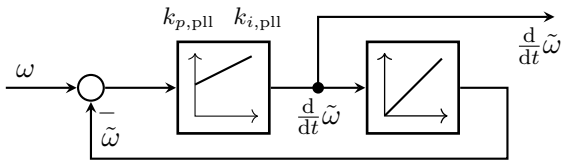

Figure 4.10: *Block diagram of the phase-locked loop (PLL) for estimation of the derivative* $\frac{\mathrm{d}}{\mathrm{d}t}\tilde{\omega}$ *of the rotational speed* ω.

Table 4.3: *Parameters of large-scale* 2.0 MW *wind turbine system.*

description	**symbol=value**
large-scale wind turbine	
air density	$\rho = 1.293\,\frac{\mathrm{kg}}{\mathrm{m}^3}$
turbine radius	$r_T = 40\,\mathrm{m}$
power coefficient	$c_P(\lambda, \beta)$ as in (2.3)
turbine inertia	$\Theta_T = 8.6 \cdot 10^6\,\mathrm{kg\,m}^2$
nominal speed	$\omega_{T,\mathrm{nom}} = 1.930\,\frac{\mathrm{rad}}{\mathrm{s}}$
nominal turbine power	$p_{T,\mathrm{nom}} = 2.0 \cdot 10^6\,\mathrm{W}$
isotropic PMSM in large-scale wind turbine	
pole pairs	$n_p = 48$
stator resistance	$R_s = 0.01\,\Omega$
stator inductance	$L_s^d = L_s^q = 3.0 \cdot 10^{-3}\,\mathrm{H}$
PM-flux linkage	$\psi_{\mathrm{pm}} = 12.9\,\mathrm{V\,s}$
machine inertia	$\Theta_M = 1.3 \cdot 10^6\,\mathrm{kg\,m}^2$
nominal speed	$\omega_{M,\mathrm{nom}} = 1.749\,\frac{\mathrm{rad}}{\mathrm{s}}$
nominal machine power	$p_{M,\mathrm{nom}} = 2.0 \cdot 10^6\,\mathrm{W}$

4.2.5.3 Friction compensation

The friction torque τ_{fric} (in N m) of the laboratory setup depends on the rotational speed ω_{m_t} and comprise linear viscous and nonlinear friction. The friction was measured (see Fig. 4.3 for PMSM-RSM and Fig. 4.7 for EESM-DFIM) and is feedforwarded to compensate for its influence, see (4.32).

4.2.5.4 Additional considerations for the scaling process

The experiments are conducted for a $p_{T,\mathrm{nom}} = 2\,\mathrm{MW}$ wind turbine and two laboratory setups with *chosen* power ratings of $p_{t,\mathrm{nom}} = 5\,\mathrm{kW}$ (PMSM-RSM) and $p_{t,\mathrm{nom}} = 4\,\mathrm{kW}$ (EESM-DFIM).

Remark 4.2.4. *It is beneficial to choose the power rating of the emulated turbine in the laboratory smaller than the power rating of the used electric machines, to ensure a sufficient power reserve for the necessary compensations and emulations (see Sect. 4.2.5). For the PMSM-RSM laboratory setup, the rated power of the emulated turbine is chosen to be* 5.00 kW*. This corresponds to* 53 % *of the nominal power of the less powerful machine (RSM, see Tab. 4.4).*

4.3 Implementation and experimental results

For the investigation of the impact of an open-switch fault on the overall wind turbine system performance, the scaling method as described above is used. The method is applied to the drive train PMSM-RSM and the drive train EESM-DFIM (recall Sect. 4.1.2 and Sect. 4.1.3). Table 4.3 collects all parameters of the full-scale 2 MW wind turbine system. For both drive trains, the following three experiments are conducted using a measured wind profile[43]:

[43]The wind speed was measured at the FINO1 research platform (54° 00′ 53, 5″ N, 06° 35′ 15, 5″ E) on the 23rd of September 2009 between 8:10 - 08:20 am (with a time resolution of 10 Hz). The author is deeply grateful to the FINO-Project (BMU, PTJ, BSH, DEWI GmbH) for providing the wind data used in this thesis.

($E_{4.1}$) The fault-free wind turbine system is fed with the wind profile, as shown in Fig. 4.11 for the PMSM and in Fig. 4.14 for the EESM.

($E_{4.2}$) Similar to Experiment ($E_{4.1}$), but in the converter connected to the stator of PMSM / EESM an open-switch fault is present in switch $\mathtt{S}_s^a$. For the current control, all three proposed methods of the post-fault control (pfc = improved anti-windup, modified SVM and optimal d-current injection for PMSM / fault-optimal current reference generation for EESM) as derived in Sect. 3.3.1 or Sect. 3.3.2 are applied. In the measurement plots all corresponding quantities are marked with the index $\square_{\mathrm{pfc}}$.

($E_{4.3}$) Similar to Experiment ($E_{4.2}$), but the stator current vector length is limited to $\hat{i}_{s,\max}$ (in A) which is necessary to produce the nominal torque using MTPA for the fault-free case. This limitation represents a saturation of the admissible current magnitude and ensures that the post-fault control strategy does not cause overheating in the stator of the machine. The corresponding quantities are marked with the index $\square_{\mathrm{pfc,sat}}$.

The current reference limitation for Experiment ($E_{4.3}$) is implemented by the function[44]

$$\boldsymbol{i}_{s,\mathrm{ref,sat}}^{dq} = \mathbf{sat}_{\hat{i}_{s,\max}}(\boldsymbol{i}_{s,\mathrm{ref}}^{dq}). \tag{4.39}$$

The computation of $\hat{i}_{s,\max}$ will be explained in detail for each machine in the corresponding sections.
Due to the huge torque ripples in case of an open-switch fault and using standard control, the case with open-switch fault and *without* post-fault control is not investigated to avoid damaging the laboratory setup.

4.3.1 Wind turbine system with PMSM under open-switch converter faults

To investigate the impact of an open-switch converter fault on a WTS with PMSM, the experiments as described above are conducted and denoted by Experiments ($E_{4.1,\mathrm{PMSM}}$), ($E_{4.2,\mathrm{PMSM}}$) and ($E_{4.3,\mathrm{PMSM}}$), respectively. The parameters of laboratory setup and scaling are summarized in Tab. 4.4.
The laboratory setup and the implementation of scaling and control at the real-time system are depicted in Fig. 4.11. The turbine emulating RSM and the generator emulating PMSM are coupled by a torque sensor. Both machines are equipped with an encoder providing angle and speed information. The stators of both machines are fed by a converter. The three-phase machine currents are measured. The converter switching signals are created by space-vector modulation. The reference voltages for the SVM are made available by the real-time system. The unscaled measurement results are used in the real-time system for the current control. For the turbine and generator emulation, the rotational speeds are up-scaled to the large-scale system. Turbine controller and wind turbine are emulated for the large-scale system. The resulting reference torques are down-scaled to the small-scale laboratory setup and fed to the torque control. For the turbine emulating machine, the friction compensation torque (see Fig. 4.3) and the inertia emulation torque (4.36) are added.
The current $\hat{i}_{s,\max}$, for limiting the stator currents, is calculated based on the nominal torque of the down-scaled turbine, i.e.

$$\tau_{t,\mathrm{nom}} = \frac{p_{t,\mathrm{nom}}}{\omega_{m_t,\mathrm{nom}}}, \quad (\text{in N m}) \tag{4.40}$$

[44] Recall the definition of $\mathbf{sat}_{\hat{i}_{s,\max}}$ in the nomenclature section.

Table 4.4: *Parameters of PMSM-RSM laboratory setup and scaling factors.*

description	**symbol=value**
isotropic PMSM in laboratory	
pole pairs	$n_p = 3$
stator resistance	$R_s = 0.15\,\Omega$
stator inductance	$L_s^d = L_s^q = 3.35 \cdot 10^{-3}\,\mathrm{H}$
PM-flux linkage	$\psi_{\mathrm{pm}} = 0.376\,5\,\mathrm{V\,s}$
machine inertia	$\Theta_{m_m} = 1.630 \cdot 10^{-2}\,\mathrm{kg\,m^2}$
nominal speed	$\omega_{m_m,\mathrm{nom}} = 209.4\,\frac{\mathrm{rad}}{\mathrm{s}}$
nominal machine power	$p_{m_m,\mathrm{nom}} = 14.5 \cdot 10^3\,\mathrm{W}$
anisotropic RSM in laboratory	
pole pairs	$n_p = 2$
stator resistance	$R_s = 0.4\,\Omega$
stator inductances	nonlinear (see [118, Fig. 2])
machine inertia	$\Theta_{m_t} = 1.890 \cdot 10^{-2}\,\mathrm{kg\,m^2}$
nominal speed	$\omega_{m_t,\mathrm{nom}} = 157.1\,\frac{\mathrm{rad}}{\mathrm{s}}$
nominal machine power	$p_{m_t,\mathrm{nom}} = 9.4 \cdot 10^3\,\mathrm{W}$
additional parameters	
emulated inertia	$\Theta_{\mathrm{emu}} = 3.70\,\mathrm{kg\,m^2}$
proportional gain PLL	$k_{p,\mathrm{pll}} = 2\,\frac{1}{\mathrm{s}}$
integral gain PLL	$k_{i,\mathrm{pll}} = 1\,\frac{1}{\mathrm{s}^2}$
scaling to small-scale wind turbine	
turbine nominal power	$p_{t,\mathrm{nom}} = 5.000 \cdot 10^3\,\mathrm{W}$
virtual gear ratio	$g_{\mathrm{virt}} = \frac{157.1\,\frac{\mathrm{rad}}{\mathrm{s}}}{1.930\,\frac{\mathrm{rad}}{\mathrm{s}}} = 81.41$
scaling of air density	$\mu_\rho = 1.000$
scaling of time	$\mu_{\mathrm{time}} = 1.000$
scaling of power	$\mu_p = 2.500 \cdot 10^{-3}$
scaling of rotational speed	$\mu_\omega = 1.000$
scaling of velocity	$\mu_v = 3.017 \cdot 10^{-1}$
scaling of torque	$\mu_\tau = 2.500 \cdot 10^{-3}$
scaling of inertia	$\mu_\theta = 2.500 \cdot 10^{-3}$

depending on the nominal power $p_{t,\mathrm{nom}}$ of the down-scaled wind turbine and the nominal speed $\omega_{m_t,\mathrm{nom}}$ of the down-scaled turbine. Rewriting the torque equation of (2.15) gives

$$\hat{i}_{s,\max} := \frac{2\tau_{t,\mathrm{nom}}}{3n_p\hat{\psi}_{\mathrm{pm}}} = \frac{2p_{t,\mathrm{nom}}}{3n_p\hat{\psi}_{\mathrm{pm}}\omega_{m_t,\mathrm{nom}}}, \tag{4.41}$$

which is used in (4.39). Thus it is ensured, that the length of the reference current vector in the faulty case does not exceed the length of the reference current in the fault-free case.

Remark 4.3.1. *Using the saturation method in* (4.39) *to limit the reference current, the angle* φ_0 *stays the same as in the unsaturated case. But due to the change in* $i^q_{s,\mathrm{ref}}$*, a different angle* φ_0 *might be optimal (see Sect. 3.3.1.4). As the optimal angle* $\varphi_0^\star$ *does not change much with* i_s^q *(see Fig. 3.28) and the quadratic error does not increase very steep around the* $\varphi_0^\star$*-trajectory (see red line in Fig. 3.27), the impact of this slight deviation from* $\varphi_0^\star$ *is very limited.*

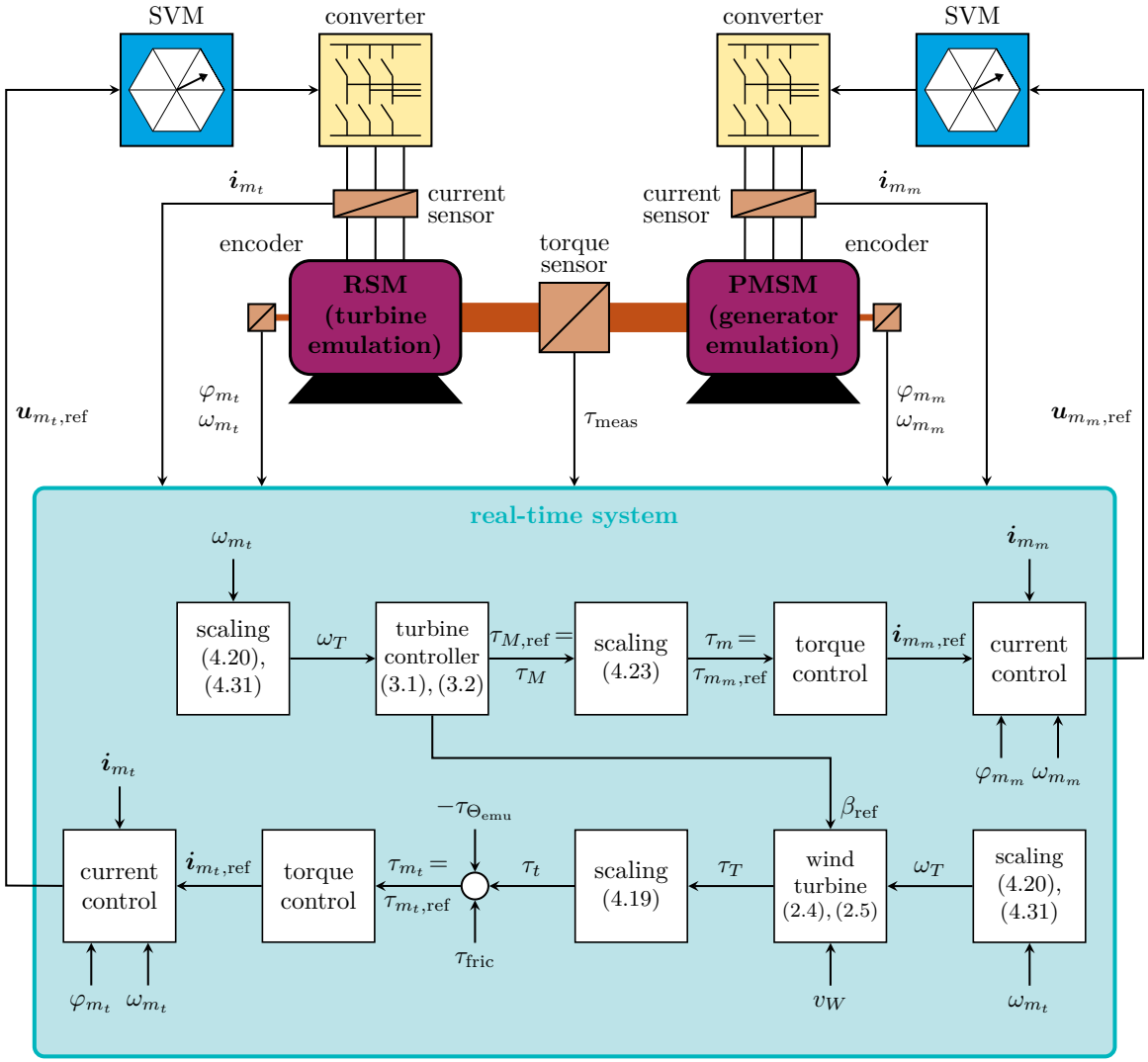

Figure 4.11: *Illustration of laboratory setup and implementation of scaling and control at the real-time system for drive train PMSM-RSM.*

Table 4.5: *Produced energy of WTS within* 600 s *for Experiments* ($\mathrm{E}_{4.1,\mathrm{PMSM}}$), ($\mathrm{E}_{4.2,\mathrm{PMSM}}$) *and* ($\mathrm{E}_{4.3,\mathrm{PMSM}}$).

experiment	produced energy	relative value
Experiment ($\mathrm{E}_{4.1,\mathrm{PMSM}}$)	$E_M(600\,\mathrm{s}) = -325\,\mathrm{kW\,h}$	100 %
Experiment ($\mathrm{E}_{4.2,\mathrm{PMSM}}$)	$E_{M,\mathrm{pfc}}(600\,\mathrm{s}) = -322\,\mathrm{kW\,h}$	99 %
Experiment ($\mathrm{E}_{4.3,\mathrm{PMSM}}$)	$E_{M,\mathrm{pfc,sat}}(600\,\mathrm{s}) = -303\,\mathrm{kW\,h}$	93 %

Table 4.5 summarizes the measurement results for Experiments ($\mathrm{E}_{4.1,\mathrm{PMSM}}$), ($\mathrm{E}_{4.2,\mathrm{PMSM}}$) and ($\mathrm{E}_{4.3,\mathrm{PMSM}}$) by comparing the produced energies after 600 s. For Experiment ($\mathrm{E}_{4.2,\mathrm{PMSM}}$), the energy production is only decreased by 1 % and for Experiment ($\mathrm{E}_{4.3,\mathrm{PMSM}}$), it is decreased by 7 % compared to the fault-free WTS. The details for that and the differences between the experiments will be discussed using Fig. 4.12 and Fig. 4.13 showing the measurement results.

Figure 4.12 shows the turbine quantities for all three experiments. In the upper plot, the wind speed v_W and its nominal value $v_{W,\mathrm{nom}}$ are depicted. The speed varies slightly around the nominal speed. From 150 s until 530 s, $v_W > v_{W,\mathrm{nom}}$ (except short fluctuations). Hence,

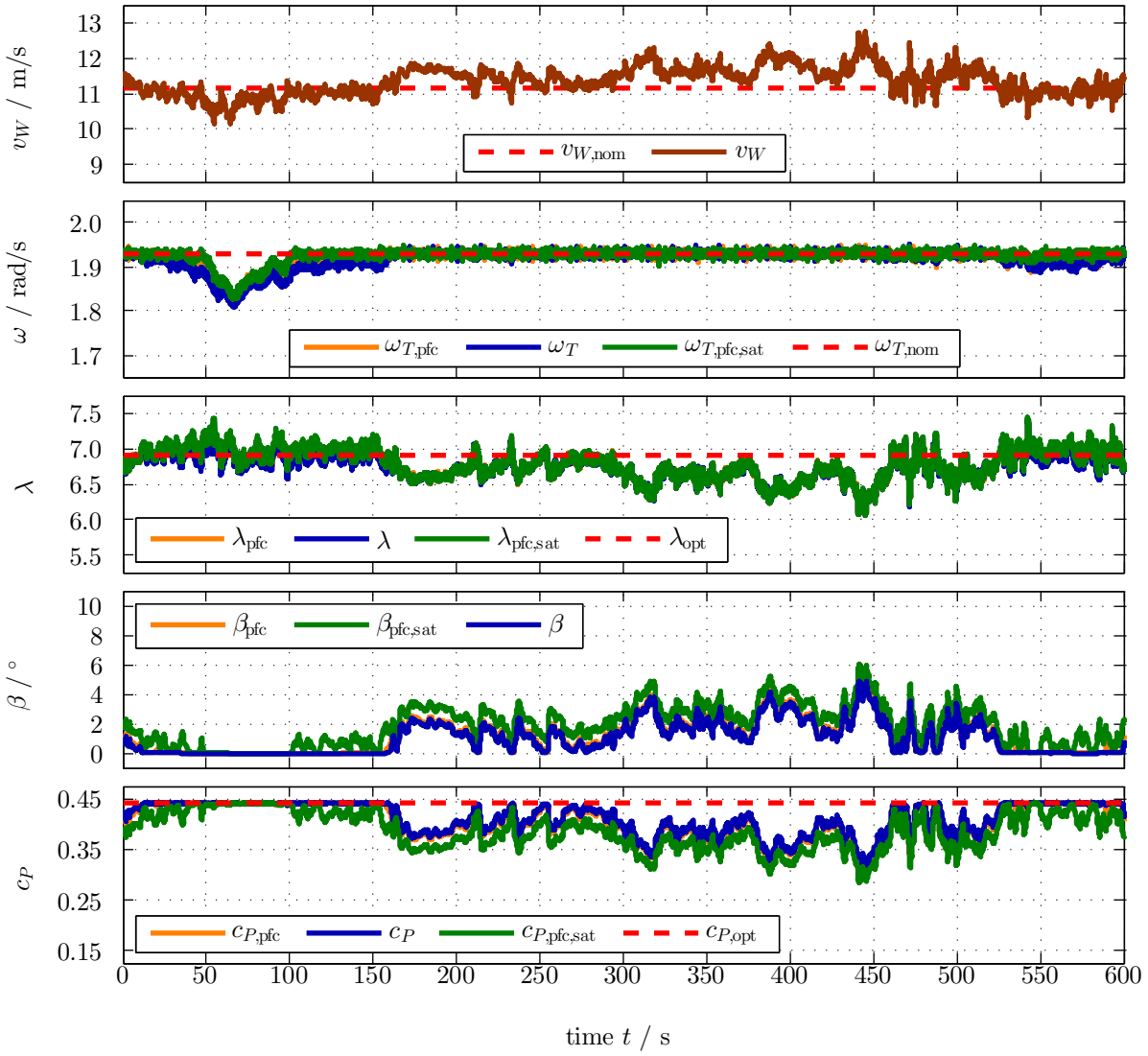

Figure 4.12: *Comparison of the measurement results for Experiments* ($\mathrm{E}_{4.1,\mathrm{PMSM}}$), ($\mathrm{E}_{4.2,\mathrm{PMSM}}$) *and* ($\mathrm{E}_{4.3,\mathrm{PMSM}}$)*—turbine quantities.*

the wind turbine operates in regime III (see Sect. 3.1) and the control should limit the power production to the nominal value. For the other time periods, $v_W < v_{W,\mathrm{nom}}$, i.e. the turbine operates in regime II and the control purpose is maximum power point tracking. The second plot shows the turbine angular speed $\omega_{T,\mathrm{pfc}}$ for the faulty case (Experiment ($\mathrm{E}_{4.2,\mathrm{PMSM}}$)), for the faulty case with saturation $\omega_{T,\mathrm{pfc,sat}}$ (Experiment ($\mathrm{E}_{4.3,\mathrm{PMSM}}$)), for the fault-free case ω_T (Experiment ($\mathrm{E}_{4.1,\mathrm{PMSM}}$)) and the nominal rotational speed $\omega_{T,\mathrm{nom}}$. The two rotational speeds $\omega_{T,\mathrm{pfc}}$ and ω_T are (almost) equal throughout the whole experiment. $\omega_{T,\mathrm{pfc,sat}}$ equals $\omega_{T,\mathrm{nom}}$ when $v_W > v_{W,\mathrm{nom}}$; whereas when $v_W < v_{W,\mathrm{nom}}$, $\omega_{T,\mathrm{pfc,sat}}$ is higher than ω_T. Subplot three depicts the tip speed ratio. λ_{opt} is the optimal value for maximum power production of the wind turbine operating in regime II. λ, λ_{pfc} and $\lambda_{\mathrm{pfc,sat}}$ are the measured values for the fault-free case, the faulty case and the faulty case with saturation, respectively. Between the two measured tip speed ratios λ and λ_{pfc} no significant discrepancy is visible. $\lambda_{\mathrm{pfc,sat}}$ deviates for regime II and is slightly higher than λ. The fourth subplot shows the pitch angles β, β_{pfc} and $\beta_{\mathrm{pfc,sat}}$. For regime II, both pitch angles β and β_{pfc} are zero, for maximum power point tracking. For regime III, the pitch controller is active to limit the produced power to the rated value. β_{pfc} is slightly

higher than β. For the faulty case with saturation, the pitch angle $\beta_{\text{pfc,sat}}$ deviates for almost all time from zero. Only for relatively low wind speeds, for $t \in [50\,\text{s}, 100\,\text{s}]$, the pitch angle is zero. The lower subplot shows the optimal power factor $c_{P,\text{opt}}$, the power factor c_P for the fault-free case, the power factor $c_{P,\text{pfc}}$ for the faulty case and the power factor $c_{P,\text{pfc,sat}}$ for the faulty case with saturation. For partial load (i.e. regime II), the power factors c_P and $c_{P,\text{pfc}}$ reach for both measurements their optimal value. For rated power, the power factors are reduced; $c_{P,\text{pfc}}$ slightly more than c_P. $c_{P,\text{pfc,sat}}$ only reaches for very low wind speeds ($t \in [50\,\text{s}, 100\,\text{s}]$) its optimal value. For all other times, $\beta_{\text{pfc,sat}}$ deviates from the optimal value $\beta_{\text{opt}} = 0°$ and $c_{P,\text{pfc,sat}}$ is smaller than c_P and $c_{P,\text{pfc}}$.

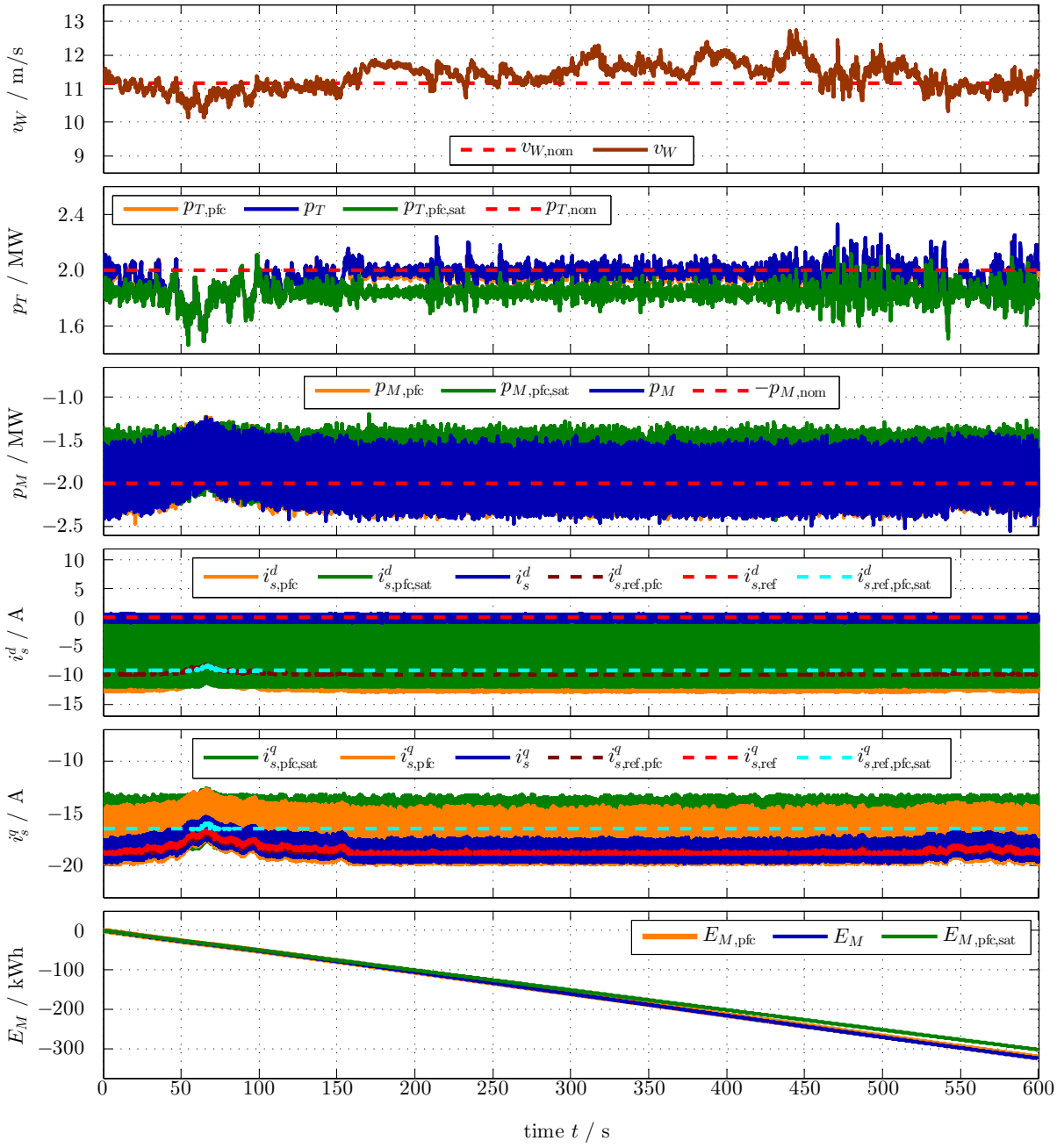

Figure 4.13: *Comparison of the measurement results for Experiments* ($\text{E}_{4.1,\text{PMSM}}$), ($\text{E}_{4.2,\text{PMSM}}$) *and* ($\text{E}_{4.3,\text{PMSM}}$)*—drive and electric quantities* ($E_M(600\,\text{s}) = -325\,\text{kW h}$, $E_{M,\text{pfc}}(600\,\text{s}) = -322\,\text{kW h}$, $E_{M,\text{pfc,sat}}(600\,\text{s}) = -303\,\text{kW h}$*).*

In Fig. 4.13, the measurement results of the drive and electric quantities for all three Experiments ($E_{4.1,PMSM}$), ($E_{4.2,PMSM}$) and ($E_{4.3,PMSM}$) are depicted. The first subplot repeats the wind speed v_W and the nominal wind speed $v_{W,nom}$. The second subplot shows the turbine power $p_{T,pfc}$ for the faulty case, the turbine power $p_{T,pfc,sat}$ for the faulty case with saturation, the turbine power p_T for the fault-free case and the nominal turbine power $p_{T,nom}$. For regime II, the measured powers are most of the time below $p_{T,nom}$. p_T and $p_{T,pfc}$ do not differ much from each other. For regime III, both powers vary around $p_{T,nom}$. Due to fast changes in the wind speed and the slow mechanical wind turbine system (huge inertias and not instantaneous changing pitch angle β), it is not possible to limit the turbine power to its nominal value for all time. E.g. at around 470 s, p_T exceeds its nominal value by almost 20 %. For the operation above nominal wind speed (regime III), $p_{T,pfc}$ is slightly smaller than p_T. In contrast, $p_{T,pfc,sat}$ varies for the whole time around 1.85 MW and (almost) never reaches $p_{T,nom}$. Only for $t \in [50\,\text{s}, 100\,\text{s}]$, it coincides with $p_{T,pfc}$ and p_T. Subplot three shows the machine powers p_M, $p_{M,pfc}$, $p_{M,pfc,sat}$ and $p_{M,nom}$. p_M, $p_{M,pfc}$ and $p_{M,pfc,sat}$ are negative, as the electric machine is working in generator mode. All measured powers are oscillating in a band, due to the switching of the converter and, additionally in the faulty cases, due to the influence of the open-switch fault. Due to losses in the electric machine, e.g. ohmic losses at the resistors, p_M and $p_{M,pfc}$ are oscillating around absolute values smaller than $p_{M,nom}$. $p_{M,pfc,sat}$ is oscillating around an even further reduced value. The average of all machine powers does not exceed the nominal power, although p_T does sometimes, see subplot two. The fourth subplot shows the d-currents and their reference values. In the fault-free case, the reference value is $i^d_{s,ref} = 0\,\text{A}$. i^d_s tracks its reference with an oscillation band of 1 A. Due to the optimal d-current injection of the post-fault control, $i^d_{s,ref,pfc}$ and $i^d_{s,ref,pfc,sat}$ are not zero. $i^d_{s,pfc}$ and $i^d_{s,pfc,sat}$ oscillate around their reference values, but due to the fault, both currents dip towards zero in each oscillation (recall zoom in Fig. 3.29). Because of the current limitation is $i^d_{s,ref,pfc,sat} \leq i^d_{s,ref,pfc}$. Subplot five shows the q-currents and their reference values. The reference values $i^q_{s,ref}$ and $i^q_{s,ref,pfc}$ only differ for regime II, due to the differing rotational speed (see subplot two in Fig. 4.12 and control law (3.2)). $i^q_{s,ref,pfc,sat}$ is almost all the time constant and at its maximum value (because of the saturation) of around $-17\,\text{A}$. Due to the fault, the oscillation bands of $i^q_{s,pfc}$ and $i^q_{s,pfc,sat}$ are bigger than the oscillation band of i^q_s. But all signals do track their reference values on average. The lower subplot shows the produced energy E_M of the electric machine for the fault-free case (Experiment ($E_{4.1,PMSM}$)), $E_{M,pfc}$ for the faulty case (Experiment ($E_{4.2,PMSM}$)) and $E_{M,pfc,sat}$ for the faulty case with saturation (Experiment ($E_{4.3,PMSM}$)). The trajectories of E_M and $E_{M,pfc}$ are almost identical. The energy production in the faulty case with saturation is reduced. Comparing the total values after 600 s, i.e. $E_M(600\,\text{s}) = -325\,\text{kW h}$, $E_{M,pfc}(600\,\text{s}) = -322\,\text{kW h}$ and $E_{M,pfc,sat}(600\,\text{s}) = -303\,\text{kW h}$, shows that E_M and $E_{M,pfc}$ are (almost) identical. In the faulty case with saturation 93 % of the energy of the fault-free case is produced.
Summarizing, although an open-switch fault in the converter is present, due to the modified post-fault control strategy, the energy production of the wind turbine system is without saturation[45] (almost) identical to the fault-free case. When the current is saturated, still 93 % of the energy of the fault-free case can be produced. If a current vector larger than $\hat{i}_{s,max}$ is technically feasible, an open-switch fault does not necessarily have to result in a loss of produced energy.

4.3.2 Wind turbine system with EESM under open-switch converter faults

To investigate the impact of an open-switch converter fault in a WTS with EESM, the experiments, as described at the beginning of this section, are conducted and denoted by Experiments ($E_{4.1,EESM}$), ($E_{4.2,EESM}$) and ($E_{4.3,EESM}$), respectively. The scaling method as described

[45] In this case the absolute value of the current vector is up to 13 % larger than $\hat{i}_{s,max}$.

in Sect. 4.2.2 is used for the drive train EESM-DFIM. For the scaling process, the wind turbine parameters as given in Tab. 4.3 are used. The parameters of the laboratory setup and the scaling factors are collected in Tab. 4.6.

Table 4.6: *Parameters of EESM-DFIM laboratory setup and scaling factors.*

description	**symbol=value**
anisotropic EESM in laboratory	
pole pairs	$n_p = 2$
stator resistance	$R_s = 0.38\,\Omega$
excitation resistance	R_e nonlinear (see Fig. B.3)
inductances	nonlinear (see Appendix. B)
machine inertia	$\Theta_{m_m} = 0.273\,\mathrm{kg\,m^2}$
nominal speed	$\omega_{m_m,\mathrm{nom}} = 157.1\,\frac{\mathrm{rad}}{\mathrm{s}}$
nominal machine power	$p_{m_m,\mathrm{nom}} = 10 \cdot 10^3\,\mathrm{W}$
isotropic DFIM in laboratory	
pole pairs	$n_p = 2$
stator resistance	$R_s = 0.72\,\Omega$
rotor resistance	$R_r = 0.55\,\Omega$
inductances	nonlinear
machine inertia	$\Theta_{m_t} = 9.37 \cdot 10^{-2}\,\mathrm{kg\,m^2}$
nominal speed	$\omega_{m_t,\mathrm{nom}} = 157.1\,\frac{\mathrm{rad}}{\mathrm{s}}$
nominal machine power	$p_{m_t,\mathrm{nom}} = 10 \cdot 10^3\,\mathrm{W}$
additional parameters	
emulated inertia	$\Theta_{\mathrm{emu}} = 7.01\,\mathrm{kg\,m^2}$
proportional gain PLL	$k_{p,\mathrm{pll}} = 2\,\frac{1}{\mathrm{s}}$
integral gain PLL	$k_{i,\mathrm{pll}} = 1\,\frac{1}{\mathrm{s}^2}$
scaling to small-scale wind turbine	
turbine nominal power	$p_{t,\mathrm{nom}} = 4.000 \cdot 10^3\,\mathrm{W}$
virtual gear ratio	$g_{\mathrm{virt}} = \frac{100.0\,\frac{\mathrm{rad}}{\mathrm{s}}}{1.930\,\frac{\mathrm{rad}}{\mathrm{s}}} = 51.82$
scaling of air density	$\mu_\rho = 1.000$
scaling of time	$\mu_{\mathrm{time}} = 1.000$
scaling of power	$\mu_p = 2.000 \cdot 10^{-3}$
scaling of rotational speed	$\mu_\omega = 1.000$
scaling of velocity	$\mu_v = 2.885 \cdot 10^{-1}$
scaling of torque	$\mu_\tau = 2.000 \cdot 10^{-3}$
scaling of inertia	$\mu_\theta = 2.000 \cdot 10^{-3}$

The laboratory setup and the implementation of scaling and control at the real-time system are depicted in Fig. 4.14. The principle setup is similar to the setup with PMSM-RSM (see Fig. 4.11). For the DFIM, stator *and* rotor are fed by a converter. The *abc*-currents are measured for stator and rotor. Hence, for the DFIM six currents are measured and six reference voltages are sent to the SVMs. In contrast to the PMSM, the rotor of the ESSM is fed with a dc-current. The current is provided by a dc-source, which is fed with a reference dc-voltage by the real-time system. The real-time system for the EESM-DFIM drive-train differs from the real-time system for the PMSM-RSM drive-train only in the torque and current control and in the additional compensation of the "breaking torque" τ_{i_e} due to the excitation current.

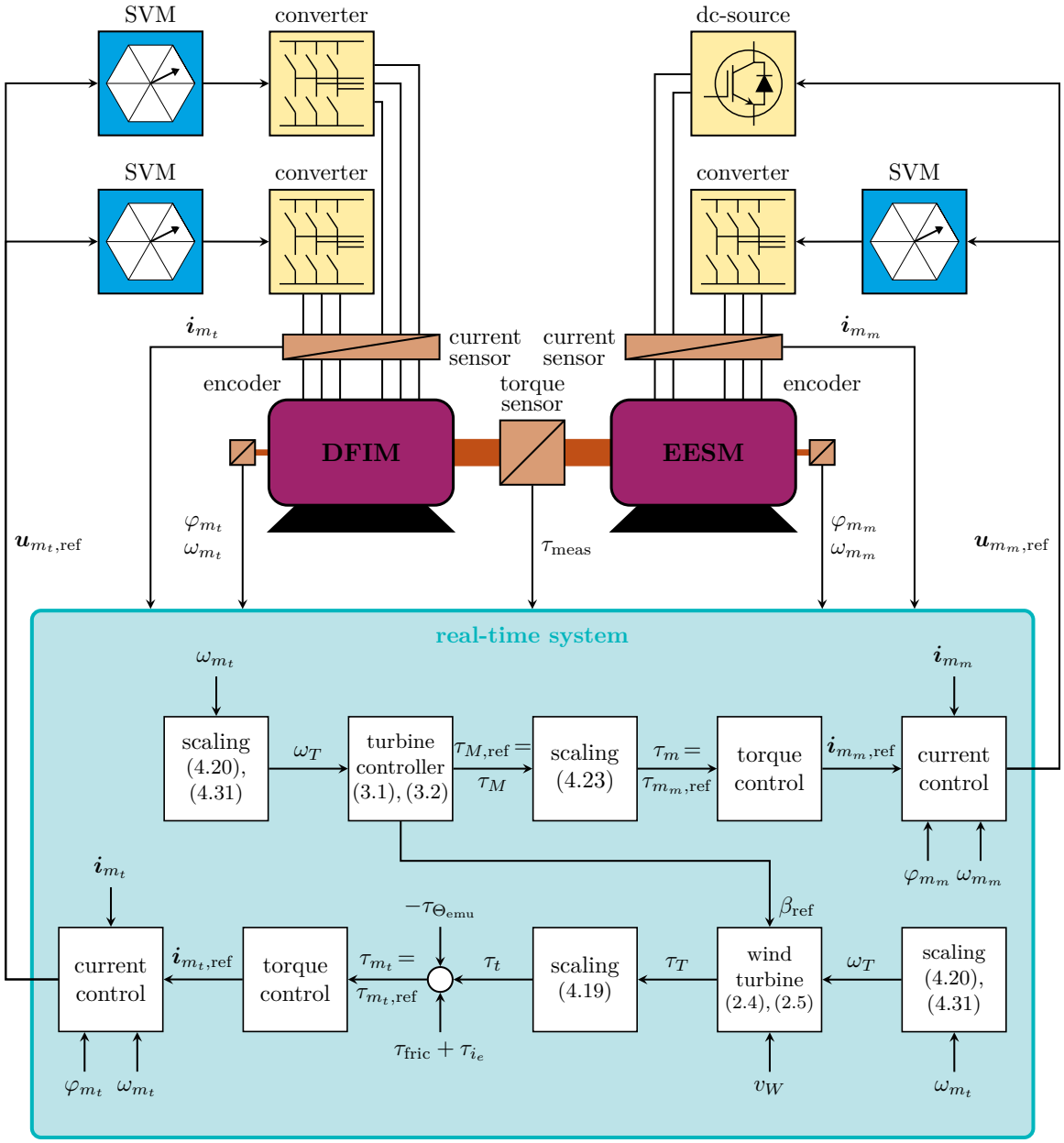

Figure 4.14: *Illustration of laboratory setup and implementation of scaling and control at the real-time system for drive train EESM-DFIM.*

For the EESM, the current $\hat{i}_{s,\max}$ used in (4.39) is calculated based on the nominal torque of the scaled down turbine, i.e.

$$\tau_{t,\mathrm{nom}} = \frac{p_{t,\mathrm{nom}}}{\omega_{m_t,\mathrm{nom}}}, \quad (\text{in N m}) \tag{4.42}$$

depending on the nominal power $p_{t,\mathrm{nom}}$ of the scaled down wind turbine and the nominal speed $\omega_{m_t,\mathrm{nom}}$ of the scaled down turbine. The maximum current $\hat{i}_{s,\max}$ is determined by using the MTPA-trajectory of the EESM (Fig. 3.12 and Sect. 3.2.3.2). By that, it is ensured that the length of the stator reference current vector in the faulty case does not exceed the length of the reference stator current in the fault-free case.

Table 4.7: *Produced energy of WTS within* 600 s *for Experiments* ($\mathrm{E}_{4.1,\mathrm{EESM}}$), ($\mathrm{E}_{4.2,\mathrm{EESM}}$) *and* ($\mathrm{E}_{4.3,\mathrm{EESM}}$).

experiment	produced energy	relative value
Experiment ($\mathrm{E}_{4.1,\mathrm{EESM}}$)	$E_M(600\,\mathrm{s}) = -327\,\mathrm{kW\,h}$	100 %
Experiment ($\mathrm{E}_{4.2,\mathrm{EESM}}$)	$E_{M,\mathrm{pfc}}(600\,\mathrm{s}) = -314\,\mathrm{kW\,h}$	96 %
Experiment ($\mathrm{E}_{4.3,\mathrm{EESM}}$)	$E_{M,\mathrm{pfc,sat}}(600\,\mathrm{s}) = -312\,\mathrm{kW\,h}$	95 %

Table 4.7 summarizes the measurement results for Experiments ($\mathrm{E}_{4.1,\mathrm{EESM}}$), ($\mathrm{E}_{4.2,\mathrm{EESM}}$) and ($\mathrm{E}_{4.3,\mathrm{EESM}}$) by comparing the produced energy after 600 s. For Experiment ($\mathrm{E}_{4.2,\mathrm{EESM}}$), the energy production is decreased by 4 % and, for Experiment ($\mathrm{E}_{4.3,\mathrm{EESM}}$), it is decreased by 5 % compared to the fault-free WTS. The details for that and the differences between the experiments will be discussed using the measurement results in Fig. 4.15 and Fig. 4.16.

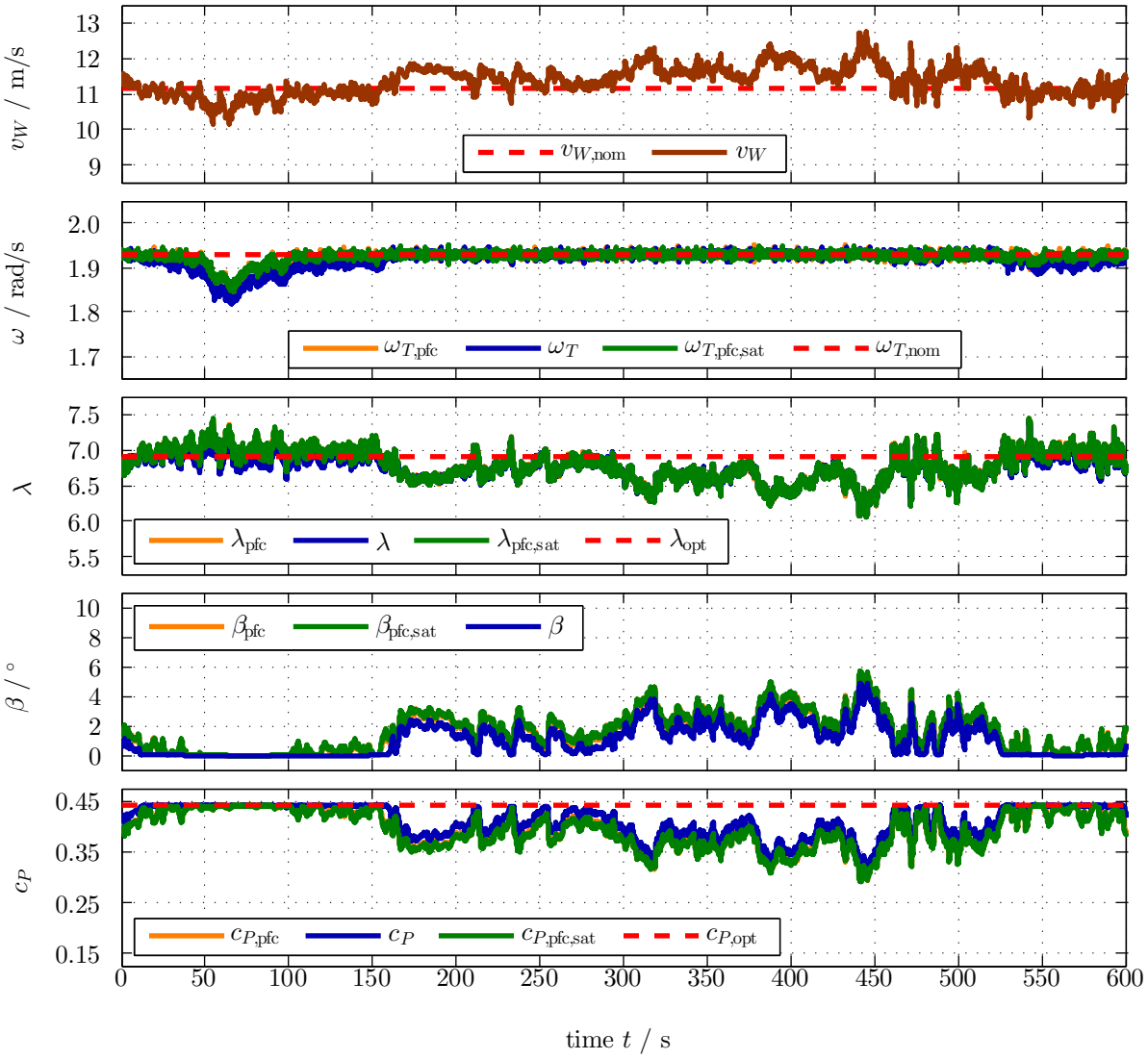

Figure 4.15: *Comparison of the measurement results for Experiments* ($\mathrm{E}_{4.1,\mathrm{EESM}}$), ($\mathrm{E}_{4.2,\mathrm{EESM}}$) *and* ($\mathrm{E}_{4.3,\mathrm{EESM}}$)*—turbine quantities.*

Figure 4.15 shows the comparison of the turbine quantities of the WTS with EESM for all three

Experiments ($E_{4.1,EESM}$), ($E_{4.2,EESM}$) and ($E_{4.3,EESM}$). The upper subplot depicts the wind speed v_W and its nominal value $v_{W,nom}$. The second subplot shows the turbine rotational speed ω_T and its nominal value $\omega_{T,nom}$. For both post-fault cases, the rotational speeds $\omega_{T,pfc}$ and $\omega_{T,pfc,sat}$ are, in regime II ($v_W < v_{W,nom}$), higher as ω_T for the fault-free case. For regime III ($v_W \geq v_{W,nom}$) all rotational speeds are similar. Subplot three shows the tip speed ratios λ, λ_{pfc}, $\lambda_{pfc,sat}$ and λ_{opt}. For regime II, λ_{pfc} and $\lambda_{pfc,sat}$ are larger than λ. In subplot four, it is visible, that for maintaining nominal speed in regime III and in parts of regime II (except for $t \in [50\,\mathrm{s}, 100\,\mathrm{s}]$) larger pitch angles β_{pfc} and $\beta_{pfc,sat}$ are necessary than for the fault-free case. Taking this into account, it is comprehensible, that the power factor c_P—shown in subplot five—does for both post-fault cases not exceed the power factor for the fault-free case. Especially for regime III, $c_{P,pfc}$ and $c_{P,pfc,sat}$ are smaller than c_P.
The first subplot of Fig. 4.16 shows the wind speed v_W and its nominal value, again. The second subplot shows the turbine powers and the nominal turbine power. The values of $p_{T,pfc}$ and $p_{T,pfc,sat}$ do (almost) never reach the nominal power $p_{T,nom}$. For small wind speeds in regime II ($t \in [50\,\mathrm{s}, 100\,\mathrm{s}]$), the three experiments do coincide. The same effect can be observed for the machine power in subplot three. Subplot four shows the excitation currents and their references. Due to the changed current reference generation in the post-fault case, the excitation currents $i_{e,pfc}$ and $i_{e,pfc,sat}$ are larger than i_e. For the stator d-currents depicted in subplot five it is vice versa. While for the MTPA-strategy, the optimal current $i^d_{s,ref}$ is slightly positive. For the post-fault control strategy, $i^d_{s,ref,pfc}$ and $i^d_{s,ref,pfc,sat}$ are negative. The post-fault currents do oscillate strongly and even reach zero. Subplot six shows the stator q-currents. The references for the fault-free case and for the post-fault case do also differ. The currents are in a band around their reference values. While the band for the post-fault case is a bit larger, the currents $i^q_{s,pfc}$ and $i^q_{s,pfc,sat}$ do not go to zero. Looking at subplots four to six, (almost) no differences between the currents and their references for Experiment ($E_{4.2,EESM}$) and Experiment ($E_{4.3,EESM}$) are visible. Hence, the stator current reference vector for the post-fault control does not exceed the threshold $\hat{i}_{s,max}$. Due to the increased excitation currents $i_{e,pfc}$ and $i_{e,pfc,sat}$ in the post-fault control, (almost) the same torque as in the fault-free case is produced, although the amplitude of the q-current is reduced and a negative d-current is induced, which reduces the flux linkage in d-direction. For the post-fault control of the EESM, a limitation of the stator currents to $\hat{i}_{s,max}$ does not seem to make any difference. The summed-up energies are shown in the lower subplot. There is less produced energy within the shown 600 s for both post-fault cases $E_{M,pfc}(600\,\mathrm{s}) = -314\,\mathrm{kW\,h}$ and $E_{M,pfc}(600\,\mathrm{s}) = -312\,\mathrm{kW\,h}$ than for the fault-free case with $E_M(600\,\mathrm{s}) = -327\,\mathrm{kW\,h}$. The fact, that produced energy for Experiment ($E_{4.2,EESM}$) and Experiment ($E_{4.3,EESM}$) are almost identical, underpins the observations made for the currents. The small reduction by 4 % and 5 % for both post-fault control strategies compared to the fault-free case, can be explained by the tiny deviations in torque control using the post-fault control strategy (observe the small deviations in actual torque from its reference in Fig. 3.37).
Summarizing, the experiments show, that although an open-switch fault is present in the machine-side converter of the EESM, with the proposed post-fault control strategy, the wind turbine system can still be operated and only 5 % of the energy is lost.

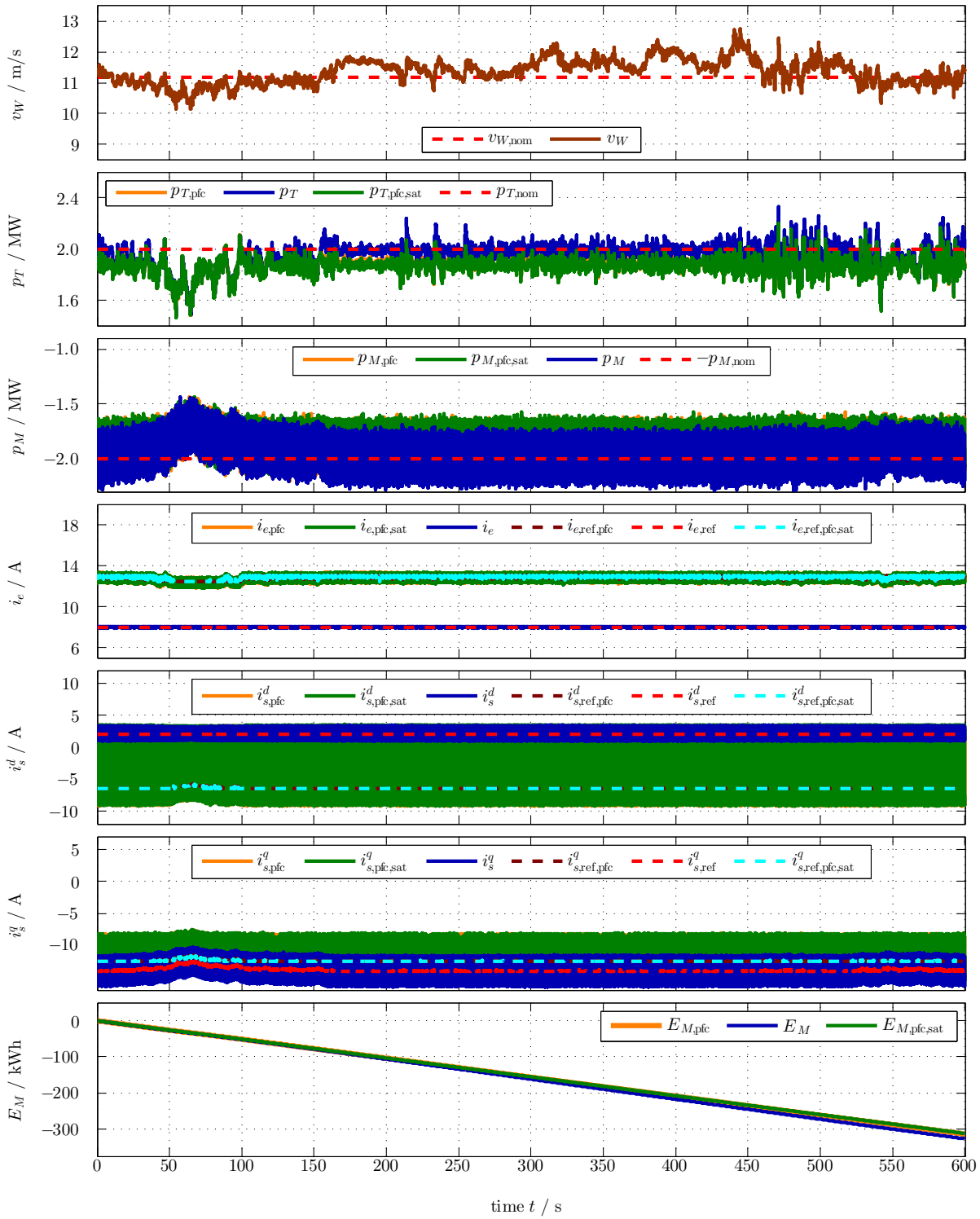

Figure 4.16: *Comparison of the measurement results for Experiments* ($\mathrm{E}_{4.1,\mathrm{EESM}}$), ($\mathrm{E}_{4.2,\mathrm{EESM}}$) *and* ($\mathrm{E}_{4.3,\mathrm{EESM}}$)*—drive and electric quantities (*$E_M(600\,\mathrm{s}) = -327\,\mathrm{kW\,h}$, $E_{M,\mathrm{pfc}}(600\,\mathrm{s}) = -314\,\mathrm{kW\,h}$, $E_{M,\mathrm{pfc}}(600\,\mathrm{s}) = -312\,\mathrm{kW\,h}$*)*

Chapter 5

Conclusion and outlook

In this thesis the modelling and control of large-scale direct-drive wind turbine systems under open-switch faults in the machine-side converter were discussed. Open-switch faults are severe types of faults which would cause secondary faults in the other WTS components without proper countermeasures. Hence, WTS are usually shut down when an open-switch fault is detected. This causes losses in energy and revenue. To investigate the possibilities of finding a post-fault control strategy, the WTS and the converter with open-switch fault had to be modelled and the overall control system had to be designed.

For the modelling and control of WTSs under open-switch faults, new models and control strategies were derived. A nonlinear mathematical model of EESMs including damper windings was introduced. To obtain the necessary flux linkage maps, a method to measure these maps for EESMs was proposed. Static and dynamic measurements showed strong agreement between simulation and measurement results. It was also shown that linear modelling of EESMs leads to significant deviations between model and real machine, especially for the machine torque. The obtained flux linkage maps were used to design the current controllers and to obtain a maximum torque per ampere control strategy for the EESM. Measurement and simulation results showed an acceptable control performance.

In order to be able to efficiently simulate a converter with open-switch fault, a mathematical model was derived. The accuracy of this model was validated by measurements. The post-fault control was first derived for a linear PMSM and afterwards for a nonlinear EESM. The three parts of the post-fault control strategy are (i) an improved anti-windup strategy, (ii) a modified space-vector modulation (using flat-top modulation) and (iii) an optimal d-axis current injection for PMSMs and a fault-optimal current reference generation for EESMs. Measurements show that the relative measures $\mathfrak{e}$ for analysing the impacts of open-switch faults can be reduced below 1 % for the PMSM and below 2 % for the EESM.

The beneficial impact of the post-fault control strategies on the wind turbine system performance under open-switch fault was investigated. For this investigation, a scaling of the drive train dynamics of large-scale wind turbine systems for real-time emulation at small-scale laboratory setups based on the ratios of physical SI-units was derived. Using this scaling, the post-fault strategies were applied to WTSs with PMSM and EESM and compared to the fault-free systems. Measurements show that for WTSs with PMSM using the post-fault control strategies, 99 % of the produced energy in the fault-free case can be produced without restrictions on the stator current. Limiting the stator currents to their nominal values, still 93 % of the fault-free energy production is feasible. For WTSs with EESM, 96 % of the fault-free energy production without restrictions on the stator current and 95 % with limitation of the stator current are possible when the proposed post-fault control strategy is applied.

These results show that it is possible for direct-drive WTSs to produce 93 % or more of the

energy in the fault-free case *with* open-switch fault present in the machine-side converter, *without* any changes in the hardware and *without* overloading the electric machine/generator. This is achieved solely by applying a modified post-fault control strategy. Hence, instead of shutting down the WTS in the event of an open-switch fault, almost as much energy can be produced as in the fault-free case.
For further research, it might be of interest to adapt the proposed post-fault strategies to other generator types, that are typically used in WTS with gear box, e.g. DFIM and induction machine (IM). The post-fault control strategies can be adapted to the grid-side of a converter and to electric machines in motor mode as well. Besides the considered wind turbine application, it seems to be promising to also use the obtained EESM flux linkage maps for torque control at higher speeds, for improved field weakening and maximum torque per voltage strategies, e.g. in electric vehicles.

Bibliography

[1] K. Schechner and C. M. Hackl, "Scaling of the drive train dynamics of large-scale wind turbine systems for real-time emulation in small-scale laboratory setups," *IEEE Transactions on Industrial Electronics*, vol. 66, pp. 6779–6788, Sep. 2019.

[2] C. M. Hackl, U. Pecha, and K. Schechner, "Modeling and Control of Permanent-Magnet Synchronous Generators Under Open-Switch Converter Faults," *IEEE Transactions on Power Electronics*, vol. 34, pp. 2966–2979, March 2019.

[3] C. M. Hackl, P. Jané-Soneira, M. Pfeifer, K. Schechner, and S. Hohmann, "Full- and reduced-order state-space modeling of wind turbine systems with permanent magnet synchronous generator," *Energies*, vol. 11, no. 7, 2018.

[4] C. Dirscherl, C. Hackl, and K. Schechner, "Modellierung und Regelung von modernen Windkraftanlagen: Eine Einführung," in *Elektrische Antriebe – Regelung von Antriebssystemen* (D. Schröder, ed.), ch. 24, pp. 1540–1614, Springer-Verlag, 2015.

[5] K. Schechner, F. Bauer, and C. M. Hackl, "Nonlinear DC-link PI Control for Airborne Wind Energy Systems During Pumping Mode," in *Airborne Wind Energy*, pp. 241–276, Springer, 2018.

[6] K. Schechner and C. M. Hackl, "Detection of rotational periodic torque deviations in variable-speed wind turbine systems using disturbance observer and phase-locked loop," *Journal of Physics: Conference Series*, vol. 1037, no. 3, p. 032022, 2018.

[7] C. Hackl and K. Schechner, "Non-ideal feedforward torque control of wind turbines: Impacts on annual energy production & gross earnings," *Journal of Physics: Conference Series*, vol. 753, no. 11, p. 112010, 2016.

[8] C. Dirscherl, C. M. Hackl, and K. Schechner, "Pole-placement based nonlinear state-feedback control of the DC-link voltage in grid-connected voltage source power converters: A preliminary study," in *2015 IEEE Conference on Control Applications (CCA)*, pp. 207–214, Sept 2015.

[9] C. Dirscherl, C. Hackl, and K. Schechner, "Explicit model predictive control with disturbance observer for grid-connected voltage source power converters," in *Proceedings of the 2015 IEEE International Conference on Industrial Technology*, pp. 999–1006, 2015.

[10] C. Kost, S. Shammugam, V. Jülch, H.-T. Nguyen, and T. Schlegl, "Stromgestehungskosten Erneuerbare Energien," tech. rep., Fraunhofer-Institut für Solare Energiesysteme (ISE), 2018.

[11] M. Durstewitz, G. Behem, V. Berkhout, E. Buchmann, R. Cernusko, S. Faulstich, B. Hahn, M.-A. Lutz, S. Pfaffel, F. Rehwald, and S. Spriestersbach, "Windenergie Report Deutschland 2017," tech. rep., Fraunhofer-Institut für Energiewirtschaft und Energiesystemtechnik (IEE), 2018.

[12] IRENA, "Renewable Energy Statistics 2018," tech. rep., The International Renewable Energy Agency, 2018.

[13] F. Blaabjerg and K. Ma, "Wind Energy Systems," *Proceedings of the IEEE*, vol. 105, pp. 2116–2131, Nov 2017.

[14] W. Qiao and D. Lu, "A Survey on Wind Turbine Condition Monitoring and Fault Diagnosis—Part I: Components and Subsystems," *IEEE Transactions on Industrial Electronics*, vol. 62, pp. 6536–6545, Oct 2015.

[15] F. Blaabjerg and K. Ma, "Future on Power Electronics for Wind Turbine Systems," *IEEE Journal of Emerging and Selected Topics in Power Electronics*, vol. 1, pp. 139–152, Sep. 2013.

[16] H. Polinder, J. A. Ferreira, B. B. Jensen, A. B. Abrahamsen, K. Atallah, and R. A. McMahon, "Trends in Wind Turbine Generator Systems," *IEEE Journal of Emerging and Selected Topics in Power Electronics*, vol. 1, pp. 174–185, Sep. 2013.

[17] S. Yang, A. Bryant, P. Mawby, D. Xiang, L. Ran, and P. Tavner, "An Industry-Based Survey of Reliability in Power Electronic Converters," *IEEE Transactions on Industry Applications*, vol. 47, pp. 1441–1451, May 2011.

[18] K. Rothenhagen and F. W. Fuchs, "Performance of diagnosis methods for IGBT open circuit faults in three phase voltage source inverters for AC variable speed drives," in *2005 European Conference on Power Electronics and Applications*, pp. 1–10, Sept 2005.

[19] B. Wang, J. Cai, X. Du, and L. Zhou, "Review of power semiconductor device reliability for power converters," *CPSS Transactions on Power Electronics and Applications*, vol. 2, no. 2, pp. 101–117, 2017.

[20] S. Yang, D. Xiang, A. Bryant, P. Mawby, L. Ran, and P. Tavner, "Condition Monitoring for Device Reliability in Power Electronic Converters: A Review," *IEEE Transactions on Power Electronics*, vol. 25, pp. 2734–2752, Nov 2010.

[21] H. Zhao and L. Cheng, "Open-switch fault-diagnostic method for back-to-back converters of a doubly fed wind power generation system," *IEEE Transactions on Power Electronics*, vol. 33, pp. 3452–3461, April 2018.

[22] B. Lu and S. K. Sharma, "A literature review of IGBT fault diagnostic and protection methods for power inverters," *IEEE Transactions on Industry Applications*, vol. 45, pp. 1770–1777, Sept 2009.

[23] H. T. Eickhoff, R. Seebacher, A. Muetze, and E. G. Strangas, "Enhanced and fast detection of open-switch faults in inverters for electric drives," *IEEE Transactions on Industry Applications*, vol. 53, pp. 5415–5425, Nov 2017.

[24] U. M. Choi, J. S. Lee, F. Blaabjerg, and K. B. Lee, "Open-circuit fault diagnosis and fault-tolerant control for a grid-connected NPC inverter," *IEEE Transactions on Power Electronics*, vol. 31, pp. 7234–7247, Oct 2016.

[25] J. S. Lee, K. B. Lee, and F. Blaabjerg, "Open-switch fault detection method of a back-to-back converter using NPC topology for wind turbine systems," *IEEE Transactions on Industry Applications*, vol. 51, pp. 325–335, Jan 2015.

[26] U. M. Choi, K. B. Lee, and F. Blaabjerg, "Diagnosis and tolerant strategy of an open-switch fault for T-type three-level inverter systems," *IEEE Transactions on Industry Applications*, vol. 50, pp. 495–508, Jan 2014.

[27] U. M. Choi, H. G. Jeong, K. B. Lee, and F. Blaabjerg, "Method for detecting an open-switch fault in a grid-connected NPC inverter system," *IEEE Transactions on Power Electronics*, vol. 27, pp. 2726–2739, June 2012.

[28] W.-S. Im, J.-S. Kim, J.-M. Kim, D.-C. Lee, and K.-B. Lee, "Diagnosis methods for IGBT open switch fault applied to 3-phase AC/DC PWM converter," *Journal of Power Electronics*, vol. 12, no. 1, 2012.

[29] N. M. A. Freire, J. O. Estima, and A. J. M. Cardoso, "Open-circuit fault diagnosis in PMSG drives for wind turbine applications," *IEEE Transactions on Industrial Electronics*, vol. 60, pp. 3957–3967, Sept 2013.

[30] I. Jlassi, J. O. Estima, S. K. E. Khil, N. M. Bellaaj, and A. J. M. Cardoso, "Multiple Open-Circuit Faults Diagnosis in Back-to-Back Converters of PMSG Drives for Wind Turbine Systems," *IEEE Transactions on Power Electronics*, vol. 30, pp. 2689–2702, May 2015.

[31] M. N. Soares, M. Yves, M. Kinnaert, J. Helsen, and J. Gyselinck, "Robust Power-Electronic-Converter Fault Detection and Isolation Technique for DFIG Wind Turbines," *Journal of Physics: Conference Series*, vol. 1037, no. 3, p. 032043, 2018.

[32] J. O. Estima and A. J. M. Cardoso, "A new approach for real-time multiple open-circuit fault diagnosis in voltage-source inverters," *IEEE Transactions on Industry Applications*, vol. 47, pp. 2487–2494, Nov 2011.

[33] D. U. Campos-Delgado, J. A. Pecina-Sanchez, D. R. Espinoza-Trejo, and E. R. Arce-Santana, "Diagnosis of open-switch faults in variable speed drives by stator current analysis and pattern recognition," *IET Electric Power Applications*, vol. 7, pp. 509–522, July 2013.

[34] N. M. A. Freire, J. O. Estima, and A. J. M. Cardoso, "A Voltage-Based Approach Without Extra Hardware for Open-Circuit Fault Diagnosis in Closed-Loop PWM AC Regenerative Drives," *IEEE Transactions on Industrial Electronics*, vol. 61, pp. 4960–4970, Sep. 2014.

[35] H. Yan, Y. Xu, J. Zou, Y. Fang, and F. Cai, "A Novel Open-Circuit Fault Diagnosis Method for Voltage Source Inverters With a Single Current Sensor," *IEEE Transactions on Power Electronics*, vol. 33, pp. 8775–8786, Oct 2018.

[36] W. Yang, P. J. Tavner, C. J. Crabtree, Y. Feng, and Y. Qiu, "Wind turbine condition monitoring: technical and commercial challenges," *Wind Energy*, vol. 17, no. 5, pp. 673–693, 2014.

[37] W. S. Im, J. M. Kim, D. C. Lee, and K. B. Lee, "Diagnosis and fault-tolerant control of three-phase AC-DC PWM converter systems," *IEEE Transactions on Industry Applications*, vol. 49, pp. 1539–1547, July 2013.

[38] P. Sobanski and T. Orlowska-Kowalska, "Analysis of space vector modulation technique in inverter-fed fault-tolerant induction motor drive," in *2014 16th International Power Electronics and Motion Control Conference and Exposition*, pp. 1024–1029, Sept 2014.

[39] W. S. Im, J. J. Moon, J. M. Kim, D. C. Lee, and K. B. Lee, "Fault tolerant control strategy of 3-phase AC-DC PWM converter under multiple open-switch faults conditions," in *2012 Twenty-Seventh Annual IEEE Applied Power Electronics Conference and Exposition (APEC)*, pp. 789–795, Feb 2012.

[40] S. M. Jung, K. Lee, and H. W. Kim, "Post-fault operation of open-circuit fault in three-phase PWM converter," in *2014 16th International Power Electronics and Motion Control Conference and Exposition*, pp. 311–316, Sept 2014.

[41] J. S. Lee and K. B. Lee, "An open-switch fault detection method and tolerance controls based on SVM in a grid-connected T-type rectifier with unity power factor," *IEEE Transactions on Industrial Electronics*, vol. 61, pp. 7092–7104, Dec 2014.

[42] J. S. Lee and K. B. Lee, "Open-switch fault tolerance control for a three-level NPC/T-type rectifier in wind turbine systems," *IEEE Transactions on Industrial Electronics*, vol. 62, pp. 1012–1021, Feb 2015.

[43] N. M. A. Freire, *Fault-tolerant permanent magnet synchronous generator drives for wind turbine applications*. PhD thesis, University of Coimbra, 2013.

[44] N. M. A. Freire and A. J. M. Cardoso, "Fault-Tolerant PMSG Drive With Reduced DC-Link Ratings for Wind Turbine Applications," *IEEE Journal of Emerging and Selected Topics in Power Electronics*, vol. 2, pp. 26–34, March 2014.

[45] N. M. A. Freire and A. J. M. Cardoso, "A Fault-Tolerant PMSG Drive for Wind Turbine Applications With Minimal Increase of the Hardware Requirements," *IEEE Transactions on Industry Applications*, vol. 50, pp. 2039–2049, May 2014.

[46] A. Gaeta, G. Scelba, and A. Consoli, "Modeling and control of three-phase PMSMs under open-phase fault," *IEEE Transactions on Industry Applications*, vol. 49, pp. 74–83, Jan 2013.

[47] O. Wallmark, L. Harnefors, and O. Carlson, "Post-fault operation of fault-tolerant inverters for PMSM drives," in *2005 European Conference on Power Electronics and Applications*, pp. 1–10, Sept 2005.

[48] S. Bolognani, M. Zordan, and M. Zigliotto, "Experimental fault-tolerant control of a PMSM drive," *IEEE Transactions on Industrial Electronics*, vol. 47, pp. 1134–1141, Oct 2000.

[49] H. T. Eickhoff, R. Seebacher, A. Muetze, and E. G. Strangas, "Post-Fault Operation Strategy for Single Switch Open-Circuit Faults in Electric Drives," *IEEE Transactions on Industry Applications*, vol. 54, pp. 2381–2391, May 2018.

[50] K. Fischer, T. Stalin, H. Ramberg, T. Thiringer, J. Wenske, and R. Karlsson, "Investigation of converter failure in wind turbines," *Elforsk report*, vol. 12, p. 58, 2012.

[51] C. M. Hackl, *Non-identifier based adaptive control in mechatronics: Theory and Application*. No. 466 in Lecture Notes in Control and Information Sciences, Berlin: Springer International Publishing, 2017.

[52] H. Eldeeb, C. M. Hackl, L. Horlbeck, and J. Kullick, "A unified theory for optimal feed-forward torque control of anisotropic synchronous machines," *International Journal of Control*, vol. 91, no. 10, pp. 2273–2302, 2018.

[53] D. Schröder, *Elektrische Antriebe - Regelung von Antriebssystemen*. Berlin Heidelberg: Springer-Verlag, 4 ed., 2015.

[54] R. De Doncker, D. W. Pulle, and A. Veltman, *Advanced Electrical Drives*. Power Systems, Berlin: Springer-Verlag, 2011.

[55] M. Ahmad, *High Performance AC Drives: Modelling Analysis and Control*. Springer Science & Business Media, 2010.

[56] D. Schröder, *Elektrische Antriebe — Grundlagen (6. Auflage)*. Berlin: Springer-Verlag, 2017.

[57] E. Bolte, *Elektrische Maschinen: Grundlagen · Magnetfelder · Erwärmung · Funktionsprinzipien · Betriebsarten · Einsatz · Entwurf · Wirtschaftlichkeit*. Springer-Verlag, 2018.

[58] I. Jeong, B. Gu, J. Kim, K. Nam, and Y. Kim, "Inductance Estimation of Electrically Excited Synchronous Motor via Polynomial Approximations by Least Square Method," *IEEE Transactions on Industry Applications*, vol. 51, pp. 1526–1537, March 2015.

[59] R. Grune, *Verlustoptimaler Betrieb einer elektrisch erregten Synchronmaschine für den Einsatz in Elektrofahrzeugen*. PhD thesis, Technische Universität Berlin, 2013.

[60] P. Krause, O. Wasynczuk, and S. D. Sudhoff, *Analysis of electric machinery and drive systems*. John Wiley & Sons, 2 ed., 2002.

[61] P. Vas, *Electrical Machines and Drives: A space-vector theory approach*, vol. 25. Oxford University Press on Demand, 1992.

[62] S. D. Umans, A. Fitzgerald, and C. Kingsley, *Electric machinery*. McGrew-Hill Series in Electrical Engineering, 2013.

[63] A. Doria-Cerezo, C. Batlle, and G. Espinosa-Perez, "Passivity-based control of a wound-rotor synchronous motor," *IET Control Theory Applications*, vol. 4, pp. 2049–2057, October 2010.

[64] R. S. Munoz-Aguilar, A. Doria-Cerezo, E. Fossas, and R. Cardoner, "Sliding Mode Control of a Stand-Alone Wound Rotor Synchronous Generator," *IEEE Transactions on Industrial Electronics*, vol. 58, pp. 4888–4897, Oct 2011.

[65] S. C. Carpiuc, C. Lazar, and D. I. Patrascu, "Optimal torque control of the externally excited synchronous machine," *Journal of Control Engineering and Applied Informatics*, vol. 14, no. 2, pp. 80–88, 2012.

[66] A. Doria-Cerezo, V. I. Utkin, R. S. Munoz-Aguilar, and E. Fossas, "Control of a Stand-Alone Wound Rotor Synchronous Generator: Two Sliding Mode Approaches via Regulation of the d-Voltage Component," *IEEE Transactions on Control Systems Technology*, vol. 20, pp. 779–786, May 2012.

[67] O. Haala, B. Wagner, M. Hofmann, and M. März, "Optimal current control of externally excited synchronous machines in automotive traction drive applications," *International Journal of Electrical, Computer, Energetic, Electronic and Communication Engineering*, vol. 7, no. 9, pp. 1133–1139, 2013.

[68] Y. Kim and K. Nam, "Copper-Loss-Minimizing Field Current Control Scheme for Wound Synchronous Machines," *IEEE Transactions on Power Electronics*, vol. 32, pp. 1335–1345, Feb 2017.

[69] J. Tang and Y. Liu, "Comparison of copper loss minimization and field current minimization for Electrically Excited Synchronous Motor in mild hybrid drives," in *2017 19th European Conference on Power Electronics and Applications (EPE'17 ECCE Europe)*, pp. 1–10, Sep. 2017.

[70] Y. Nie, I. P. Brown, and D. C. Ludois, "Deadbeat-Direct Torque and Flux Control for Wound Field Synchronous Machines," *IEEE Transactions on Industrial Electronics*, vol. 65, pp. 2069–2079, March 2018.

[71] D. Uzel, Z. Peroutka, V. Šmídl, T. Košan, and K. Zeman, "Self-Sensing Control of Wound Rotor Synchronous Motor Drive for Mine Hoist," *IEEE Transactions on Industrial Electronics*, vol. 65, pp. 2009–2017, March 2018.

[72] I. Jeong, J. Kim, Y. Kim, and K. Nam, "Extended MTPA with cross coupling inductances for electrically excited synchronous motors," in *2013 IEEE Energy Conversion Congress and Exposition*, pp. 867–873, Sep. 2013.

[73] M. Seilmeier, "Modelling of electrically excited synchronous machine (EESM) considering nonlinear material characteristics and multiple saliencies," in *Proceedings of the 2011 14th European Conference on Power Electronics and Applications*, pp. 1–10, Aug 2011.

[74] R. Wang, S. Pekarek, and M. Bash, "Alternative excitation strategies for a wound rotor synchronous machine drive," in *2012 IEEE Energy Conversion Congress and Exposition (ECCE)*, pp. 2300–2307, Sep. 2012.

[75] H. Liu, L. Xu, M. Shangguan, and W. N. Fu, "Finite Element Analysis of 1 MW High Speed Wound-Rotor Synchronous Machine," *IEEE Transactions on Magnetics*, vol. 48, pp. 4650–4653, Nov 2012.

[76] S. L. Kellner and B. Piepenbreier, "General PMSM d,q-model using optimized interpolated absolute and differential inductance surfaces," in *2011 IEEE International Electric Machines Drives Conference (IEMDC)*, pp. 212–217, May 2011.

[77] N. R. Averous, M. Stieneker, S. Kock, C. Andrei, A. Helmedag, R. W. D. Doncker, K. Hameyer, G. Jacobs, and A. Monti, "Development of a 4 MW full-size wind-turbine test bench," *IEEE Journal of Emerging and Selected Topics in Power Electronics*, vol. 5, pp. 600–609, Jun. 2017.

[78] L. J. Fingersh, M. M. Hand, and A. S. Laxson, "Wind turbine design cost and scaling model," tech. rep., National Renewable Energy Laboratory (NREL), 2006.

[79] F. Campagnolo, *Wind tunnel testing of scaled wind turbine models: aerodynamics and beyond*. PhD thesis, Politecnico di Milano, 2013.

[80] C. L. Bottasso, F. Campagnolo, and V. Petrović, "Wind tunnel testing of scaled wind turbine models: Beyond aerodynamics," *Journal of Wind Engineering and Industrial Aerodynamics*, vol. 127, pp. 11–28, Apr. 2014.

[81] H. R. Martin, "Development of a scale model wind turbine for testing of offshore floating wind turbine systems," Master's thesis, Maine Maritime Academy, 2011.

[82] B. J. Koo, A. J. Goupee, R. W. Kimball, and K. F. Lambrakos, "Model tests for a floating wind turbine on three different floaters," *Journal of Offshore Mechanics and Arctic Engineering*, vol. 136, p. 021904, Mar. 2014.

[83] Y. Zhang, A. Huston, R. D. Palmer, R. Albertson, F. Kong, and S. Wang, "Using scaled models for wind turbine EM scattering characterization: Techniques and experiments," *IEEE Transactions on Instrumentation and Measurement*, vol. 60, pp. 1298–1306, Apr. 2011.

[84] A. Miller, E. Muljadi, and D. S. Zinger, "A variable speed wind turbine power control," *IEEE Transactions on Energy Conversion*, vol. 12, pp. 181–186, Jun 1997.

[85] T. Hardy and W. Jewell, "Hardware-in-the-loop wind turbine simulation platform for a laboratory feeder model," *IEEE Transactions on Sustainable Energy*, vol. 5, pp. 1003–1009, July 2014.

[86] D. Dolan and P. W. Lehn, "Real-time wind turbine emulator suitable for power quality and dynamic control studies," in *Proceedings of the International Conference on Power Systems Transients*, 2005.

[87] F. Huerta, R. L. Tello, and M. Prodanovic, "Real-time power-hardware-in-the-loop implementation of variable-speed wind turbines," *IEEE Transactions on Industrial Electronics*, vol. 64, pp. 1893–1904, March 2017.

[88] L. Peretti and V. Särkimäki, "Mechanical drive train emulation by means of electrical drives - a generalised approach," in *IECON 2012 - 38th Annual Conference on IEEE Industrial Electronics Society*, pp. 1888–1893, Oct 2012.

[89] L. Peretti, V. Särkimäki, and J. Faber, "A wind turbine emulator for generator control algorithm development," in *2013 IEEE International Conference on Industrial Technology (ICIT)*, pp. 228–233, Feb 2013.

[90] B. Neammanee, S. Sirisumrannukul, and S. Chatratana, "Development of a wind turbine simulator for wind generator testing," *International Energy Journal*, vol. 8, no. 1, pp. 21–28, 2007.

[91] C. Dirscherl, J. Fessler, C. M. Hackl, and H. Ipach, "State-feedback controller and observer design for grid-connected voltage source power converters with LCL-filter," in *2015 IEEE Conference on Control Applications (CCA)*, pp. 215–222, Sep. 2015.

[92] R. Teodorescu, M. Liserre, and P. Rodríguez, *Grid Converters for Photovoltaic and Wind Power Systems*. Chichester, United Kingdom: John Wiley & Sons, Ltd., 2011.

[93] R. Gasch and J. Twetle, *Windkraftanlagen — Grundlagen, Entwurf, Planung und Betrieb*. Vieweg+Teubner Verlag, 8. ed., 2013.

[94] S. Heier, *Windkraftanlagen: Systemauslegung, Netzintegration und Regelung*. Vieweg+Teubner Verlag, 5. ed., 2009.

[95] T. Ackermann, ed., *Wind Power in Power Systems*. Chichester, United Kingdom: John Wiley & Sons, Ltd., 2012.

[96] T. Burton, D. Sharpe, N. Jenkins, and E. Bossanyi, *Wind energy handbook*. John Wiley & Sons, 2 ed., 2011.

[97] G. Michalke, *Variable Speed Wind Turbines – Modelling, Control, and Impact on Power Systems*. PhD thesis, Technische Universität Darmstadt, 2008.

[98] F. W. Koch, *Simulation und Analyse der dynamischen Wechselwirkung von Windenergieanlagen mit dem Elektroenergiesystem*. PhD thesis, Universität Duisburg-Essen, 2005.

[99] J. Slootweg, S. W. H. De Haan, H. Polinder, and W. Kling, "General model for representing variable speed wind turbines in power system dynamics simulations," *IEEE Transactions on Power Systems*, vol. 18, no. 1, pp. 144–151, 2003.

[100] S. M. Muyeen, M. H. Ali, R. Takahashi, T. Murata, J. Tamura, Y. Tomaki, A. Sakahara, and E. Sasano, "Comparative study on transient stability analysis of wind turbine generator system using different drive train models," *IET Renewable Power Generation*, vol. 1, pp. 131–141, June 2007.

[101] G. Müller and B. Ponick, *Grundlagen elektrischer Maschinen*. New York: John Wiley & Sons, 2012.

[102] G. Müller and B. Ponick, *Theorie elektrischer Maschinen*, vol. 3. Wiley-VCH, 6. ed., 2009.

[103] P. L. Xu and Z. Q. Zhu, "Carrier signal injection-based sensorless control for permanent-magnet synchronous machine drives considering machine parameter asymmetry," *IEEE Transactions on Industrial Electronics*, vol. 63, pp. 2813–2824, May 2016.

[104] R. L. de Araujo Ribeiro, C. B. Jacobina, E. R. C. da Silva, and A. M. N. Lima, "Fault detection of open-switch damage in voltage-fed PWM motor drive systems," *IEEE Transactions on Power Electronics*, vol. 18, pp. 587–593, Mar 2003.

[105] K. H. Kim, D. U. Choi, B. G. Gu, and I. S. Jung, "Fault model and performance evaluation of an inverter-fed permanent magnet synchronous motor under winding shorted turn and inverter switch open," *IET Electric Power Applications*, vol. 4, pp. 214–225, April 2010.

[106] S. M. Jung, J. S. Park, H. W. Kim, K. Y. Cho, and M. J. Youn, "An MRAS-based diagnosis of open-circuit fault in PWM voltage-source inverters for PM synchronous motor drive systems," *IEEE Transactions on Power Electronics*, vol. 28, pp. 2514–2526, May 2013.

[107] Q.-H. Tran, T.-W. Chun, and H.-H. Lee, "Fault tolerant strategy for inverter stage in indirect matrix converter," in *IECON 2013 - 39th Annual Conference of the IEEE Industrial Electronics Society*, pp. 4844–4849, Nov 2013.

[108] J. Mullen and J. B. Hoagg, "Wind turbine torque control for unsteady wind speeds using approximate-angular-acceleration feedback," in *Inproceedings of the 52nd IEEE Conference on Decision and Control*, (Florence, Italy), pp. 397–402, 2013.

[109] L. Y. Pao and K. E. Johnson, "Control of wind turbines: Approaches, challenges, and recent developments," *IEEE Control Systems Magazine*, vol. 31, no. 2, pp. 44–62, 2011.

[110] M. Schubert, "Verfahren zur Regelung einer Windenergieanlage und Windenergieanlage mit einem Rotor," Patent DE102004054608B4, 2006.

[111] C. Dirscherl and C. M. Hackl, "Local Stability Analysis and Controller Design for Speed-Controlled Wind Turbine Systems in Regime II.5," *Energies*, vol. 11, no. 5, 2018.

[112] D. Schröder, *Leistungselektronische Schaltungen: Funktion, Auslegung und Anwendung*. Berlin, Heidelberg: Springer DE, 2012.

[113] D. G. Holmes and T. A. Lipo, *Pulse width modulation for power converters: principles and practice*, vol. 18. John Wiley & Sons, 2003.

[114] U. Pecha, "Modellierung eines fehlerhaften 2-Level-Spannungszwischenkreisumrichters und darauf basierende Adaption der Stromregelung des Generators in Windkraftanlagensystemen mit Permanentmagnet-Synchronmaschine," Master's thesis, Research Group "Control of Renewable Energy Systems", Technische Universität München, 2017.

[115] C. M. Hackl, M. J. Kamper, J. Kullick, and J. Mitchell, "Current control of reluctance synchronous machines with online adjustment of the controller parameters," in *2016 IEEE 25th International Symposium on Industrial Electronics (ISIE)*, pp. 153–160, June 2016.

[116] R. Valentine, *Motor Control Electronics Handbook*. McGraw-Hill Handbooks, McGraw-Hill Companies, 1998.

[117] dSPACE GmbH, "Catalog 2018," 2018.

[118] H. Eldeeb, C. M. Hackl, L. Horlbeck, and J. Kullick, "Analytical solutions for the optimal reference currents for MTPC/MTPA, MTPV and MTPF control of anisotropic synchronous machines," in *Proceedings of the IEEE International Electric Machines & Drives Conference (IEMDC 2017)*, (Miami, FL, USA), 2017.

[119] E. Buckingham, "On physically similar systems; illustrations of the use of dimensional equations," *Physical Review*, vol. 4, no. 4, p. 345, 1914.

[120] MathWorks, "Documentation Matlab R2017b," 2017.

[121] "Discussion with P. Landsmann on the measurement of exciter flux maps," 2018-04-17.

[122] S. Kuehl and R. M. Kennel, "Measuring magnetic characteristics of synchronous machines by applying position estimation techniques," *IEEE Transactions on Industry Applications*, vol. 50, pp. 3816–3824, Nov 2014.

[123] "Discussions with A. Bujandrić, C. Dirscherl, H. Eldeeb, C. M. Hackl, J. Kullick, M. Landerer, M. Lindner, R. Moderegger, N. Monzen, U. Pecha, P. Schmitz," 2013-2019.

List of Figures

List of Tables

Appendix A

Space-vector theory

Working with three-phase systems requires space-vector theory, which will be revisited here briefly.

A.1 Clarke transformation

The Clarke transformation transforms a three-phase *abc*-coordinate system shifted (spatially or/and temporally) by 120° into the orthogonal $\alpha\beta\gamma$-coordinate system (see Fig. A.1).

A.1.1 General Clarke transformation

The general Clarke transformation matrix $\boldsymbol{T}_C$ and its inverse $\boldsymbol{T}_C^{-1}$ depend on the scaling factor κ and are defined as follows

$$\boldsymbol{T}_C := \kappa \begin{bmatrix} 1 & -\frac{1}{2} & -\frac{1}{2} \\ 0 & \frac{\sqrt{3}}{2} & -\frac{\sqrt{3}}{2} \\ \frac{1}{\sqrt{2}} & \frac{1}{\sqrt{2}} & \frac{1}{\sqrt{2}} \end{bmatrix}, \qquad \boldsymbol{T}_C^{-1} := \frac{1}{\kappa} \begin{bmatrix} \frac{2}{3} & 0 & \frac{\sqrt{2}}{3} \\ -\frac{1}{3} & \frac{\sqrt{3}}{3} & \frac{\sqrt{2}}{3} \\ -\frac{1}{3} & -\frac{\sqrt{3}}{3} & \frac{\sqrt{2}}{3} \end{bmatrix}, \qquad \kappa \in \mathbb{R}. \tag{A.1.1}$$

Applying the Clarke transformation and the inverse Clarke transformation to quantities $\boldsymbol{\xi}^{abc}$ and $\boldsymbol{\xi}^{\alpha\beta\gamma}$ yields,

$$\boldsymbol{\xi}^{\alpha\beta\gamma} := \begin{pmatrix} \xi^\alpha \\ \xi^\beta \\ \xi^\gamma \end{pmatrix} = \boldsymbol{T}_C \boldsymbol{\xi}^{abc} \quad \text{and} \quad \boldsymbol{\xi}^{abc} := \begin{pmatrix} \xi^a \\ \xi^b \\ \xi^c \end{pmatrix} = \boldsymbol{T}_C^{-1} \boldsymbol{\xi}^{\alpha\beta\gamma}, \tag{A.1.2}$$

respectively. $\boldsymbol{\xi}^{abc} \in \mathbb{R}^3$ with elements ξ^a, ξ^b, ξ^c is a vector in the *abc*-coordinate system and $\boldsymbol{\xi}^{\alpha\beta\gamma} \in \mathbb{R}^3$ with elements ξ^α, ξ^β, ξ^γ is a vector in the $\alpha\beta\gamma$-coordinate system.

A.1.2 Reduced Clarke transformation

If it is known, that the *abc*-quantities fulfil the condition

$$\forall t \geq 0 : \qquad \xi^a(t) + \xi^b(t) + \xi^c(t) = 0, \tag{A.1.3}$$

the reduced Clarke transformation can be used, i.e.

$$\boldsymbol{\xi}^{\alpha\beta} := \begin{pmatrix} \xi^\alpha \\ \xi^\beta \end{pmatrix} = \boldsymbol{T}_c \boldsymbol{\xi}^{abc}, \qquad \boldsymbol{\xi}^{abc} = \boldsymbol{T}_c^{-1} \boldsymbol{\xi}^{\alpha\beta}, \tag{A.1.4}$$

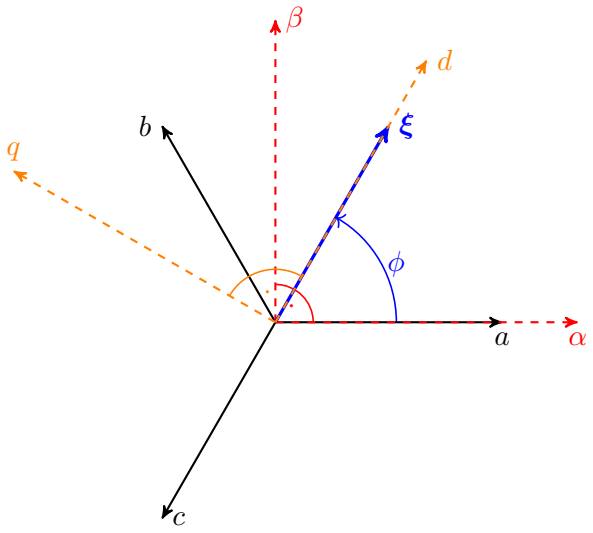

Figure A.1: *Different coordinate systems (abc-coordinate system, fixed orthogonal αβ-coordinate system and rotating orthogonal dq-coordinate system) and space-vector* $\boldsymbol{\xi}$.

with reduced Clarke transformation matrix and reduced inverse:

$$\boldsymbol{T}_c := \kappa \begin{bmatrix} 1 & -\frac{1}{2} & -\frac{1}{2} \\ 0 & \frac{\sqrt{3}}{2} & -\frac{\sqrt{3}}{2} \end{bmatrix}, \qquad \boldsymbol{T}_c^{-1} := \frac{1}{\kappa} \begin{bmatrix} \frac{2}{3} & 0 \\ -\frac{1}{3} & \frac{\sqrt{3}}{3} \\ -\frac{1}{3} & -\frac{\sqrt{3}}{3} \end{bmatrix}. \tag{A.1.5}$$

The zero component ξ^γ can be neglected, since $\xi^\gamma = \frac{\kappa}{\sqrt{2}}(\xi^a + \xi^b + \xi^c) \overset{(A.1.3)}{=} 0$.

A.1.3 Choice of scaling factor

For the scaling factor κ, two choices are common. For a power correct transformation, the choice

$$\kappa = \sqrt{\frac{2}{3}} \tag{A.1.6}$$

is used, for an amplitude correct scaling, the factor

$$\kappa = \frac{2}{3} \tag{A.1.7}$$

is used. The power calculation depends on the choice of κ, since

$$\begin{aligned} p &= \left(\boldsymbol{u}^{abc}\right)^\top \boldsymbol{i}^{abc} = \left(\boldsymbol{T}_C^{-1}\boldsymbol{u}^{\alpha\beta\gamma}\right)^\top \boldsymbol{T}_C^{-1}\boldsymbol{i}^{\alpha\beta\gamma} \\ &= \left(\boldsymbol{u}^{\alpha\beta\gamma}\right)^\top \underbrace{\left(\boldsymbol{T}_C^{-1}\right)^\top \boldsymbol{T}_C^{-1}}_{:=\boldsymbol{T}_{C,p}} \boldsymbol{i}^{\alpha\beta\gamma} = \left(\boldsymbol{u}^{\alpha\beta\gamma}\right)^\top \boldsymbol{T}_{C,p}\boldsymbol{i}^{\alpha\beta\gamma} \end{aligned} \tag{A.1.8}$$

with

$$\boldsymbol{T}_{C,p} = \left(\boldsymbol{T}_C^{-1}\right)^\top \boldsymbol{T}_C^{-1} = \frac{1}{\kappa^2}\begin{bmatrix}\frac{2}{3} & 0 & 0\\ 0 & \frac{2}{3} & 0\\ 0 & 0 & \frac{2}{3}\end{bmatrix} \quad \text{or} \quad \boldsymbol{T}_{c,p} = \left(\boldsymbol{T}_c^{-1}\right)^\top \boldsymbol{T}_c^{-1} = \frac{1}{\kappa^2}\begin{bmatrix}\frac{2}{3} & 0\\ 0 & \frac{2}{3}\end{bmatrix}. \tag{A.1.9}$$

The power calculates to

$$p = \tfrac{2}{3\kappa^2}\left(\boldsymbol{u}^{\alpha\beta\gamma}\right)^\top \boldsymbol{i}^{\alpha\beta\gamma} \tag{A.1.10}$$

and simplifies with negligible zero component (i.e. $u^\gamma = 0$ and/or $i^\gamma = 0$) to

$$p = \tfrac{2}{3\kappa^2}\left(\boldsymbol{u}^{\alpha\beta}\right)^\top \boldsymbol{i}^{\alpha\beta}\,. \tag{A.1.11}$$

A.2 Park transformation

The Park transformation rotates a vector by the (possibly time varying) angle ϕ (in rad), see Fig. A.1.

A.2.1 General Park transformation

The general Park transformation matrix and its inverse are given by

$$\boldsymbol{T}_P(\phi) := \begin{bmatrix}\cos(\phi) & -\sin(\phi) & 0\\ \sin(\phi) & \cos(\phi) & 0\\ 0 & 0 & 1\end{bmatrix} \quad \text{and} \quad \boldsymbol{T}_P^{-1}(\phi) := \begin{bmatrix}\cos(\phi) & \sin(\phi) & 0\\ -\sin(\phi) & \cos(\phi) & 0\\ 0 & 0 & 1\end{bmatrix}, \tag{A.2.12}$$

respectively. Their derivatives are

$$\begin{aligned}\tfrac{\mathrm{d}}{\mathrm{d}t}\boldsymbol{T}_P(\phi) :=& \omega\begin{bmatrix}-\sin(\phi) & -\cos(\phi) & 0\\ \cos(\phi) & -\sin(\phi) & 0\\ 0 & 0 & 0\end{bmatrix} = \omega\boldsymbol{J}_{3\times3}\boldsymbol{T}_P(\phi) = \omega\boldsymbol{T}_P(\phi)\boldsymbol{J}_{3\times3}\,,\\ \tfrac{\mathrm{d}}{\mathrm{d}t}\boldsymbol{T}_P^{-1}(\phi) :=& \omega\begin{bmatrix}-\sin(\phi) & \cos(\phi) & 0\\ -\cos(\phi) & -\sin(\phi) & 0\\ 0 & 0 & 0\end{bmatrix} = -\omega\boldsymbol{J}_{3\times3}\boldsymbol{T}_P^{-1}(\phi) = -\omega\boldsymbol{T}_P^{-1}(\phi)\boldsymbol{J}_{3\times3}\,,\end{aligned} \tag{A.2.13}$$

where

$$\boldsymbol{J}_{3\times3} := \begin{bmatrix}0 & -1 & 0\\ 1 & 0 & 0\\ 0 & 0 & 0\end{bmatrix} = \begin{bmatrix}\boldsymbol{J} & \boldsymbol{0}_{2\times1}\\ \boldsymbol{0}_{1\times2} & 0\end{bmatrix} \neq \boldsymbol{T}_P(\tfrac{\pi}{2}) \quad \text{and} \quad \omega = \tfrac{\mathrm{d}}{\mathrm{d}t}\phi\,. \tag{A.2.14}$$

The transformation of a vector $\boldsymbol{\xi}^{\alpha\beta\gamma}$ in the stator-fixed $\alpha\beta\gamma$-coordinate system into the rotating *dqo*-coordinate system yields a vector $\boldsymbol{\xi}^{dqo} \in \mathbb{R}^3$ with elements ξ^d, ξ^q, ξ^o (or vice versa), i.e.

$$\boldsymbol{\xi}^{dqo} := \begin{pmatrix}\xi^d\\ \xi^q\\ \xi^o\end{pmatrix} = \boldsymbol{T}_P^{-1}(\phi)\boldsymbol{\xi}^{\alpha\beta\gamma} \quad \text{and} \quad \boldsymbol{\xi}^{\alpha\beta\gamma} = \boldsymbol{T}_P(\phi)\boldsymbol{\xi}^{dqo}\,. \tag{A.2.15}$$

The different coordinate systems are illustrated in Fig. A.1.

Remark A.2.1 (Combination of Clarke and Park transformation)**.** *Combining Clarke and Park transformation leads to the following transformation rules*

$$\boldsymbol{\xi}^{dqo} = \boldsymbol{T}_P^{-1}(\phi)\boldsymbol{T}_C\boldsymbol{\xi}^{abc} = \kappa \begin{bmatrix} \cos(\phi) & \cos(\phi - \frac{2\pi}{3}) & \cos(\phi - \frac{4\pi}{3}) \\ -\sin(\phi) & -\sin(\phi - \frac{2\pi}{3}) & -\sin(\phi - \frac{4\pi}{3}) \\ \frac{1}{\sqrt{2}} & \frac{1}{\sqrt{2}} & \frac{1}{\sqrt{2}} \end{bmatrix} \boldsymbol{\xi}^{abc} \tag{A.2.16}$$

and

$$\boldsymbol{\xi}^{abc} = \boldsymbol{T}_C^{-1}\boldsymbol{T}_P(\phi)\boldsymbol{\xi}^{dqo} = \frac{2}{3\kappa} \begin{bmatrix} \cos(\phi) & -\sin(\phi) & \frac{1}{\sqrt{2}} \\ \cos(\phi - \frac{2\pi}{3}) & -\sin(\phi - \frac{2\pi}{3}) & \frac{1}{\sqrt{2}} \\ \cos(\phi - \frac{4\pi}{3}) & -\sin(\phi - \frac{4\pi}{3}) & \frac{1}{\sqrt{2}} \end{bmatrix} \boldsymbol{\xi}^{dqo}. \tag{A.2.17}$$

A.2.2 Reduced Park transformation

For the reduced Park transformation the following matrices are used

$$\boldsymbol{T}_p(\phi) := \begin{bmatrix} \cos(\phi) & -\sin(\phi) \\ \sin(\phi) & \cos(\phi) \end{bmatrix} \quad \text{and} \quad \boldsymbol{T}_p^{-1}(\phi) := \begin{bmatrix} \cos(\phi) & \sin(\phi) \\ -\sin(\phi) & \cos(\phi) \end{bmatrix}. \tag{A.2.18}$$

Their time derivatives are given by

$$\begin{aligned} \tfrac{\mathrm{d}}{\mathrm{d}t}\boldsymbol{T}_p(\phi) :=& \omega \begin{bmatrix} -\sin(\phi) & -\cos(\phi) \\ \cos(\phi) & -\sin(\phi) \end{bmatrix} = \omega\boldsymbol{J}\boldsymbol{T}_p(\phi) = \omega\boldsymbol{T}_p(\phi)\boldsymbol{J}, \\ \tfrac{\mathrm{d}}{\mathrm{d}t}\boldsymbol{T}_p^{-1}(\phi) :=& \omega \begin{bmatrix} -\sin(\phi) & \cos(\phi) \\ -\cos(\phi) & -\sin(\phi) \end{bmatrix} = -\omega\boldsymbol{J}\boldsymbol{T}_p^{-1}(\phi) = -\omega\boldsymbol{T}_p^{-1}(\phi)\boldsymbol{J}, \end{aligned} \tag{A.2.19}$$

with

$$\boldsymbol{J} := \boldsymbol{T}_p(\tfrac{\pi}{2}) = \begin{bmatrix} 0 & -1 \\ 1 & 0 \end{bmatrix} \quad \text{and} \quad \omega \overset{\text{(A.2.14)}}{=} \tfrac{\mathrm{d}}{\mathrm{d}t}\phi\,. \tag{A.2.20}$$

The reduced Park transformation is obtained as follows

$$\boldsymbol{\xi}^{dq} := \begin{pmatrix} \xi^d \\ \xi^q \end{pmatrix} = \boldsymbol{T}_p^{-1}(\phi)\boldsymbol{\xi}^{\alpha\beta} \quad \text{or (vice-versa)} \quad \boldsymbol{\xi}^{\alpha\beta} = \boldsymbol{T}_p(\phi)\boldsymbol{\xi}^{dq}. \tag{A.2.21}$$

A.3 Line-to-line transformation

Transforming phase quantities $\boldsymbol{\xi}^{abc}$ into line-to-line quantities $\boldsymbol{\xi}^{a\text{-}b\text{-}c} = (\xi^{a\text{-}b}, \xi^{b\text{-}c}, \xi^{c\text{-}a})^\top$ is done using transformation matrix $\boldsymbol{T}_{\mathrm{ltl}}$, i.e.

$$\boldsymbol{\xi}^{a\text{-}b\text{-}c} := \begin{pmatrix} \xi^{a\text{-}b} \\ \xi^{b\text{-}c} \\ \xi^{c\text{-}a} \end{pmatrix} := \underbrace{\begin{bmatrix} 1 & -1 & 0 \\ 0 & 1 & -1 \\ -1 & 0 & 1 \end{bmatrix}}_{=:\boldsymbol{T}_{\mathrm{ltl}}} \underbrace{\begin{pmatrix} \xi^a \\ \xi^b \\ \xi^c \end{pmatrix}}_{=:\boldsymbol{\xi}^{abc}}. \tag{A.3.22}$$

Remark A.3.1. *The matrix* $\boldsymbol{T}_{\mathrm{ltl}}$ *is not invertible, i.e.* $\det(\boldsymbol{T}_{\mathrm{ltl}}) = 0$*. This implies, there exists not just one combination of line value* $\boldsymbol{\xi}^{abc}$ *that cause the line-to-line values* $\boldsymbol{\xi}^{a\text{-}b\text{-}c}$*, but an infinite number of combinations of line values* $\boldsymbol{\xi}^{abc}$*.*

If the phase quantities fulfil condition (A.1.3), the matrix $\boldsymbol{T}_{\mathrm{ltl}}$ can be altered to obtain an invertible matrix given by

$$\boldsymbol{T}^{\star}_{\mathrm{ltl}} = \begin{bmatrix} 1 & -1 & 0 \\ 0 & 1 & -1 \\ 0 & 1 & 2 \end{bmatrix} \quad \Longleftrightarrow \quad (\boldsymbol{T}^{\star}_{\mathrm{ltl}})^{-1} = \begin{bmatrix} 1 & \frac{2}{3} & \frac{1}{3} \\ 0 & \frac{2}{3} & \frac{1}{3} \\ 0 & -\frac{1}{3} & \frac{1}{3} \end{bmatrix}. \tag{A.3.23}$$

So, if (A.1.3) holds, the phase quantities can be computed as follows

$$\boldsymbol{\xi}^{abc} = \begin{bmatrix} 1 & \frac{2}{3} & \frac{1}{3} \\ 0 & \frac{2}{3} & \frac{1}{3} \\ 0 & -\frac{1}{3} & \frac{1}{3} \end{bmatrix} \boldsymbol{\xi}^{a\text{-}b\text{-}c}. \tag{A.3.24}$$

Appendix B

Measurement of EESM flux linkage maps

This chapter describes the necessary steps to measure the flux linkage maps of an EESM without damper windings. Although, the used EESM in the laboratory (see Sect. 4.1) has damper windings, the proposed method can be used for measuring the machine parameters for synchronous operation. Only for changes in the currents (i.e. $\frac{\mathrm{d}}{\mathrm{d}t}\boldsymbol{i} \neq 0$), the damper windings influence the EESM (see (2.33)). This will also be shown in Sect. B.3 where the model is validated by comparing simulations and measurements.
The measurement of the EESM flux linkage maps can be divided into two steps. First the stator flux linkage maps are measured and afterwards the excitation flux linkage is determined.

B.1 Measurement of stator flux linkages

The system of equations (2.30) for an EESM without damper windings can be separated into stator and excitation to

$$\left.\begin{aligned} \boldsymbol{u}_s^{dq} &= \boldsymbol{R}_s^{dq}\boldsymbol{i}_s^{dq} + \tfrac{\mathrm{d}}{\mathrm{d}t}\boldsymbol{\psi}_s^{dq}\left(\boldsymbol{i}_s^{dq}, i_e\right) + \omega_e \boldsymbol{J}\boldsymbol{\psi}_s^{dq}\left(\boldsymbol{i}_s^{dq}, i_e\right) \\ u_e &= R_e(i_e)i_e + \tfrac{\mathrm{d}}{\mathrm{d}t}\psi_e\left(\boldsymbol{i}_s^{dq}, i_e\right). \end{aligned}\right\} \tag{B.1.1}$$

The flux linkages $\boldsymbol{\psi}_s^{dq}$ and ψ_e only depend on the three currents i_s^d, i_s^q and i_e. For steady state operation (i.e. $\frac{\mathrm{d}}{\mathrm{d}t}(\cdot) = 0$), the stator equation simplifies and the stator flux linkage can be computed directly by

$$\boldsymbol{\psi}_s^{dq}\left(\boldsymbol{i}_s^{dq}, i_e\right) = \tfrac{1}{\omega_e}\boldsymbol{J}^{-1}\left(\boldsymbol{u}_s^{dq} - \boldsymbol{R}_s^{dq}\boldsymbol{i}_s^{dq}\right). \tag{B.1.2}$$

Remark B.1.1 (Rotational speed)**.** *For the measurement of the flux linkage maps, a non-zero rotational speed (e.g. $\omega_e = 100\,\frac{\mathrm{rad}}{\mathrm{s}}$) is applied by the connected machine (here a DFIM) to avoid division in* (B.1.2) *by $\omega_e = 0\,\frac{\mathrm{rad}}{\mathrm{s}}$.*

Remark B.1.2 (Stator voltage)**.** *The stator voltages $\boldsymbol{u}_s^{dq}$ are usually not measured and, due to the converter, a signal with switched values (see Sect. 2.4.2). So instead of the applied stator voltages $\boldsymbol{u}_s^{dq}$, their reference values $\boldsymbol{u}_{s,\mathrm{ref}}^{dq}$ can be used for the flux linkage computation as in* (B.1.2)*. For steady state operation and a fault-free converter, the mean values of $\boldsymbol{u}_s^{dq}$ over one switching period and the reference values $\boldsymbol{u}_{s,\mathrm{ref}}^{dq}$ are equal (see Sect. 3.2.1).*

The measurement is conducted over a grid of $i_s^d \in [-i_{s,\max}; i_{s,\max}]$ and $i_s^q \in [-i_{s,\max}; i_{s,\max}]$ and constant i_e. This measurement is repeated for different values of $i_e \in [0; i_{e,\max}]$. Figure B.1

shows ψ_s^d for $i_e \in \{0, 6, 12, 18\}$ A. For increasing values of i_e, the absolute value of ψ_s^d increases, but the surface becomes flatter. Hence, the nonlinear behaviour of flux linkages and the resulting differential inductances (directional derivatives, see Sect. 2.3.3.2) over the currents i_s^d, i_s^q and i_e is clearly visible.

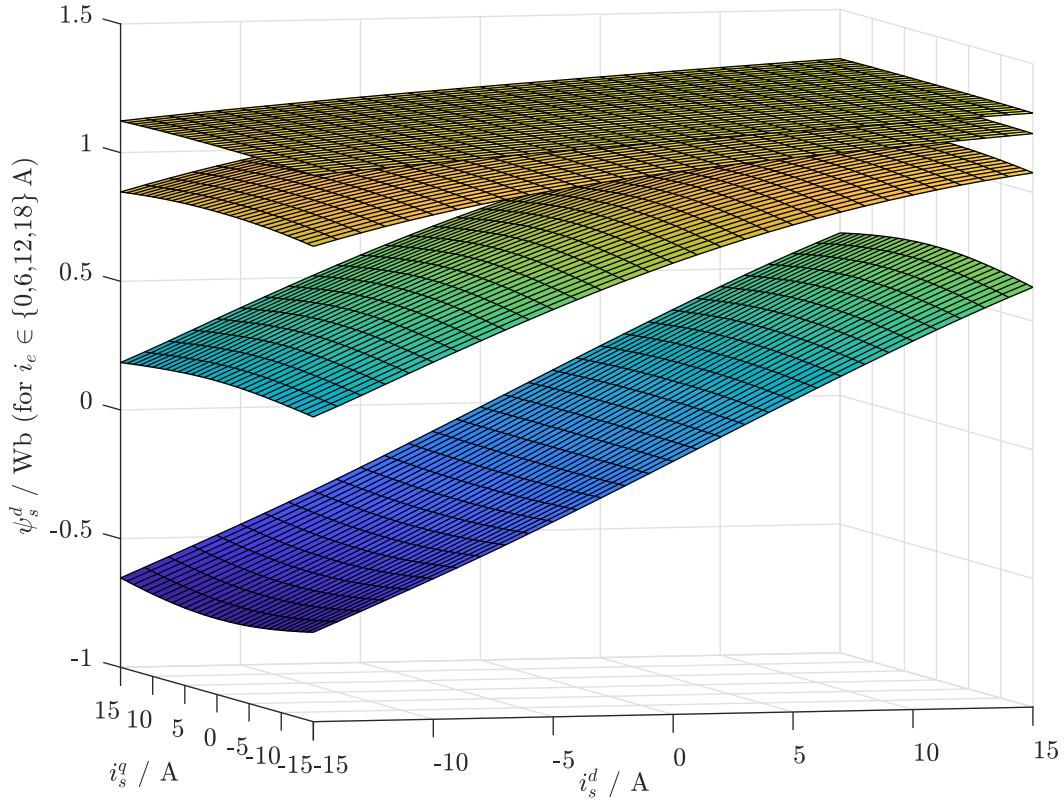

Figure B.1: *Plot of flux linkage ψ_s^d for $i_e \in \{0, 6, 12, 18\}$ A (lower plot for $i_e = 0$ A; increasing with i_e).*

B.1.1 Symmetrizing

The symmetry of the flux linkage of the EESM is used to correct possible measurement errors. Therefore, for ψ_s^d, the mean value of $\psi_{s,\mathrm{meas}}^d(i_s^d, i_s^q, i_e)$ and $\psi_{s,\mathrm{meas}}^d(i_s^d, -i_s^q, i_e)$ is used for both data points. For ψ_s^q, the mean value of $\psi_{s,\mathrm{meas}}^q(i_s^d, i_s^q, i_e)$ and $-\psi_{s,\mathrm{meas}}^q(i_s^d, -i_s^q, i_e)$ is used for both data points

$$\psi_s^d(i_s^d, i_s^q, i_e) = \psi_s^d(i_s^d, -i_s^q, i_e) = \tfrac{1}{2}\left(\psi_{s,\mathrm{meas}}^d(i_s^d, i_s^q, i_e) + \psi_{s,\mathrm{meas}}^d(i_s^d, -i_s^q, i_e)\right) \tag{B.1.3}$$

$$\psi_s^q(i_s^d, i_s^q, i_e) = -\psi_s^q(i_s^d, -i_s^q, i_e) = \tfrac{1}{2}\left(\psi_{s,\mathrm{meas}}^q(i_s^d, i_s^q, i_e) - \psi_{s,\mathrm{meas}}^q(i_s^d, -i_s^q, i_e)\right). \tag{B.1.4}$$

B.1.2 Removing outliers

Symmetrizing already reduces the influence of measurement errors. To further reduce the influence of outliers, the surfaces of ψ_s^d and ψ_s^q are smoothed, by using a linear regression algorithm (here *loess*-fitting of Matlab is used [120]).

B.1.3 Interpolation

In view of the high computational load, calculation efficiency and real-time application, look-up tables (LUTs) are usually read using linear interpolation only. Hence, if necessary, the collected

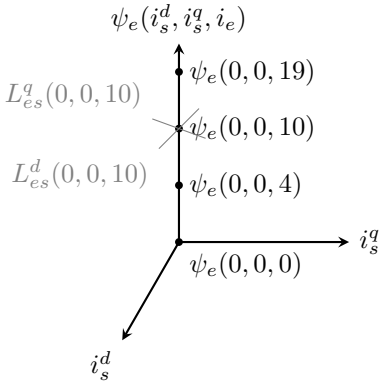

Figure B.2: *Schematic for* $\psi_e(0,0,i_e)$.

data could be interpolated in advance (e.g. using spline interpolation; here *thinplateinterp*-interpolation of Matlab is used [120]). This might give increased smoothness of the look-up tables for control, etc.

B.1.4 Computation of differential stator inductances

The differential inductances are the directional derivatives of the flux linkages in (2.38). Hence, based on the directional derivatives of the stator flux linkages, the values for L_s^{dd}, L_s^{dq}, L_{se}^d, L_s^{qd}, L_s^{qq}, L_{se}^q (the upper two rows of the inductance matrix $\boldsymbol{L}$ in (2.40)) can be calculated numerically and stored in LUTs as well.

B.2 Measurement of excitation flux linkage

So far, the two stator flux linkages ψ_s^d and ψ_s^q and the upper two rows of the inductance matrix $\boldsymbol{L}$ in (2.40) are known. For the complete reduced-order EESM model without damper windings, as derived in Sect. 2.3.3.2, the excitation flux linkage ψ_e and the lower row of the inductance matrix $\boldsymbol{L}$ is missing.

Assumption (AS.20) *Due to the construction of the electric machine, there is a constant relation* χ *between the stator-exciter coupling inductances [61, Sect. 2.8], i.e.*

$$\chi = \frac{L_{es}^d}{L_{se}^d} = \frac{L_{es}^q}{L_{se}^q}. \tag{B.2.5}$$

The relation χ is constant, but yet unknown and has to be determined for the used machine. For the calculation of the excitation flux linkage, a different method than that for the stator has to be used. Here, only the idea of the necessary steps to determine the excitation flux linkage is briefly sketched. Each step will be explained in detail in the following subsection.

Due to (B.2.5), the principle shape of the excitation flux linkage is already known. For each data point (i_s^d, i_s^q, i_e) the derivatives of ψ_e in i_s^d-direction ($\equiv L_{es}^d = \chi L_{se}^d$) and in i_s^q-direction ($\equiv L_{es}^q = \chi L_{se}^q$) provide the principle shape for the ψ_e flux linkage map. Figure B.2 shows a schematic for $\psi_e(0,0,i_e)$. The differential inductances L_{es}^d and L_{es}^q are the tangents of ψ_e in i_s^d- and i_s^q-direction, respectively. While the principle shape of the ψ_e flux linkage maps is clear, the offset to the i_s^d-i_s^q-plane (see Fig. B.2) is still unknown. The value of ψ_e for one point (i_s^d, i_s^q, i_e) is therefore sufficient to obtain the offset of the ψ_e-surface to the i_s^d-i_s^q-plane. The values for $\psi_e(0,0,i_e)$ can be obtained, if the excitation resistance $R_e(i_e, \omega_m)$ is known [121]. The procedure for computing the excitation flux linkage maps can be summarized in the following steps:

- **Step 1**: Measuring $R_e(i_e, \omega_m)$ for several $i_e \in [0; i_{e,\max}]$ and $\omega_m \in [-\omega_{m,\max}; \omega_{m,\max}]$.
- **Step 2**: Determining the values for $\psi_e(0, 0, i_e)$ for $i_e \in [0; i_{e,\max}]$.
- **Step 3**: Using L_{es}^d and L_{es}^q to calculate ψ_e for each measured data point $(i_s^d, i_s^q, i_e) \in [-i_{s,\max}; i_{s,\max}] \times [-i_{s,\max}; i_{s,\max}] \times [0; i_{e,\max}]$ by numerical integration.
- **Step 4**: Obtaining L_e by directional differentiation $\frac{\partial \psi_e}{\partial i_e}$ of ψ_e in i_e-direction for all measured data points $(i_s^d, i_s^q, i_e) \in [-i_{s,\max}; i_{s,\max}] \times [-i_{s,\max}; i_{s,\max}] \times [0; i_{e,\max}]$.
- **Step 5**: Determining the optimal relation $\chi = \frac{L_{es}^d}{L_{se}^d} = \frac{L_{es}^q}{L_{se}^q}$ by comparing simulation and measurement results.

Each step will be explained in more detail in the following subsections.

B.2.1 Step 1: Measurement of excitation resistance

The excitation resistance R_e is not a constant value. Due to the brush-slip-ring connection between rotor and machine, R_e is a function of the excitation current i_e and the machine speed ω_m. Figure B.3 shows this dependency. For small values of i_e, R_e depends on ω_m. For higher values of i_e, this dependency is not visible any more. In steady state operation ($\frac{\mathrm{d}}{\mathrm{d}t}(\cdot) = 0$), the resistance can be calculated using

$$R_e = \frac{u_e}{i_e}. \tag{B.2.6}$$

To obtain a complete map of $R_e(i_e, \omega_m)$, the resistance should be calculated for all applicable values of $i_e \in [0; i_{e,\max}]$ and $\omega_m \in [-\omega_{m,\max}; \omega_{m,\max}]$.

Remark B.2.1 (Special treatment of $i_e = 0$ and $\omega_m = 0$)**.** *For small values of $i_e \approx 0$, the calculation* (B.2.6) *is not reasonable any more (division by zero) and $R_e(0, \omega_m)$ has to be extrapolated from values with $i_e > 0$. Calculating R_e for $\omega_m = 0$ might also be prone to failure. Due to small deviations in the production process, the resistance of the brush-slip-ring connection might be angle dependent. To avoid that, $R_e(i_e, 0)$ should be interpolated based on values for $\omega_m < 0$ and $\omega_m > 0$.*

B.2.2 Step 2: Determining of excitation flux linkage for zero stator currents

Integration of the second equation in (B.1.1) leads to

$$\psi_e(i_s^d, i_s^q, i_e) = \int_0^t \left(u_e(\tau) - R_e(\tau) i_e(\tau)\right) \mathrm{d}\tau \tag{B.2.7}$$

and give a direct tool to "measure" the excitation flux linkage. Based on a measurement with $i_s^d = i_s^q = 0$, as shown in Fig B.4, the excitation flux linkage ψ_e can be computed for different values of i_e (the stator terminals are not connected, to secure $i_s^d = i_s^q = 0$). Based on the voltage ramp in the first subplot and the resulting current i_e, shown in the second subplot, the flux linkage ψ_e, shown in the lower subplot, can be computed. Starting the integration for values $(i_s^d, i_s^q, i_e) = (0, 0, 0)$ preserves the initial value $\psi_{e,0} = \psi_e(0, 0, 0) = 0$. Figure B.5 shows the resulting $\psi_e(0, 0, i_e)$ as a function of i_e (with the measured raw-data $\psi_{e,\mathrm{raw}}$ and the trendline ψ_e).

Remark B.2.2 (Using integration method for complete operating area)**.** *It is not advisable, to use the above described integration method to determine ψ_e for the complete operating*

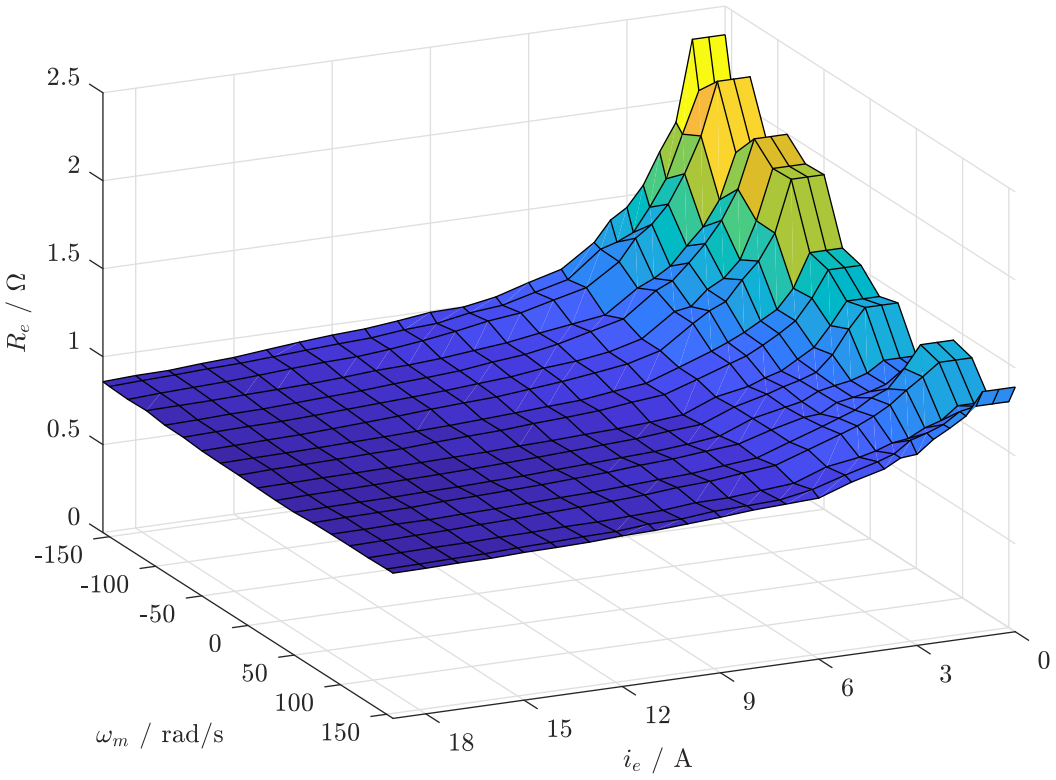

Figure B.3: *Excitation resistance R_e depending on rotational speed ω_m and excitation current i_e.*

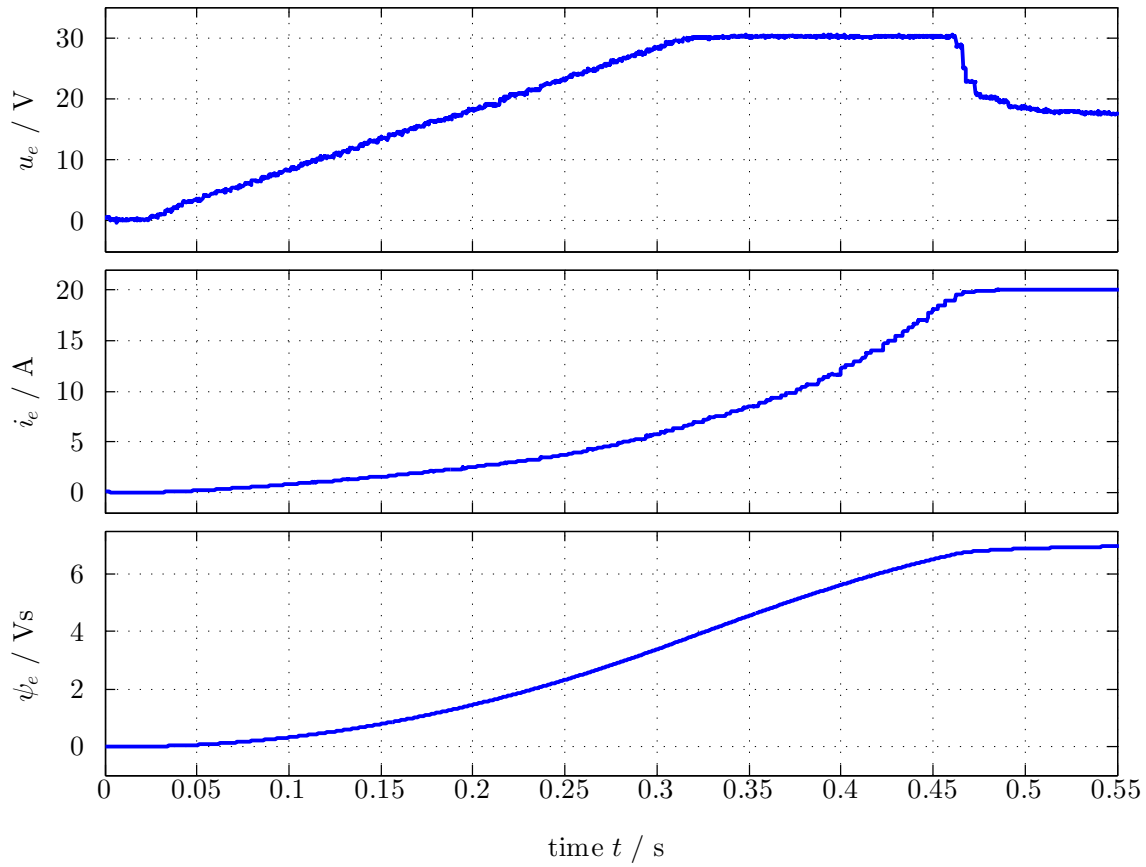

Figure B.4: *Excitation voltage ramp with resulting current and integrated excitation flux linkage.*

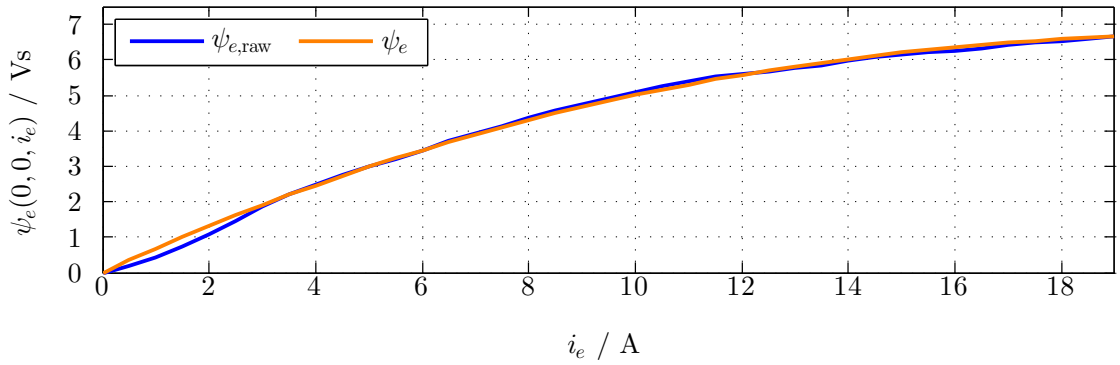

Figure B.5: $\psi_e(0,0,i_e)$ *as function of* i_e *(measured raw-data* $\psi_{e,\mathrm{raw}}$ *and trendline* ψ_e*).*

area $(i_s^d, i_s^q, i_e) \in [-i_{s,\max}; i_{s,\max}] \times [-i_{s,\max}; i_{s,\max}] \times [0; i_{e,\max}]$. *Only* $\psi_{e,0}$ *is a well defined initial value for the integration, so each measurement has to start at* $(i_s^d, i_s^q, i_e) = (0,0,0)$. *Additionally, as numerical integration, especially with measured signals, is prone to drifting, only short measurements are admissible, to obtain reliable results. The necessity of using the starting point* $(i_s^d, i_s^q, i_e) = (0,0,0)$ *and only short measurements, makes using this method cumbersome and hence not advisable for determining* ψ_e *for the complete operating area* $(i_s^d, i_s^q, i_e) \in [-i_{s,\max}; i_{s,\max}] \times [-i_{s,\max}; i_{s,\max}] \times [0; i_{e,\max}]$.

B.2.3 Step 3: Computation of complete excitation flux linkage

Similar to ψ_s^d and ψ_s^q, ψ_e is computed for fixed values of $i_e \in [0; i_{e,\max}]$ and the maps are combined afterwards (see Fig. B.2).

B.2.3.1 Computation of excitation coupling inductances

For the computation of ψ_e, the differential inductances L_{es}^d and L_{es}^q have to be known. They can be calculated based on L_{se}^d and L_{se}^q by using (B.2.5), i.e.

$$L_{es}^d \overset{(B.2.5)}{=} \chi L_{se}^d \quad \text{and} \quad L_{es}^q \overset{(B.2.5)}{=} \chi L_{se}^q. \tag{B.2.8}$$

B.2.3.2 Computation of excitation flux linkage map

For the values on the axes $i_s^d = 0$ and $i_s^q = 0$, the computation is performed in steps of Δi_s (in A), where n and Δi_s are chosen such that $n\Delta i_s = i_{s,\max}$ (see Fig. B.6). For $i \in [1; n]$ and $j \in [1; n]$, ψ_e is then given for the m-th excitation current (where m and Δi_e (in A) are chosen such that $i_{e,\max} = m\Delta i_e$) by

$$\left.\begin{aligned}
\psi_e[i,0,m] &= \psi_e[i-1,0,m] + \tfrac{L_{es}^d[i-1,0,m]+L_{es}^d[i,0,m]}{2}\Delta i_s, && \text{for } i_s^d > 0 \wedge i_s^q = 0\\
\psi_e[-i,0,m] &= \psi_e[-i+1,0,m] - \tfrac{L_{es}^d[-i+1,0,m]+L_{es}^d[-i,0,m]}{2}\Delta i_s, && \text{for } i_s^d < 0 \wedge i_s^q = 0\\
\psi_e[0,j,m] &= \psi_e[0,j-1,m] + \tfrac{L_{es}^q[0,j-1,m]+L_{es}^q[0,j,m]}{2}\Delta i_s, && \text{for } i_s^d = 0 \wedge i_s^q > 0\\
\psi_e[0,-j,m] &= \psi_e[0,-j+1,m] - \tfrac{L_{es}^q[0,-j+1,m]+L_{es}^q[0,-j,m]}{2}\Delta i_s, && \text{for } i_s^d = 0 \wedge i_s^q < 0.
\end{aligned}\right\} \tag{B.2.9}$$

The values of ψ_e which are not on the axes $i_s^d = 0$ or $i_s^q = 0$ can be calculated using different paths from the origin $\psi_e[0,0,m]$ with minimal length (see green and red path in Fig. B.6). To reduce uncertainties due to measurement errors, both possibilities are combined and a modification of

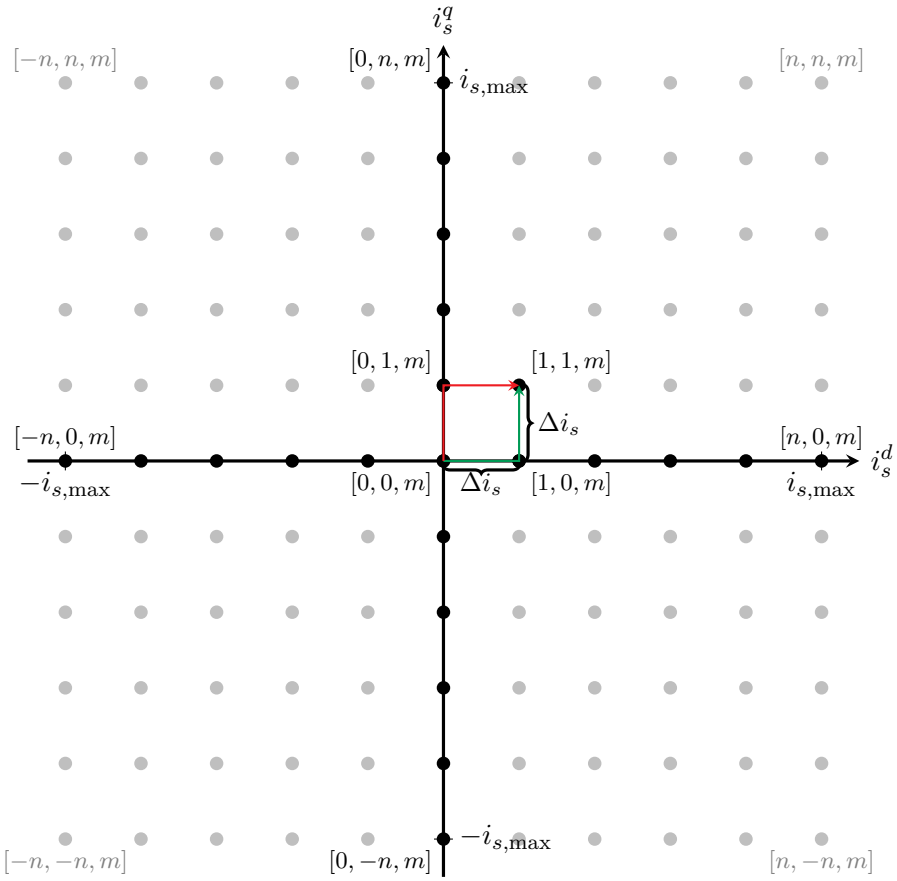

Figure B.6: i_s^d-i_s^q-*plain with discrete measurement points for the m-th excitation current.*

the method proposed in [122] is used, which leads to

$$\left.\begin{aligned}
\psi_e[i,j,m] &= \left\{\begin{array}{l}\frac{1}{2}\Big[\psi_e[i-1,j,m] + \frac{L_{es}^d[i-1,j,m]+L_{es}^d[i,j,m]}{2}\Delta i_s \\ \quad +\psi_e[i,j-1,m] + \frac{L_{es}^q[i,j-1,m]+L_{es}^q[i,j,m]}{2}\Delta i_s\Big]\end{array}\right\}, && \text{for } i_s^d > 0 \wedge i_s^q > 0 \\
\psi_e[-i,j,m] &= \left\{\begin{array}{l}\frac{1}{2}\Big[\psi_e[-i+1,j,m] - \frac{L_{es}^d[-i+1,j,m]+L_{es}^d[-i,j,m]}{2}\Delta i_s \\ \quad +\psi_e[-i,j-1,m] + \frac{L_{es}^q[-i,j-1,m]+L_{es}^q[-i,j,m]}{2}\Delta i_s\Big]\end{array}\right\}, && \text{for } i_s^d < 0 \wedge i_s^q > 0 \\
\psi_e[i,-j,m] &= \left\{\begin{array}{l}\frac{1}{2}\Big[\psi_e[i-1,-j,m] + \frac{L_{es}^d[i-1,-j,m]+L_{es}^d[i,-j,m]}{2}\Delta i_s \\ \quad +\psi_e[i,-j+1,m] - \frac{L_{es}^q[i,-j+1,m]+L_{es}^q[i,-j,m]}{2}\Delta i_s\Big]\end{array}\right\}, && \text{for } i_s^d > 0 \wedge i_s^q < 0 \\
\psi_e[-i,-j,m] &= \left\{\begin{array}{l}\frac{1}{2}\Big[\psi_e[-i+1,-j,m] - \frac{L_{es}^d[-i+1,-j,m]+L_{es}^d[-i,-j,m]}{2}\Delta i_s \\ \quad +\psi_e[-i,-j+1,m] - \frac{L_{es}^q[-i,-j+1,m]+L_{es}^q[-i,-j,m]}{2}\Delta i_s\Big]\end{array}\right\}, && \text{for } i_s^d < 0 \wedge i_s^q < 0.
\end{aligned}\right\} \tag{B.2.10}$$

B.2.4 Step 4: Computation of differential excitation inductance

After obtaining the excitation flux linkage ψ_e, the differential excitation inductance L_e can be computed by directional differentiation of ψ_e with respect to i_e.

B.2.5 Step 5: Determining the optimal relation of stator-exciter coupling

In order to determine the optimal relation $\chi = \frac{L^d_{es}}{L^d_{se}} = \frac{L^q_{es}}{L^q_{se}}$ for the EESM in the laboratory, measurements for several values of $\chi \in \{0.6, 0.65, \ldots, 1.05, 1.1\}$ are conducted. Beyond this range, the system in the laboratory becomes unstable. Note that the value of $\chi = \frac{3}{2}$ is used in [59, p. 39], [61, Sect. 2.8] and [73] for machine modelling with linear secant inductances ($\neq$ differential inductances). However, this value does not work for this machine. To find the optimal choice of χ, an experiment was conducted, where the computed nonlinear flux linkage maps were used for simulations and measurements in the laboratory for the controllers introduced in (3.33), but without compensation (3.35). In the simulation, the flux linkage maps were also used for modelling of the EESM.

Figure B.7 shows the comparison of simulation and measurement results for $\chi = 1$. For all investigated values of χ, the reference trajectories were identical. The upper plot shows the mechanical rotational speed ω_m and its reference. The speed deviates sometimes from $\omega_{m,\mathrm{ref}} = 50\,\frac{\mathrm{rad}}{\mathrm{s}}$ due to the huge steps in the torque of the EESM and the limited control performance of the speed-controlled load machine (DFIM, see Sect. 4.1.3). The second subplot shows the current i^d_s and its reference. The third subplot depicts the error $e_{i^d_s} := i^d_{s,\mathrm{meas}} - i^d_{s,\mathrm{sim}}$ (in A) between simulation and measurement. Simulation and measurement results do fit in steady state properly (the error is symmetric to the zero axis). Only for step changes in the reference $i^d_{s,\mathrm{ref}}$ or the other currents i^d_s and i_e, short differences in the transients are visible. The q-current, its reference and the error $e_{i^q_s} := i^q_{s,\mathrm{meas}} - i^q_{s,\mathrm{sim}}$ (in A) are shown in subplot four and five. While there are thin spikes in the error during transients, for steady state, the error is small and symmetric to zero. Subplots six and seven show the current i_e, its reference and the error $e_{i_e} := i_{e,\mathrm{meas}} - i_{e,\mathrm{sim}}$ (in A). Again, thin spikes in the error are visible during transients. But additionally, for $i_{e,\mathrm{ref}} = 0$, differences between simulation and measurement are visible. For higher values of $i_{e,\mathrm{ref}}$ the steady state error is symmetric around zero. The last two subplots show the machine torque τ_m and the error $e_{\tau_m} := \tau_{m,\mathrm{meas}} - \tau_{m,\mathrm{sim}}$ (in N m). Due to its dependence on the machine flux linkages and currents (see Sect. 2.3.3.2 and (2.41)), the behaviour of the machine torque is a combination of the behaviour of both quantities. There are thin spikes in the error during transients, for $i_{e,\mathrm{ref}} = 0$ and for higher values of $i_{e,\mathrm{ref}}$ there are also small steady state errors. The steady state error is symmetric to zero.

To compare conformity of simulation model and real world, simulation and measurement results for all $\chi \in \{0.6, 0.65, \ldots, 1.05, 1.1\}$ were evaluated and the following root mean square errors

$$\mathfrak{E}_{i^d_s} := \sqrt{\sum_{i=1}^{n} \left(i^d_{s,\mathrm{meas}}[i] - i^d_{s,\mathrm{sim}}[i] \right)^2 \frac{T_{\mathrm{sw}}}{1\,\mathrm{s}}} \qquad (\text{in A}) \tag{B.2.11}$$

$$\mathfrak{E}_{i^q_s} := \sqrt{\sum_{i=1}^{n} \left(i^q_{s,\mathrm{meas}}[i] - i^q_{s,\mathrm{sim}}[i] \right)^2 \frac{T_{\mathrm{sw}}}{1\,\mathrm{s}}} \qquad (\text{in A}) \tag{B.2.12}$$

$$\mathfrak{E}_{i_e} := \sqrt{\sum_{i=1}^{n} \left(i_{e,\mathrm{meas}}[i] - i_{e,\mathrm{sim}}[i] \right)^2 \frac{T_{\mathrm{sw}}}{1\,\mathrm{s}}} \qquad (\text{in A}) \tag{B.2.13}$$

$$\mathfrak{E}_{\tau} := \sqrt{\sum_{i=1}^{n} \left(\tau_{m,\mathrm{meas}}[i] - \tau_{m,\mathrm{sim}}[i] \right)^2 \frac{T_{\mathrm{sw}}}{1\,\mathrm{s}}} \qquad (\text{in N m}) \tag{B.2.14}$$

over the whole time span $t \in [0; 55\,\mathrm{s}]$ were computed. These mean square errors are plotted in Fig. B.8 over χ. The first subplot shows $\mathfrak{E}_{i^d_s}$, the second subplot $\mathfrak{E}_{i^q_s}$, the third subplot $\mathfrak{E}_{i_e}$ and the lower subplot $\mathfrak{E}_{\tau}$.

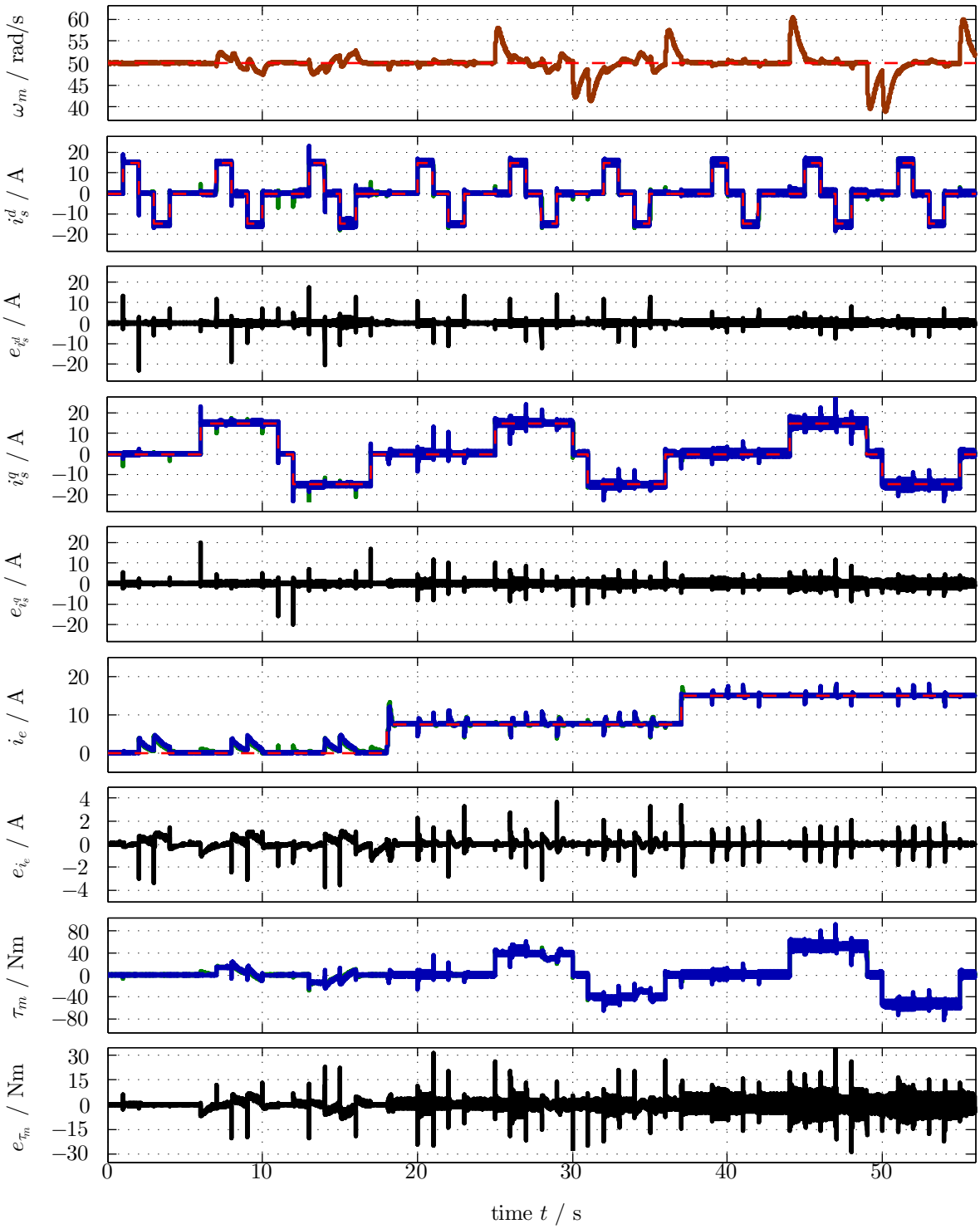

Figure B.7: *Comparison of measurement and simulation results for $\chi = 1$ with colour code:* — *measured quantity,* — *simulation quantity and* - - - *reference.*

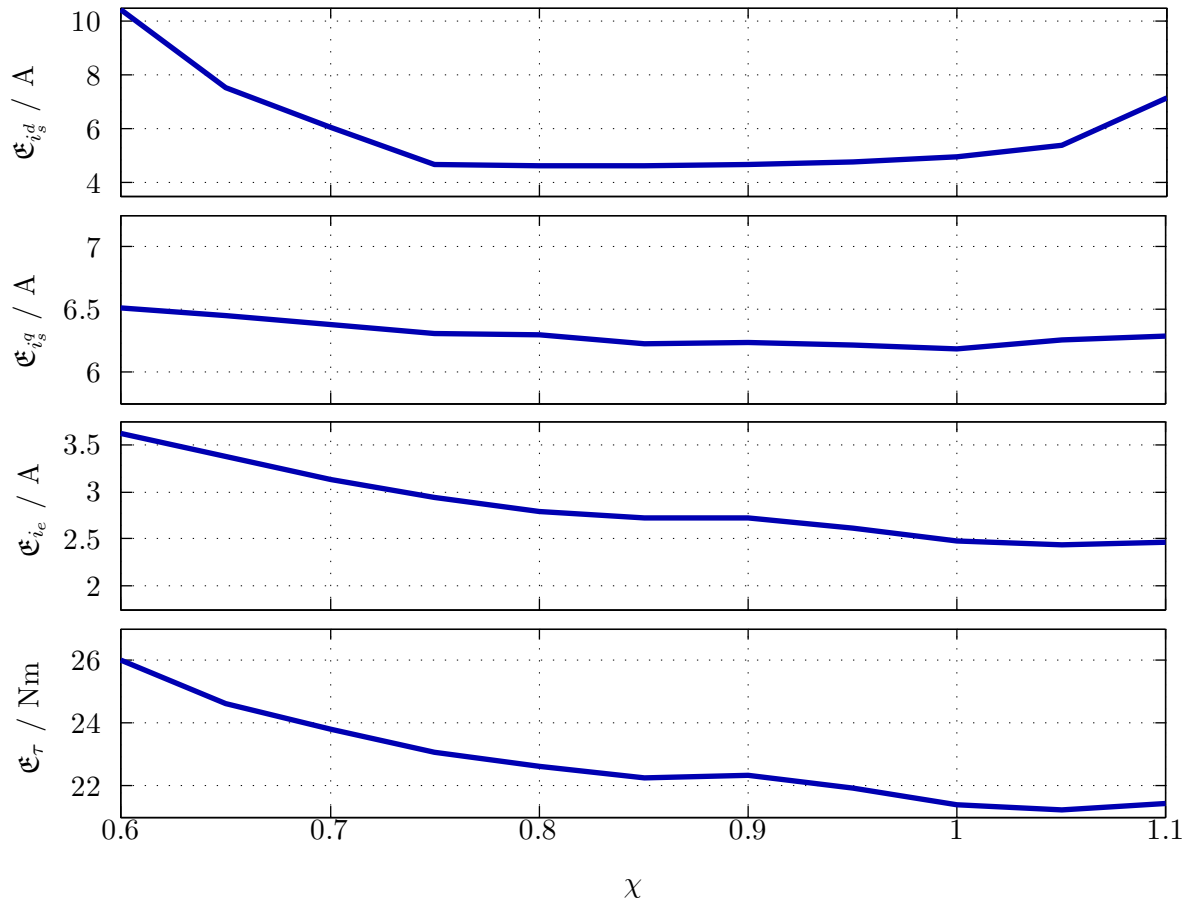

Figure B.8: *Plot of errors* $\mathfrak{E}_{i_s^d}$, $\mathfrak{E}_{i_s^q}$, $\mathfrak{E}_{i_e}$ *and* $\mathfrak{E}_\tau$ *over* χ.

In conclusion, $\chi = 1$ minimizes (almost) all four errors $\mathfrak{E}_{i_s^d}$, $\mathfrak{E}_{i_s^q}$, $\mathfrak{E}_{i_e}$ and $\mathfrak{E}_\tau$ (see Fig. B.8). Hence, $\chi = 1$ is chosen as optimal ratio between the inductances L_{se}^d/L_{se}^q and L_{es}^d/L_{es}^q, respectively.

B.3 Verification of machine model with nonlinear flux linkages

The validation of the developed model is done in two steps. First the static behaviour is compared, afterwards the dynamic behaviour is discussed.
The flux linkage maps for constant excitation current $i_e = 6\,\mathrm{A}$ and $i_e = 18\,\mathrm{A}$ are shown in Fig. B.9 and Fig. B.10, respectively. The upper three plots show the flux linkages ψ_s^d, ψ_s^q and ψ_e over i_s^d and i_s^q. The lower nine subplots show the differential inductances L_s^{dd}, L_s^{dq}, L_{se}^d, L_s^{qd}, L_s^{qq}, L_{se}^q, L_{es}^d, L_{es}^q and L_e of the EESM, respectively. For a better visibility, the i_s^d-axis is reversed for the inductances. Comparing Fig. B.9 and Fig. B.10 shows that the flux linkages are flatter for $i_e = 18\,\mathrm{A}$, because of saturation effects. Therefore all inductances are smaller for $i_e = 18\,\mathrm{A}$ than for $i_e = 6\,\mathrm{A}$.

B.3.1 Static verification

For the static validation, the torque τ_{meas} measured in the laboratory[46], the calculated torque τ_{calc} using the nonlinear flux linkage maps and the calculated torque $\tau_{\mathrm{calc},L}$ using constant

[46]The torque measured by the torque sensor (see Fig. 4.4) is corrected using the friction curve (see Fig. 4.7) and the "breaking torque" τ_{i_e} (see Fig. 4.6) to obtain the real torque τ_{meas} produced by the EESM.

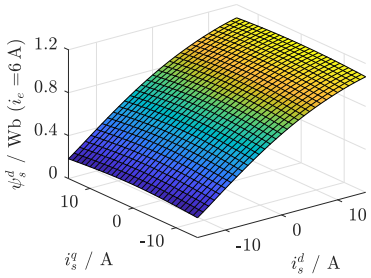

(a) d-component ψ_s^d of stator flux linkage.

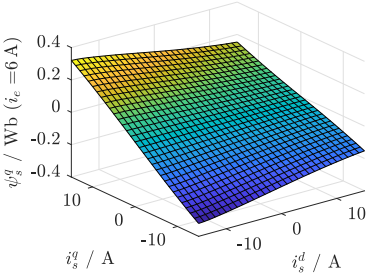

(b) q-component ψ_s^q of stator flux linkage.

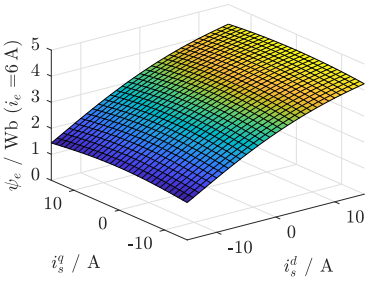

(c) Excitation flux linkage ψ_e.

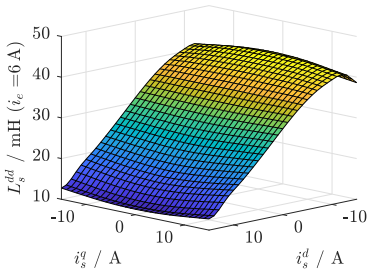

(d) Differential dd-component $L_s^{dd} := \frac{\partial \psi_s^d}{\partial i_s^d}$ of stator inductance.

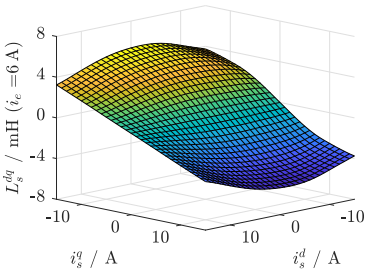

(e) Differential dq-component $L_s^{dq} := \frac{\partial \psi_s^d}{\partial i_s^q}$ of stator inductance.

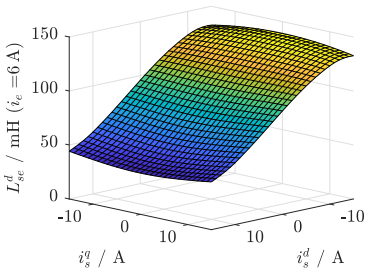

(f) Differential d-component $L_{se}^d := \frac{\partial \psi_s^d}{\partial i_e}$ of stator coupling inductance.

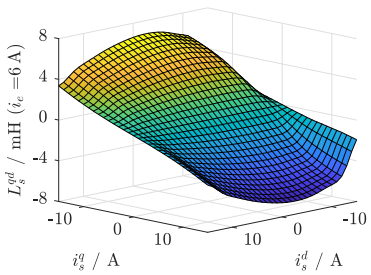

(g) Differential qd-component $L_s^{qd} := \frac{\partial \psi_s^q}{\partial i_s^d}$ of stator inductance.

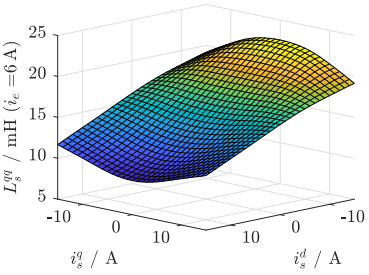

(h) Differential qq-component $L_s^{qq} := \frac{\partial \psi_s^q}{\partial i_s^q}$ of stator inductance.

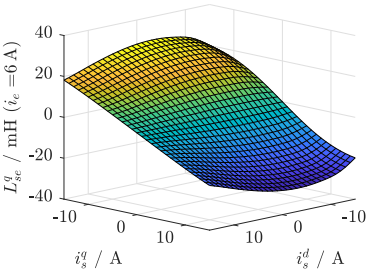

(i) Differential q-component $L_{se}^q := \frac{\partial \psi_s^q}{\partial i_e}$ of stator coupling inductance.

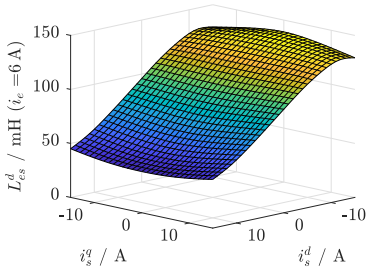

(j) Differential d-component $L_{es}^d := \frac{\partial \psi_e}{\partial i_s^d}$ of excitation coupling inductance.

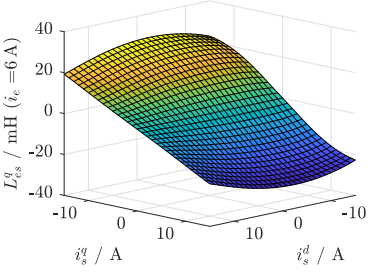

(k) Differential q-component $L_{es}^q := \frac{\partial \psi_e}{\partial i_s^q}$ of excitation coupling inductance.

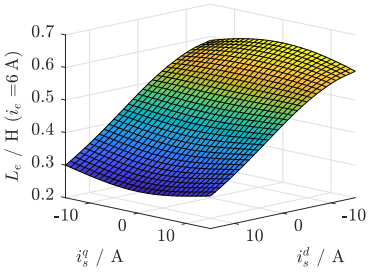

(l) Differential excitation inductance $L_e := \frac{\partial \psi_e}{\partial i_e}$.

Figure B.9: *Flux linkages and differential inductances of the EESM excited by* $i_e = 6\,\mathrm{A}$.

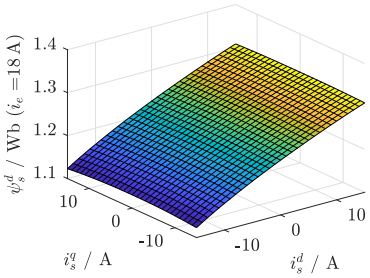

(a) d-component ψ_s^d of stator flux linkage.

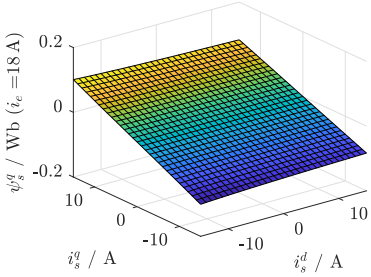

(b) q-component ψ_s^q of stator flux linkage.

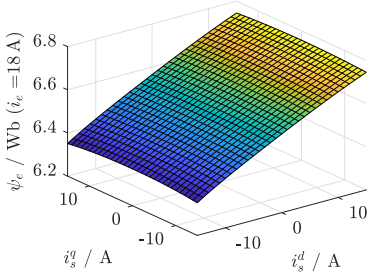

(c) Excitation flux linkage ψ_e.

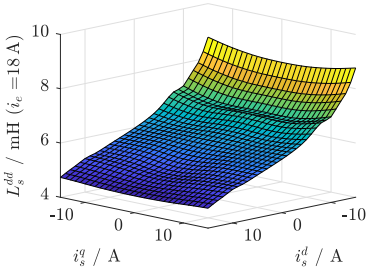

(d) Differential dd-component $L_s^{dd} := \frac{\partial \psi_s^d}{\partial i_s^d}$ of stator inductance.

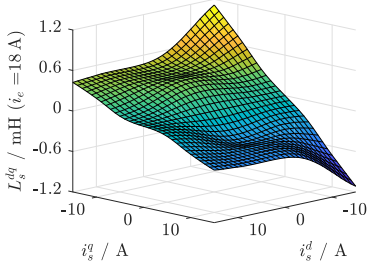

(e) Differential dq-component $L_s^{dq} := \frac{\partial \psi_s^d}{\partial i_s^q}$ of stator inductance.

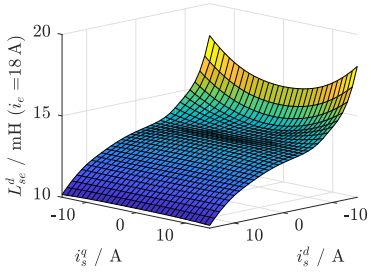

(f) Differential d-component $L_{se}^d := \frac{\partial \psi_s^d}{\partial i_e}$ of stator coupling inductance.

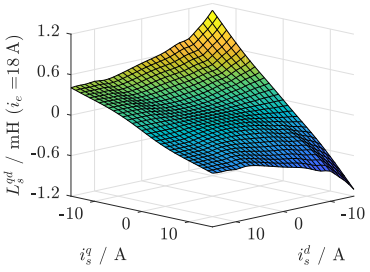

(g) Differential qd-component $L_s^{qd} := \frac{\partial \psi_s^q}{\partial i_s^d}$ of stator inductance.

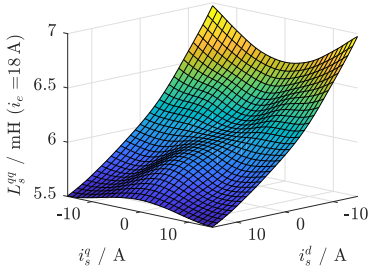

(h) Differential qq-component $L_s^{qq} := \frac{\partial \psi_s^q}{\partial i_s^q}$ of stator inductance.

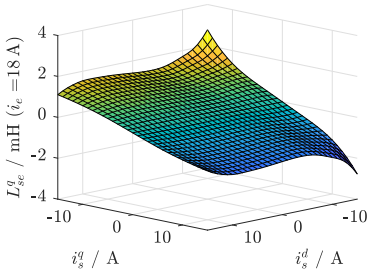

(i) Differential q-component $L_{se}^q := \frac{\partial \psi_s^q}{\partial i_e}$ of stator coupling inductance.

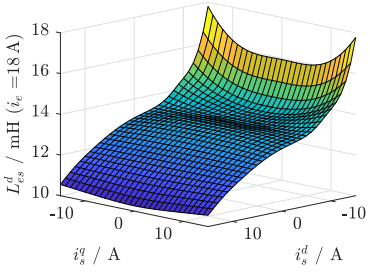

(j) Differential d-component $L_{es}^d := \frac{\partial \psi_e}{\partial i_s^d}$ of excitation coupling inductance.

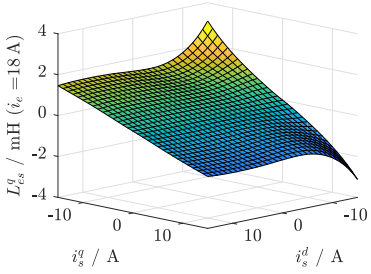

(k) Differential q-component $L_{es}^q := \frac{\partial \psi_e}{\partial i_s^q}$ of excitation coupling inductance.

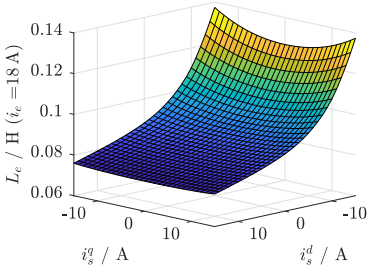

(l) Differential excitation inductance $L_e := \frac{\partial \psi_e}{\partial i_e}$.

Figure B.10: *Flux linkages and differential inductances of the EESM excited by* $i_e = 18\,\mathrm{A}$.

inductances[47] are compared. Figure B.11 shows the three torques in the upper subplots for $i_e = 6\,\mathrm{A}$, $i_e = 12\,\mathrm{A}$ and $i_e = 18\,\mathrm{A}$. The lower subplot shows the errors $\tau_{\mathrm{meas}} - \tau_{\mathrm{calc}}$ and $\tau_{\mathrm{meas}} - \tau_{\mathrm{calc},L}$. For a better visibility, the axes i_s^d and i_s^q are reversed in the lower subplots. It can be seen, that the error $\tau_{\mathrm{meas}} - \tau_{\mathrm{calc}}$ using the nonlinear flux linkage maps is very small for all cases and currents. On the contrary, the error $\tau_{\mathrm{meas}} - \tau_{\mathrm{calc},L}$ reaches values larger than 50 % of the measured torque τ_{meas}. The error is smaller for values close to the chosen reference point ($i_s^d = 0\,\mathrm{A}$, $i_s^q = 0\,\mathrm{A}$ and $i_e = 10\,\mathrm{A}$). But for $i_e = 6\,\mathrm{A}$ and $i_e = 18\,\mathrm{A}$, the error $\tau_{\mathrm{meas}} - \tau_{\mathrm{calc},L}$ can become very large (see Fig. B.11(j) and Fig. B.11(l)). Concluding, the use of constant inductances causes huge deviations between EESM model and real machine and should be avoided.

B.3.2 Dynamic verification

Measured and simulated quantities are compared for the validation of the dynamic behaviour as well. For measurement and simulations, the same controllers as in (3.35) with constant gains (3.36) were used. The measurement results are compared with two simulation results:

($\mathrm{S}_{\mathrm{B.1}}$) Using measured flux linkage maps for EESM simulation.

($\mathrm{S}_{\mathrm{B.2}}$) Using constant inductances and flux linkages (for $i_s^d = 0\,\mathrm{A}$, $i_s^q = 0\,\mathrm{A}$ and $i_s^d = 10\,\mathrm{A}$, as were the basis for the controller tuning in (3.36)) for EESM simulation.

Figure B.12 shows all three results. In subplot one, the rotational speed ω_m of the machine and its reference are depicted. Subplots two and three show the d-currents and the errors between measurement and simulations. The measured and simulated currents do match in steady state. During the transients, there are short spikes in the error signals. The q-currents and the respective errors are shown in subplots four and five. Here, the signals match in steady state as well. During transients short spikes are visible in the error signal. Subplots six and seven depict the current i_e and the errors between measurement and simulations. The signals do match better for higher currents i_e, but for smaller currents, the model with constant inductances (Simulation ($\mathrm{S}_{\mathrm{B.2}}$)) does deviate from the measurement significantly. The last two subplots show the torques and the error of the torque signals. The signals of measurement and Simulation ($\mathrm{S}_{\mathrm{B.1}}$), using the nonlinear flux linkage maps, do match very closely. The error is small, except for thin spikes for transients for $i_{e,\mathrm{ref}} = 0$, and symmetric to zero. On the contrary, the torque of Simulation ($\mathrm{S}_{\mathrm{B.2}}$), using constant inductances, deviates significantly from the measurement results for all torques $\tau_m \neq 0$. Although the currents of measurement and both simulations are very similar throughout the whole plot, the torque of Simulation ($\mathrm{S}_{\mathrm{B.2}}$) deviates significantly from measurement and Simulation ($\mathrm{S}_{\mathrm{B.1}}$).
Figure B.13 shows the same measurement and simulations as in Fig. B.12, but additionally the voltages $u_{s,\mathrm{ref}}^d$, $u_{s,\mathrm{ref}}^q$ and $u_{e,\mathrm{ref}}$. The upper subplot shows the mechanical speed ω_m and its reference, subplot two shows i_s^d, subplot three i_s^q and subplot four i_e. The subplots were already described above. Subplot five depicts $u_{s,\mathrm{ref}}^d$. As the actual applied voltage is not measured, since it is a switched signal due to the converter (see Sect. 2.4.2 and Sect. 3.2.1), the reference voltage is shown as approximation ($u_{s,\mathrm{ref}}^d \approx u_s^d$ over one switching period T_{sw}). The voltages of measurement and Simulation ($\mathrm{S}_{\mathrm{B.1}}$) do coincide. But $u_{s,\mathrm{ref}}^d$ of Simulation ($\mathrm{S}_{\mathrm{B.2}}$) deviates significantly. The same is true for $u_{s,\mathrm{ref}}^q$ depicted in subplot six. For $u_{e,\mathrm{ref}}$ shown in the lower subplot, the signals of measurement and both simulations do match.

[47] For the model with constant inductances, the nonlinear flux linkage maps are evaluated at $i_s^d = 0\,\mathrm{A}$, $i_s^q = 0\,\mathrm{A}$ and $i_e = 10\,\mathrm{A}$ and are used as constants.

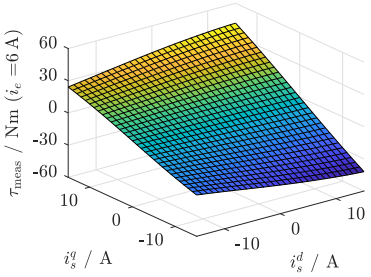

(a) Measured torque τ_{meas} for $i_e = 6\,\mathrm{A}$.

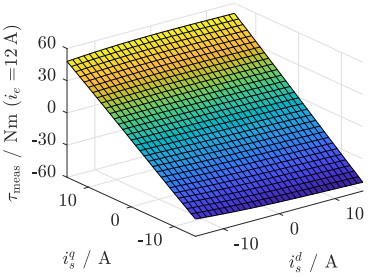

(b) Measured torque τ_{meas} for $i_e = 12\,\mathrm{A}$.

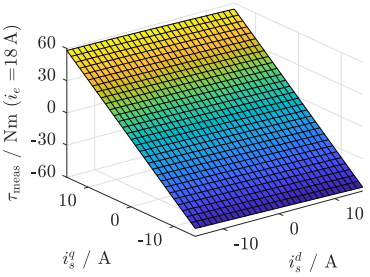

(c) Measured torque τ_{meas} for $i_e = 18\,\mathrm{A}$.

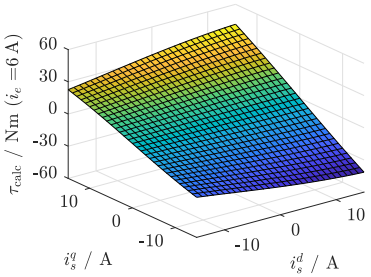

(d) Calculated torque τ_{calc} for $i_e = 6\,\mathrm{A}$.

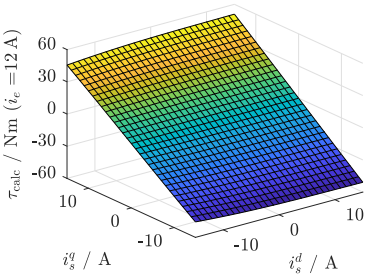

(e) Calculated torque τ_{calc} for $i_e = 12\,\mathrm{A}$.

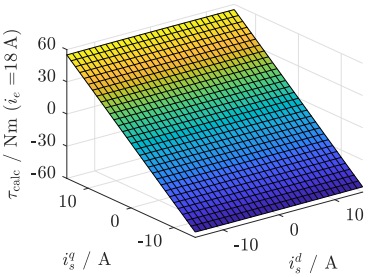

(f) Calculated torque τ_{calc} for $i_e = 18\,\mathrm{A}$.

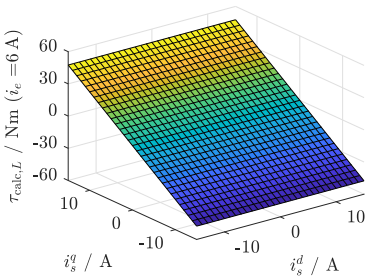

(g) Calculated torque $\tau_{\mathrm{calc},L}$ for $i_e = 6\,\mathrm{A}$.

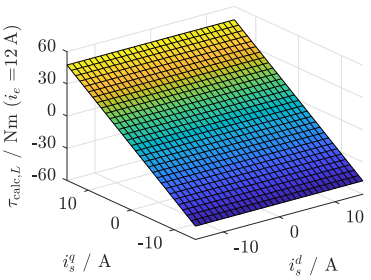

(h) Calculated torque $\tau_{\mathrm{calc},L}$ for $i_e = 12\,\mathrm{A}$.

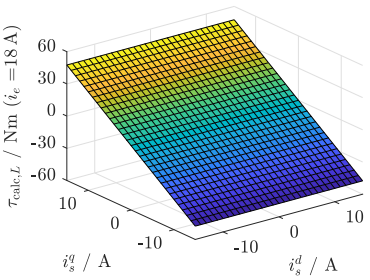

(i) Calculated torque $\tau_{\mathrm{calc},L}$ for $i_e = 18\,\mathrm{A}$.

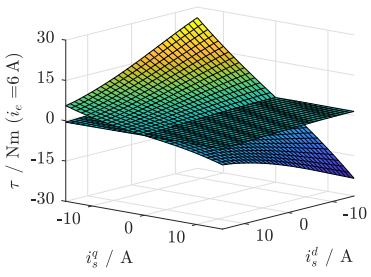

(j) Torque differences $\tau_{\mathrm{meas}} - \tau_{\mathrm{calc}}$ and $\tau_{\mathrm{meas}} - \tau_{\mathrm{calc},L}$ for $i_e = 6\,\mathrm{A}$.

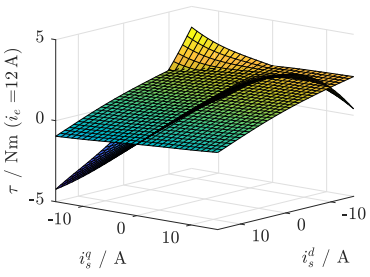

(k) Torque differences $\tau_{\mathrm{meas}} - \tau_{\mathrm{calc}}$ and $\tau_{\mathrm{meas}} - \tau_{\mathrm{calc},L}$ for $i_e = 12\,\mathrm{A}$.

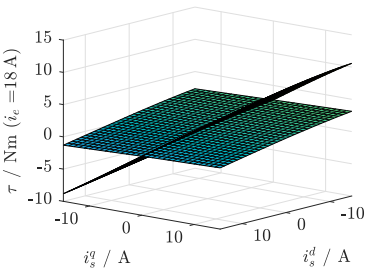

(l) Torque differences $\tau_{\mathrm{meas}} - \tau_{\mathrm{calc}}$ and $\tau_{\mathrm{meas}} - \tau_{\mathrm{calc},L}$ for $i_e = 18\,\mathrm{A}$.

Figure B.11: *Measured torque, calculated torque, calculated torque for L = const. and torque differences for the EESM excited by $i_e = 6\,\mathrm{A}$, $i_e = 12\,\mathrm{A}$ and $i_e = 18\,\mathrm{A}$.*

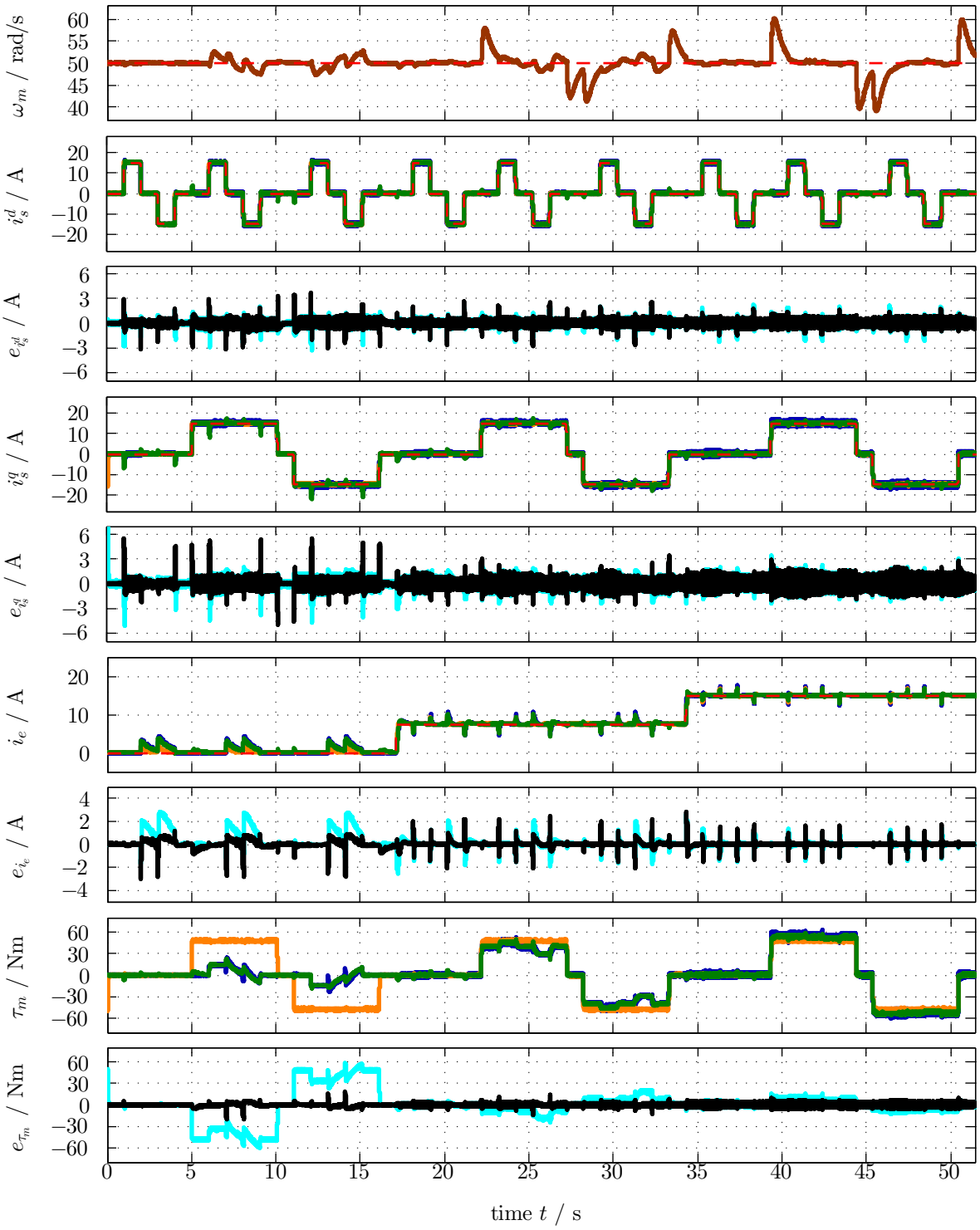

Figure B.12: *Comparison of measurement and simulation results for different modelling approaches with colour code:* — *measured quantity,* — *Simulation* ($S_{B.1}$) *quantity,* — *Simulation* ($S_{B.2}$) *quantity,* — *error "measurement – Simulation* ($S_{B.1}$)*",* — *error "measurement – Simulation* ($S_{B.2}$)*" and* - - - *reference.*

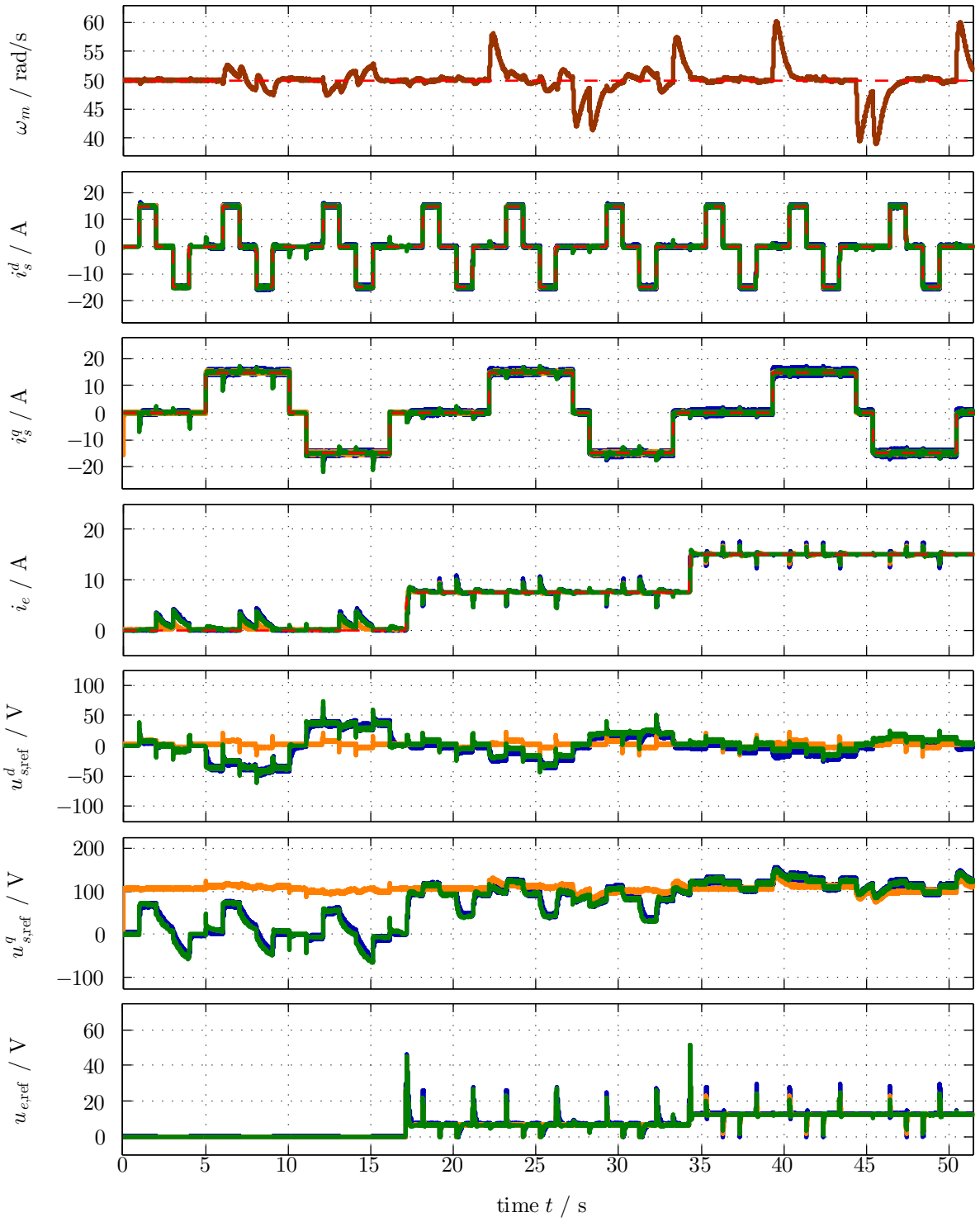

Figure B.13: *Comparison of measurement and simulation results for different modelling approaches with colour code:* — *measured quantity,* — *Simulation* ($S_{B.1}$) *quantity,* — *Simulation* ($S_{B.2}$) *quantity and* - - - *reference.*

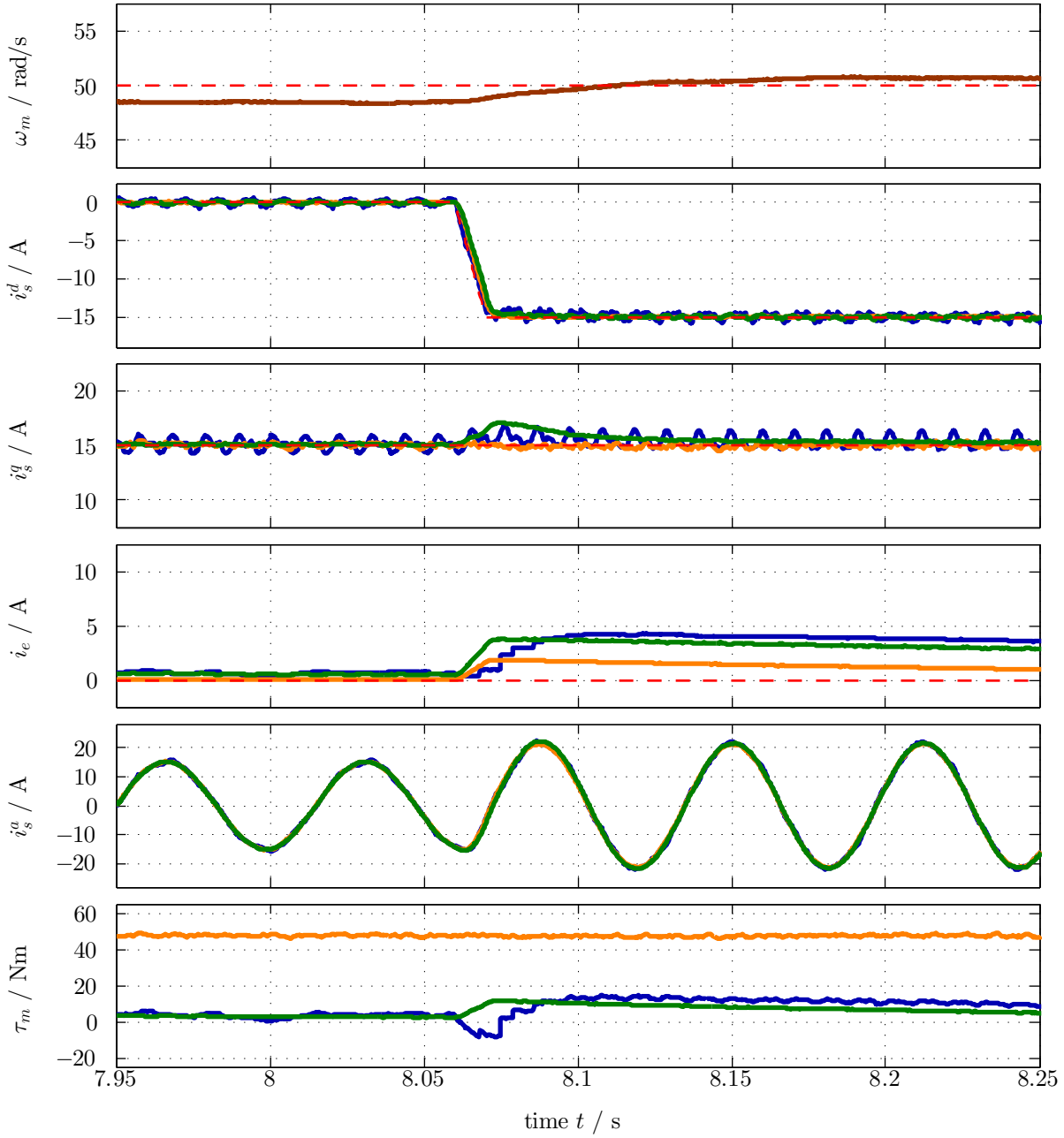

Figure B.14: *Comparison of measurement and simulation results for different modelling approaches with colour code:* — *measured quantity,* — *Simulation* ($S_{B.1}$) *quantity,* — *Simulation* ($S_{B.2}$) *quantity and* - - - *reference (zoom).*

In Fig. B.14, a zoom of Fig. B.12 around 8 s is shown. The first subplot shows the mechanical speed ω_m and its reference. The second subplot shows the current i_s^d. For the reference ramp[48] at 8.05 s, the measured and simulated signals follow the reference. Subplot three shows i_s^q. The measured signal oscillates more than those of Simulation ($S_{B.1}$) and Simulation ($S_{B.2}$). While Simulation ($S_{B.2}$) is not influenced by the step change in i_s^d, measurement and Simulation ($S_{B.1}$) are affected. Subplot four shows i_e. One sees the low time resolution of the dc-source used for excitation. Measurement and Simulation ($S_{B.1}$) are similar after the step change. Simulation ($S_{B.2}$)

[48]For the reference signals, ramps were used to limit the gradient and, thereby, reduce the influence of the damper windings.

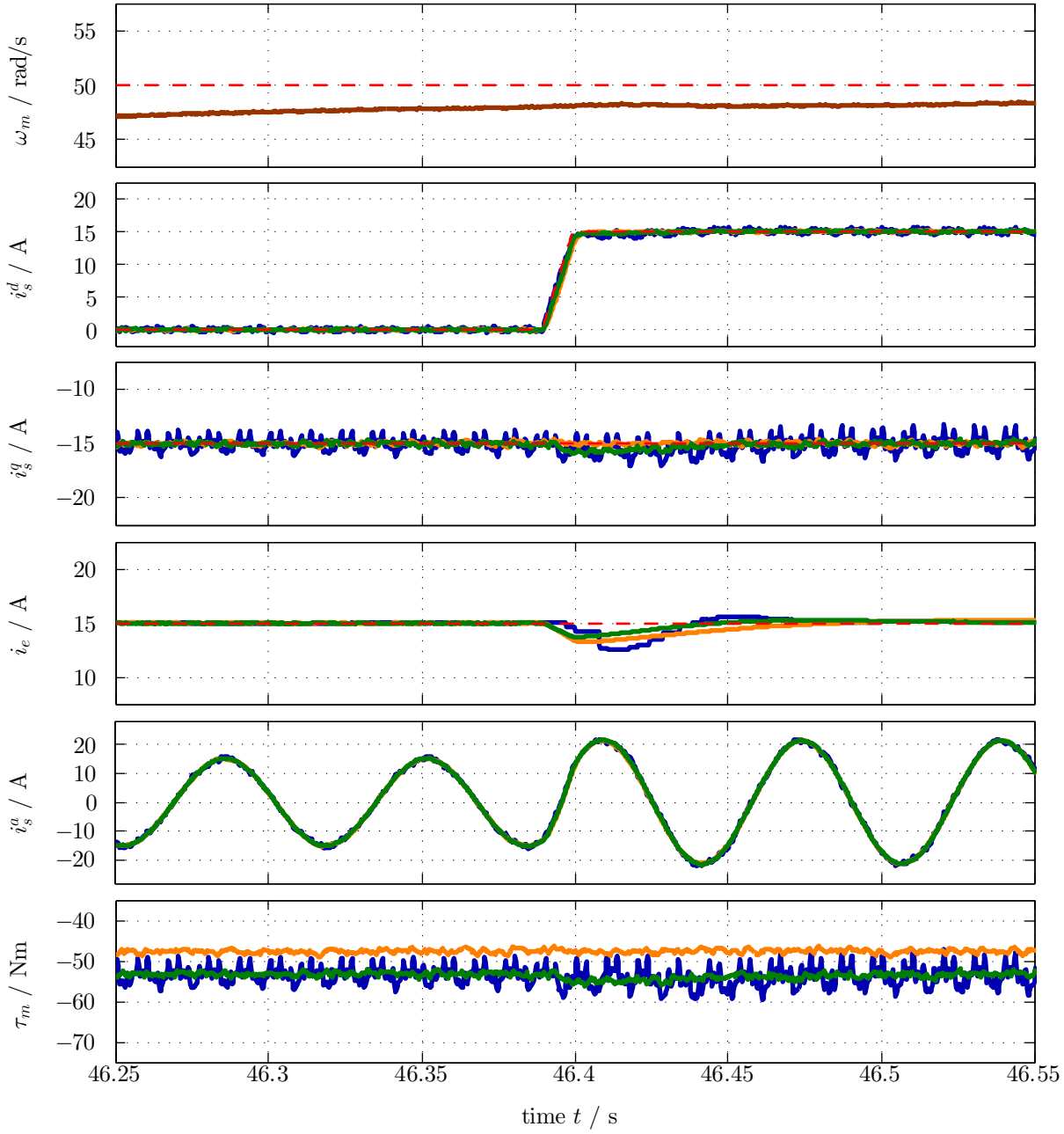

Figure B.15: *Comparison of measurement and simulation results for different modelling approaches with colour code:* — *measured quantity,* — *Simulation* ($S_{B.1}$) *quantity,* — *Simulation* ($S_{B.2}$) *quantity and* - - - *reference (zoom).*

deviates from the measurement. In subplot five, the current i_s^a of phase a is shown. Except for some small deviations directly after the reference ramp, measurement and both simulations do match. The last subplot depicts the machine torque τ_m. The torque signal of Simulation ($S_{B.2}$) is significantly deviating from the measurement for the whole experiment. Besides the short period of time after 8.05 s, measurement and Simulation ($S_{B.1}$) results are similar. While the torque of Simulation ($S_{B.1}$) becomes positive after 8.05 s, the measured torque becomes negative. This is due to the fact, that for Simulation ($S_{B.1}$), i_e rises faster while i_s^d decreases. Therefore, a positive d-flux linkage is present in the machine, which causes for a positive current i_s^q, a positive torque τ_m (see Sect. 2.3.3 and Fig. B.9-Fig. B.11). For the measurement, the d-flux

linkage first becomes negative (and so the torque τ_m) until i_e increases and the d-flux linkage becomes positive.
Figure B.15 shows a zoom of Fig. B.12 around 46.4 s. The signals are the same as in Fig. B.14, which was described above. Although the signals i_e (subplot four) of measurement and Simulation ($\mathrm{S_{B.1}}$) are different directly after the reference ramp around 46.4 s, the torque τ_m (subplot six) does not differ as much as in Fig. B.14. This is due to the saturation of the d-flux linkage for high values of i_e (compare Fig. B.9 and Fig. B.10) and the small changes of ψ_s^d for changes in i_s^d. The torque τ_m of Simulation ($\mathrm{S_{B.2}}$) has again a constant offset compared to the measurement signal.
All in all, the results of measurement and Simulation ($\mathrm{S_{B.1}}$) match very well. Deviations only appear during transients due to the damper windings in the EESM and the low time resolution of the dc-source for excitation. Both effects were *not* modelled and, hence, were not simulated. Simulation of the machine using constant inductances as in Simulation ($\mathrm{S_{B.2}}$) leads to matching currents (due to the controller), but wrong torque and wrong voltages. In conclusion, modelling of EESMs with constant inductances leads to wrong results (at least for the investigated EESM in the laboratory).